Analysis of the Aerodynamics of Tumbling Spacecraft During Orbital Decay and Reentry

by

Candice Kaplan Martin

A dissertation submitted in partial fulfillment
of the requirements for the degree of
Doctor of Philosophy
(Aerospace Engineering)
in the University of Michigan
2021

Doctoral Committee:

Professor James W. Cutler, Chair
Professor Iain D. Boyd
Professor Ilya Vladimir Kolmanovsky
Professor Aaron D. Ridley

Candice K. Martin
cikaplan@umich.edu
ORCID iD: 0000-0001-9355-7024

ACKNOWLEDGEMENTS

So many people (and also many cats) made this work possible. I would first like to thank all the members, past and current, of the Nonequilibrium Gas and Plasma Dynamics Laboratory at the University of Michigan. Especially helpful and supportive were my qualifying exams study group: Kaelan Hansson, Mike Holloway, Alex Vazsonyi, and Kevin Doetsch. I could not have gotten to this point without them!

I would also like to give credit to the other women in NGPDL. Thank you to Lauren Mackey, Astrid Raisanen, Erin Farbar, and Mackenzie Meyer, for being amazing role models for me. You made it a lot easier to go through this process, since you did it so well first.

Thanks to the National Science Foundation for providing me the opportunity to pursue this graduate work in the first place through awarding me their graduate fellowship.

Thank you to my committee members: Professor Ilya Vladimir Kolmanovsky, Professor Aaron Ridley, and of course Professor Jamie Cutler (go Colonials!).

And of course thank you to Professor Iain Boyd, for supporting my growth in the lab and outside of it. Your feedback was always appreciated and made me a much better engineer!

Thanks to my mom, for always sending and bringing me happy stickers and ham - both essential to power through coding or writing sessions.

Thanks to my father for instilling in me confidence and courage from a young age.

Thanks to the rest of my family as well, especially my Uncle John. I've come a long way from burning the bacon in 2004!

Also thanks to all the myriad of other smart friends I have. Kate, Connor, Ann, Amanda, Nathan, Katy, Luke, Jonny, and many more that I can't name here or else my thesis would be over

400 pages.

And of course, thank you to my husband Eric, who always told me that I could do this when it felt like it was so far away. Now we're Drs. Martin, a true physics-aerospace love story for the ages.

Last (but certainly not least) I would like to thank Astro, Luna, Gemma, Goldie, and my handful of foster kittens. You truly have reminded me what matters by sitting on my hands as I type this.

TABLE OF CONTENTS

LIST OF FIGURES

FIGURE

LIST OF TABLES

TABLE

LIST OF APPENDICES

APPENDIX

ABSTRACT

Space debris present many potential problems, such as collisions with functional spacecraft and safety hazards. As more satellites are launched every year, the population of space debris is growing faster than satellites and space objects are reentering the Earth's atmosphere. With little data on the reentry and breakup of space debris, there is a need for high-fidelity modeling of various space objects experiencing orbital decay and reentry. Accurate prediction of aerodynamic forces on high altitude orbiting and reentering space objects is necessary for understanding reentry trajectories. Much of low Earth orbit (LEO) consists of free-molecular flow regimes in which the molecules in the very rarefied atmosphere never collide with one another. Reentry takes objects from free-molecular through transitional and finally into the continuum regime that is dominated by inter-molecular collisions. These flow regimes (free-molecular, transitional, and continuum) can be classified by the Knudsen number, a non-dimensional ratio of gas molecules' mean free path, or average distance between collisions, and a characteristic length, usually a maximum length or diameter of a body submerged in the gas flow. An analytical modeling approach for evaluating forces and moments in three dimensions in the free-molecular flow regime is presented. The free-molecular approach is compared with a Direct Simulation Monte Carlo (DSMC) modeling approach. DSMC is a well-verified numerical particle-based probabilistic simulation that emulates the Boltzmann equation for non-equilibrium flows, which include rarefied flows. In this work, DSMC post-processing in three dimensions is extended to yield aerodynamic forces and moments dependent on the body orientation. DSMC is considered to be the most accurate method to analyze flowfields in rarefied regimes, however, the free-molecular method is preferable to the DSMC method due to computational cost, so long as it is sufficiently accurate. The free-molecular method

can save computational time when compared with a DSMC simulation by a factor of up to 7,500. Three bodies are used to compare the free-molecular and DSMC modeling approaches: a CubeSat (TBEx), a reentry capsule (REBR), and a rocket motor (Star48B). The bodies are chosen due to their relevance to the current and future space environment. There are over 1,000 nanosatellites, such as CubeSats, in orbit as of 2021, both operational and non-operational; and over 2,500 planned nanosatellite launches in the next six years. Reentry capsules are of current interest as well due to their potential for re-use. The SpaceX Dragon is an example of a full-scale reentry capsule designed to be reusable. Other reentry capsules are targeted for space exploration, such as the NASA Orion, whose mission is lunar exploration, and there have been entry capsules designed for Mars exploration as well. Additionally, more reentry capsules are expected to be launched in the near future for the purpose of gathering reentry data that can be useful in comparing to and improving computational results such as those presented in this thesis. Finally, rocket motors are commonly left in orbit after delivering payloads to their mission orbits and make up a significant population of current space debris. There are over 4,000 pieces of space debris associated with rocket bodies in LEO as of 2020. The differences between the DSMC and free-molecular results on all three bodies are discussed at length. An orbital decay model is presented in order to determine how differing modes of modeling aerodynamic coefficients affects orbital lifetime predictions. Tumbling approximations of the bodies are found to change the orbital lifetime predictions non-negligibly. The developed free-molecular analytical model provides good agreement for all three bodies at Knudsen numbers of 10 and above. At this condition, free-molecular drag results match DSMC drag results within 3%. Agreement wanes as Knudsen number decreases, and for Knudsen numbers of 0.1 or lower, the free-molecular model gives errors in aerodynamic forces as high as 28% leading to errors in time-to-reenter of 25%. The exact Knudsen number at which the free-molecular analysis becomes unacceptable varies by shape, indicating that for specific shapes, individual analysis must be done to quantify where the free-molecular modeling technique fails. This level of disagreement matches expectations for less rarefied flow. The free-molecular method developed saves computational cost when compared to DSMC by a factor of over 7000, and is

recommended for use throughout the majority of LEO.

CHAPTER 1

Introduction

Space debris is the expanding collection of defunct man-made objects in orbit around the Earth. Collisions of space debris with functional spacecraft can damage or destroy spacecraft hardware as well as impact the spacecraft's orbit, negatively affecting its mission; maneuvers to avoid collisions can add expense to space missions via more necessary ground control and detection of incoming craft or debris, as well as the launch cost of including onboard thrusters on spacecraft which increases mass. Collisions can also damage spacecraft therefore reducing operational lifetime. Collisions also cause space debris to proliferate in orbit, an extreme example is the 2009 collision of the Iridium-33 satellite with the nonoperational Russian Cosmos 2251 satellite which created over 1,500 pieces of debris tracked by the U.S. space tracking system [14]. Since 1957, there have been more than 550 collisions and collision-like phenomena (explosions, breakups and anomalous events) contributing to over 128 million debris objects currently in orbit [1].

Space debris also presents safety hazards: approximately 100 large man-made objects deorbit and reenter the atmosphere every year; many fragments of these reentered debris survive reentry and impact the ground over a large footprint of hundreds of square kilometers [15]. Space debris mitigation is therefore a problem of broad and current interest in the space science and engineering communities, as well as the public policy community, as orbital space is shared among many

nations. Current international space policy allows spacecraft to plan to remain in orbit for a maximum of 25 years after mission end; however, at altitudes above 600-700 km, orbiting objects have lifetimes that are much longer [16].

Low Earth Orbit (LEO), which is defined between approximately 160 and 2000 kilometers, is the region most heavily populated by space debris and operational satellites. As the population of satellites in LEO has grown over time, space debris has increased significantly. Figure 1.1 shows a histogram of all objects launched into Earth's orbit since the beginning of the space age in 1957. Figure 1.1 clearly shows that the majority of launches have placed objects into LEO; and it makes clear that the number of objects placed in orbit only increases as time goes on. The European Space Agency's Space Debris Office estimates that 10,680 satellites placed into Earth's orbit since 1957. 6,250, or about 59%, of these satellites are still in space today. 3,400 of them are still functioning. Although LEO is close enough to Earth that orbital decay occurs over time due to atmospheric drag, only 41% of launched satellites have reentered since Sputnik was launched [1]!

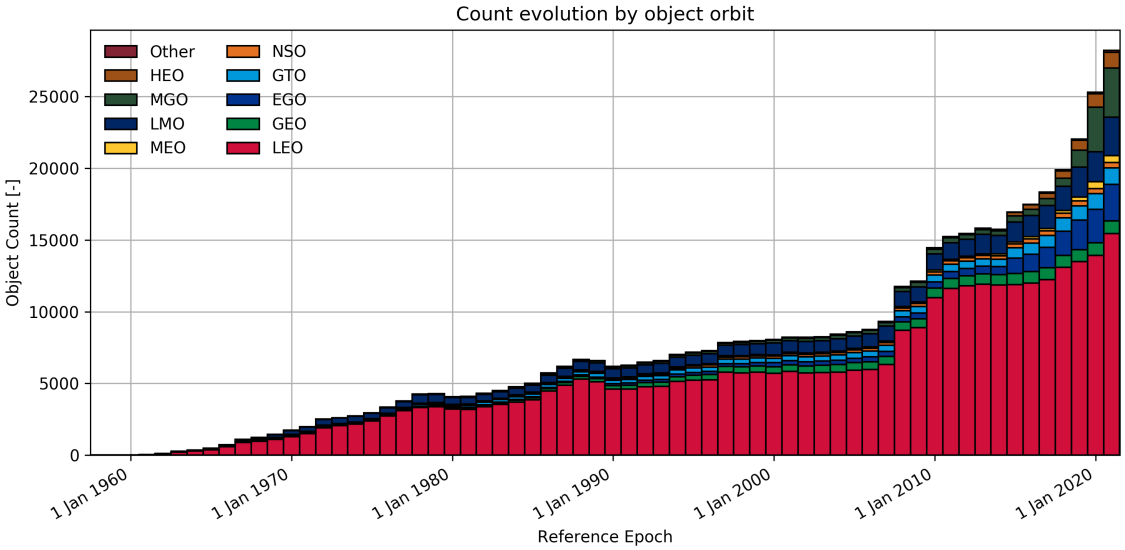

Figure 1.1: Total number of objects launched into space according to orbit type, from [1].

The acronyms used in Figure 1.1 are defined in Table 1.1. Figure 1.1 makes it clear that the

majority of objects in space reside in LEO, where spacecraft are subject to passive aerodynamic forces in orbit. Many satellites are not equipped with thrusters due to cost and size requirements. Even with thrusters or control systems, accurate modeling of aerodynamic forces in orbit can assist in mission planning.

Figure 1.2 plots the same count as in Figure 1.1, but classifies the objects by type instead of orbit. The acronyms listed in Figure 1.1 are defined in Table 1.2.

Table 1.1: Orbit type acronyms [1].

Acronym	**Description**	**Definition by Altitude of Apogee (km)**
GEO	Geostationary Orbit	35600
IGO	Inclined Geosynchronous Orbit	31600-51600
EGO	Extended Geostationary Orbit	31600-51600
NSO	Navigation Satellites Orbit	18100-24300
GTO	GEO Transfer Orbit	31600-40000
MEO	Medium Earth Orbit	2000-31600
GHO	GEO-superGEO Crossing Orbits	31600-40000
LEO	**Low Earth Orbit**	0-2000
HAO	High Altitude Earth Orbit	$>$ 40000
MGO	MEO-GEO Crossing Orbits	31600-40000
HEO	Highly Eccentric Earth Orbit	$>$ 40000
LMO	LEO-MEO Crossing Orbits	2000-31600
UFO	Undefined Orbit	-
ESO	Escape Orbits	-

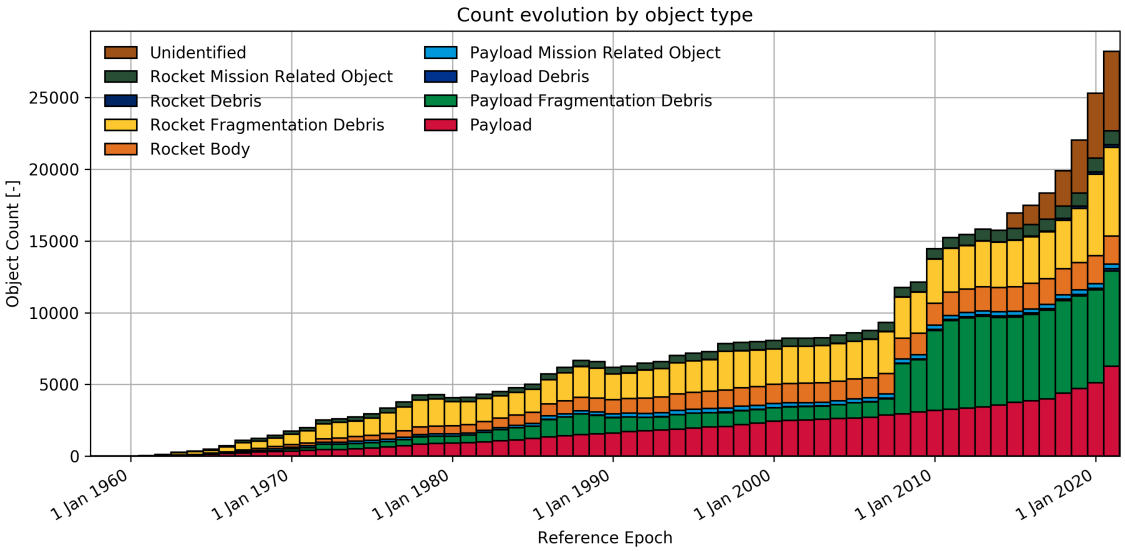

Figure 1.2: Total number of objects launched into space according to object type, from [1].

Table 1.2: Space object categorization according to [1].

Acronym	**Space Object**	**Definition**
PL	Payloads	operational satellites
PM	Payload Mission Related Objects	debris that had a purpose for the payload, i.e. optical instrument covers
PF	Payload Fragmentation Debris	traceable debris from a payload, including post-collisional debris
PD	Payload Debris	fragmented debris correlated with a payload object source
RB	Rocket Body	launch related object, i.e. rocket stages
RM	Rocket Mission Related Objects	debris that served a purpose for the rocket body, i.e. engines
RF	Rocket Fragmentation Debris	traceable debris from a rocket body, including post-collisional debris
RD	Rocket Debris	fragmented debris correlated with a rocket body source
UI	Unidentified	debris with no identifiable source

It can be seen from Figure 1.2 and Table 1.2 that the majority of tracked objects in orbit are space debris (every object type excepting PL is space debris!).

Small satellites such as nanosatellites, which include CubeSats, present an additional problem for LEO, especially when looking toward the near-future. Nanosatellites are small satellites

with a payload mass of 1 kg to 10 kg and include all forms of CubeSats. The small spacecraft are extremely cost-effective and are being launched with increasing frequency. Figure 1.3 charts the number of nanosatellites launched into orbit since the first CubeSat was launched in 1998. There have been over 1,400 nanosatellites launched and over 2,500 nanosatellites are planned to be launched in the next 6 years [2]. Nano and CubeSats are only becoming a larger source of space objects, and therefore, space debris.

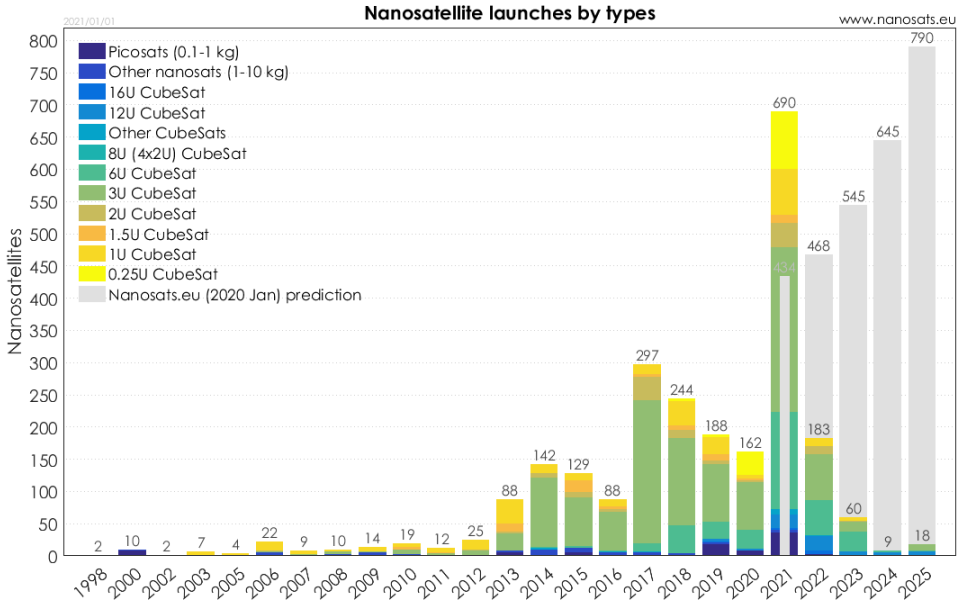

Figure 1.3: Total number of nanosatellites launched into space according to type, from [2]. Predictions of future launches are included.

Constellations are networks of connected small satellites that typically provide either observational data or communications infrastructure; the Iridium network is an early example of a constellation. As the costs of small satellites are reduced, more constellations are proposed. Constellations of small satellites can include over 500 satellites; however, the majority of proposed constellations have less than 50 elements [3].

Figure 1.4 shows the number of satellites launched as part of constellations as a function of

time. The number of not-classified (NC) satellites, or constellation satellites with no published launch date, indicates that the number of satellites in orbit will increase quickly in the near-future due to constellations.

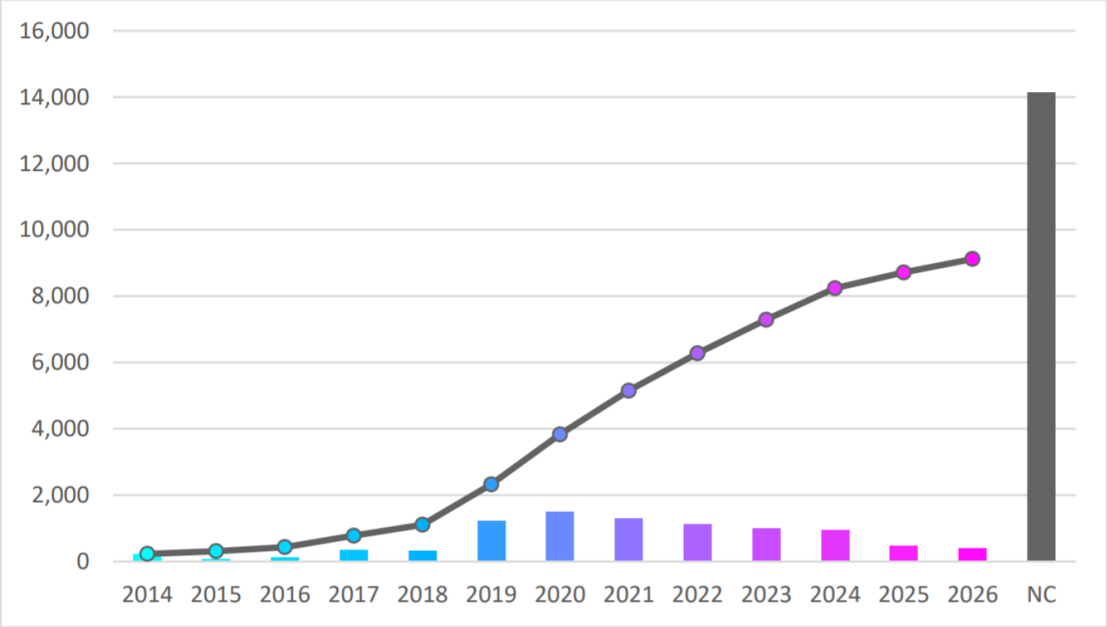

Figure 1.4: Expected number of spacecraft in orbit due to constellations. Bars represent the estimated number of satellites launched yearly, while the black line represents the cumulative sum. "NC" stands for intended constellations that have not published launch dates. From [3].

Figures 1.1-1.4 clearly indicate that satellite launches are an ever-increasing source of space debris, especially in LEO and that the number of launches is increasing. Predictions of collisions, and accurate lifetime estimates, will become more and more important as this problem grows. A crucial component of orbital lifetime and trajectory predictions is an understanding of the aerodynamic environment and the passive reentry that occurs for nonfunctional space objects.

There is very limited data on the reentry and breakup of spacecraft. Currently, computer simulations are necessary to predict reentry dynamics and trajectories. Because of a lack of data in this environment, these simulations do not perform as well as needed, and struggle to predict certain reentry phenomena. Ailor et al. [15] present as an example the overestimation of heat transfer

during the free-molecular region, which generates breakup altitudes that are higher than actually occur. Precise determination of breakup altitudes are essential for calculating an accurate ground impact area, which is one of the reasons it is desirable to obtain accurate simulations of reentry phenomena.

There has been some work done on high-fidelity modeling of spacecraft dynamics experiencing rarefied flow. There is current interest in improving predictions of spacecraft dynamics in all orbital regimes. For example, Pilinksi et al. developed a semi-empirical model based on observations of upper launch stages and spheres in orbit, in order to improve predictions of ballistic coefficients of randomly tumbling objects in elliptical orbits in LEO [17]. Ballistic coefficient modeling is the current standard when approximating orbital decay [13], and is the simplest way to describe aerodynamics of a spacecraft. The interest in improving ballistic coefficient modeling indicates that any improvement on predictions of dynamics in orbit is of interest to the broader space engineering community at the moment.

As an example of work done on modeling free-molecular flow dynamics, K. Hart et al. developed analytic closed-form expressions for aerodynamic force and moment coefficients of theoretical shapes, such as a sphere, in free-molecular flow [18]. These expressions were extended for superimposed composites of the theoretical shapes, allowing for modeling of most spacecraft geometries. The analytical modeling was for two-dimensional parameterized shapes. This is a different application of the analytical free-molecular solution than the one desired for this thesis work. This work seeks to build a free-molecular model capable of handling any arbitrary shape in three dimensions; with outputs for three-dimensional forces and moments.

As for DSMC aerodnyamics coupled with orbital flight: C. Turansky and B. Argrow developed an algorithm involving their DSMC code Voldipar to simulate deorbiting dynamics of a

typical airfoil and an asymmetric "Arbject" [4]. This analysis decoupled the rotational motion of the tested objects from the rarefied flow experienced. The two-dimensional approach allowed for a large amount of DSMC simulations the results of which were applied to two-dimensional orbital-aerodynamic equations of motion to simulate the flight of the objects through the lower thermopshere. A similar approach of non-coupling of the rotational motion with the flow experienced is applied in this work, extended to three-dimensional analysis of vastly different bodies, with comparison to a free-molecular analytical model results, and several modes of projecting orbital decay.

Predictions of aerodynamic forces on high altitude orbiting and reentering space debris are necessary for understanding reentry trajectories and orbital lifetimes. Orbital decay occurs throughout LEO due to the forces experienced on a spacecraft caused by the rarefied atmosphere. Tumbling of spacecraft occurs throughout LEO [19]; this tumbling is affected by torques caused by aerodynamic forces. Aerodynamic drag, lift, and other forces are a result of the properties of the oncoming flow and the flow-facing area. Tumbling of a spacecraft, or space debris, alters the forces experienced by the craft, and can change orbital lifetimes. The current standard of predicting orbital lifetimes based on an approximation of drag coefficients using one flow-facing area affects predictions of spacecraft mission lifetimes which can have associated costs [6, 7]. Three-dimensional modeling, with six degrees of freedom, is necessary for capturing the moments imposed on spacecraft and debris experiencing flow.

With current computational power, there is no need to guess at drag coefficients for spacecraft. However, there is a cost associated with high-fidelity modeling; especially when considering three-dimensional movement. This begs the question: what difference can higher fidelity modeling make, and for what conditions can lower-fidelity analytical models improve the current standard

of reentry and orbital lifetime predictions?

1.1 Flow Regimes and Their Modeling Implications

There are several ways to model aerodynamic phenomena. Aerodynamic forces are the result of flowing gas impacting and interacting with bodies submerged in the flow. The Earth's atmosphere is gaseous, and modeling or describing the composition of it is not in the scope of this work. However, due to the gravitational pull of the Earth, the density of the atmosphere is striated. Atmospheric flow, then, does not act as one medium at all altitudes of the atmosphere.

In fact, there are different regimes with which gaseous media are described. The parameter used to describe the flow regime a body is in is the Knudsen number, Kn, given in Equation 1.1. In Equation 1.1, λ is the mean free path of the gas; and L is a characteristic length of the physical body in the flow. The mean free path of the gas is the average distance a particle will travel before colliding with another particle while the characteristic length is some representative measurement of body length, i.e. a spacecraft's maximum length or diameter.

$$Kn = \frac{\lambda}{L} \tag{1.1}$$

When the Knudsen number is low, i.e. ≤ 0.01, the gas can be assumed to be a continuous medium in equilibrium. Flows with Knudsen numbers lower than 0.01 are considered continuum flows. Continuum flows can be described by the Navier-Stokes, or if inviscid, the Euler equations. These equations are equilibrium applications of the broader, particle based Boltzmann equation [20]. The Navier-Stokes and Euler equations can be discretized across a volume mesh and continuum flowfields can be solved using many different computational fluid dynamics (CFD)

models. Examples of this include flow of air across an airplane wing or water around a ship.

As the Knudsen number approaches infinity, the flow becomes collisionless. This regime is called free-molecular flow. Some have defined free-molecular flow as a Knudsen number of 100 or greater [4], some have cited a Knudsen number of much greater than one to be consistent with collisionless flow. Generally, a Knudsen number of 10 or above is considered firmly free-molecular [20]. Examples of this are satellites in high-altitude orbit around planets with an atmosphere.

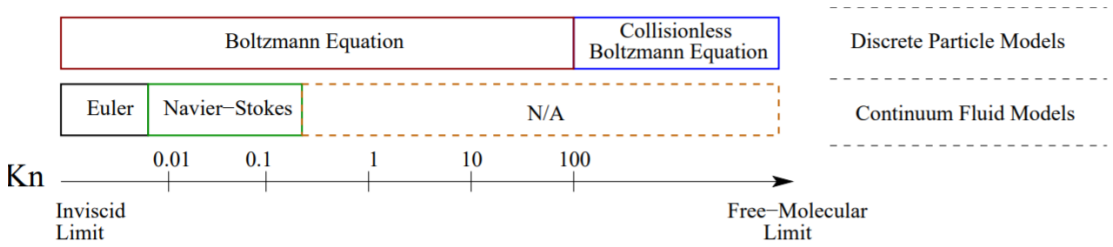

Figure 1.5: Flow regimes according to Knudsen numbers and their respective valid descriptive equations, from [4].

The free-molecular regime is collisionless, and therefore the collision term in the Boltzmann equation is zero. Free-molecular analysis applies an equilibrium velocity distribution function (VDF) to the freestream; doing so and equating the collision term to zero yields analytical expressions for surface properties of an object in free-molecular flow. The free-molecular analytical approach developed is described in full in Chapter 2. Figure 1.5 demonstrates the flow regimes and valid modeling approaches and equation sets used for solving different flowfields.

In-between continuum and free molecular regimes lies the transition regime. In this regime, collisions happen, but not often enough to establish an equilibrium. Therefore, in order to describe these transitional flows, the entire Boltzmann equation must be modeled. The Direct Simulation Monte Carlo (DSMC) method probablistically solves the Boltzmann equation by using reference particles, each one representing a large amount of real-life particles or molecules. These parti-

cle methods are relatively computationally expensive when compared with typical computational fluid dynamics (CFD) simulations, and especially computationally expensive when compared to analytical solutions.

Spacecraft in LEO can experience free molecular, transitional, and continuum flow regimes as they orbit, deorbit, and reenter, so modeling approaches to understand the forces experienced on a spacecraft or piece of space debris cannot be "one-size-fits-all." Figure 1.6 demonstrates the regimes experienced for a satellite of certain characteristic length over altitude. Figure 1.6 is calculated using mean free paths for the atmosphere from the U.S. Standard Atmosphere, 1976 [12].

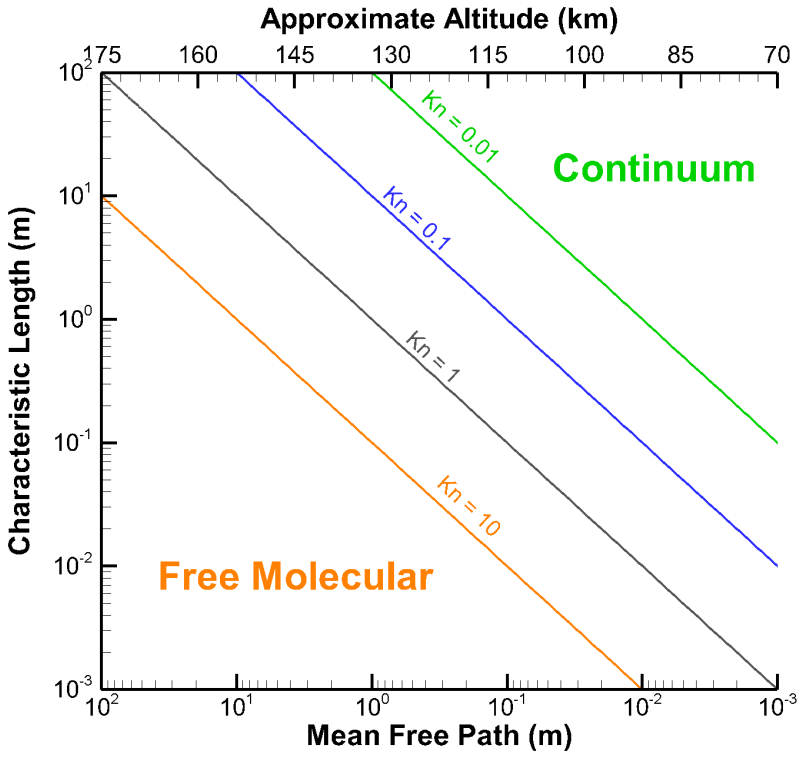

Figure 1.6: Knudsen numbers and gas flow regimes plotted with LEO altitudes.

DSMC modeling approaches are much more computationally expensive than free-molecular analytical modeling techniques. Cost is discussed at length in this thesis, but as an example,

one DSMC simulation of a rocket stage body at a Knudsen number of 1 cost 55 core-hours (C-Hs). At the same Knudsen number, for the same body, a free-molecular simulation cost 0.5 core-hours. This is a difference in cost of 99%! One goal of this thesis work is to determine where, according to Knudsen number, free-molecular modeling can replace DSMC modeling for accurate force and moment results on spacecraft in three dimensions. In order to accomplish this, several steps must be taken. One, a detailed free-molecular model is developed and verified. Two, a post-processing algorithm for three-dimensional DSMC results is written in order to yield force and moment information. And third, DSMC and free-molecular analytical results are compared for different body shapes and over a range of altitudes in order to determine where free-molecular approaches are accurate enough that DSMC methods are not needed.

1.2 Thesis Overview and Bodies Studied

In Chapter 2, the methods for generation of aerodynamically imposed forces and moments on bodies are described. First, the extension of the DSMC code MONACO's post-processing algorithm is explained. Next, the free-molecular model is described, and verified, using theoretical body shapes and drag and lift coefficient results. Both methods rely on appropriate mesh representation of spacecraft bodies. Surface properties and force contributions are calculated on surface elements and then integrated over the meshed bodies to yield overall forces and moments. An orbital decay model is also developed as another means to test the performance and differences between the DSMC force results and the free-molecular force results on different bodies.

Three different bodies are chosen to explore and demonstrate the modeling approaches and their differences. First, in Chapter 3, a small 3U CubeSat mission, the Tandem Beacon Experiment

(TBEx) is examined. TBEx is chosen due to the proliferation of CubeSats in LEO, and the data that is available on the TBEx. There have been over 2,000 CubeSats launched since 1998, and the number of launches increases every year [2]. CubeSats, therefore, are now and will continue to be prevalent, and force and moment information on CubeSats can aid in mission planning as well as provide insights on time-to-deorbit. CubeSats are small, and therefore experience free-molecular flow as part of their orbiting. The TBEx's orbit is firmly in the free-molecular regime [21]. However, to compare models, its orbit is projected to different altitudes, and the TBEx is modeled at Knudsen numbers ranging from 100 to 0.1.

Second, in Chapter 4, a small reentry data gathering mission capsule, the Reentry Breakup Recorder (REBR), is modeled. The REBR is chosen for study due to its published flight data [10] as well as its resemblance to many other full-scale reentry vehicles, such as the SpaceX Dragon. Reentry capsules of all sizes will continue to be an important spacecraft shape profile for future launches, on planet Earth and even for planets such as Mars, so modeling of forces and moments on them is extremely interesting and relevant. The REBR's flight data is purely in the continuum regime, however its orbit is projected upwards to compare models. The REBR body is used for comparing modeling approaches at Knudsen numbers from 10 to 0.01.

Third, in Chapter 5, a Delta stage three rocket motor, the Star48B, is modeled. The Star48B is chosen because it is representative of a typical large piece of space debris left in orbit. The Star48B is an interesting shape, providing the opportunity to model something with multiple meshing challenges. The Star48B is modeled using both the free-molecular and the DSMC approaches at Knudsen numbers from 10 to 0.05.

Figure 1.7 visually shows the range of Knudsen numbers in the transition and free-molecular regimes each body in this thesis work is examined at.

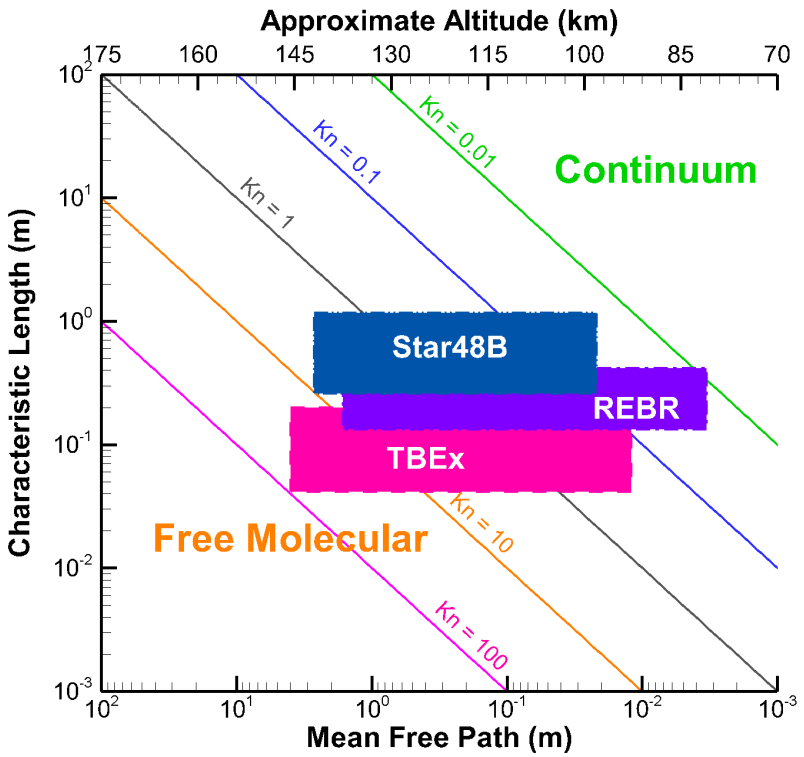

Figure 1.7: Bodies modeled in this thesis work corresponding with their range of modeled Knudsen numbers.

All three bodies' force and moments results from both approaches are compared and commented on, highlighting where the free-molecular approach performs well and where its accuracy degrades as the flow regime becomes denser. The final chapter summarizes conclusions made in Chapters 3, 4, and 5 with notes on how this work adds to the space engineering communities' knowledge and recommendations for future work using both the DSMC and free-molecular analytical approaches to calculate forces and moments.

CHAPTER 2

Numerical Methods

The primary focus of this work is to determine what flow regimes require high fidelity modeling to capture an acceptable representation of aerodynamic forces experienced on a body. Flow regimes are characterized by Knudsen number; therefore it is desirable to understand at what Knudsen number a flowfield requires high-fidelity modeling in order to capture satisfactory aerodynamic force information.

For this dissertation work, three models are specifically developed and implemented to answer this question: a post-processing code for three dimensional DSMC flowfields over an arbitray body, an analytical model that takes an arbitrary body surface as input and outputs aerodynamic forces and moments according to free molecular assumption theory, and an orbital decay model that takes coefficients of aerodynamic forces as input and determines the long-term decay of a body from orbit. The third model, an orbital decay model, is developed in order to estimate effects of the fidelity of the model chosen on long-term satellite or space debris orbital lifetime predictions, as discussed previously, these predictions have far-reaching consequences in the application of space research.

2.1 The DSMC Method

MONACO was first developed in the 1990s as a parallel-optimized DSMC application suitable for workstation architectures [22]. MONACO is a well-verified DSMC code with numerous applications and users. MONACO has been updated and improved over the years by Professor Boyd's Nonequilibrium Gas and Plasma Dynamics Laboratory members, and three dimensional capability of MONACO was implemented and verified by 1999 [23].

This dissertation research uses MONACO as a tool to evaluate aerodynamic forces and moments on bodies experiencing flowfields akin to those experienced in Earth's low Earth orbit. MONACO itself was not adapted significantly for this thesis work so the explanation of the DSMC algorithm used will be brief, with focus instead falling on the post-processing code developments.

2.1.1 The MONACO Implementation

DSMC stands for Direct Simulation Monte Carlo. The method is a non-deterministic emulation of the Boltzmann equation seen in Equation 2.1 [5]. The Boltzmann equation describes what happens in any fluid, or particle, flow completely: the left-hand side of the equation describes particle motion through phase space (physical location $\vec{r}$ in three dimensions, and a velocity $\vec{C}$ in three dimensions) while the right-hand side describes the inter-molecular collisions. The collision term describes the change in particle velocity due to interactions with other particles moving through similar phase space. Essentially the Boltzmann equation describes a particle "flux" behavior: the particles move through space, and experience changes in their velocities, due to their own prescribed motion as well as collisions, or interactions with other particles.

$$\frac{\partial(nf)}{\partial t} + \vec{C} \cdot \frac{\partial(nf)}{\partial \vec{r}} + \vec{a} \cdot \frac{\partial(nf)}{\partial \vec{C}} = \int_{-\infty}^{\infty} \int_{0}^{4\pi} n^2 \big(f(\vec{C'}) f(\vec{Z'}) - f(\vec{C}) f(\vec{Z}) \big) g \sigma d\Omega d\vec{Z} \tag{2.1}$$

DSMC is a particle-based method that uses a set number of representative particles (each representing a much larger number of real life particles) to track and predict collision behavior and particle motion over time therefore emulating the Boltzmann equation in its entirety. Because the Boltzmann equation applies to any dilute flow, and DSMC tracks particle motion, the method is applicable to essentially any flowfield. Therefore, DSMC is appropriate for flows too rarefied for computational fluid dynamics (CFD). CFD techniques use the Navier-Stokes conservation equations, or a reduced form of those equations that require extra assumptions about the fluid flow, such as incompressibility of the fluid. These conservation equations describe the force balance in a fluid: flowfields applicable to these techniques must be concentrated enough to be treated as a continuum. Due to this, sufficiently dilute flows cannot be solved using CFD.

DSMC simulations, especially in three-dimensions, can be very computationally expensive. The computational cost is proportional to the number of representative particles used; a large number of particles are necessary for an accurate simulation of a flowfield; in three-dimensions, even more particles are needed to solve the flowfield space. Although the number of molecules in a real gas are represented by a reduced number of modeling particles, hundres of thousands to millions of particles must be simulated with DSMC techniques. The cost of three-dimensional accurate DSMC simulations will be discussed at length in this thesis as the principle investigation is to determine when these costly simulations are necessary for accurate aerodynamic information.

The computational cost difference between analytical methods using equations on the surface of a body only (such as the free molecular analytical model discussed in the next section) versus DSMC simulation is several orders of magnitude. High-fidelity modeling gives a more-accurate picture but the investigation is to define where the cost of this modeling is justifiably necessary.

DSMC techniques are able to effectively model the Boltzmann equation by decoupling the particle motion (Equation 2.1 left hand side) from collisions (Equation 2.1 right-hand side) between particles by using a time step smaller than the mean collisional time. The mean collisional time (or mean free time) is the average time between collisions for any particular particle in a gas. Particles are assumed to be able to translate in straight lines according to their current velocity if the time step is less than, or at least on the order of, the mean collisional time.

The basic DSMC algorithm has the following steps: move the representative particles throughout the grid according to each particle's velocity and the time step, compute the interactions of surfaces and particles, determine the cell in which each particle is located, statistically compute collisions between particles within the same cell, and sample the particle information for each cell [22]. Once the simulation has achieved steady-state via a certain user-determined number of time steps, overall particle information is output and can be post-processed into macroscopic properties and aerodynamic forces and moments.

The DSMC algorithm imposes certain grid requirements. Collisions are performed in each cell stochastically due to the representative nature of the DSMC particles. During each time step, simulated particles are randomly paired up within cells and tested for a collision [20]. Collisional cell sizes then must be smaller than the local mean free path; otherwise collisions may be induced over unphysically large distances. This nonphysical transfer of mass, momentum, and energy through impossible collisions would create dissipation error that would cause the momentum transfer to

the body surface to be incorrect. Since the momentum transfer from collisions of particles with the body surface results in the flow induced aerodynamic force, an improperly refined grid would essentially waste all the computational cost of a high-fidelity DSMC simulation by yielding incorrect force information. However, this grid constraint influences computational cost and can even prevent DSMC simulations. If a grid contains a large amount of cells, depending on resources, out-of-memory errors may occur, or the simulation computational cost may exceed what a user determines necessary. Even in extremely rarefied flows, compression of the mean free path determines the refinement of a surface mesh. A hyper-refined surface mesh can propagate into many millions of cells in even a small volume mesh in three-dimensions. Such meshing considerations will be discussed at length in the results section of this thesis.

2.1.2 Application to Spacecraft Aerodynamic Forces and Moments

Particle information at the end of a MONACO simulation yields macroscopic properties commonly used to describe forces induced by a flow onto a surface. Pressure and shear stress are a result of momentum transfer from particles colliding with the surface, in the normal-through and tangential directions, respectively. MONACO calculates these momentum transfers to each surface element. One aspect of this thesis work is to develop a way to parse the surface element macroscopic properties into forces and moments experienced by an arbitrary body in three dimensions.

For use with MONACO, bodies are represented as a grid: a collection of disparate cells with a boundary definition of "wall." In two dimensions, these cells, or surface elements, are line segments. In three dimensions, these surface elements are triangles or quadrilaterals with their own area. In order to calculate total forces and moments experienced by the body, the forces are

calculated on each surface element and summed, or integrated, over the body. Equation 2.2 states this concept of body force integration over surface elements.

$$\vec{F}_{body} = \sum^{N=\text{all surface elements}} dF_{\text{surface element}} \tag{2.2}$$

Each body, or grid, input into MONACO has its own X, Y, and Z Cartesian coordinate system. In addition to calculating forces in the traditional aerodynamic directions (i.e. drag, lift, and sometimes side), cardinal Cartesian direction forces are desired, to check over the drag and lift forces and in the pursuit of torques, or moments, experienced by the body that lead to tumbling behaviors.

Each surface element experiences forces due to the pressure and shear stress the flow induces on it. The pressure force acts in the direction "through" the surface element, while the shear stress force acts in a direction tangential to the surface element. Surface normals are calculated in the direction outward from the body, so the pressure force is equal to the negative surface element's normal vector times the pressure felt times the surface element's area. MONACO samples the particle momentum transfer in each cardinal direction, therefore yields the shear stress experienced by each surface element in X, Y, and Z directions. Figure 2.1 illustrates the breakdown of these forces on a surface element, with the relative velocity of the flow the body is experiencing pictured as the thick arrow outside the surface element. The relative velocity vector refers to the fact that in this thesis, bodies orbiting Earth or reentering are held steady and their velocity is instead felt as a relative incoming velocity of the flow.

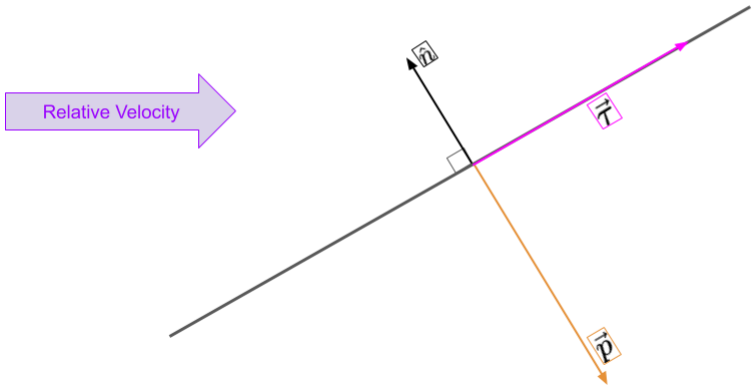

Figure 2.1: Pressure and shear stress forces felt on a surface element with normal vector $\hat{n}$.

X, Y, and Z forces on each surface element can then be found using Equation 2.3, where $n_{X,Y,Z}$ refer to the component of the surface normal in each Cartesian direction, and $\tau_{X,Y,Z}$ refers to the shear stress yielded in each Cartesian direction. Theses forces are integrated using the method in Equation 2.2 to yield overall forces felt by the body in each dimension.

$$\begin{aligned} dF_X &= (-p \cdot n_X + \tau_x) \cdot A \\ dF_Y &= (-p \cdot n_Y + \tau_y) \cdot A \\ dF_Y &= (-p \cdot n_Z + \tau_z) \cdot A \end{aligned} \tag{2.3}$$

As well as forces, moments experienced by the body are calculated by first calculating each surface element's moments and then summing over the body, illustrated in Equation 2.4.

$$\vec{M}_{body} = \sum^{N=\text{all surface elements}} dM_{\text{surface element}} \tag{2.4}$$

Moments on each cell are calculated using $d\vec{M} = \vec{R} \times d\vec{F}$, where $\vec{R}$ is the distance between the

surface element's centroid and the body's centroid. Usually moments would be calculated about the bodies' center of mass, however, no mass information is provided to MONACO or Oxford3d at this time. Mass information on the grid may be important for future work focusing on different bodies with known very uneven mass distributions, such as a fuel-filled rocket nozzle. For this thesis work, the mass distribution across all bodies worked with is assumed to be uniform.

In order to understand the effect that aerodynamic moments have on satellite motion, angular acceleration is derived from the calculated moments. The Euler equations are used to calculate maximum induced angular acceleration by the model-yielded moments. Equation 2.5 are the Euler equations, where I_{XX}, I_{YY}, and I_{ZZ} are a body's moments of inertia about it's primary axes [24], α_X, α_Y, and α_Z are the angular accelerations about the body's primary axes, and ω_X, ω_Y, and ω_Z are the angular velocities about the primary axes. According to Equations 2.5, the maximum angular accelerations are incurred from a moment applied to a body not currently tumbling (angular velocities of zero).

$$\begin{aligned} M_X &= I_{XX}\alpha_X + (I_{ZZ} - I_{YY})\omega_Y\omega_Z \\ M_Y &= I_{YY}\alpha_Y + (I_{XX} - I_{ZZ})\omega_X\omega_Z \\ M_Z &= I_{ZZ}\alpha_Z + (I_{YY} - I_{XX})\omega_X\omega_Y \end{aligned} \tag{2.5}$$

Experiencing a moment from rest would cause a body to experience the angular accelerations in Equation 2.6. These equations are applied on the separate bodies in this thesis work to analyze the effect aerodynamic moments have on a body's tendency to tumble in orbital decay.

$$\begin{aligned} \alpha_X &= \frac{M_X}{I_{XX}} \\ \alpha_Y &= \frac{M_Y}{I_{YY}} \\ \alpha_Z &= \frac{M_Z}{I_{ZZ}} \end{aligned} \tag{2.6}$$

In this way, Oxford3d postprocesses MONACO data across the body and outputs forces in and moments about the X, Y, and Z body-defined Cartesian coordinate system. However, drag and lift are extremely important in aerodynamic and orbital analysis of satellite bodies as they are given in directions that can be transformed easily across different coordinate systems.

Addressing drag first, drag is defined as being in the opposite direction to the body velocity. For this thesis work, that translates to in the same direction as the relative, or incoming flow, velocity. Figure 2.2 displays the pressure, shear, and drag force applied to our same demonstrative surface element feeling the incoming flow velocity.

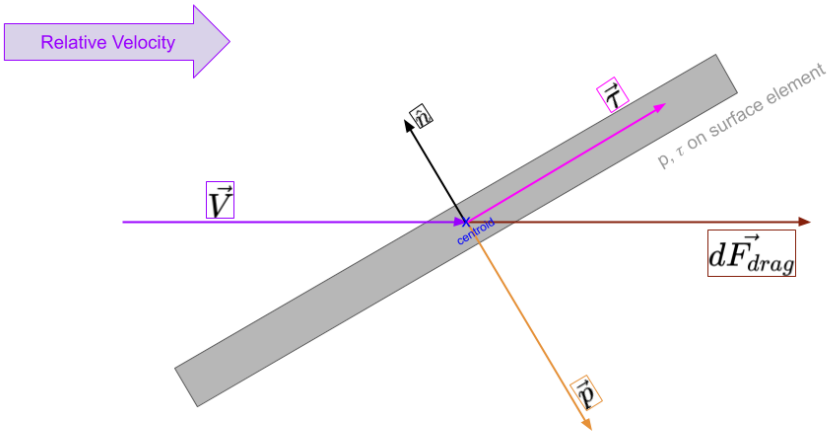

Figure 2.2: Drag force felt by a surface element on a body with normal vector $\hat{n}$.

The drag direction is calculated directly by using the incoming flow velocity (determined by

the user in MONACO): $\hat{d} = \frac{\vec{V}}{|\vec{V}|}$. Then the pressure and shear forces on each surface element can be decomposed in this direction by projecting each vector onto that normal. Because $\hat{d}$ is normalized, this is simply the dot product. The final equation for drag felt by a single surface element is listed in Equation 2.7; this is then integrated over the body to yield total drag force.

$$\begin{aligned} \vec{dF_{Drag}} = &\big[(-pn_X d_X + \tau_x d_X) \cdot A\big]\hat{i} + \\ &\big[(-pn_Y d_Y + \tau_Y d_Y) \cdot A\big]\hat{j} + \\ &\big[(-pn_Z d_Z + \tau_Z d_Z) \cdot A\big]\hat{k} \end{aligned} \tag{2.7}$$

Lift is more difficult to calculate in three dimensions. Whereas drag has a defined direction, lift is defined as perpendicular to the drag force. Therefore, in three dimensions lift is not constrained. In MONACO simulations, the body coordinate system is not aligned within any larger coordinate system such as an orbital or ballistic path, so there is no single way to choose an "up" direction counter to a gravity direction. Therefore, this dissertation research also includes the development of an algorithm to choose lift direction.

For our purposes, though three dimensional bodies are studied in this thesis work, in many cases the incoming flow velocity is defined in one or two dimensions. For these situations, the dot product definition can be used to obtain a perpendicular lift direction. If the velocity is defined in more than two dimensions, a cross product between the relative velocity vector and a chosen "dummy" vector is performed to get a defined lift direction. The chosen crossed-with, or "dummy" vector, is also checked to ensure it is not parallel to the velocity vector which would yield an error. Table 2.1 displays the results of this lift-direction-choosing algorithm for flow velocities

defined in one or two dimensions to demonstrate the choosing algorithm. In Table 2.1, the velocity components v_X, v_Y, v_Z are positive quantities.

Table 2.1: Lift Directions from Developed Algorithm for Plane-Constrained Velocities.

Plane	$\vec{V}$	$\hat{l}$
X	$(v_X, 0, 0)$	$(0, 0, 1)$
Y	$(0, v_Y, 0)$	$(0, 0, 1)$
Z	$(0, 0, v_Z)$	$(0, -1, 0)$
X-Y	$(v_X, v_Y, 0)$	$(-\sqrt{\frac{1}{2}}, \sqrt{\frac{1}{2}}, 0)$
X-Z	$(v_X, 0, v_Z)$	$(-\sqrt{\frac{1}{2}}, 0, \sqrt{\frac{1}{2}})$
Y-Z	$(0, v_Y, v_Z)$	$(0, -\sqrt{\frac{1}{2}}, \sqrt{\frac{1}{2}})$

Therefore we assign the lift direction, and can now break down the shear stress and pressure felt by each surface element into forces using the same method as we do with the drag force.

Using our established lift direction, we can break down shear stress and pressure felt by each surface element into forces in the lift direction. Figure 2.3 displays the found lift direction and force against an example surface element.

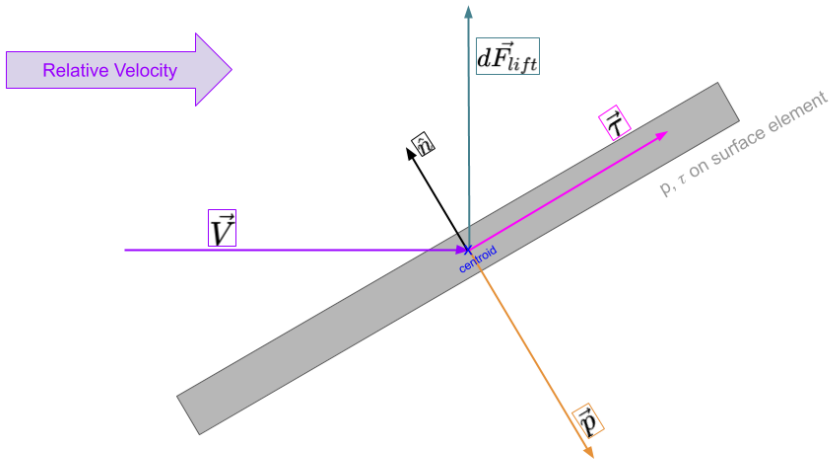

Figure 2.3: Lift force felt by a surface element on a body with normal vector $\hat{n}$.

The normalized direction of lift is $\hat{l}$. Equation 2.8 displays the full equation for the surface

element's lift contribution, which is integrated over the body to yield total lift force.

$$\begin{aligned} d\vec{F_{Lift}} = &\big[(-pn_X l_X + \tau_x l_X) \cdot A\big]\hat{i} + \\ &\big[(-pn_Y l_Y + \tau_Y l_Y) \cdot A\big]\hat{j} + \\ &\big[(-pn_Z l_Z + \tau_Z l_Z) \cdot A\big]\hat{k} \end{aligned} \tag{2.8}$$

2.2 The Free Molecular Analytical Model

Free molecular flow occurs in high altitude orbit; this regime is defined as having a Knudsen number of much greater than one [20] [25]. Equation 2.9 provides the definition of the Knudsen number, where λ is the mean free path of the atmospheric air particles and L is the characteristic length of the spacecraft.

$$Kn = \frac{\lambda}{L} \tag{2.9}$$

Free molecular flow is so rarefied that it can be assumed to be collisionless and equilibrium kinetic theory using Maxwellian velocity distribution functions (VDF) can be applied to free molecular flow onto the surface of a spacecraft flying in orbit. The net momentum fluxes of the free molecular gas due to the orbital velocity of the spacecraft and gas temperature yields the pressure and shear stress experienced by a spacecraft element. Pressure is the net normal momentum flux; shear stress is the net tangential momentum flux.

Equations 2.10 and 2.11 can be obtained by applying the collisionless, thermal equilibrium assumption to the incident flow colliding with a surface and solving for net momentum flux of the colliding flow. The net flux is calculated using a reflected flux which imagines a reservoir of gas

in thermal equilibrium behind the real surface [20].

$$p = (2-\alpha)\Big[n_i k T_i \bigg(\frac{s_3}{\sqrt{\pi}} exp(-s_3^2) + \big(\frac{1}{2} + s_3^2\big)(1 + erf(s_3))\bigg)\Big] \\ +\alpha\Big[\frac{1}{2} n_i k (T_i T_w)^{1/2} \big(exp(-s_3^2 + \sqrt{\pi} s - 3[1 + erf(s_3)])\big)\Big] \tag{2.10}$$

$$\tau = \alpha n_i k T_i s_t \bigg(\frac{exp(-s_3^2)}{\sqrt{\pi}} + s_3[1 + erf(s_3)]\bigg) \tag{2.11}$$

Equation 2.10 is the surface pressure experienced by a spacecraft surface element in free molecular flow; Equation 2.11 is the shear stress experienced by a spacecraft surface element in free molecular flow [20]. n_i is the incident number density of the air particles, k is the Boltzmann constant, T_i is the incident air temperature. α is the accommodation coefficient, representing the fraction of collisions of the fluid particles with the surface that are diffuse, versus specular. A diffuse reflection off of a surface yields a particle velocity in the Maxwellian velocity distribution accommodated to the temperature of the surface. A specular reflection is a mirror-like reflection of the particle where the normal component of the particle velocity is simply reversed in direction.

s_3 is the speed ratio of the flow normal to the surface shown in Equation 2.12 and s_t is the speed ratio of the flow tangential to the surface shown in Equation 2.13. u_1, u_2, and u_3 are the bulk velocity components of the flow oriented with each particular surface elements' coordinate basis; u_3 is perpendicular through the surface element.

$$s_3 = \sqrt{\frac{m u_3^2}{2 k T_i}} \tag{2.12}$$

$$s_t = \sqrt{\frac{m(u_1^2 + u_2^2)}{2kT_i}} \tag{2.13}$$

In the DSMC code MONACO, individual representative particles collide with the surface and the momentum transfer is calculated in each direction - X, Y, and Z. In the free molecular analytical model (developed and implemented in Matlab), Equation 2.10 and 2.11 are used. Both of these equations revolve around u_3, breaking the fores into two dimensions, a normal direction "through" the surface, and a tangential direction ($(u_1^2 + u_2^2)$) "along" the surface. However, force breakdown in the three cardinal directions X, Y and Z is necessary for moment calculation and comparison with the MONACO method. Therefore the tangential force needs to be further decomposed into two separate directions (u_1 and u_2).

In order to calculate the directional shear stress, each surface element yields a vector basis: the normal vector going through the surface element, and two tangential vectors to the surface. This surface element basis coordinate system and the forces addressed to each basis direction are illustrated in Figure 2.4. The surface element's basis is $\hat{n}$, the normal vector, and $\hat{o}$ and $\hat{m}$, the orthogonal tangential unit vectors.

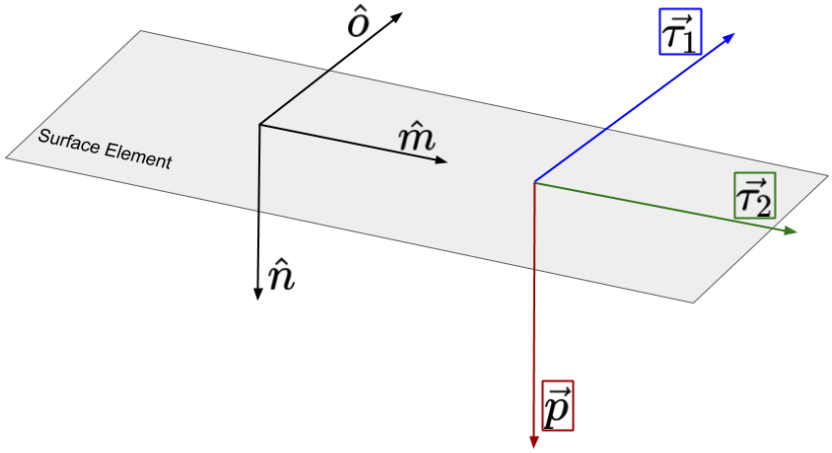

Figure 2.4: The pressure and shear stress forces felt on a surface element demonstrated with the surface element's basis of vectors.

Each surface element's basis is calculated using the surface element's normal vector by using the cross product and by ensuring that the tangential-plane basis vectors $\hat{o}$ and $\hat{m}$ do not point counter to the bulk flow velocity. The tangential basis vectors cannot be counter to the bulk flow for calculation of shear stress forces. $\hat{o}$ and $\hat{m}$ are ensured to be in the bulk velocity direction via using the dot product with the flow velocity and reversing the basis vector if that dot product is negative. $\hat{m}$ is found first by crossing the normal vector $\hat{n}$ with a dummy vector then ensuring that it is normalized and not counter to the flow velocity; then $\hat{o}$ is found by crossing $\hat{n}$ with $\hat{m}$ and again ensuring $\hat{o}$ is not counter to the flow velocity by checking the dot product. In this way, a flow-constrained basis is defined for each surface element on the body.

With the surface element's basis, s_t can be split up into directions according to the bulk flow direction, and τ_1 and τ_2 forces are calculated on the surface element. τ_1 and τ_2 are defined in Equations 2.14 and 2.15. $\hat{o}$ is parallel to $\vec{u_1}$ and therefore $\vec{\tau_1}$, $\hat{m}$ is parallel to $\vec{u_2}$ and $\vec{\tau_2}$, and $\hat{n}$ is parallel to $\vec{u_3}$ and $\vec{p}$.

$$\tau_1 = \alpha n_i k T_i s_1 \left(\frac{exp(-s_3^2)}{\sqrt{\pi}} + s_3[1 + erf(s_3)] \right) \tag{2.14}$$

$$\tau_2 = \alpha n_i k T_i s_2 \left(\frac{exp(-s_3^2)}{\sqrt{\pi}} + s_3[1 + erf(s_3)] \right) \tag{2.15}$$

Using τ_1 and τ_1, the X, Y, and Z components of shear stress on each surface element can be calculated using the basis normal vectors for that element. Equation 2.16 gives the breakdown of the shear components into our bodies' X, Y and Z Cartesian directions.

$$\begin{aligned} \tau_x &= \tau_1 \cdot o_x + \tau_2 \cdot m_x \\ \tau_y &= \tau_1 \cdot o_y + \tau_2 \cdot m_y \\ \tau_z &= \tau_1 \cdot o_z + \tau_2 \cdot m_z \end{aligned} \tag{2.16}$$

The free molecular model uses only analytical equations for each surface element; there is no tracking of particle-surface interaction. Therefore an additional algorithm is developed within this dissertation research in order to determine which surface elements on the three-dimensional bodies experience oncoming flow (and which surface elements are blocked by other surface elements). This is performed by tracing back each node in the direction of the flow velocity and checking a small tolerance of area for a blocking node. The tolerance area should be user-edited depending on the mesh used; if there are sufficiently small surface elements, the tolerance should be near-zero. If all nodes being checked are "blocked" by flow-preceding nodes, the surface element is declared as blocked and $u_{1,2,3}$ are set to zero.

Having pressure and shear stress in the X, Y, and Z directions, the forces, moments, and lift and drag are calculated as stated in Section 2.1.2.

2.2.1 Free Molecular Aerodynamic Analysis Verification

The developed free molecular analysis method is verified using theoretical drag and lift coefficients on simple shapes. Three shapes are used: a flat plate, a sphere, and a right angle cylinder. The flat plate is oriented at different angles to the oncoming flow: $0°$, $30°$, $45°$, $60°$, and $90°$. Figure 2.5 shows the cylinder mesh employed for verification, Figure 2.6 displays the flat plate mesh employed for verification, and Figure 2.7 shows the sphere mesh employed for verification. The plate mesh measures 1 m by 1 m and is a structured mesh. The sphere mesh has a diameter of 1 m and is an unstructured mesh. The cylinder mesh has a diameter of 0.5 m and a length of 1 m, and is an unstructured mesh.

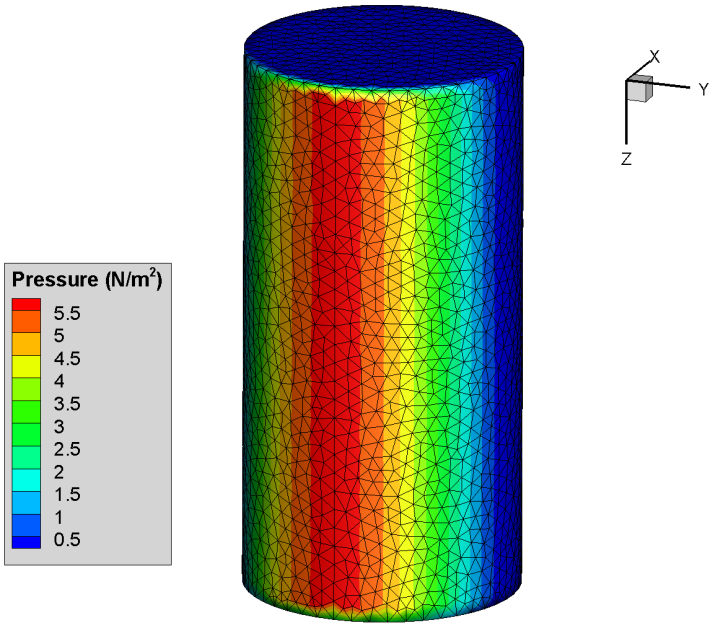

Figure 2.5: Cylinder mesh experiencing free molecular flow in the hypersonic limit.

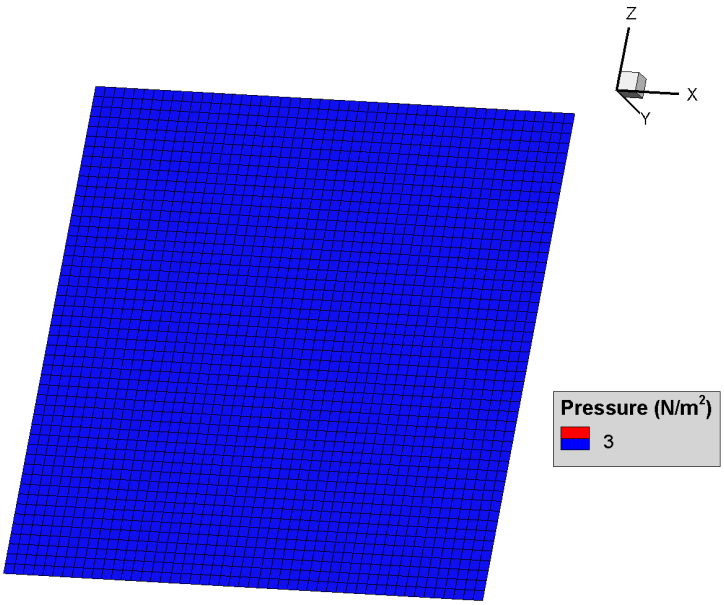

Figure 2.6: Flat plate mesh experiencing free molecular flow at an angle of 90° in the hypersonic limit.

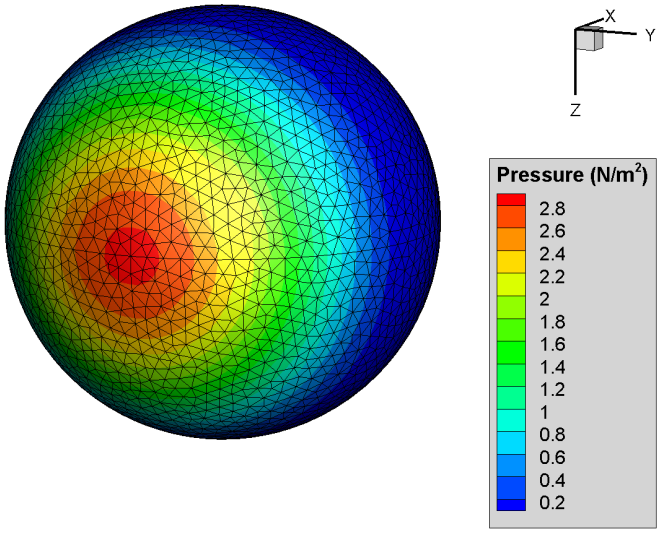

Figure 2.7: Sphere mesh experiencing free molecular flow in the hypersonic limit.

The wall temperature of the bodies is confined to $T_w = 300$ K, an average value experienced

by spacecraft in LEO demonstrated in the upcoming sections. Accommodation coefficients of 0 and 1 are tested for verification to establish that the modeling technique works for specular and diffuse reflections, respectively. The area is the front-facing projected area, and the density of the incoming flow is calculated for 300 km based on the NRLMSISE-00 atmospheric model [9].

To verify the modeling approach in the free molecular limit, a Kn of 2600 is used, corresponding to an orbital altitude of 300 km. Using the definition of speed ratio $s = \sqrt{\frac{mu^2}{2kT_i}}$, with u being the magnitude of oncoming velocity, limiting cases of the lift and drag coefficients can be derived for the prototype bodies. The drag and lift coefficients are defined as usual: $C_D = \frac{F_D}{\frac{1}{2}\rho V^2 A}$ and $C_L = \frac{F_L}{\frac{1}{2}\rho V^2 A}$.

There are two limiting cases: $s \to 0$, or creeping flow, and $s \to \infty$, or hypersonic flow. Using Equations 2.7, 2.8, 2.10, 2.11, and the definitions of coefficient of drag and lift, hypothetical limits for the coefficients are derived in the creeping and hypersonic limits. The sphere and cylinder are both perfectly symmetric, so they experience no lift. The lift coefficient modeling is verified with the flat plate modeling.

Equations 2.17 and 2.18 display the creeping limit for the coefficient of drag experienced by a sphere in free molecular flow. These equations experience a singularity at $s = 0$, therefore in verification, $s = 0.01$ is the smallest value used. In both the specular and diffuse approaches, the hypersonic limit for the drag coefficient of the sphere is the same, displayed in Equation 2.19.

$$\lim_{s\to 0} C_{D_{diff}} = \frac{16}{3}\frac{1}{\sqrt{\pi}s} + \frac{2\sqrt{\pi}}{3s}\sqrt{\frac{T_w}{T_i}} \tag{2.17}$$

$$\lim_{s\to 0} C_{D_{spec}} = \frac{16}{3}\frac{1}{\sqrt{\pi}s} \tag{2.18}$$

$$\lim_{s>>1} C_D = 2 \tag{2.19}$$

Speed ratio values between 0.01 and 1000 are used to test the modeling approach. The sphere coefficients of drag converge on 1.998 in the hypersonic limit using the developed free molecular flow analytical model; verifying the approach within 0.1% for hypersonic applications. The coefficients of drag for the sphere versus the speed ratio are plotted in Figures 2.8 and 2.9. The low-limit speed ratio theory only stretches so far: there is a singularity as s approaches 0, around this value the theoretical equations explode. In reality, as flow speed creeps to zero, the drag and lift experienced by a body also drop to zero and therefore the coefficients will as well. This leads to limited agreement between the model and the theoretical equations at low speeds; however, this thesis is focused on hypersonic applications of models to bodies experiencing lift and drag so the agreement in the hypersonic limit is emphasized.

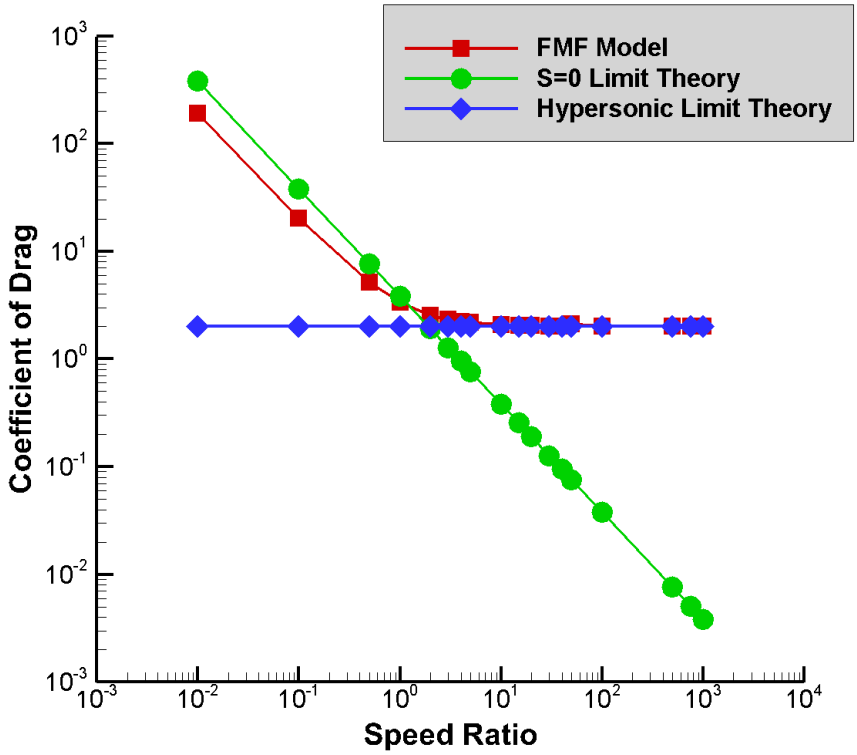

Figure 2.8: Diffuse sphere drag coefficient plotted versus speed ratio according to theoretical Equations 2.17 and 2.19 and the computational model.

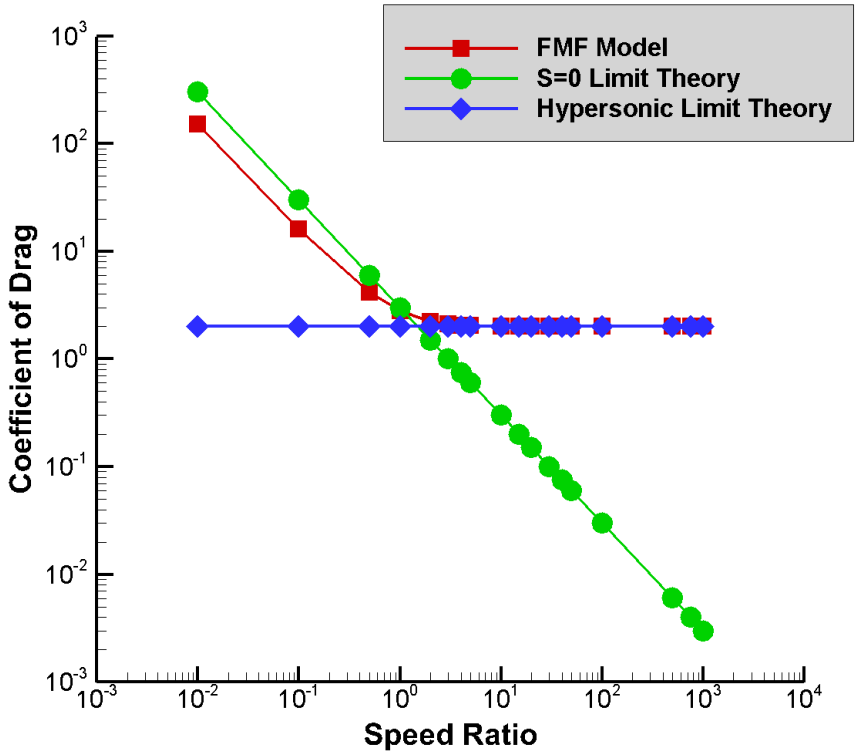

Figure 2.9: Specular sphere drag coefficient plotted versus speed ratio according to theoretical Equations 2.18 and 2.19 and the computational model.

Equations 2.20 and 2.21 display the creeping limit for the coefficient of drag experienced by a right circular cylinder (with projected area $A = 2 \cdot \text{radius} \cdot \text{height}$) in free molecular flow. Equations 2.22 and 2.23 display the hypersonic limit for the coefficient of drag experienced by a right circular cylinder in free molecular flow.

$$\lim_{s \to 0} C_{D_{diff}} = \frac{\sqrt{\pi}}{s} \left(\frac{3}{2} + \frac{\pi}{4} \sqrt{\frac{T_w}{T_i}} \right) \tag{2.20}$$

$$\lim_{s \to 0} C_{D_{spec}} = \frac{2\sqrt{\pi}}{s} \tag{2.21}$$

$$\lim_{s>>1} C_{D_{diff}} = 2 \tag{2.22}$$

$$\lim_{s>>1} C_{D_{spec}} = \frac{8}{3} \tag{2.23}$$

The specular cylinder coefficient of drag converges on 2.66 in the hypersonic limit using the developed free molecular flow analytical model verifying the approach within 0.07% for hypersonic applications. The diffuse cylinder coefficient of drag converges on 2.0004 in the hypersonic limit using the developed free molecular flow analytical model verifying the approach within 0.02% for hypersonic applications. The coefficients of drag for the cylinder versus the speed ratio are plotted in Figures 2.10 and 2.11.

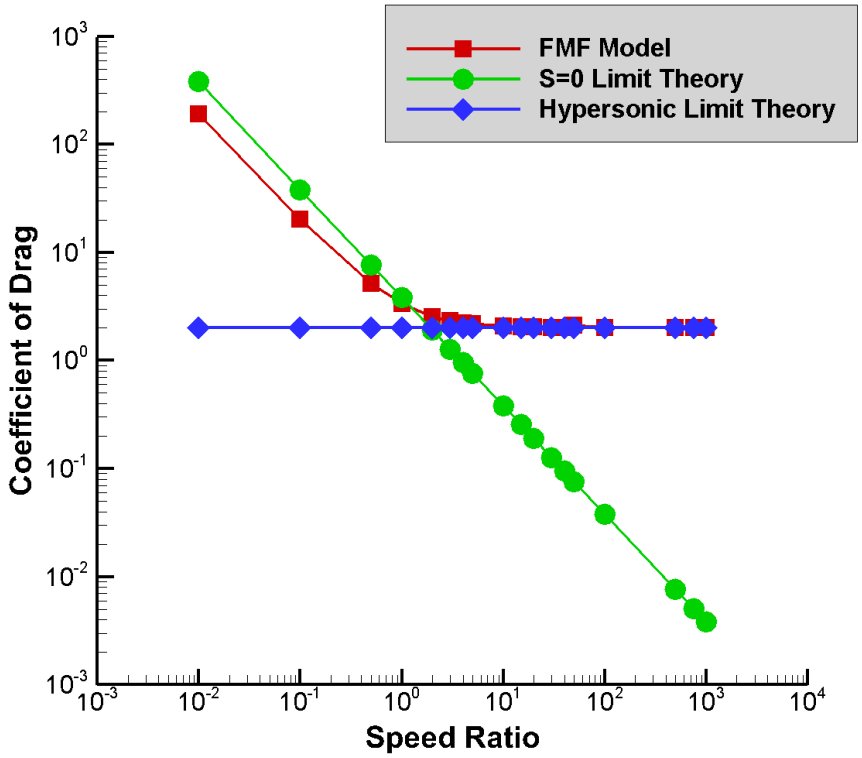

Figure 2.10: Diffuse cylinder drag coefficient plotted versus speed ratio according to theoretical Equations 2.20 and 2.22 and the computational model.

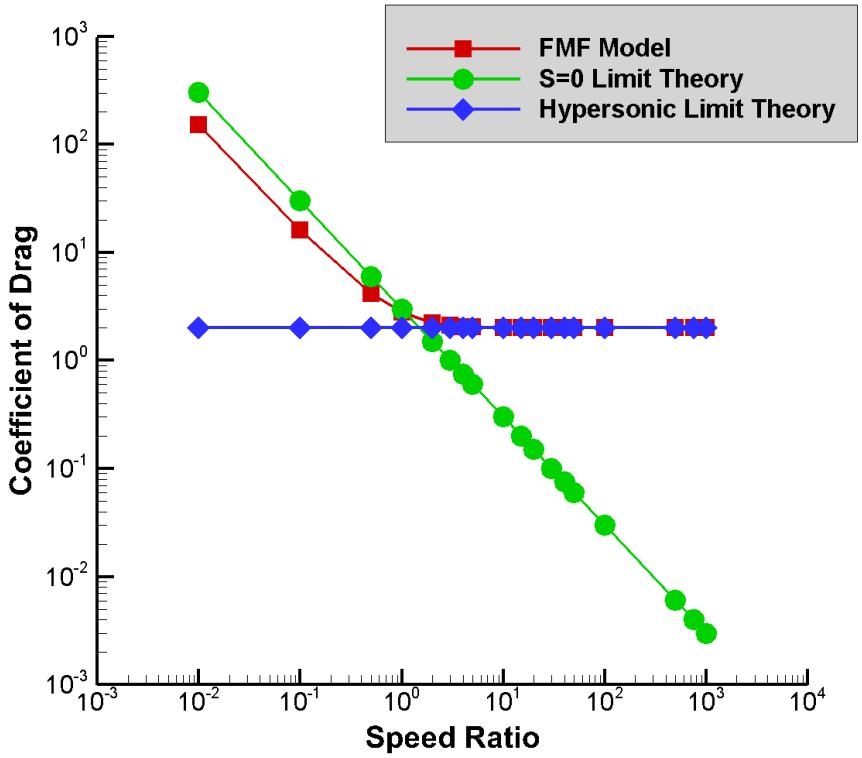

Figure 2.11: Specular cylinder drag coefficient plotted versus speed ratio according to theoretical Equations 2.21 and 2.23 and the computational model.

Angles of attack of the flow, β, are introduced in the verification of the model using the flat plate. The aerodynamic coefficients of drag and lift for diffuse and specular flat plates in the creeping limit are given in Equations 2.24, 2.25, 2.26, and 2.27.

$$\lim_{s\to 0} C_{D_{diff}} = \frac{2}{\sqrt{\pi} s}\left[1 + \sin^2\beta\left(1 + \pi\sqrt{\frac{T_w}{T_i}}\right)\right] \tag{2.24}$$

$$\lim_{s\to 0} C_{D_{spec}} = \frac{8}{\sqrt{\pi}}\frac{\sin^2\beta}{s} \tag{2.25}$$

$$\lim_{s\to 0} C_{L_{diff}} = \frac{\sin\beta\cos\beta}{\sqrt{\pi}s}\left(2+\pi\sqrt{\frac{T_w}{T_i}}\right) \tag{2.26}$$

$$\lim_{s\to 0} C_{L_{spec}} = \frac{8}{\sqrt{\pi}}\frac{\sin\beta\cos\beta}{s} \tag{2.27}$$

The aerodynamic coefficients for diffuse and specular flat plates in the hypersonic limit are given in Equations 2.28, 2.29, 2.30, and 2.31.

$$\lim_{s>>1} C_{D_{diff}} = 2\sin\beta \tag{2.28}$$

$$\lim_{s>>1} C_{D_{spec}} = 4\sin^3\beta \tag{2.29}$$

$$\lim_{s>>1} C_{L_{diff}} = \frac{\sin\beta\cos\beta}{s}\sqrt{\pi\frac{T_w}{T_i}} \tag{2.30}$$

$$\lim_{s>>1} C_{L_{spec}} = 4\sin^2\beta\cos\beta \tag{2.31}$$

Equations 2.17 through 2.31 are derived using [25] as a basis.

As an example of the flat plate verification process, the coefficients of drag for the flat plate at an angle of attack of 60° versus the speed ratio are plotted in Figures 2.12 and 2.13. The coefficients of lift for the flat plate at an angle of attack of 60° versus the speed ratio are plotted in Figures 2.14 and 2.15.

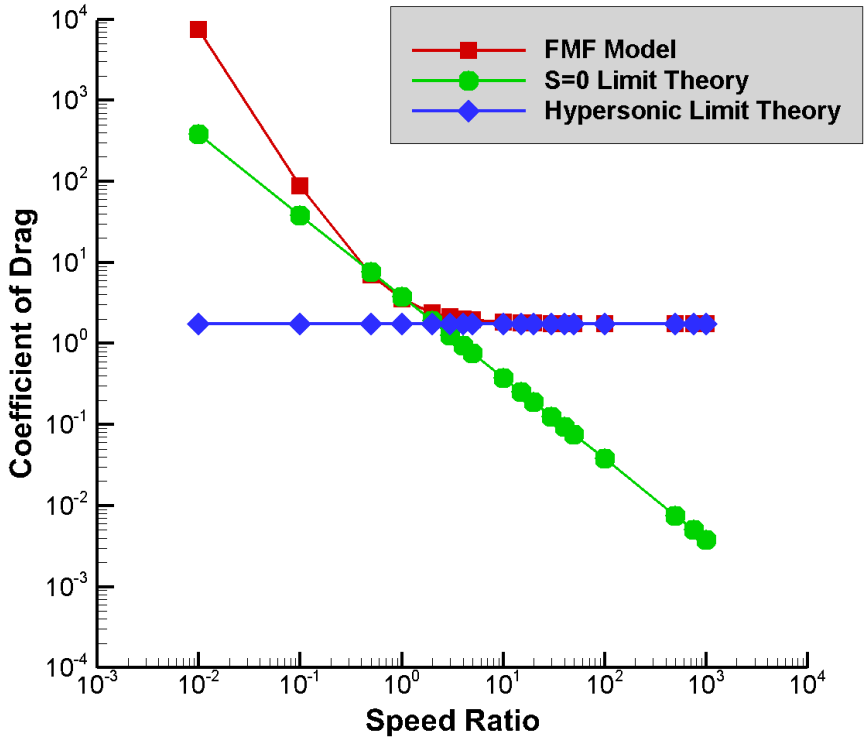

Figure 2.12: Diffuse flat plate at an angle of attack of $60°$ drag coefficient plotted versus speed ratio according to theoretical Equations 2.24 and 2.28 and the computational model.

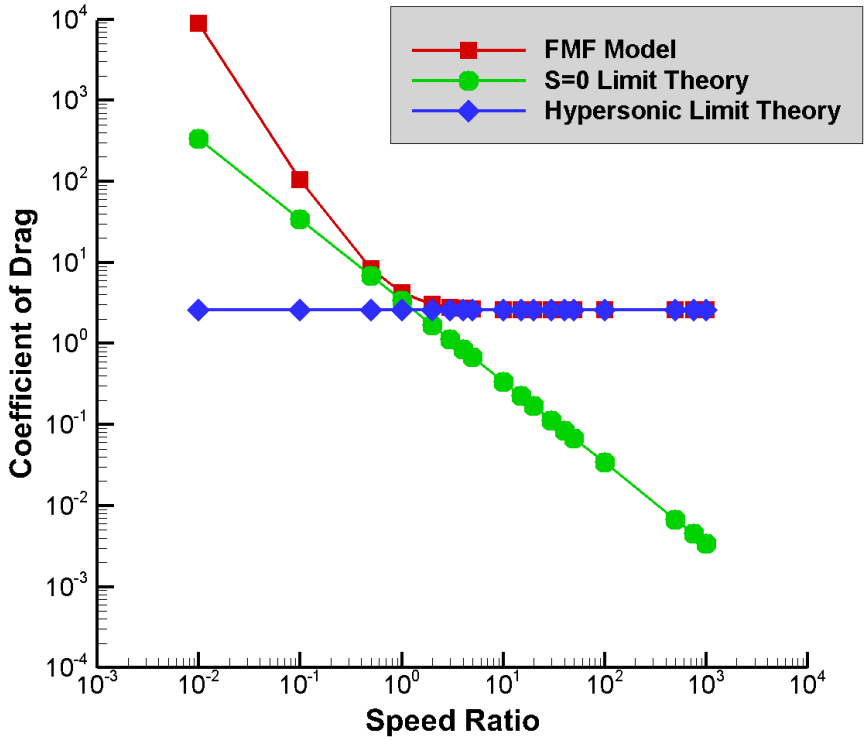

Figure 2.13: Specular flat plate at an angle of attack of 60° drag coefficient plotted versus speed ratio according to theoretical Equations 2.25 and 2.29 and the computational model.

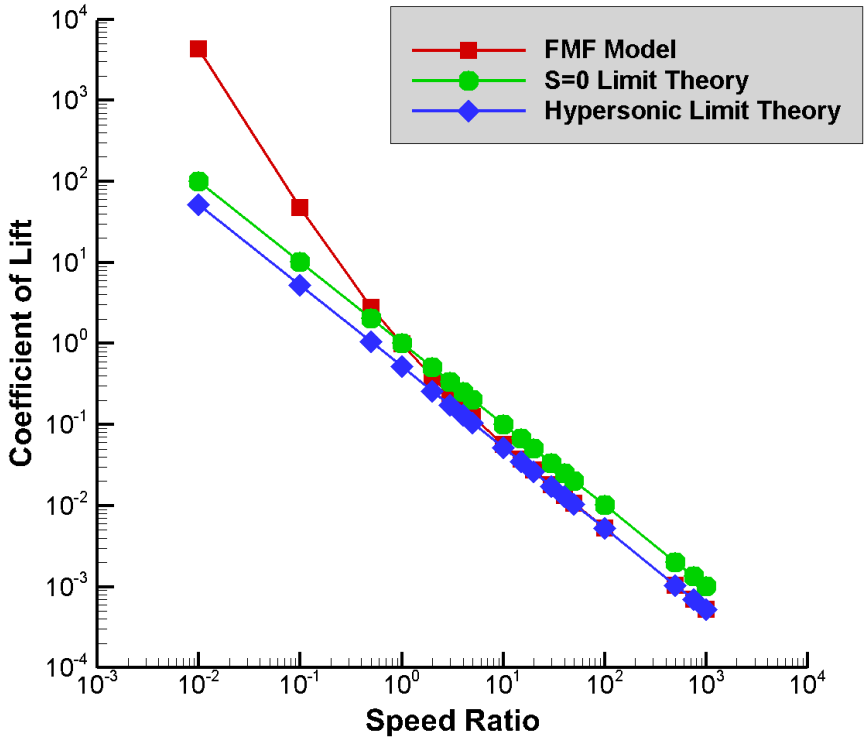

Figure 2.14: Diffuse flat plate at an angle of attack of 60° lift coefficient plotted versus speed ratio according to theoretical Equations 2.26 and 2.30 and the computational model.

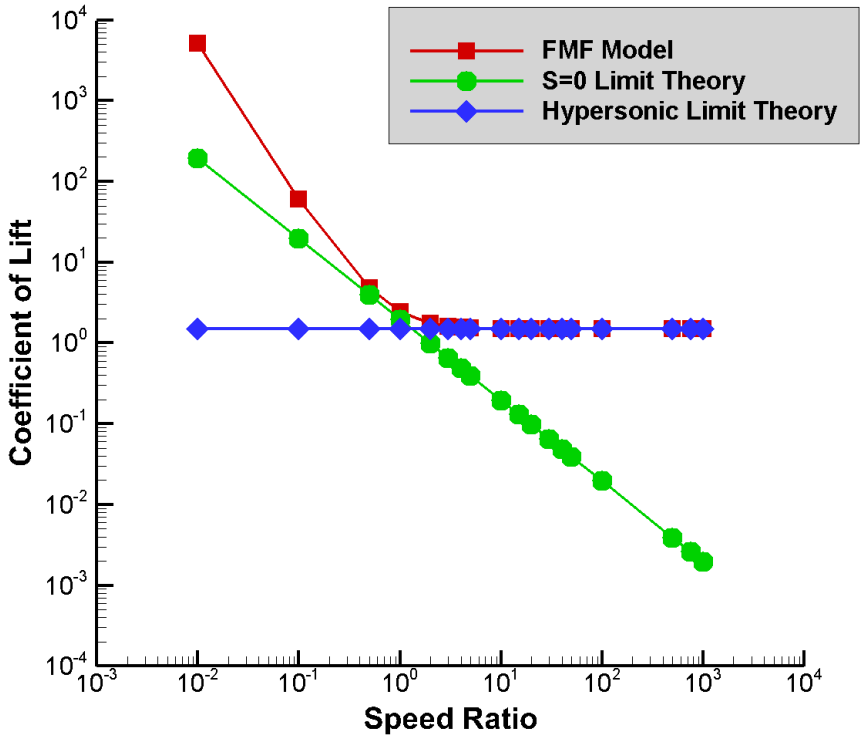

Figure 2.15: Specular flat plate at an angle of attack of 60° lift coefficient plotted versus speed ratio according to theoretical Equations 2.27 and 2.31 and the computational model.

This thesis is concerned with the hypersonic limit of the free molecular model as its primary focus is examining bodies experiencing orbital and reentry velocities. Therefore, verification in the hypersonic limit of the free molecular regime is desired. The flat plate verification is further useful due to the analogous surfaces in several spacecraft bodies, i.e. any modular CubeSat. Table 2.2 displays the model's results as well as the theoretical results for the drag coefficient of each body at a speed ratio of 1000. Note that percent difference between the theoretical coefficient and the modeled coefficient is not calculated if the theoretical coefficient is 0; however the model approaches or achieves a zero value for each instance of a theoretical null coefficient. The modeling approach is verified within 0.11% for the hypersonic coefficients of drag.

Table 2.2: Coefficients of drag for verification bodies calculated using the theoretical hypersonic limit and the free molecular analytical model at $s = 1000$.

Shape	Reflection	$\beta°$	Modeled C_D	$\lim_{s>>1} C_D$	% Error
Sphere	Diffuse	-	2.00	2	0.07
Sphere	Specular	-	2.00	2	0.11
Cylinder	Diffuse	-	2.00	2	0.02
Cylinder	Specular	-	2.66	2.67	0.07
Flat Plate	Diffuse	0	1.15×10^{-5}	0	-
Flat Plate	Specular	0	0.00	0	-
Flat Plate	Diffuse	30	1.00	1	0.03
Flat Plate	Specular	30	0.50	0.5	0.00
Flat Plate	Diffuse	45	1.41	1.41	0.04
Flat Plate	Specular	45	1.41	1.41	0.00
Flat Plate	Diffuse	60	1.73	1.73	0.05
Flat Plate	Specular	60	2.60	2.60	0.00
Flat Plate	Diffuse	90	2.00	2	0.06
Flat Plate	Specular	90	4.00	4	0.00

Table 2.3 displays the results from the modeled approach and the theoretical value for the coefficient of lift experienced by the flat plate in hypersonic flow ($s = 1000$). The developed modeling approach is verified within 0.2% for the hypersonic coefficients of lift.

Table 2.3: Coefficients of lift for the verification flat plate calculated using the theoretical hypersonic limit and the free molecular analytical model at $s = 1000$.

Shape	Reflection	$\beta°$	Modeled C_L	$\lim_{s>>1} C_L$	% Error
Flat Plate	Diffuse	0	0.00	0	-
Flat Plate	Specular	0	0.00	0	-
Flat Plate	Diffuse	30	5.23×10^{-4}	5.22×10^{-4}	0.17
Flat Plate	Specular	30	0.87	0.87	0.00
Flat Plate	Diffuse	45	6.03×10^{-4}	6.03×10^{-4}	0.12
Flat Plate	Specular	45	1.41	1.41	0.00
Flat Plate	Diffuse	60	5.23×10^{-4}	5.22×10^{-4}	0.10
Flat Plate	Specular	60	1.50	1.5	0.00
Flat Plate	Diffuse	90	0.00	0	-
Flat Plate	Specular	90	0.00	0	-

2.3 The Orbital Decay Model

2.3.1 The Gaussian Perturbation Equations

In order to examine the effects of changing aerodynamic coefficients on satellite dynamics, an orbital decay model is constructed. The ideal model would be applicable to both circular and elliptical orbits and be able to project long-term decay using only initial orbital elements and coefficients of drag and lift as inputs. For this model, the coefficients would be held steady, emulating a stable, unchanging orientation - or alternatively, representing an average of coefficients experienced in a short time span by a tumbling body. This orbital decay model allows for comparison of the impact that different aerodynamic coefficient modeling techniques have on projection of orbital lifetimes. Additionally, aerodynamic forces are small compared to the gravitational pull the Earth; therefore long time-scales are necessary to see substantive differences in decay due to aerodynamic coefficients. The orbital decay model is developed by applying the Gaussian perturbation equations to the satellite of choice, using aerodynamic forces as the sole perturbation.

The Gaussian perturbation equations are defined for a small perturbation force on the satellite given in Equation 2.32. Perturbations must be small when compared with the gravitational pull of the Earth, or larger body in the astrodynamic two-body problem [5]. Note that the force in Equation 2.32 is the specific force felt by the satellite (i.e. the satellite's acceleration), it is the force normalized by the mass of the satellite m_{sat}.

The perturbation force is illustrated in a satellite-fixed frame shown in Figure 2.16; the blue ball is representative of the Earth and the red square represents any satellite orbiting Earth. The black line ellipse is the satellite's unperturbed orbit. $\vec{r}$ is the position vector of the satellite in an Earth-fixed frame; θ is the satellite's true anomaly at a moment in time, where true anomaly is a

Keplerian orbital element equaling the angle between the satellite's position vector on the elliptical orbit and the line of periapsis. $\hat{r}$, $\hat{\theta}$, and $\hat{z}$ define the satellite-fixed frame; $\hat{r}$ is parallel to $\vec{r}$ and $\hat{\theta}$ is parallel to the satellite's velocity, tangent to the orbit. $\hat{z}$ is the cross-product of $\hat{r}$ and $\hat{\theta}$ and points "out" of the page.

$$d\vec{F} = S\hat{r} + T\hat{\theta} + N\hat{z} \tag{2.32}$$

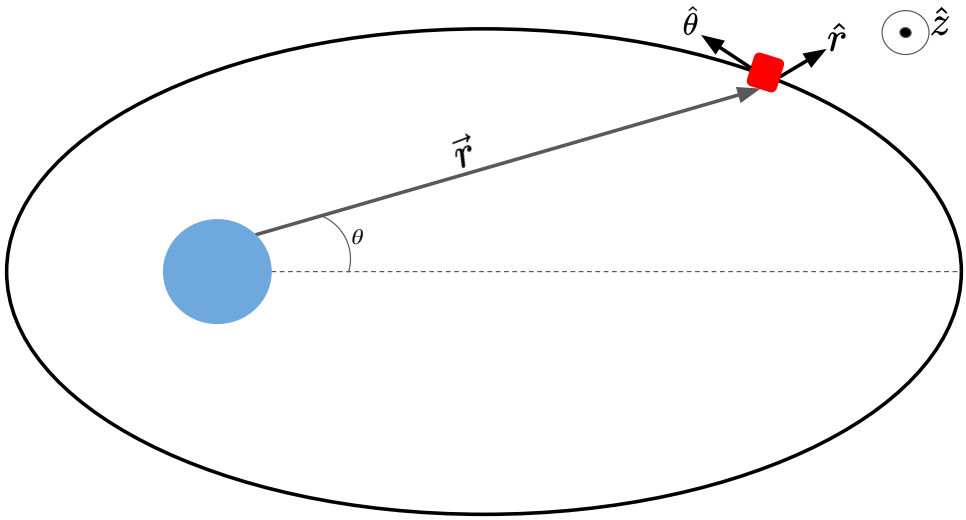

Figure 2.16: The satellite fixed frame applied in the Gaussian perturbation equations illustrated for a satellite experiencing an elliptical orbit.

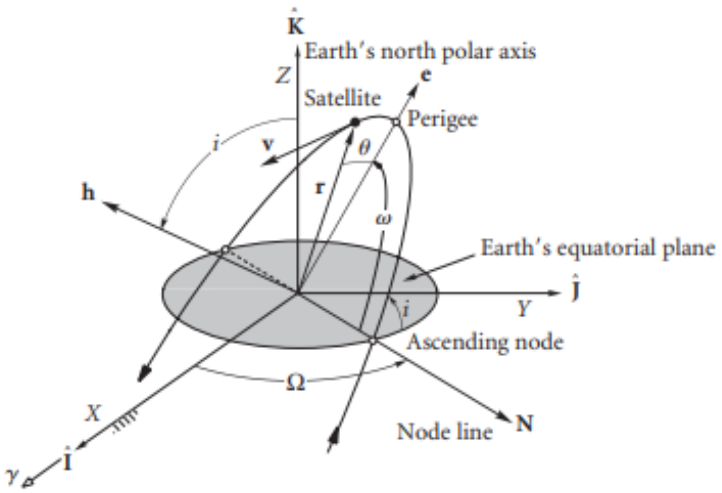

Figure 2.17: The six Keplerian orbital elements illustrated in a Geocentric equatorial frame [5].

The Gaussian perturbation equations demonstrate the change in the six classic Keplerian orbital elements over time due to a small perturbing force. The six Keplerian orbital elements completely describe a satellite's position and velocity along an orbit at a particular time. They are: a, the orbit's semi-major axis length; e, the orbital eccentricity; i, the orbital inclination; Ω, the right ascension of the ascending node (RAAN); ω, the argument of perigee; and θ, the true anomaly. Figure 2.17 illustrates the six Keplerian elements for a satellite orbiting the Earth. Small perturbations change the orbit over time and these changes can be enacted by altering orbital elements. This approach is used because many satellites in LEO have eccentric orbits; for circular orbits, where eccentricity is zero, machine-precision zero is used in modeling the orbital decay.

Equations 2.33-2.38 are the Gaussian perturbation equations, where $u = \omega + \theta$ is the argument of latitude [26]. p is the semi-latus rectum calculated in Equation 2.40; and r is the distance between the Earth and the satellite, given by the orbit equation in Equation 2.39 [5]. Note that Equation 2.38 accounts for the change in true anomaly due to the nominal orbital motion ($\frac{\sqrt{\mu p}}{r^2}$) as well as the change in true anomaly caused by the perturbation ($\sqrt{\frac{p}{\mu}}\frac{1}{e}\left[S\cos\theta - T\sin\theta\left(\frac{2+e\cos\theta}{1+e\cos\theta}\right)\right]$).

$$\frac{da}{dt} = \frac{2a^2}{\sqrt{\mu p}}[Se\sin\theta + T(1 + e\cos\theta)] \tag{2.33}$$

$$\frac{de}{dt} = \sqrt{\frac{p}{\mu}}\left[S\sin\theta + T\left(\frac{e + 2\cos\theta + e\cos^2\theta}{1 + e\cos\theta}\right)\right] \tag{2.34}$$

$$\frac{di}{dt} = \frac{r}{\sqrt{\mu p}}\cos u \cdot N \tag{2.35}$$

$$\frac{d\Omega}{dt} = \frac{r}{\sqrt{\mu p}}\frac{\sin u}{\sin i} \cdot N \tag{2.36}$$

$$\frac{d\omega}{dt} = \sqrt{\frac{p}{\mu}}\frac{1}{e}\left[- S\cos\theta + T\sin\theta\left(\frac{2 + e\cos\theta}{1 + e\cos\theta}\right)\right] - \cos i\frac{d\Omega}{dt} \tag{2.37}$$

$$\frac{d\theta}{dt} = \frac{\sqrt{\mu p}}{r^2} + \sqrt{\frac{p}{\mu}}\frac{1}{e}\left[S\cos\theta - T\sin\theta\left(\frac{2 + e\cos\theta}{1 + e\cos\theta}\right)\right] \tag{2.38}$$

$$r = a\big(\frac{1 - e^2}{1 + e\cos\theta}\big) \tag{2.39}$$

$$p = a(1 - e^2) \tag{2.40}$$

2.3.2 Circular Orbit Verification

The Australian IPS Radio & Space Services applied the Gaussian perturbation equations to circular orbits in order to examine a loss in orbital period over time due to atmospheric drag [6]. Equation 2.41 is the Keplerian equation for orbital period: a function solely of the semi-major axis.

Loss in orbital period is used in this model to calculate an inevitable reentry time, giving the lifetime prediction of a satellite in an arbitrary circular orbit.

$$P = \left(\frac{4\pi^2 a^3}{GM_E}\right)^{\frac{1}{2}} \tag{2.41}$$

Using Equation 2.41, the reduction in orbital period is: $\frac{dP}{dt} = \frac{3\pi}{\sqrt{\mu}} a^{1/2} \cdot \frac{da}{dt}$. This equation implies that the only necessary Gaussian perturbation equation to track circular orbital decay is Equation 2.33. For this particular model, the only perturbing aerodynamic force examined is aerodynamic drag. Accounting only for drag makes Equation 2.32 become $d\vec{F} = 0\hat{r} - D\hat{\theta} + 0\hat{z}$. where D is the magnitude of the specific drag force experienced by the satellite. S and N in Equation 2.32 are equal to 0, making Equations 2.35 and 2.36 obsolete. Therefore, to model circular decay, only Equation 2.33 is necessary.

The specific drag force experienced by the satellite is given in Equation 2.42. ρ is the density of the atmosphere at the current altitude of the orbit; atmospheric models are hugely impactful in modeling orbital decay and as such are discussed in a later section. C_D is the coefficient of drag, a result of other simulations. A_s is the projected area of the satellite in the direction of the induced atmospheric flow due the satellite's speed v^2, and m_{sat} is the mass of the satellite. v^2 is calculated using the vis-viva energy equation seen in Equation 2.43, which for circular orbits becomes $v^2 = \frac{\mu}{a}$ as the orbital energy ϵ is a constant across an orbit, and $a = r$ for circular orbits.

Using Equation 2.42 and the circular vis-viva equation in 2.33 yields $\frac{da}{dt} = -\sqrt{a\mu}\frac{C_D A_s}{m_{sat}}\rho$. Finally, we use this to calculate the reduction in circular orbital period due to atmospheric drag, Equation 2.44.

$$D = \frac{1}{2}\rho v^2 \frac{C_D A_s}{m_{sat}} \tag{2.42}$$

$$\frac{v^2}{2} - \frac{\mu}{r} = \epsilon \tag{2.43}$$

$$\frac{dP}{dt} = -3\pi a \rho \left(\frac{C_D A_s}{m_{sat}} \right) \tag{2.44}$$

Equation 2.44 is identical to that used in [6], corroborating the Gaussian perturbation equations as a way to predict and model orbital decay.

The approach used in the Australian model ([6]) is not flexible enough for the purpose of this thesis. Many satellites experience non-negligibly elliptical orbits, and a orbital decay method that includes lift forces is sought.

The objective is to create an orbital decay model flexible enough to handle lift, drag, circular and elliptical orbits. The complete set of Gaussian perturbation equations is therefore the basis of the developed orbital decay model.

2.3.3 Developed Orbital Decay Model

For maximum flexibility, our orbital decay model is designed to use only starting Keplerian elements as inputs. The framework of the desired model is illustrated in the diagram in Figure

2.18. In Figure 2.18, h is the current altitude of the satellite, $h = r - R_E$, where R_E is the average radius of the Earth. h_{limit} is a user-defined altitude signaling imminent reentry. For our purposes, $h_{limit} = 180$ km below which most satellites will impact Earth in a matter of hours [6].

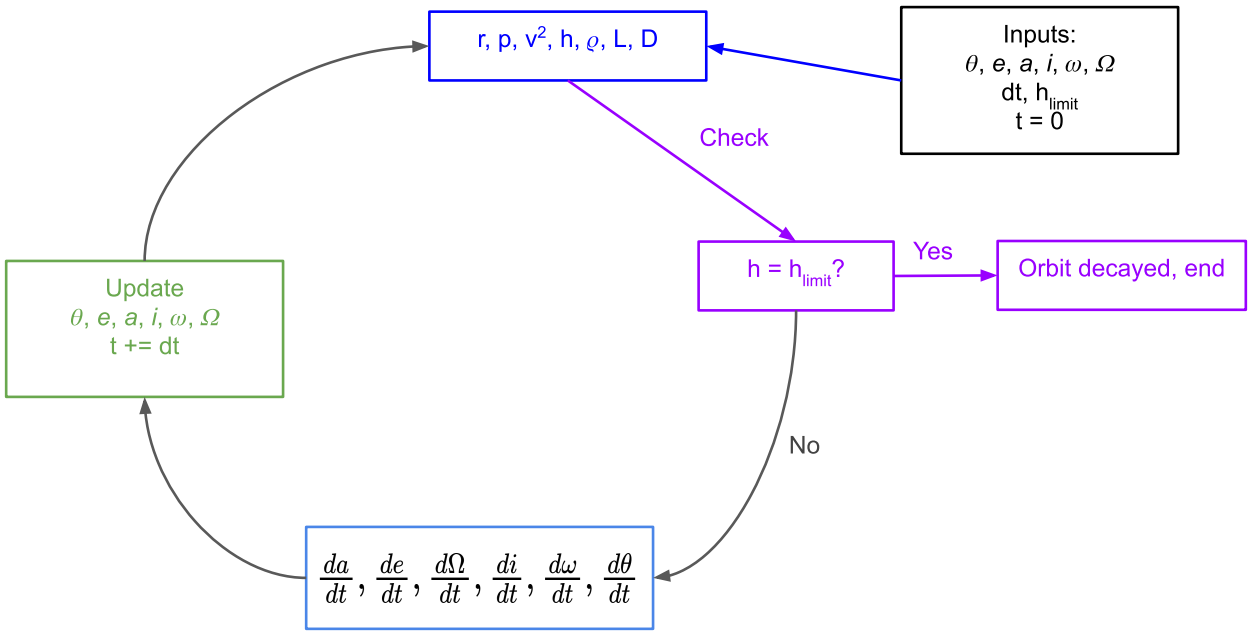

Figure 2.18: The flowchart of the desired orbital decay model.

Using an initial input of six Keplerian elements $[\theta, e, a, i, \Omega, \omega]$, we can calculate necessary orbital quantities using Equations 2.39, 2.40, and 2.43 in the form $v^2 = \mu\left(\frac{2}{r} - \frac{1}{a}\right)$. The density model used for ρ is discussed in the next section. Specific drag is given using Equation 2.42 while Equation 2.45 is the equation used for specific lift. C_L is the lift coefficient which we derive using other models for specific satellites, all other variables in Equation 2.45 are defined as before. The altitude is checked for the user-defined altitude limit, h_{limit}.

The orbital decay model used here is implemented in Matlab.

$$L = \frac{1}{2}\rho v^2 \frac{C_L A_s}{m_{sat}} \tag{2.45}$$

Equation 2.32 for both specific drag and lift perturbations is $d\vec{F} = L\hat{r} - D\hat{\theta} + 0\hat{z}$. Applying these perturbation forces ($S = L$, $T = -D$, $N = 0$) to the Gaussian perturbation equations 2.33 - 2.38 yields the following:

$$\frac{da}{dt} = \frac{2a^2}{\sqrt{\mu p}}[Le\sin\theta - D(1 + e\cos\theta)] \tag{2.46}$$

$$\frac{de}{dt} = \sqrt{\frac{p}{\mu}}\left[L\sin\theta - D\left(\frac{e + 2\cos\theta + e\cos^2\theta}{1 + e\cos\theta}\right)\right] \tag{2.47}$$

$$\frac{di}{dt} = 0 \tag{2.48}$$

$$\frac{d\Omega}{dt} = 0 \tag{2.49}$$

$$\frac{d\omega}{dt} = \sqrt{\frac{p}{\mu}}\frac{1}{e}\left[- L\cos\theta - D\sin\theta\left(\frac{2 + e\cos\theta}{1 + e\cos\theta}\right)\right] \tag{2.50}$$

$$\frac{d\theta}{dt} = \frac{\sqrt{\mu p}}{r^2} + \sqrt{\frac{p}{\mu}}\frac{1}{e}\left[L\cos\theta + D\sin\theta\left(\frac{2 + e\cos\theta}{1 + e\cos\theta}\right)\right] \tag{2.51}$$

Using this orbital decay model framework, and the atmospheric modeling equations illustrated in the following section, the modeling loop in Figure 2.18 can be completed by updating the orbital elements in time. To update the elements, the calculated derivatives are linearly applied to the "old" orbital elements through addition and multiplication by a user-defined time step, for example: $a_{new} = a_{old} + \frac{da}{dt}|_{old} \cdot dt$. The linear approach, as opposed to an ordinary differential equation

solver, is applied for full control over the parameters of the model. The loop is continued, updating the orbital elements in time, until the limiting altitude is reached and the orbit is determined to be fully decayed.

2.3.4 Atmospheric Density Models

Modeling atmospheric density is a large problem that presents its own set of challenges to the space science and engineering community. Modeling and measuring atmospheric density is the subject of many theses and is too broad to be thoroughly addressed here. We choose an atmospheric density model to ensure maximum flexibility (minimum inputs and tracking work) while also yielding orbital lifetime results nearly identical to two separate verification cases, discussed in a later section.

Many atmospheric models were considered, however for maximum flexibility we desired a model requiring no use of Earth-based tracking (i.e. no date or latitude/longitude variables). Therefore, the most accurate model with minimum inputs is implemented: the scale height model [27].

The scale height model is given in Equations 2.52 - 2.54. A subscript of "limit" signifies that these quantities are given by the U.S. Standard Atmosphere 1976 Model at the limiting reentry altitude of 180 km, and are constants in our model [12]. Equation 2.53 is the equation for the scale height at our limiting reentry altitude, where k is the Boltzmann constant, and T_{limit} is atmospheric temperature, m_{limit} is the mass of one hypothetical atmospheric particle, and g_{limit} is the acceleration due to Earth's gravity, all at the limiting reentry altitude.

Equation 2.54 is the simple gravity model employed based on the $1/r^2$ relationship between gravitational force and distance to yield gravitational acceleration due to the Earth at our reen-

try altitude. This model assumes a spherical Earth and ignores any perturbations in the Earth's gravitational field, eliminating the dependence on more variables and unnecessary inputs.

$$\rho = \rho_{limit} \exp\left(\frac{-|h - h_{limit}|}{H}\right) \tag{2.52}$$

$$H = \frac{kT_{limit}}{m_{limit} g_{limit}} \tag{2.53}$$

$$g_{limit} = g_{sealevel}\left(\frac{R_E}{R_E + h_{limit}}\right)^2 \tag{2.54}$$

Using this model additionally eliminates the need for F10.7 and A_p solar weather inputs which require a known date and atmospheric location.

2.3.5 Orbital Decay Model Verification

Our model is verified using comparisons to the circular orbital decay example presented in [6] and orbital decay of the satellite TBEx projected by STK orbital decay modeling [7].

2.3.5.1 Circular Decay Verification

Table 2.4 contains the parameters of a prototypical satellite (hereafter called CIRC, for circular orbit satellite) used as an example of the orbital decay model documented in [6]. Table 2.4 reflects that the only orbital element necessary to track orbital decay of a circular orbit is a as discussed in Section 2.3.2; however, all orbital elements are needed as inputs in the developed orbital decay model which can handle elliptical orbits. The eccentricity is designated as 1×10^{-16} to avoid

division by zero errors in the developed model.

In order to produce a one-to-one comparison, the scale height model for atmospheric density developed in the previous section is used across models. This replaces the original atmospheric density model used in [6], which depended on the solar weather inputs F10.7 and A_p for the initial decay date. This method reflects an error in the model: there is no way to update F10.7 and A_p in the native model, and both of these inputs change in time scales examined in these orbital decay models (the solar flux index F10.7 can change hourly or daily, the magnetic index changes each month, and the orbital decay examined exhibits time scales in years) [9]. Using the scale height model from the previous section eliminates the need for tracking the satellite's date throughout its decay.

Both models implement the same time step for cross-comparison: 0.1 days, or 8.64 $\times 10^3$ seconds. This time step is chosen based on the model used in [6] and implemented in both models for an effective comparison. The model used in [6] does not account for any lift, therefore the coefficient of lift is set to zero in the developed model. The threshold for reentry is 180 km as large satellites or pieces of debris will impact the Earth within a day or two after crossing that altitude [6].

Table 2.4: CIRC Parameters.

Parameter	Abbreviation	Value
Mass	m_{sat}	100 kg
Cross-Sectional Area	A_s	1 m^2
Drag Coefficient	C_D	1
Lift Coefficient	C_L	0
Starting Altitude	h	300 km
Starting Eccentricity	e	1×10^{-16}
Starting Inclination	i	0 °
Starting Argument of Perigee	ω	0 °
Starting RAAN	Ω	0 °
Starting True Anomaly	θ	0 °
Time Step	dt	0.1 days
Reentry Threshold	h_{limit}	180 km

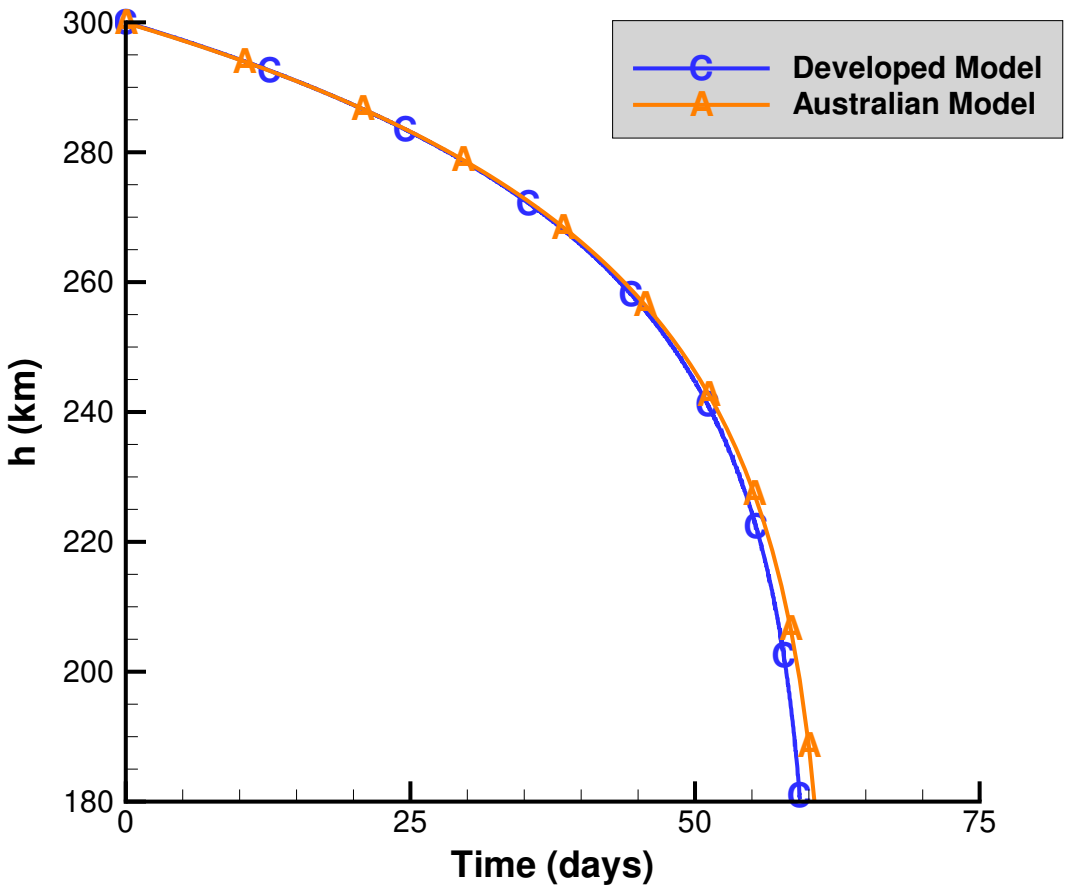

Figure 2.19: Comparison of the developed orbital decay model and the orbital decay model from [6] used on a prototypical satellite experiencing a circular orbit with the parameters listed in Table 2.4.

Figure 2.19 illustrates the results from using both models on the CIRC satellite with parameters given in Table 2.4. The developed model yielded a time-to-reenter of 59.3 days; the Australian model yielded a time-to-reenter of 60.8 days. There is a 2.47% difference in time-to-reentry between these different models, showing that the developed orbital decay model can closely emulate circular orbital decay calculated in established models.

2.3.5.2 TBEx Verification

In [7], the STK orbital decay model is performed on the TBEx satellites to estimate their time-to-decay after launch. The STK model uses date tracking for atmospheric and gravity modeling and therefore produces different results for decay of orbits with different arguments of perigee. The developed model will not show a difference in time-of-decay for different inclination, RAAN, and argument of perigee inputs due to the gravity and atmospheric models only depending on the altitude of the satellite. The model still implements changes of these Keplerian elements in order to examine their change over time due to induced atmospheric drag and lift.

Table 2.5: TBEx Parameters [7].

Parameter	Abbreviation	Value
Mass	m_{sat}	4 kg
Cross-Sectional Area	A_s	3.56×10^{-2} m^2
Drag Coefficient	C_D	2.32
Lift Coefficient	C_L	0
Starting Altitude	h	8.53×10^2 km
Starting Eccentricity	e	4.03 $\times 10^{-2}$
Starting Inclination	i	28.4 $^\circ$
Starting Argument of Perigee	ω	1.05×10^2 $^\circ$
Starting RAAN	Ω	0 $^\circ$
Starting True Anomaly	θ	180 $^\circ$
Time Step	dt	5 minutes
Reentry Threshold	h_{limit}	65 km

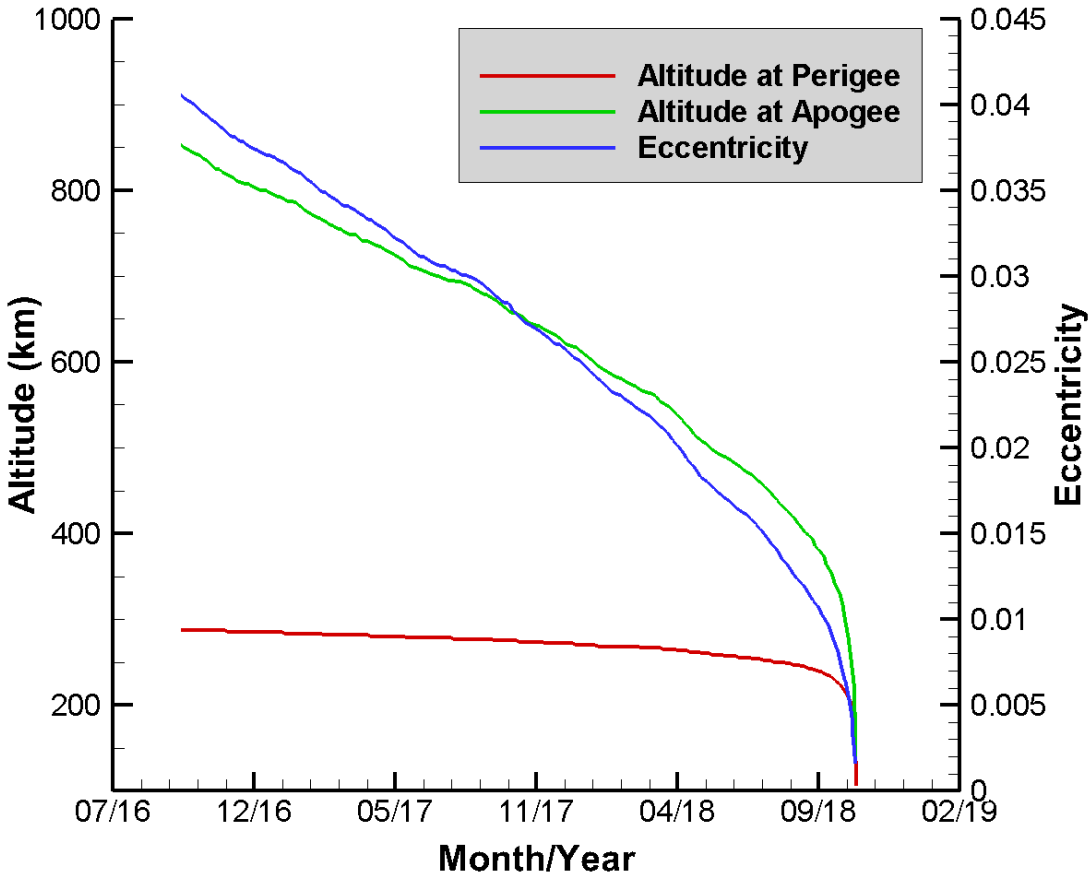

Figure 2.20: The orbital decay of a TBEx satellite with an initial argument of perigee of 105° as calculated using the STK model. Figure is adapted from [7].

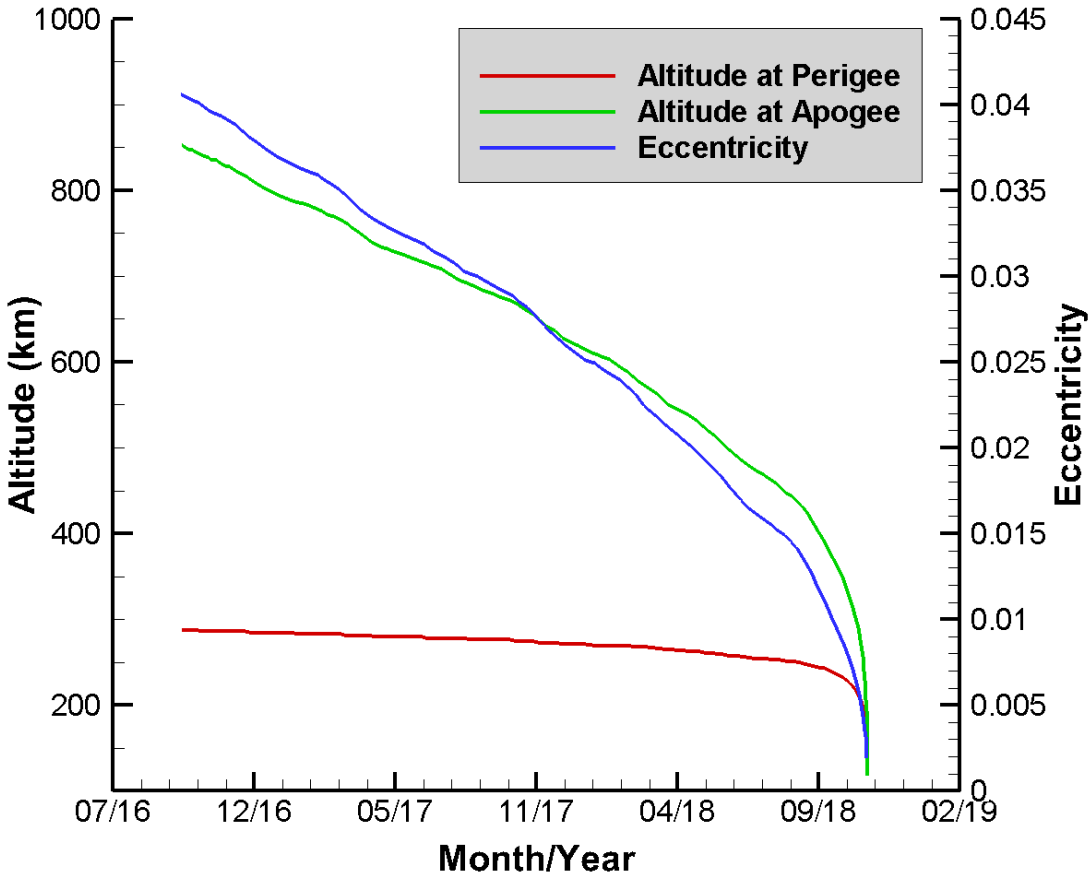

Figure 2.21: The orbital decay of a TBEx satellite with an initial argument of perigee of 300° as calculated using the STK model. Figure is adapted from [7].

Figures 2.20 and 2.21 plot the orbital decay of a TBEx satellite using the STK model from a starting altitude of about 850 km to the reentry threshold altitude of 65 km. STK uses latitude-longitude-date based tracking of the satellite in the Earth's atmosphere, and therefore the initial argument of perigee has an effect on the time-to-reenter. Using the STK model, the time-to-reenter for the TBEx satellite with an initial ω of 1.05×10^2 ° is 7.75×10^2 days, with an initial ω of 300° the time-to-reenter is 7.88×10^2 days.

The orbital decay model developed in this dissertation research does not track the satellite's

latitude, longitude, or date; therefore the initial argument of perigee will not affect time-to-reenter. The argument of perigee will evolve over time according to Equation 2.50, so it is updated throughout the course of the model's time run. Additionally, the gravity model assumes a "ball" Earth with a constant radius. Both of these assumptions cause the forces felt by the satellite in the developed model to only depend on altitude, which is not affected by latitude or longitude, and therefore not affected by ω. The ω chosen for verification against the STK TBEx orbital lifetime estimates is 105°.

The time step is chosen as 5 minutes to yield fast and accurate results. The STK model's reentry threshold is 65 km, so this is the reentry threshold used in the developed orbital decay model for cross-validation. The STK model implemented on the TBEx in [7] does not account for any lift, therefore the coefficient of lift is set to zero in the developed model.

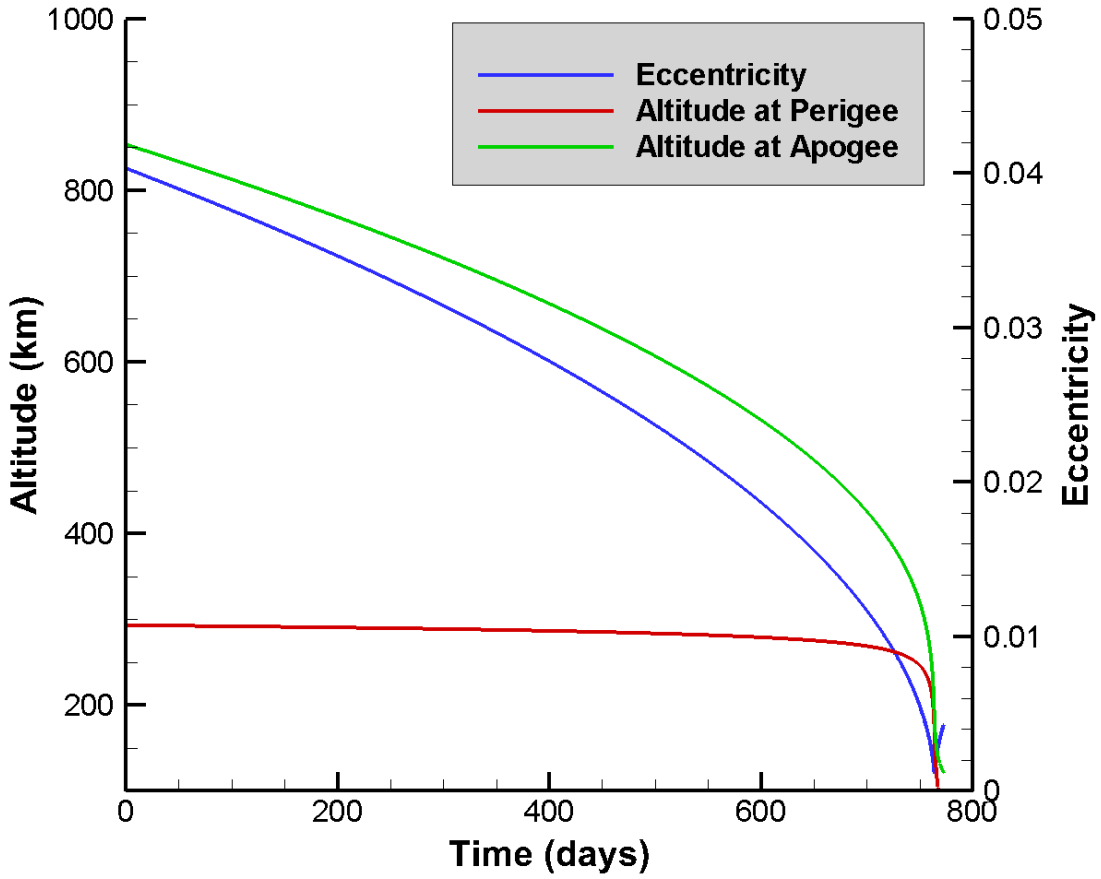

Figure 2.22: The orbital decay of a TBEx satellite with a starting argument of perigee of 300° as calculated using the developed orbital decay model.

Figure 2.22 demonstrates the results from the developed orbital decay model on the TBEx satellite with parameters in Table 2.5. The eccentricity experiences a "bounce back" in late orbital decay due to the nature of the developed model being incompatible with a eccentricity of zero.

The developed model yielded a time-to-reenter of 7.73×10^2 days; the STK model yielded a time-to-reenter of 7.75×10^2 days. There is a 0.28% difference in time-to-reentry between these different models, showing that the developed orbital decay model closely matches the yielded STK results for the TBEx satellite. The developed orbital decay model is appropriate for use in

this dissertation work.

CHAPTER 3

Analysis of the TBEx CubeSat

TBEx is the Tandom Beacon Experiment, launched on June 25, 2019. The experiments consist of two identical 3U CubeSats developed and launched by the Michigan Exploration Laboratory (MXL). These satellites were launched as part of the NASA and Department of Defense project Space Test Program-2 (STP-2) [21]. The purpose of the TBEx experiment is to study the unpredictable plasma bubbles that form in the upper atmosphere and the effect of these bubbles on communications systems.

During their mission, the two TBEx satellites, TBEx-A and TBEx-B, will send radio signals to ground stations in order to measure distortions caused by plasma bubbles. Ionospheric plasma bubbles are of interest because of the impact they have on our infrastructure when they distort important communications signals such as GPS transmissions [28].

The TBEx body is chosen for analysis due to prior work on 3U CubeSats [29] and due to the fact that it is an actual experiment with real data available which is used in determining certain independent variables to simulate. TBEx refers to the experimental body of this research; note, because TBEx-A and -B are duplicates, aerodynamic force results are identical.

TBEx is a 3U CubeSat equipped with several sensors including a magnetometer, a gyroscope, and temperature sensors; these sensors are necessary to carry out its mission. Physical differences

from a prototype 3U CubeSat are deployable solar panels on all four sides of the CubeSat and antennas on both short faces of the CubeSat. The basic CubeSat design specifications are show in Figure 3.1.

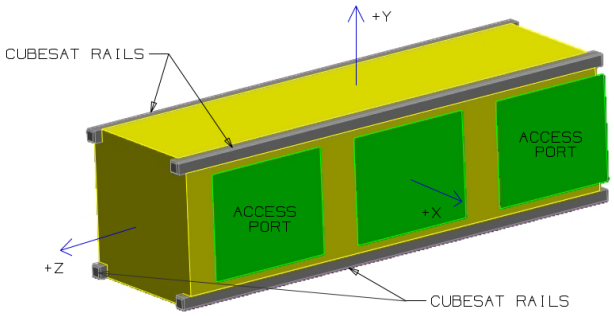

Figure 3.1: 3U CubeSat diagram from CubeSat specifications [8].

TBEx, in its non-deployed state and meeting Figure 3.1 design specifications, is shown in Figure 3.2 (a).

Figure 3.2 (a) displays the TBEx satellite that is launched into orbit. However, once it achieves orbital altitude, the satellite deploys its solar panels and antennae, thus changing the body that experiences atmospheric forces and moments. Figure 3.2 (b) displays the fully-deployed TBEx in the MXL.

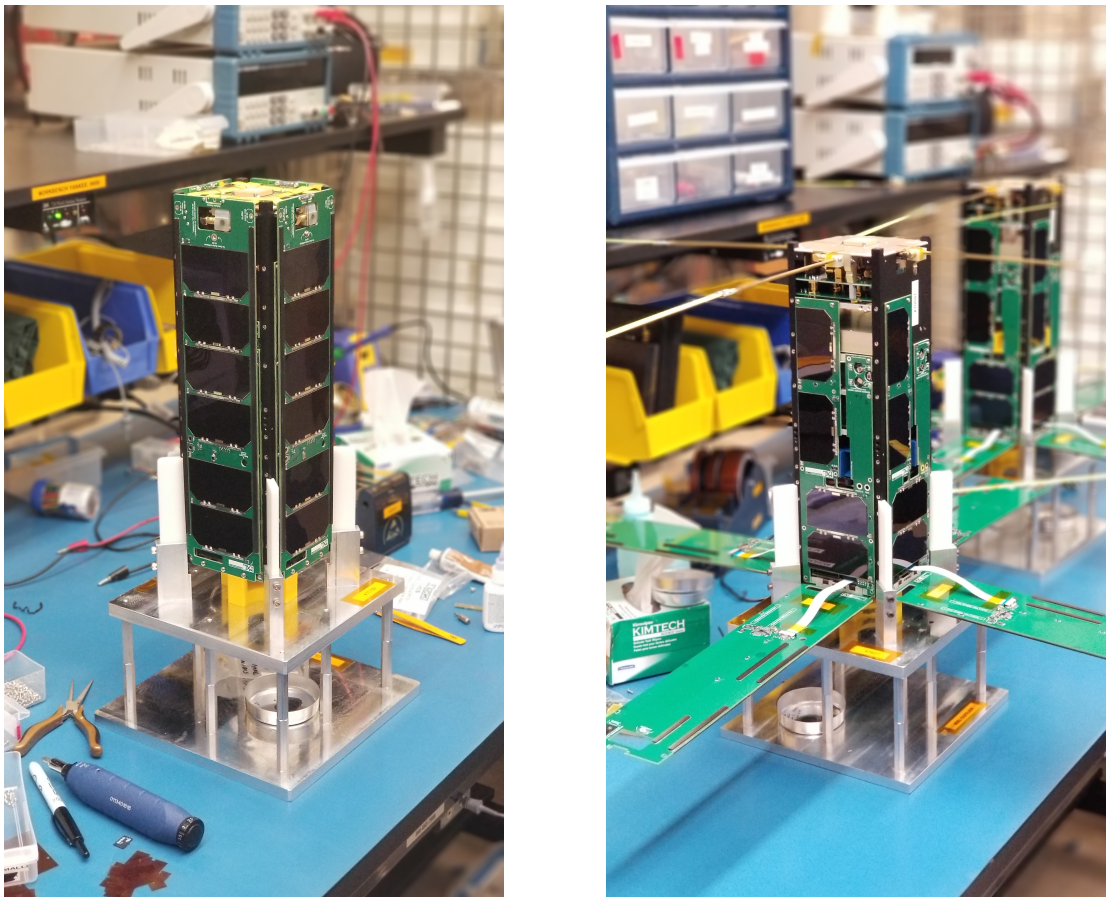

(a) (b)

Figure 3.2: TBEx CubeSat: (a) ready for launch, non-deployed, and (b) deployed in the MXL space.

The geometry modeled for TBEx must closely resemble the deployed body size and shape. The non-deployed TBEx shape has a length of 340.5 mm, and width and depth of 100 mm [8]. Each solar panel has the length of a TBEx "long side": 340 mm by 100 mm. Antennae are unfurled from the solar panels reaching a maximum length of 657 mm from the body center. Antennae are also established from the "top" of the TBEx in Figure **??**, measuring a maximum length of 480 mm from body center.

3.1 TBEx Body Experiment Design

In order to replicate the deployed TBEx shape for use with MONACO and the free molecular model, a mesh is generated using Pointwise. Figure 3.3 displays the surface mesh used to represent the TBEx body. The TBEx meshed body is formed using both structured and unstructured mesh domains. The mesh has cell areas on the order of 2.5×10^{-6} m^2, yielding a surface element side length on the order of 1.6×10^{-3} m. The volume mesh used on the TBEx is projected outwards from the body with growing cell size. The farfield volume measures 2.32 m by 2.31 m by 1.54 m. The farfield volume is limited to minimize the number of cells which impacts computational time. The flowfield does not need to be captured in its entirety since the primary goal is to capture surface-gas interactions to extract aerodynamic force and moment information. The flow needs only enough space to develop before coming into contact with the body.

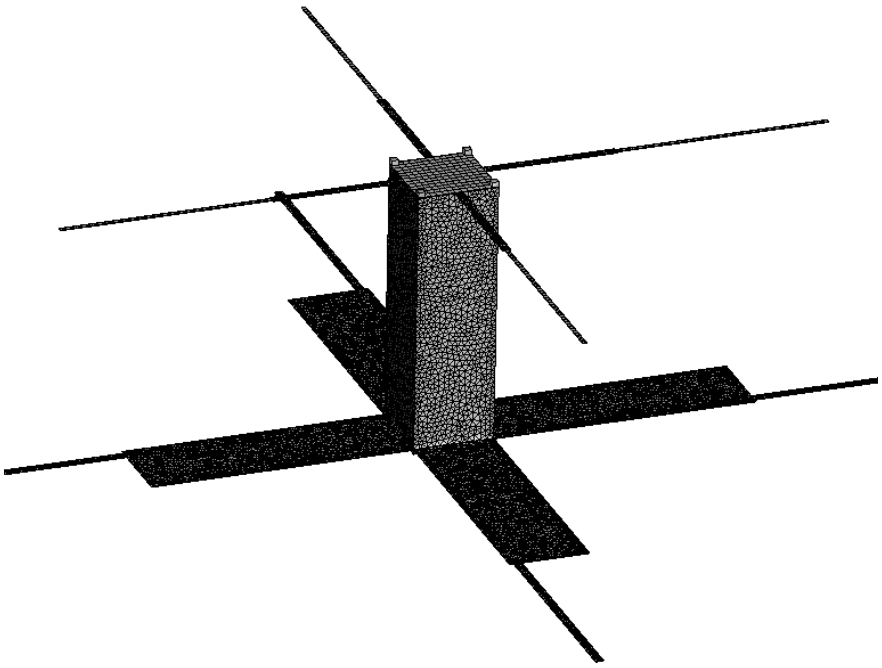

Figure 3.3: TBEx surface mesh.

The goal of this thesis work is to establish Knudsen numbers where a free molecular analytical approach to gathering aerodynamic force and moment information is no longer acceptable for desired accuracy. In order to evaluate the effect of Knudsen number on model results, altitudes must be chosen where there is a marked difference in Knudsen number as the flow regime moves from free-molecular to transitional and even into continuum for any body tested. Note that the TBEx satellites were launched into an eccentric orbit of about 850 km by 300 km; these altitudes correspond to Knudsen numbers far exceeding 2000 [12]. The two-line element data of the TBEx satellites is plotted for their perigee altitudes in Figure 3.4.

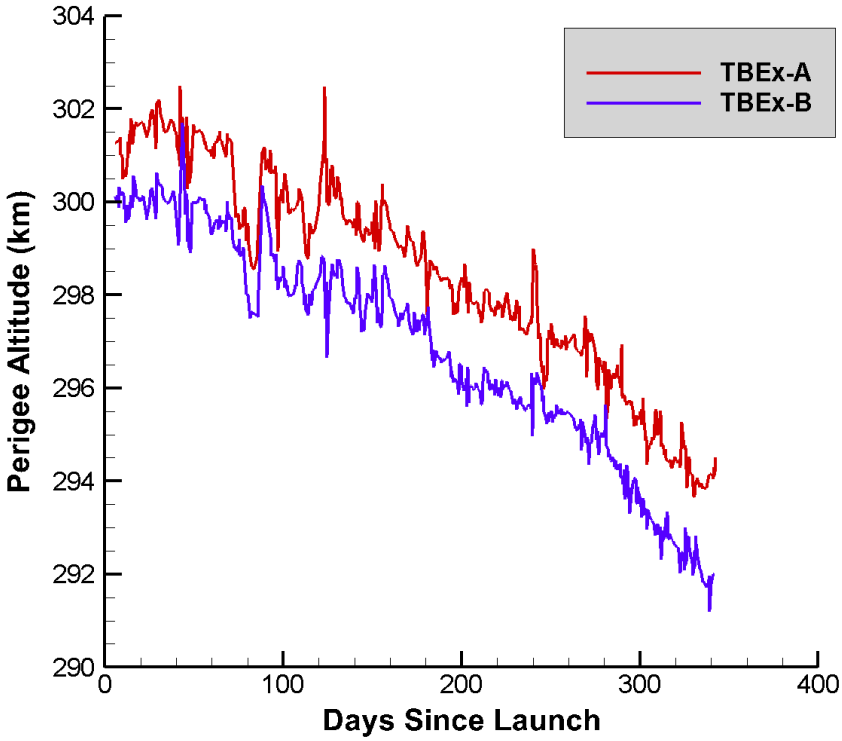

Figure 3.4: Two-line element data of TBEx-A and TBEx-B orbital decay of perigee altitudes since the launch date of June 25, 2019.

Due to the TBEx's current orbital altitudes residing in hyper-rarefied atmospheric flow, this thesis work projects the orbit to lower altitudes in order to examine the models discussed in Chapter

2. Figure 3.5 shows the Knudsen number changing over a projection of the loss of perigee for the TBEx from initial launch orbit using the model described in Section 2.3. The Knudsen number is calculated using an average length of the TBEx based on its minimum and maximum projected areas (3.56×10^{-2} m^2 and 0.13 m^2, respectively): $L = 2.75 \times 10^{-1}$ m. An average characteristic length is used to account for the TBEx's changing orientations in orbit due to its tumbling motion.

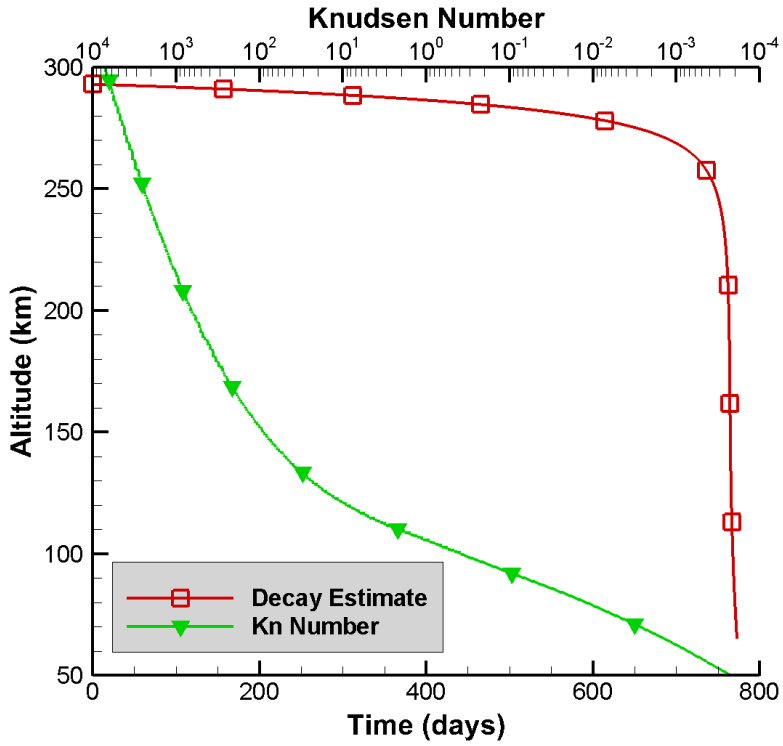

Figure 3.5: Orbital decay estimate of the TBEx's perigee altitudes plotted with the Knudsen number of the TBEx over altitude.

The limiting factor for Knudsen number studied for the TBEx case is the surface element cell size. Increased resolution of surface elements causes an exponential increase in volume cells in the flowfield overall, leading to a substantial increase in computational cost. The minimum resolution for body surface elements achieved in this study results in a side length of about 1.5×10^{-3} m; a local mean free path near the surface must be larger than this cell length. At orbital velocities, free-

stream flow is compressed; the free-stream mean free path is reduced by a factor of 10 by the time it reaches the body surface. Using the U.S. Standard Atmosphere estimates for mean free path at defined altitudes, it is decided to limit the altitude to 91 km, where the mean free path is 2.8×10^{-2} m. Reduced by a factor of 10, the local mean free path at this Knudsen number is 2.83×10^{-3} m, which is greater than the surface element lengths of the TBEx. The Knudsen number for the TBEx at 91 km is 0.1, representing transitional flow. Knudsen numbers of 0.1, 1, 10, and 100 are used to compare how well each modeling technique fares at different regimes.

Atmospheric composition is an important factor for accuracy of results, especially for inclusion of flowfield chemistry. Atmospheric composition, according to [9], is plotted for the TBEx, through all experienced altitudes, in Figure 3.6. Based on molar composition, the primary constituents are used to compose the flowfield for both models.

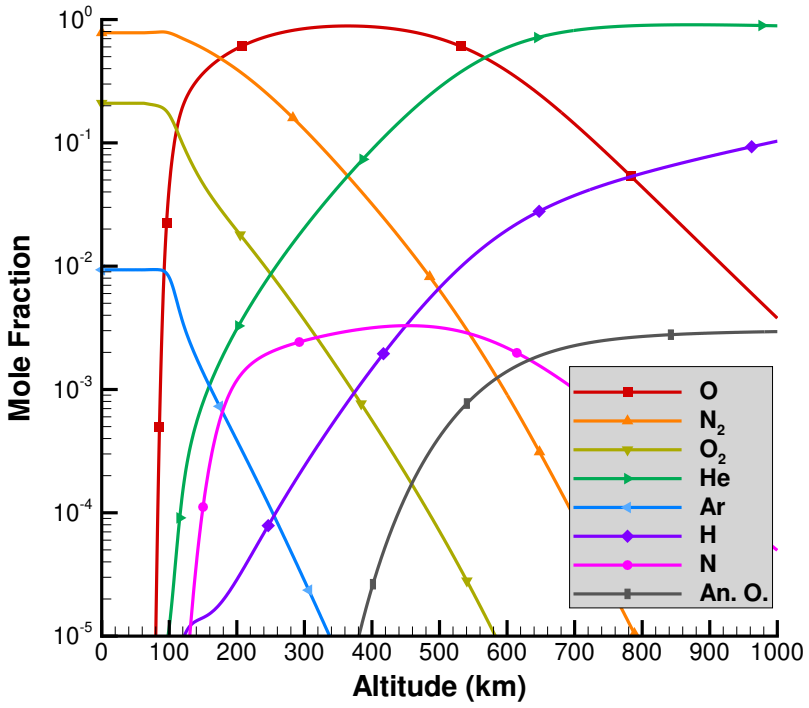

Figure 3.6: The atmospheric composition experienced through the TBEX's orbital altitudes as calculated using the NRLMSISE-00 model [9].

The atmospheric properties of each of the chosen altitudes are listed in Table 3.1. Though the actual TBEx experiment satellites are maintaining an orbit of 850 km by 300 km, the Knudsen numbers studied in this thesis work require near-reentry altitudes. At these altitudes the orbit would be decayed to the point of becoming circular [6]. The orbital speed, V, is then calculated using a circular orbit assumption. Argon is not used at higher altitudes where its mole fraction falls below 1×10^{-3}. In Table 3.1, "Alt" refers to altitude of the satellite's orbit.

Table 3.1: Atmospheric properties for the TBEx conditions analyzed [9] [12].

				Number Density (m^{-3})			
Kn	**Alt (km)**	**V ($m\ s^{-1}$)**	**T (K)**	**N_2**	**O_2**	**O**	**Ar**
100	147	7820	682	3.19×10^{16}	2.65×10^{15}	1.88×10^{16}	-
10	119	7830	384	2.94×10^{17}	4.18×10^{16}	7.95×10^{16}	1.53×10^{15}
1	104	7840	200	3.44×10^{18}	6.92×10^{17}	3.24×10^{17}	3.20×10^{16}
0.1	91	7850	187	3.80×10^{19}	9.15×10^{18}	2.81×10^{17}	4.40×10^{17}

In order to estimate body temperature for use with both models, the temperature sensor data from the orbiting TBEx is considered. The temperature data from the four different sensors on TBEx-A are displayed in Figure 3.7. The temperature varies in a cyclical way due to the orbit around the Earth: for about 45 minutes of the 90 minute period, the TBEx body experiences direct sunlight, and for the other 45 minutes, the body experiences no sunlight. Due to the speed of the orbiting TBEx, the wall temperature does not have time to accommodate to the increased radiative energy, so the temperature remains between 270 and 310 K. In this thesis work, for ease of application and comparison, we use 300 K as the wall temperature across all simulations of the TBEx.

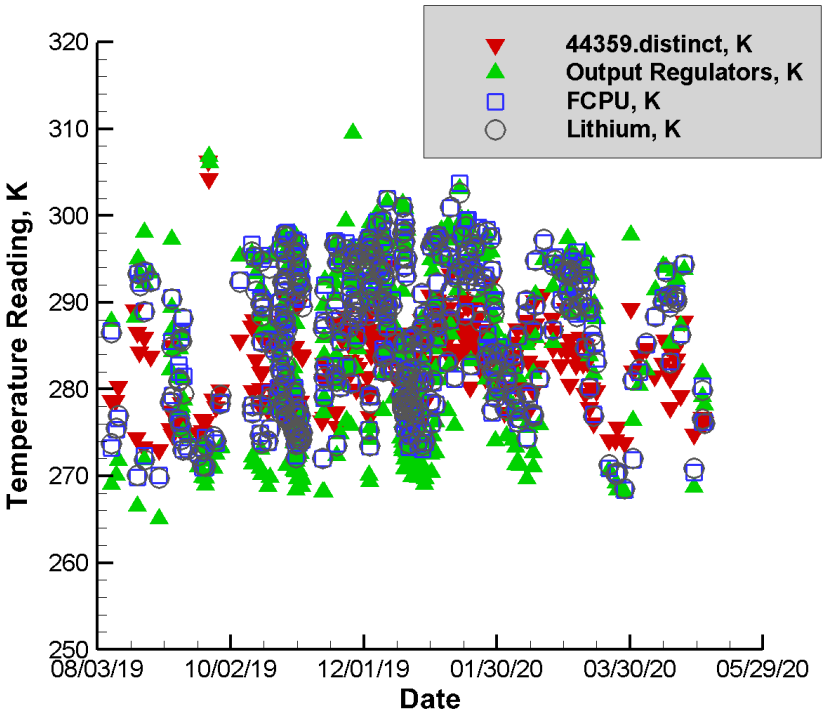

Figure 3.7: Temperature sensor data for the TBEx-A in orbit.

To understand the effect tumbling has on the experienced aerodynamic forces and moments, the TBEx gyroscope data is taken into consideration. Figure 3.8 shows the gyroscope coordinate system relative to the TBEx body. The body-defined coordinate system in Figure 3.8 does not correspond to the coordinate system used in the modeling approaches in this thesis work.

Figure 3.9 displays the average angular velocities about the gyroscope axes in Figure 3.8. About all three axes, the tumbling rate remains within one degree per second, therefore axes transformations are not necessary from the gyroscope coordinate system to this thesis' modeling coordinate system. It's understood from the gyroscope data that the TBEx will experience rotations about each of the primary axes in the gyroscope frame as well as the body frame.

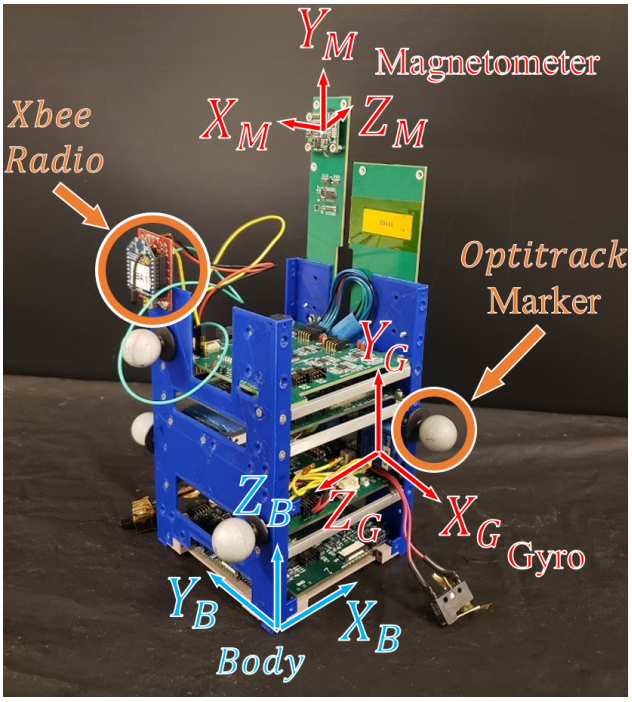

Figure 3.8: Gyroscope alignment shown on a non-deployed TBEx body under construction.

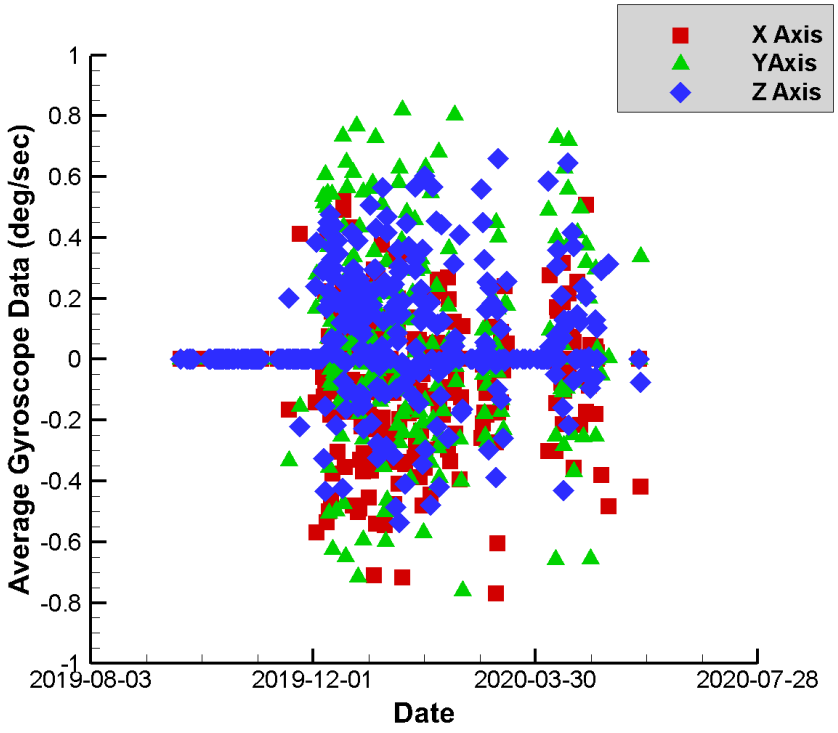

Figure 3.9: Gyroscope data for the TBEx-A in orbit.

It is apparent from Figure 3.9 that the TBEx tumbles about all three axes during orbit and reentry. This tumbling causes the TBEx to exhibit different orientations "normal to" the oncoming orbital flow. Otherwise stated, differing areas will be exposed to the flowfield, yielding differences in the aerodynamic forces and moments the TBEx experiences.

Though the TBEx rotates about all its axes, it is unnecessary to model every orientation. A small sample size of orientations needs defining: these orientations need to be interpolated to approximate average drag and lift experienced as the TBEx tumbles in orbit for use in the orbital decay model.

The TBEx body has rotational symmetry about the Z-axis when rotated 90° (seen in Figure 3.11). This is exploited to limit orientations chosen to model the TBEx.

Spherical angles are used to indicate the different selected modeling orientations. θ is projected from the positive X-axis in the X-Y plane. ψ is projected from the positive Z-axis in the Z-X plane. The body-defined axes for modeling purposes are shown in Figure 3.11, and are a consequence of the construction of the TBEx mesh.

Because the TBEx has 90° rotational symmetry about the Z-axis, two θ values are defined for modeling: 0° and 45°. These two angles represent the maximum difference in areas represented when rotating about the Z-axis. Figure 3.10 displays these two θ planes selected for modeling.

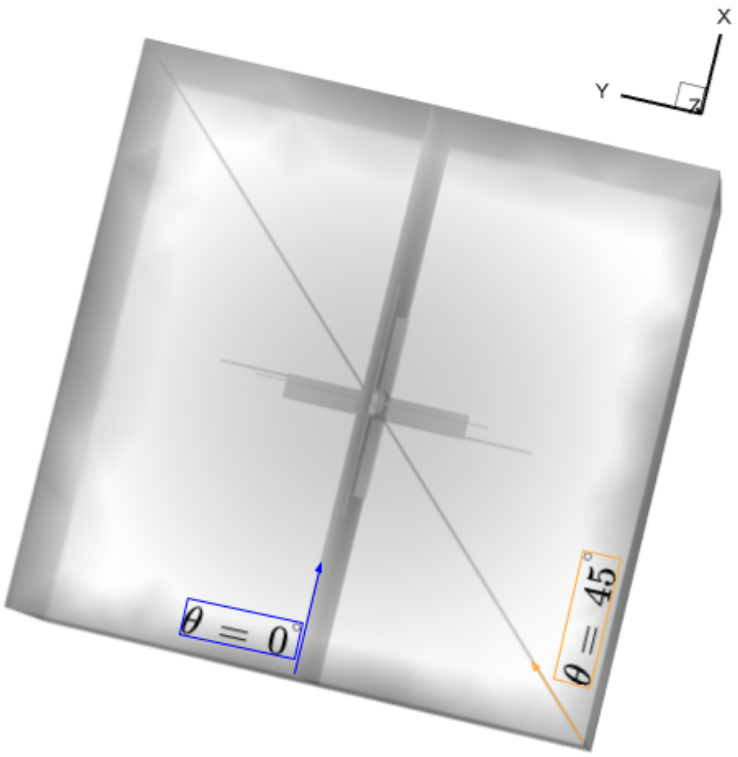

Figure 3.10: From-above view of the two θ slices of the TBEX that are modeled. The translucent box is the farfield limit of the modeling volume, the TBEx is the shape in the center of the volume. The planes bisecting the body demonstrate the θ values chosen for modeling.

There is no symmetry about the X- or Y-axes (as seen in Figure 3.11; therefore the θ planes are divided into several ψ values in order to interpolate the average forces and moments felt by the TBEx.

Table 3.2 enumerates the 16 orientations chosen to represent the TBEx body. The left-hand column of Table 3.2 is used for numbering the modeling orientations. The right-hand column of Table 3.2 contains a representative figure for each orientation. In each representative figure, the oncoming flow is pictured as one large streamline of the incoming flow at that orientation as modeled on the three-dimensional TBEx body. The red arrow in each representative figure in Table 3.2 is the incoming flow velocity for that orientation; the translucent box is the modeled

farfield volume, and the black shape in the center of the translucent box is the TBEx body. These orientations are selected based on projections of maximum difference in flow-facing area. Using points of maximum differentiation in aerodynamic forces and moments allows for an accurate interpolation of average forces and moments enacted by the body.

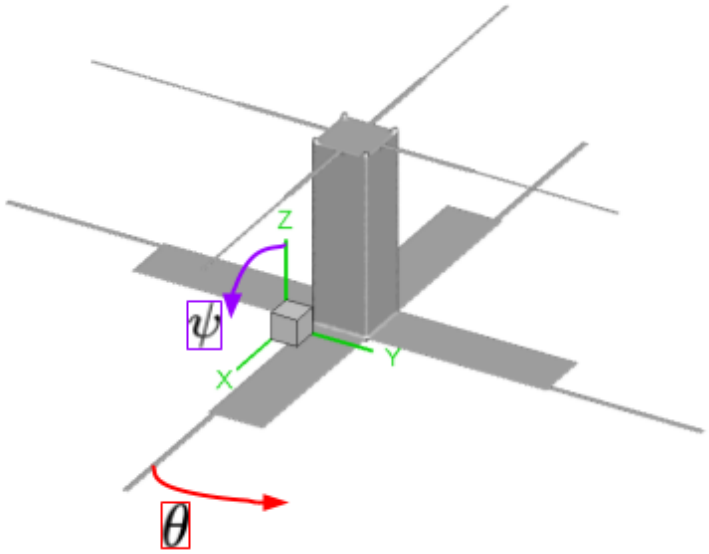

Figure 3.11: Body-defined coordinate system placed at origin for modeling of the TBEx using MONACO and free-molecular analytical techniques. θ is projected from the positive X-axis while ψ is projected from the positive Z-axis.

Table 3.2: Orientations used to model the TBEx experiencing orbital velocities at the defined Knudsen numbers.

#	θ, °	ψ, °	Representative Figure
1	0	0	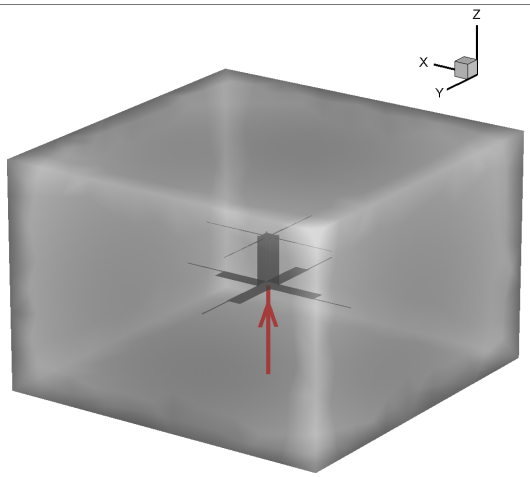
2	0	30	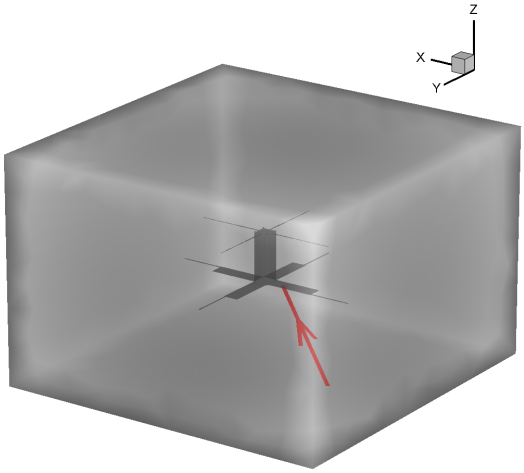

Continued on next page

Table 3.2 – continued from previous page

#	θ, °	ψ, °	Representative Figure
3	0	45	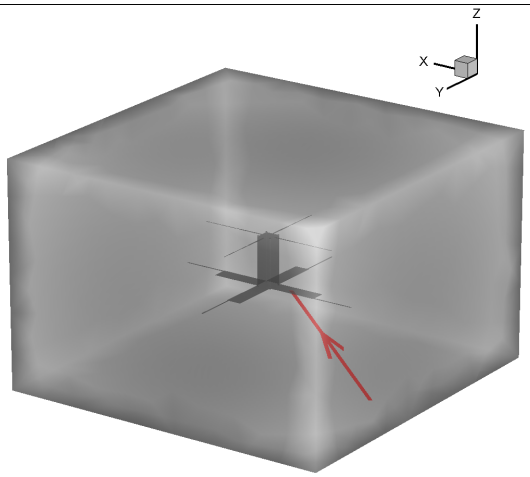
4	0	60	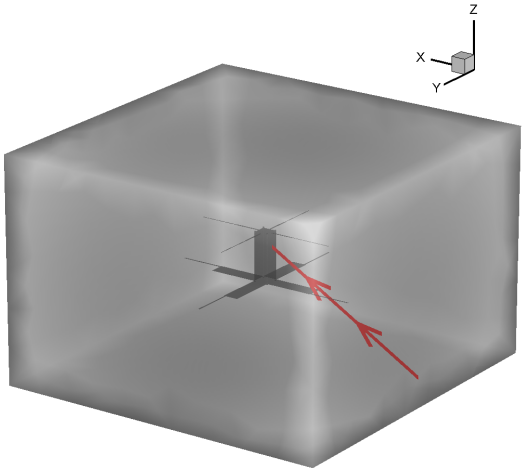

Continued on next page

Table 3.2 – continued from previous page

#	θ, °	ψ, °	Representative Figure
5	0	90	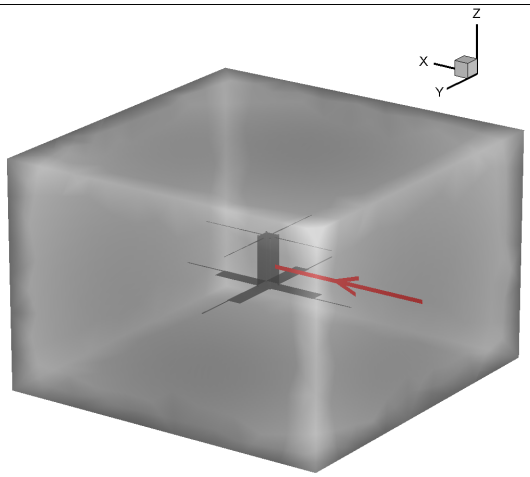
6	0	120	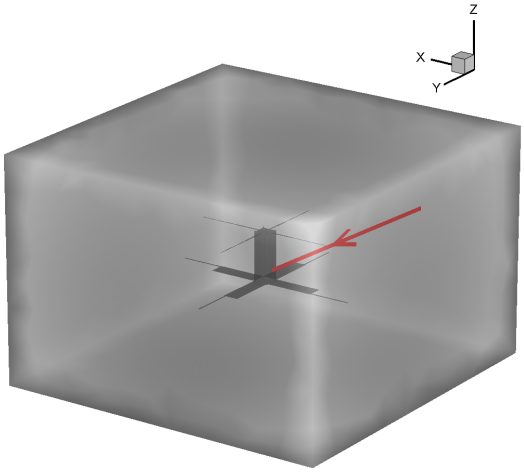

Continued on next page

Table 3.2 – continued from previous page

#	θ, °	ψ, °	Representative Figure
7	0	135	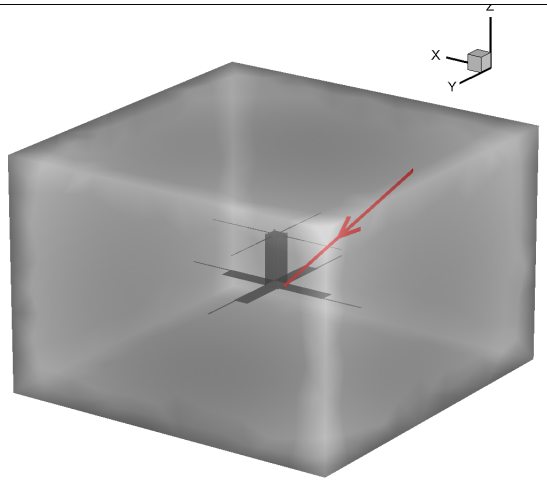
8	0	150	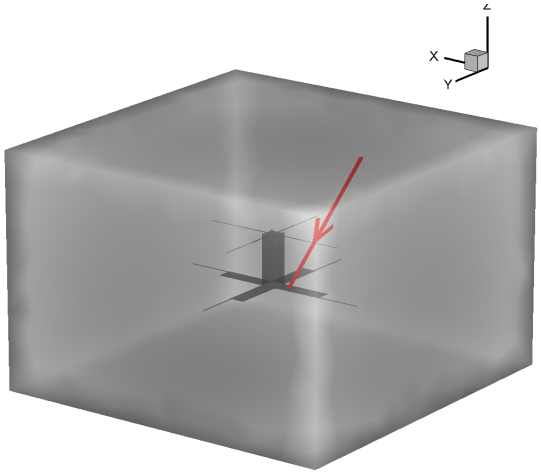

Continued on next page

Table 3.2 – continued from previous page

#	θ, °	ψ, °	Representative Figure
9	0	180	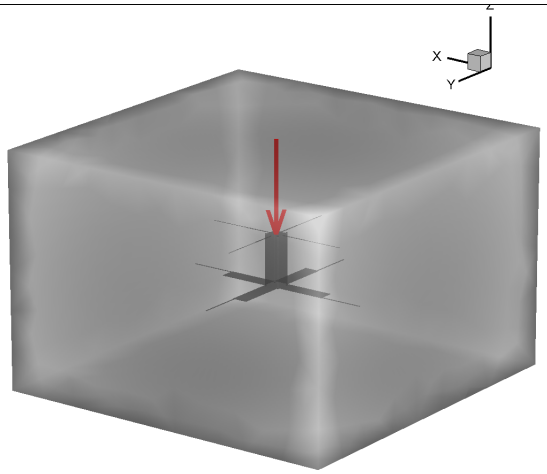
10	45	30	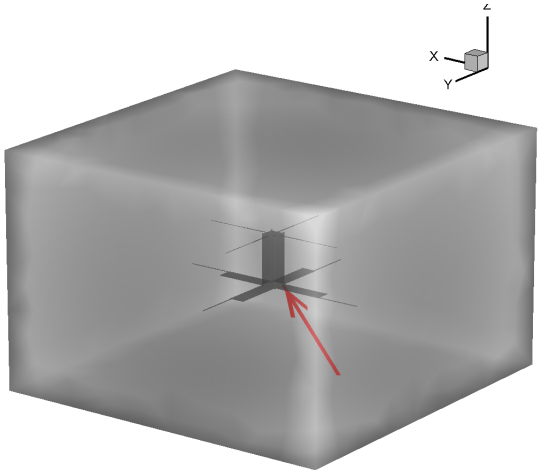

Continued on next page

Table 3.2 – continued from previous page

#	θ, °	ψ, °	Representative Figure
11	45	45	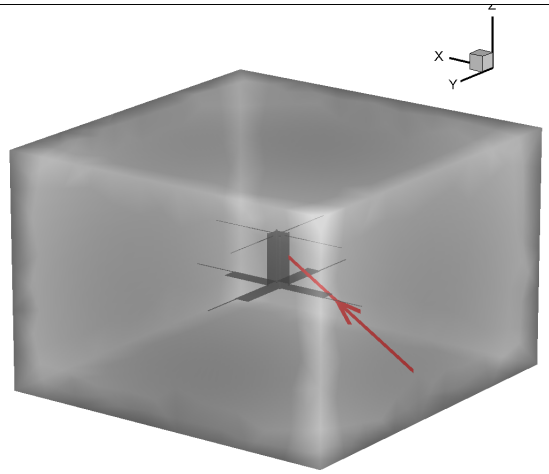
12	45	60	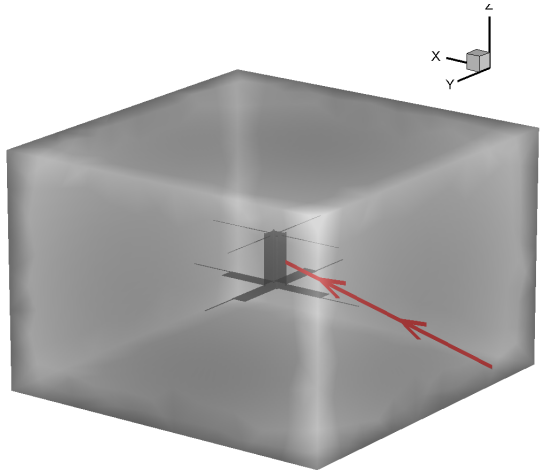

Continued on next page

Table 3.2 – continued from previous page

#	θ, °	ψ, °	Representative Figure
13	45	90	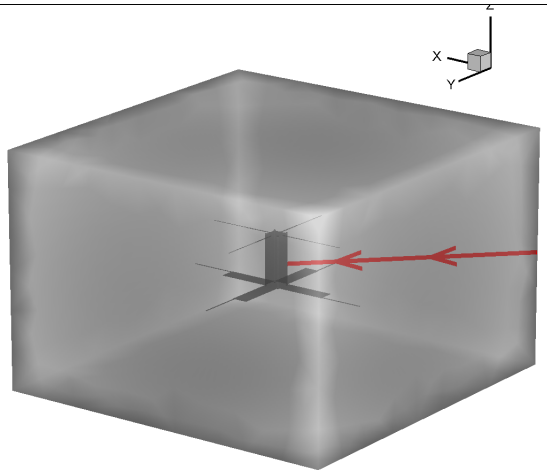
14	45	120	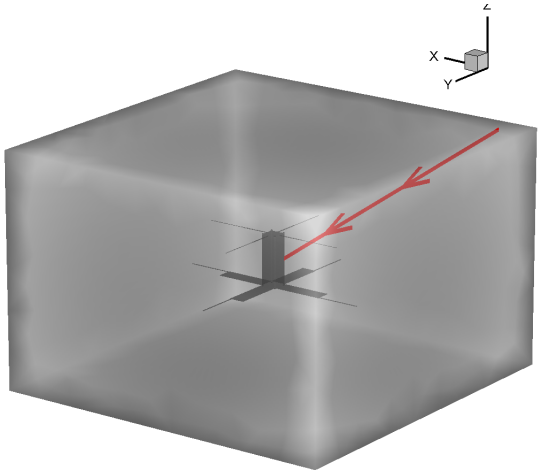

Continued on next page

Table 3.2 – continued from previous page

#	θ, °	ψ, °	Representative Figure
15	45	135	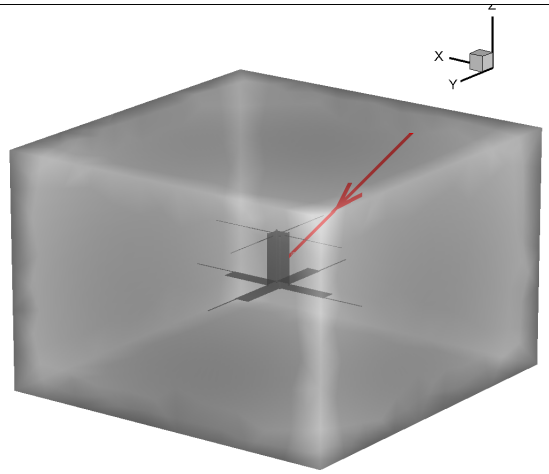
16	45	150	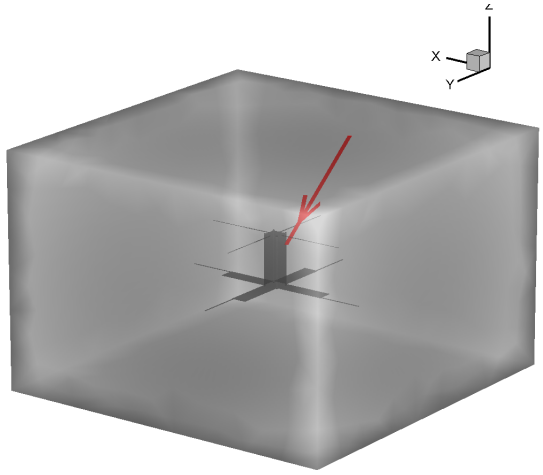

The last variable defined for modeling the TBEx is the number of sampling steps using in MONACO simulations. MONACO simulations are run to achieve a large number of particles in the flowfield, and then sampled at each time step. A simple case study is set up to determine the effect increasing the number of sampling steps has on the aerodynamic coefficients C_D and C_L and what difference this causes in orbital decay. For the TBEx simulations, sampling is begun after

80,000 time steps. After 80,000 time steps, all simulations have reached their steady-state number of particles in the flowfield. Figure 3.12 displays the number of reference particles reaching 4×10^6 before 80,000 time steps as an example. The case study is run for two orientations (orientations #1 and #5 in Table 3.2) at the altitude corresponding to $Kn = 0.1$.

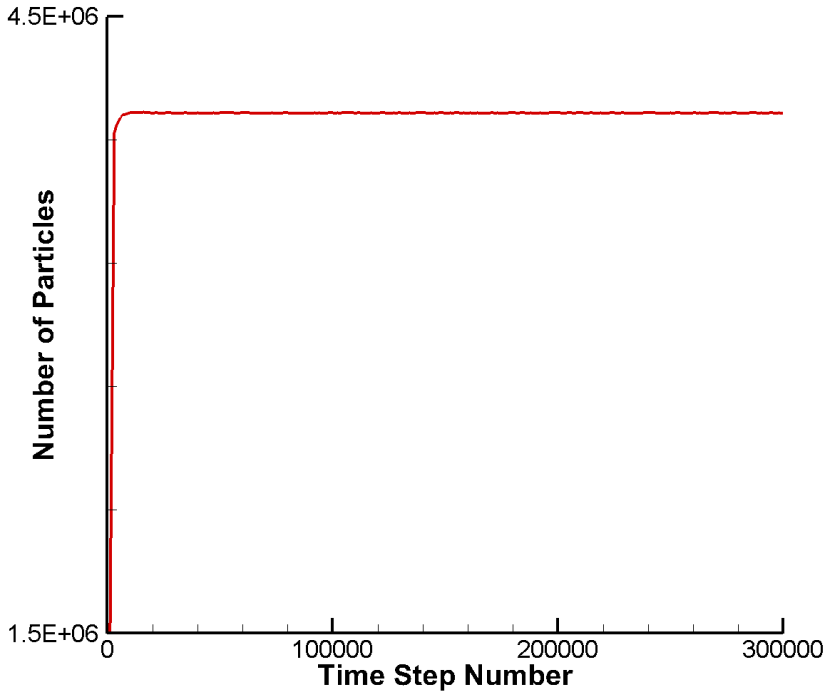

Figure 3.12: Example particle convergence results for Orientation #1, 300,000 sampling steps.

For every TBEx simulation, including the sampling size case study, the Variable Hard Sphere (VHS) model is used for collisions. 1×10^{-7} seconds is used for the time step. Table 3.3 contains the properties for the molecular species utilized in every MONACO TBEx simulation. In Table 3.3, M_W is the molecular weight, Ref. stands for Reference, Rot. stands for Rotational, Vib. stands for Vibrational. D.o.F. stands for Degrees of Freedom, Char. stands for Characteristic, Temp. stands for Temperature, and E. E. stands for Energy Exchange. None of the included species are ionized. The VHS reference temperature is 273 K and the viscosity temperature exponent is 0.75 across all

simulations. For more information on these inputs used with MONACO, please refer to [22], [23], and [20].

Table 3.3: Atmospheric species properties used in MONACO simulations of the TBEx.

Property for MONACO use	**Species**			
	N_2	**O_2**	**O**	**Ar**
M_W (kg kmol^{-1})	28.0	32.0	16.0	39.9
Ref. Diameter (m)	4.11×10^{-10}	4.07×10^{-10}	3.10×10^{-10}	4.17×10^{-10}
Rot. D.o.F.	2.0	2.0	0.0	0.0
Vib. D.o.F	1.6	1.8	0.0	0.0
Char. Temp. of Vib. (K)	3390	2270	0.0	0.0
Ref. Temp. for Rot. E. E. (K)	91.5	114	0.0	0.0
Max. Rot. Collision #	18.1	16.5	0.0	0.0
Prob. of Vib. E. E.	0.01	0.05	0.0	0.0

Table 3.4 contains the reference particle weights (the number of real particles represented by one model particle) used in each MONACO simulation for differing Knudsen numbers. The particle weights are chosen to keep a the total steady-state number of reference particles used consistent as the Knudsen number changes.

Table 3.4: Reference particle weights used in MONACO TBEx simulations at each Knudsen number.

Knudsen Number	**Reference Particle Weight (N_{Real}/N_{Model})**
100	1.1×10^{11}
10	1×10^{12}
1	1×10^{13}
0.1	1×10^{14}

The number of sampling steps is varied from 25,000 to 500,000 steps. Tables 3.5 and 3.6 display the MONACO aerodynamic coefficients for each simulation set up as described above and the number of core-hours (C-Hs) each simulation took. Understanding computational cost needed to impact solutions is an important part of this thesis work. Table 3.5 displays the sampling steps study results for Orientation #1 in Table 3.2. The aerodynamic coefficients in Table 3.5 are

calculated using a projected area of $A = 0.13$ m^2. Table 3.6 displays the sampling steps results for Orientation #5 in Table 3.2. The aerodynamic coefficients in Table 3.6 are calculated using a projected area of $A = 0.03.56 \times 10^{-2}$ m^2 [7].

Table 3.5: Orientation #1: sampling steps results for coefficient of drag and lift and total core-hours to run simulation.

Sampling Steps	C_D	C_L	**C-Hs**
25000	2.42	6.58×10^{-4}	89.4
50000	2.41	3.76×10^{-4}	110
75000	2.41	1.17×10^{-4}	147
100000	2.41	3.05×10^{-4}	166
200000	2.41	8.37×10^{-5}	247
300000	2.41	2.80×10^{-6}	333
400000	2.41	5.97×10^{-5}	415
500000	2.41	8.84×10^{-7}	511

Table 3.6: Orientation #5: sampling steps results for coefficient of drag and lift and total core-hours to run simulation.

Sampling Steps	C_D	C_L	**C-Hs**
25000	2.67	2.14×10^{-1}	82.0
50000	2.67	2.14×10^{-1}	110
75000	2.67	2.13×10^{-1}	155
100000	2.67	2.13×10^{-1}	142
200000	2.67	2.12×10^{-1}	226
300000	2.67	2.13×10^{-1}	307
400000	2.67	2.12×10^{-1}	405
500000	2.67	2.12×10^{-1}	473

The results in Tables 3.5 and 3.6 are used in the orbital decay model described in Section 2.3 in order to understand how large of an effect the number of time steps has on orbital decay projections. The difference in orbital decay projections is measured using a root-mean-square difference (RMSD) between each methods' loss-of-altitude in kilometers over the time steps taken to project the decay. The root-mean-square differences (RMSD) between the 500,000 sampling step simulations orbital decay and the 25,000 sampling steps simulations orbital decay does not

exceed 1.7×10^{-2} km. The time-to-reenter difference percentage between the 500,000 sampling step simulations and the 25,000 sampling steps simulation does not exceed 0.28%. Based on this analysis, 25,000 sampling steps is chosen for all TBEx experimental MONACO runs.

3.2 Knudsen Number of 100

As stated above, a Knudsen number of 100 is achieved for the TBEx body at 147 km of altitude. A Knudsen number of 100 is firmly in the free-molecular regime so well-matched results between the MONACO simulation and free-molecular model analysis are expected. The circular orbital speed and atmospheric composition at this altitude are listed in Table 3.1. As already noted, MONACO is run with a time step of 1×10^{-7} s. 80,000 simulation time steps are conducted before sampling begins and 25,000 further steps are run for a total of 105,000 time steps. As an example, the $\theta = 0°$, $\psi = 30°$ orientation, Orientation #2 in Table 3.2, is presented for the Knudsen number of 100 altitude. All slices of the flowfield are taken at $Y = 0.175$ m which is the center slice of the TBEx showing the X-Z plane. The TBEx body is represented by the white "cut-out" of the slice of the body.

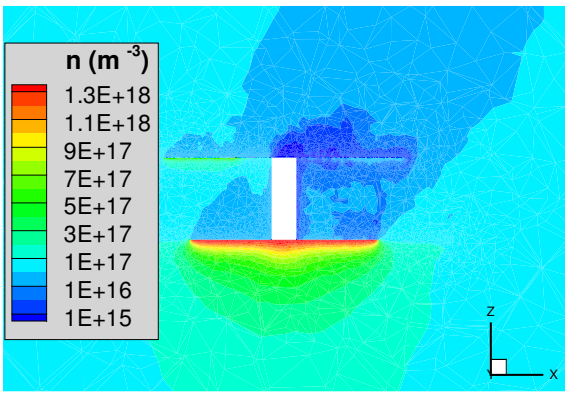

(a)

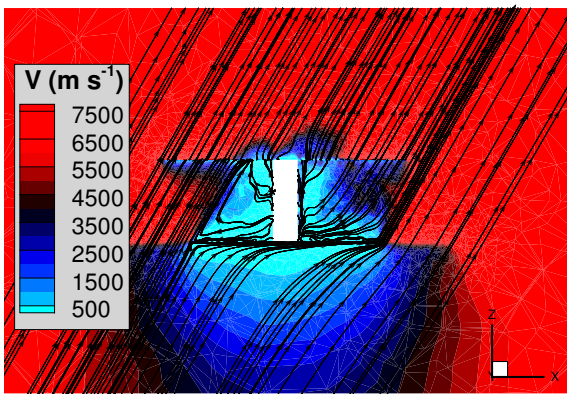

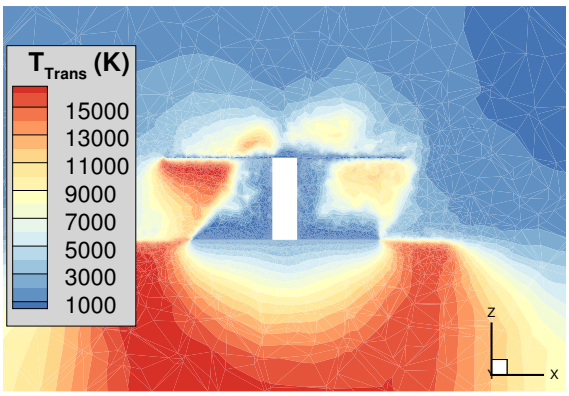

(b) (c)

Figure 3.13: Flowfield contours at $Kn = 100$, $\theta = 0°$ and $\psi = 30°$ (Orientation #2): (a) number density; (b) velocity; (c) translational temperature.

Figure 3.13 shows the flowfield contours of the $Kn = 100$, Orientation #2 case. Figure 3.13 depicts the flow phenomena expected when an object disturbs rarefied high-speed flow: instead of a shock wave, a large "bubble" of disturbed, slowed-down flow forms in front of the object. Additionally, the object, or in this case, the TBEx, blocks the incoming flow, so low density flow is seen directly behind the TBEx. The backflow of flow that impacts the aft solar panels can be seen

in the number density contours (Figure 3.13 (a)). In Figure 3.13 (b), the velocity streamlines are plotted, and the velocity ψ angle can be seen clearly by the direction of the streamlines.

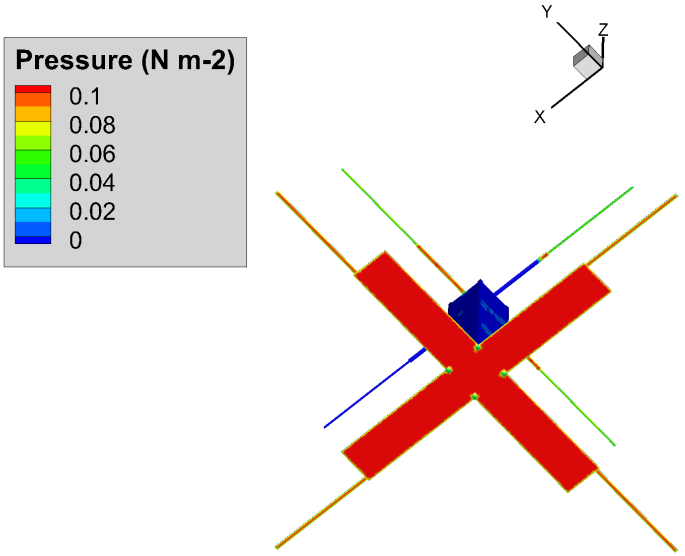

(a)

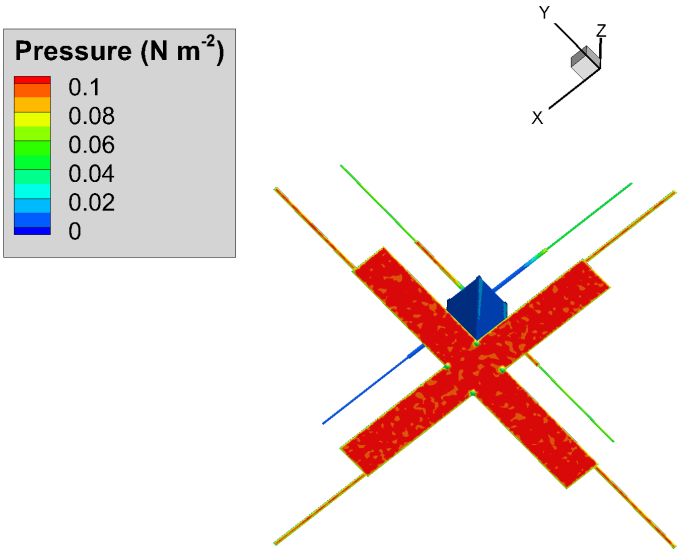

(b)

Figure 3.14: Pressure distribution at $Kn = 100$, $\theta = 0°$ and $\psi = 30°$ (Orientation #2): calculated using: (a) free molecular theory; (b) DSMC.

Figures 3.14 displays an example of the macroscopic properties (pressure, N m^{-2}) on the TBEx body wall for the $Kn = 100$, Orientation #2 case. The pressure distributions are very similar: the average pressure experienced by the surface is calculated as 3.54×10^{-2} N m^{-2} using the free-molecular method. This average is calculated by accounting for the pressure on each surface element over the entire body, for this orientation. The average pressure experienced over the body calculated by using MONACO results is $3.46 \times 10^{-2} \pm 2.80 \times 10^{-5}$ N m^{-2}, and is calculated similarly. The statistical error for the DSMC pressure calculation is due to the Poisson statistical error of the DSMC results due to the number of hits experienced by the body per surface element per time step and will be enumerated in the next section. The difference in average pressure experienced by the body at this orientation is 2.40%. For all percentage differences, the DSMC MONACO results are taken as the more-accurate results, therefore the percentile difference is how much the free-molecular analytical calculation differs from the more-accurate DSMC simulation. The DSMC simulation is more accurate because it simulates the flowfield chemistry and particle interactions with the surface of the body, whereas the free-molecular analytical model does not account for particle motion, and makes several assumptions discussed in Section 2.2.

3.2.1 $Kn = 100$: Drag and Lift

Now the drag and lift experienced over the body are calculated and compared between models. In order to create a complete picture of both $\theta = 0°$ and $\theta = 45°$ slices of the TBEx, Orientations #1 and #9 are duplicated in the $\theta = 45°$ results. Exploiting the rotational symmetry of the TBEx, the interpolated average drag and lift over these two θ curves are taken as the average drag and lift experienced by the tumbling TBEx in orbit. The average drag and lift are projected for use with the

orbital decay model because the scale of tumbling rotations (seen in Figure 3.9), 1° s^{-1}, is much smaller than the period of each orbit (90 minutes).

Figure 3.15 shows the calculated drag for all orientations (including the projected #1 and #9 for $\theta = 45^\circ$) using both models. The data points for the orientation simulation results are connected using splines to demonstrate the smooth transition of drag experienced as the body rotates. In Figure 3.15, the error bars are the Poisson statistical error of the DSMC results due to the number of hits experienced by the body per surface element per time step. The Poisson statistical error for MONACO DSMC simulations is calculated as in Equation 3.1. Using Equation 3.1, an average hits per sampling time step per surface element across the TBEx of 2.41×10^{-3}, the TBEx total number of surface elements of 23,813, and 25,000 sampling steps, the Poisson statistical error of aerodynamic DSMC results is 0.08%. Error bars are not plotted in the figures in this chapter because the statistical error is very small.

$$\text{Poisson Error } \% = \Bigg(\text{Average particle hits per sampling time step per surface element} \times \text{Number of Elements} \times \text{Number of Sampling Steps}\Bigg)^{(-1/2)} \times 100 \tag{3.1}$$

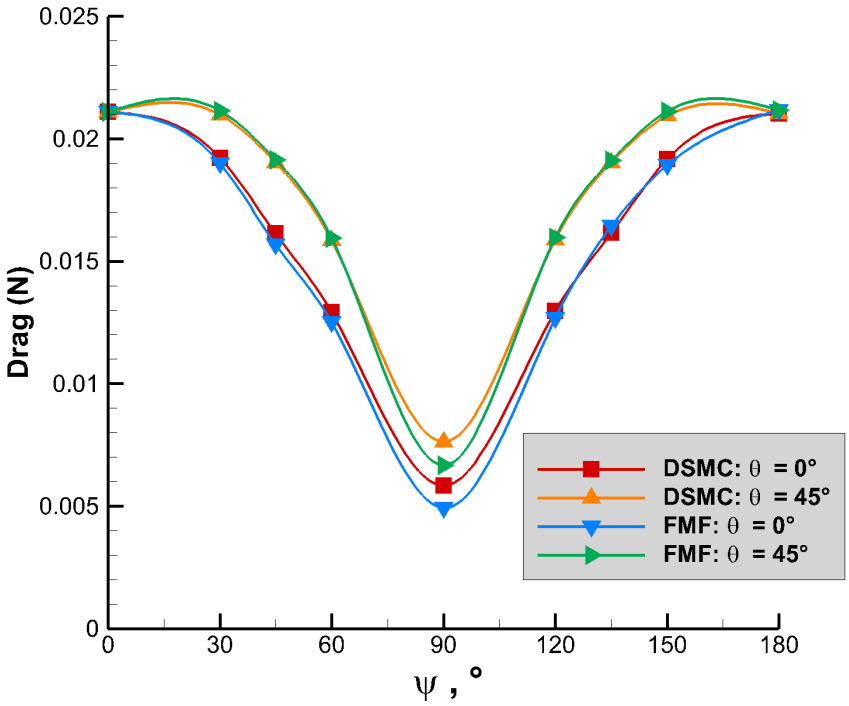

Figure 3.15: Drag calculated using DSMC and free-molecular (FMF) analytical models for all orientations analyzed of the TBEx at a Knudsen number of 100.

Figure 3.15 shows that maximum drag values are achieved for $\psi = 0°$ and $\psi = 180°$, while minimum drag is achieved for $\psi = 0°$. These maxima and minimum values correspond to the maximum and minimum flow-exposed projected areas. When $\psi = 90°$, the rectangular body of the TBEx faces the oncoming flow. When $\psi = 0°$ or $\psi = 180°$, the flow encounters the deployed solar panels, increasing the pressure force on the body and subsequently increasing the drag. The $\theta = 45°$ drag values are increased due to increased exposed area: two sides of the rectangular body are exposed versus one for $\theta = 0°$.

The average drag calculated using the DSMC MONACO modeling results is $1.62 \times 10^{-3} \pm 1.30 \times 10^{-6}$ N. The average drag calculated using the free-molecular analytical modeling results is 1.60×10^{-3} N. The percent difference between the averages is 1.12%. The normalized root-mean-

square deviance between all the drag results across both models is 2.23%. These results match what is expected: good agreement between the free-molecular analytical and the DSMC results.

Figure 3.16 shows the calculated lift for all orientations using both methods. The lift displayed in Figure 3.16 is translated into an Earth-centric frame, which yields positive lift values. Lift is two orders of magnitude smaller compared to drag due to the TBEx's near vertical symmetry. Resolved as described in Chapter 2, nearly all force applied to the TBEx body is attributed to drag. Unless a pressure gradient in a normal direction to the oncoming velocity is created by the body's geometry, drag will be the dominating force. The TBEx creates no such pressure gradient as the flow-facing area "catches" all pressure.

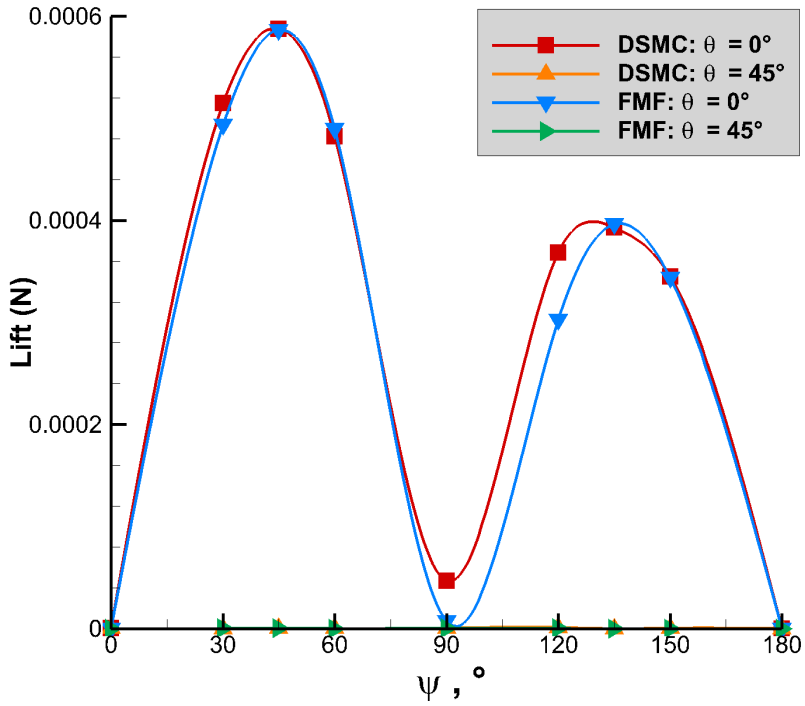

Figure 3.16: Lift calculated using DSMC and free-molecular (FMF) analytical models for all orientations of the TBEx at a Knudsen number of 100.

Figure 3.16 shows that maximum lift values are achieved for $\theta = 0$, $\psi = 45°$ and $\psi = 135°$ for

both modeling approaches. At these orientations, due to the breakdown of lift and drag directions, one of the TBEx solar panels will contribute some pressure force to the lift force. When rotating about the Z-axis for $\theta = 45°$, there is no lift-facing solar panel as the incoming flow concentrates between solar panels, therefore the lift stays near zero and nearly all force is resolved in the drag direction.

The average lift calculated using the DSMC MONACO modeling results is $1.52 \times 10^{-4} \pm 1.22 \times 10^{-7}$ N, while the average lift calculated using the free-molecular analytical modeling results is 1.43×10^{-4} N. The percent difference between the averages is 5.56%. This seems high, but is skewed by the very small lift results, especially for the $\theta = 45°$ orientations where lift remains on the order of 1×10^{-8} N. As Figure 3.16 shows, the free-molecular analytical lift results are similar to the DSMC results for all ψ values. The normalized root-mean-square difference between all the lift results across both models is 3.22%; this deviation normalizes using the range of lift, due to the lift values being very close to zero. Good agreement between models is therefore reflected in these lift results.

In order to calculate coefficients of drag and lift for use in the orbital decay model, a free-stream density is gathered from [9]. At 147 km, or TBEx's $Kn = 100$, the free-stream density $\rho = 2.13 \times 10^{-9}$ kg m^{-3}. The orbital velocity is the circular orbital speed used throughout the $Kn = 100$ results: $V = 7820$ m s^{-1}. Using the standard aerodynamic equations, the coefficients needed can be calculated as such: $C_D A = \frac{2D}{\rho V^2}$ and $C_L A = \frac{2L}{\rho V^2}$. The coefficients multiplied by the flow-facing area are used due to the average rotation of the TBEx. Figure 3.17 shows $C_D A$ and $C_L A$ calculated for all models and orientations for $Kn = 100$ experienced by the TBEx body.

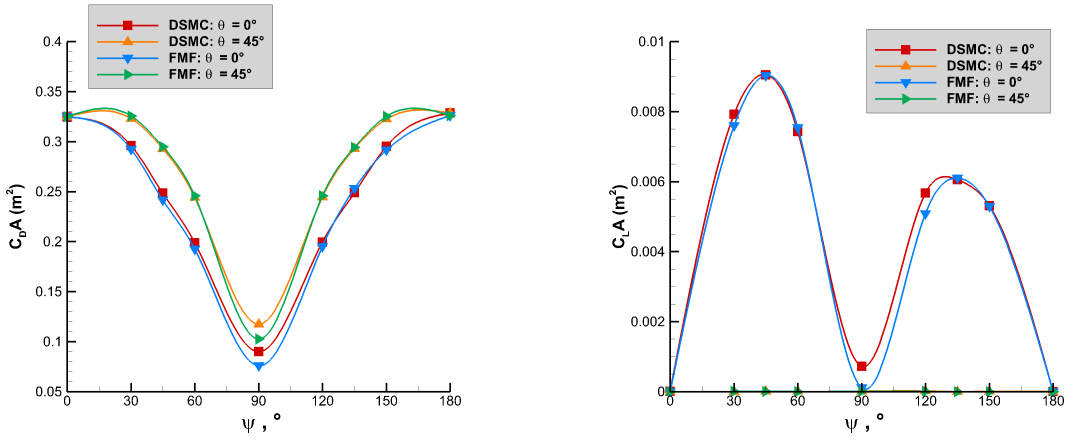

(a) (b)

Figure 3.17: Drag (a) and lift (b) coefficients calculated using DSMC and free-molecular (FMF) analytical models for all experiment orientations of the TBEx using both models for a Knudsen number of 100.

The average $C_D A$ calculated using the DSMC MONACO modeling results is $2.50 \times 10^{-1} \pm 2.00 \times 10^{-4}$ m^2, while the average $C_D A$ calculated using the free-molecular analytical modeling results is 2.46×10^{-1} m^2. The percent difference between the averages is 1.27%. The normalized root-mean-square deviance between all the $C_D A$ results across both models is 2.23%. The average $C_L A$ calculated using the DSMC MONACO modeling results is $2.34 \times 10^{-3} \pm 1.87 \times 10^{-6}$ m^2, while the average $C_L A$ calculated using the free-molecular analytical modeling results is 2.24×10^{-3} m^2. The percent difference between the averages is 4.37%. The normalized root-mean-square deviance between all the $C_L A$ results across both models is 9.51%.

3.2.2 $Kn = 100$: Moments and Angular Accelerations

The moments are taken about the TBEx body centroid as the models are not equipped to handle irregular mass distributions of bodies. The TBEx centroid is $X = 9.18 \times 10^{-2}$ m, $Y = 1.76 \times 10^{-2}$ m, $Z = 1.96 \times 10^{-2}$ m. The moments of inertia about the TBEx's primary axes (translated, but

not rotated from the meshes' coordinate system origin to the centroid) are $I_{XX} = 1.84 \times 10^{-1}$ kg m^2, $I_{YY} = 2.14 \times 10^{-1}$ kg m^2, and $I_{ZZ} = 2.14 \times 10^{-1}$ kg m^2. For the near-symmetrical TBEx, I_{YY} = I_{ZZ}: this causes Equations 2.5 to become Equations 3.2.

$$\begin{aligned} \alpha_X &= \frac{M_X}{I_{XX}} \\ \alpha_Y &= \frac{M_Y}{I_{YY}} - \frac{(I_{XX} - I_{YY})}{I_{YY}}\omega_X\omega_Z \\ \alpha_Z &= \frac{M_Z}{I_{YY}} - \frac{(I_{YY} - I_{XX})}{I_{YY}}\omega_X\omega_Y \end{aligned} \tag{3.2}$$

To measure the maximum effect a moment has on changing the body's rotation rate, ω values are set to zero, so all angular accelerations are calculated in the format of $\alpha = \frac{M}{I}$. The "extra" term in Equation 3.2 is regarded as an error on this calculation.

The gyroscope axes in Figure 3.8 are misaligned with the primary axes by rotation of 90°. However, the maximum rotation about each axis, as seen in Figure 3.9, is the same: 0.8° s^{-1}. ω_X, ω_Y, and ω_Z in Equation 3.2.2 are set to 0.8° s^{-1} in maximum error calculations about the Y and Z primary axis directions. Therefore the "error" about the Y and Z axes in Equation 3.2 becomes: $\pm|\frac{(I_{XX}-I_{YY})}{I_{YY}}\omega_X\omega_Y|$ where ω_X and ω_Y are 0.8° s^{-1}. This equates to: 2.73×10^{-5} radians s^{-2}, or 1.57×10^{-3} degrees s^{-2}, plotted as an error bar in all of the angular acceleration plots in this chapter.

Figure 3.18 displays the moment results yielded by both models across all the TBEx body orientations about the three primary axes. The aerodynamic moments about the Z-axis are smaller than those about the X- and Y-axes by three orders of magnitude. This is due to the TBEx's rotational near-symmetry about the Z-axis: the moments are caused by a only few surface elements

experiencing flow in an "unbalanced" way.

As seen in Figure 3.18 (a), the aerodynamic moments about the X-axis are incurred when the θ value of the simulation is $45°$. When $\theta = 0°$, the oncoming flow is applied in a near-symmetric way about the X-axis. The X-axis moments are maximized when $\psi = 45°$ or $135°$: at these orientations, flow is able to pass around the solar panels and makes a non-negligible impact on one side of the rectangular body. This "pushes" the TBEx and induces the maximum moments. A similar phenomenon happens at $\theta = 45°$, $\psi = 90°$, flow impacts two of the rectangular body walls, one of these wall-impacts creates the X-moment while one creates the maximum Y-impact seen in Figure 3.18 (b). An X-moment is not created when $\theta = 0°$, $\psi = 90°$ because the impacted rectangular body wall is aligned with the X-direction.

In Figure 3.18 (b), Y-moments are induced across both θ values. Maxima are reached when $\psi = 90°$ due to the process described in the previous paragraph. Minima are reached when $\psi = 45°$ and $135°$: at these orientations, flow again passes around the solar panels and impacts the rectangular body in an non-negligible way, inducing the moments in the negative Y-direction. The magnitudes of the Y-moments minima are larger for $\theta = 0°$ because all the flow is applied aligned with the X-direction which cause a larger affect on the moments about the Y-axis.

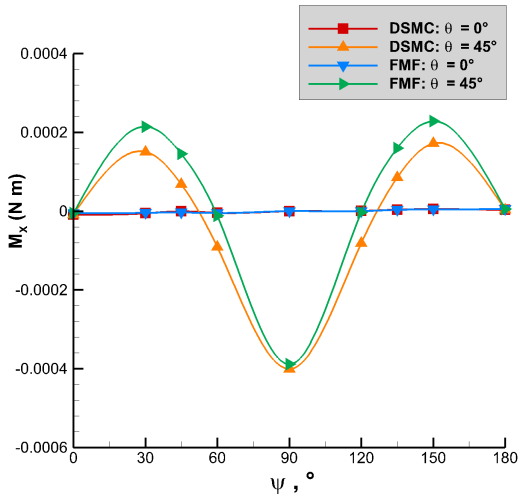

(a)

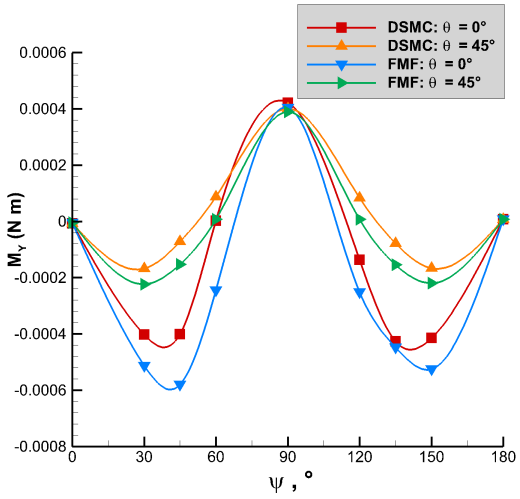

(b)

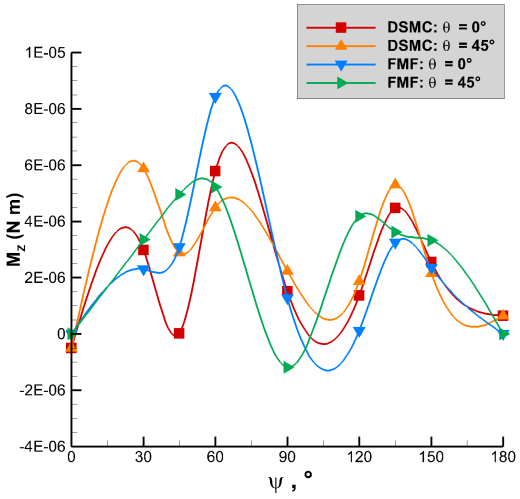

(c)

Figure 3.18: Moments calculated using DSMC and free-molecular (FMF) analytical models for all experiment orientations of the TBEx about the: (a) X axis; (b) Y axis; (c) Z axis, for a Knudsen number of 100.

The moment averages are sensitive due to the small magnitudes of the moment results and the sign changes as ψ changes. In order to compare the free-molecular and DSMC modeling approaches effectively, averages are taken according to θ value and are listed in Table 3.7. "FMF" in Table 3.7 refers to results from the free-molecular analytical model. Table 3.7 portrays clearly

that the free-molecular and DSMC modeling approaches yield similar results for this Knudsen number. This reinforces what we see in Figure 3.18, where the curves are qualitatively close together.

The sign differences between the DSMC and free-molecular results for the X- and Y- moments in Table 3.7, $\theta = 45^\circ$ are due to the free-molecular results producing more-negative minima in the Y-moment, and more-positive maxima in the X-moments. Since the moments center around zero, these maxima and minima can pull the averages towards the negative or positive side of zero.

Table 3.7: Average moments calculated for a Knudsen number of 100 for the DSMC and free-molecular analytical modeling approaches for both θ values.

Average	θ **= 0°**		θ **= 45°**	
	FMF	**DSMC**	**FMF**	**DSMC**
$\mathbf{M}_X$ **(N m)**	-6.09×10^{-7}	-7.12×10^{-7} $\pm 5.70 \times 10^{-10}$	1.41×10^{-5}	-3.58×10^{-5} $\pm 2.86 \times 10^{-8}$
$\mathbf{M}_Y$ **(N m)**	-2.10×10^{-4}	-1.18×10^{-4} $\pm 9.44 \times 10^{-8}$	-1.41×10^{-5}	3.40×10^{-5} $\pm 2.72 \times 10^{-8}$
$\mathbf{M}_Z$ **(N m)**	2.39×10^{-6}	2.22×10^{-6} $\pm 1.91 \times 10^{-9}$	2.53×10^{-6}	2.87×10^{-6} $\pm 2.30 \times 10^{-9}$

The normalized root-mean-square deviations between all the X-, Y-, and Z-axes moments (accounting for both θ values) are elevated due to the moments being extremely close to zero. The normalized root-mean-square deviation between all the X-axes moments is 6.77%. The normalized root-mean-square deviance between the Y-axes moments is 9.65%. The normalized root-mean-square deviation between the Z-axes moments is 18.0%. Because the values are so small, these normalized root-mean-square deviations still reflect good agreement between the free-molecular and DSMC methods at this Knudsen number.

The moments incurred about the Y-axis are the largest and are non-zero for the DSMC and free-molecular models for both θ values, therefore this angular acceleration is examined. While

statistical error of 0.08% till applies to the DSMC results, in this section the angular acceleration uncertainty is plotted and discussed because it is larger.

Figure 3.19 shows the calculated angular acceleration about the Y-axis for the TBEx body using both models across all orientations, with error bars as described previously. The interpolated average angular accelerations about the Y-axis incurred are -1.12×10^{-2} degrees s^{-2} using the DSMC method and -3.00×10^{-2} degrees s^{-2} using the free-molecular analytical method. The normalized root-mean-square deviation between the angular accelerations about the Y-axis is 9.65%. Again, there is good agreement between the models, as expected since angular acceleration results are proportional to the Y-moment results.

Angular acceleration is a more intuitive way of discussing how the aerodynamic moments affect the tumbling motion of the TBEx, the angular acceleration about the Y-axis is presented as an example. The free-molecular moments and angular acceleration curves have more extreme minima and maxima than the DSMC results. This is because there is inherent diffusion of surface properties when using a particle method versus an analytical method. The DSMC surface properties are calculated based on the particles that surface element encounters, which varies depending on surface element location and other factors. The analytical free-molecular method calculates a fixed value of surface properties for any surface element that experiences flow with the same normal vector. This is why the free-molecular method is an approximation, as not all flow will develop to the exact same specifications in all areas that reach the TBEx. The differences are small in this Knudsen number regime, because the particle method basically reproduces the free-molecular analytical properties on most cells. These differences are expected to increase as Knudsen number lowers.

The error bars in Figure 3.19 illustrate the effect the aerodynamic Y-moment has on the tum-

bling behavior of the TBEx. If the TBEx has an angular velocity about the Y-axis of $0.8°$ s^{-1}, the effect of aerodynamic moments will be small compared to the effect of the established tumbling motion.

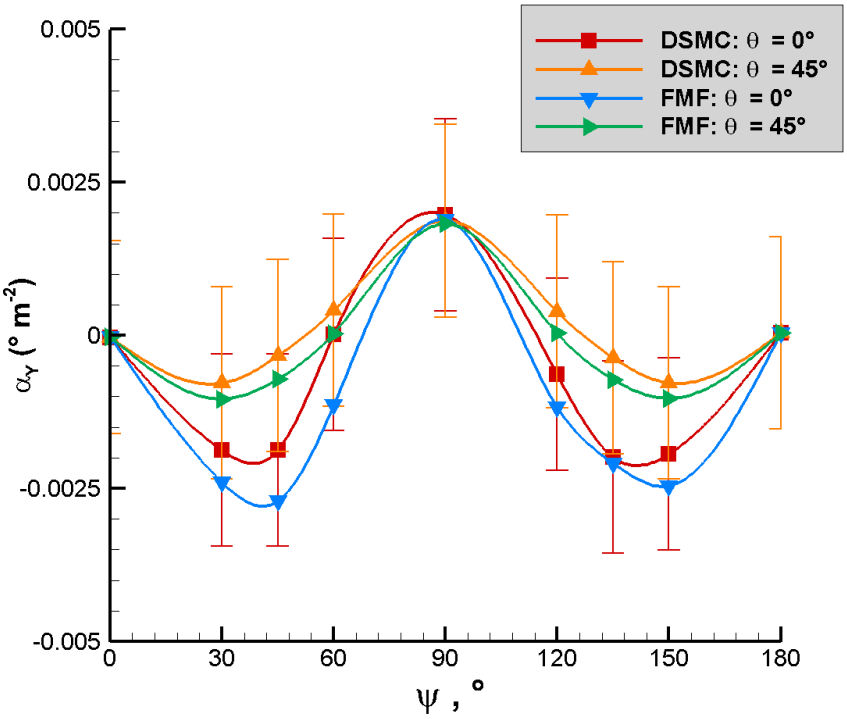

Figure 3.19: Angular acceleration about the Y-axis calculated using DSMC and free-molecular (FMF) analytical models for all experiment orientations of the TBEx, for a Knudsen number of 100. Error bars reflect the angular velocity uncertainty of 1.57×10^{-3} degrees s^{-2}.

3.3 Knudsen Number of 10

A Knudsen number of 10 is achieved for the TBEx body at 119 km of altitude. A Knudsen number of 10 is also in the free-molecular regime so well-matched results between the MONACO results and free-molecular model results is expected. The circular orbital speed and atmospheric composition at this altitude are listed in Table 3.1. As already noted, MONACO is run with a time step of 1×10^{-7} s. 80,000 simulation time steps are conducted before sampling begins and 25,000

further steps are run for a total of 105,000 time steps. As an example, the $\theta = 45°$, $\psi = 150°$ orientation, Orientation #16 in Table 3.2, is presented for the Knudsen number of 10 altitude. All slices of the flowfield are taken from the plane with the normal vector: $X = 0.71$ m, $Y = -0.71$ m, $Z = 0.0$ m, which is the center slice of the TBEx showing the $\theta = 45°$ plane. The TBEx body is represented by the white "cut-out" of the slice of the body.

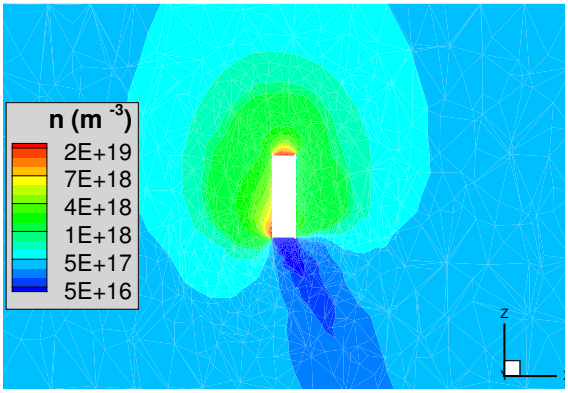

(a)

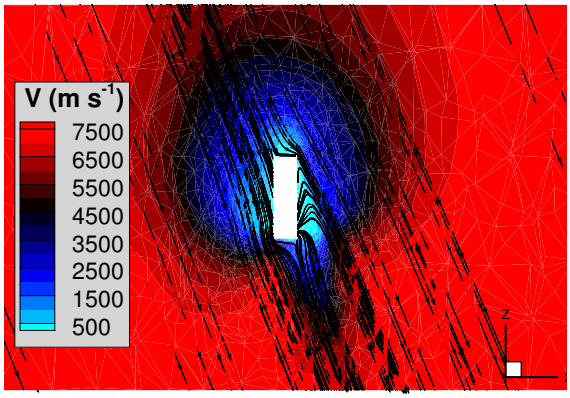

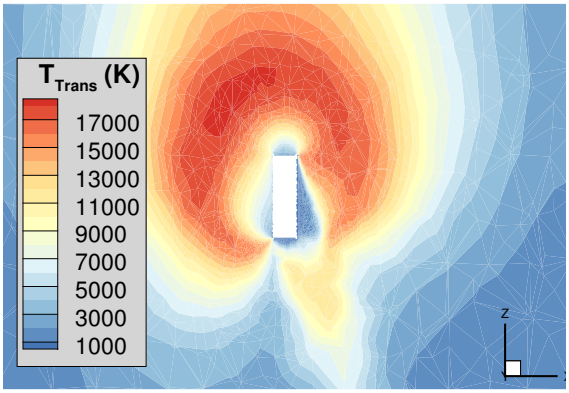

(b) (c)

Figure 3.20: Flowfield contours at $Kn = 10$, $\theta = 45°$ and $\psi = 150°$ (Orientation #16): (a) number density; (b) velocity; (c) translational temperature.

Figure 3.20 shows the flowfield contours of the $Kn = 10$, Orientation #16 case. Figure 3.20 again depicts the flow phenomena expected when an object disturbs rarefied high-speed flow: instead of a shock wave, a large "bubble" of disturbed, slowed-down flow forms upstream of the object. The general shape of the disturbed flow is similar to that in Figure 3.13, for $Kn = 100$, however due to the differing orientation of the body, the disturbed flow is in a different space. Additionally, the object, or in this case, the TBEx, blocks the incoming flow, so low density flow is seen directly behind the TBEx. The backflow of flow that impacts the side lengths of the CubeSat can be seen in the number density contours (Figure 3.20 (a)). In Figure 3.20 (b), the velocity streamlines are plotted, and the velocity ψ angle can be seen clearly by the direction of the streamlines.

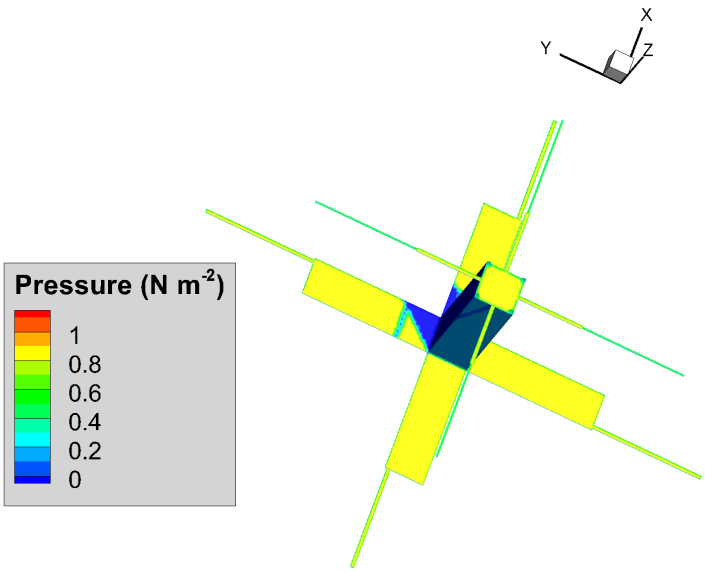

(a)

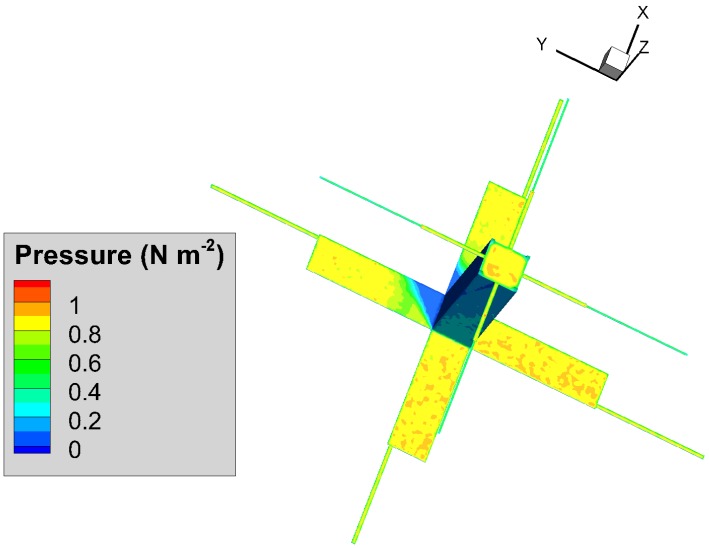

(b)

Figure 3.21: Pressure distribution at $Kn = 10$, $\theta = 45°$ and $\psi = 150°$ (Orientation #16): calculated using: (a) free molecular theory; (b) DSMC.

Figures 3.21 displays an example of the macroscopic properties (pressure, N m^{-2}) on the TBEx body wall for the $Kn = 10$, Orientation #16 case. The pressure distribution also illustrates the blocking method for the free-molecular flow method; the antenna "shadows" are clearly seen on the panels of the TBEx. The particles are diffused in the DSMC method so the shadow is not evident. The backflow experienced via the DSMC particle method is seen; Figure 3.21 (b) does not exhibit zero pressure in the shadow areas.

The pressure distributions are similar: the average pressure experienced by the surface is calculated as 3.10×10^{-1} N m^{-2} using the free-molecular method. This average is calculated by accounting for the pressure on each surface element over the entire body, for this orientation, as mentioned in Section 3.2. The average pressure experienced over the body calculated by using MONACO results is $2.99 \times 10^{-1} \pm 2.39 \times 10^{-2}$ N m^{-4}. The difference in average pressure experienced by the body at this orientation is is 3.57%.

3.3.1 $Kn = 10$: Drag and Lift

The orientations are interpolated over as described in Section 3.2. Figure 3.22 shows the calculated drag for all orientations (including the projected #1 and #9 for $\theta = 45°$) using both models. The data points for the orientation simulation results are connected using splines to demonstrate the smooth transition of drag experienced as the body rotates. The curves are duplicated and repeated for $\psi = 180°$ to $\psi = 360°$ and for subsequent symmetric θ values. The interpolated average drag and lift over these two θ curves are taken as the average drag and lift experienced by the tumbling TBEx in orbit, as described in Section 3.2. The Poisson statistical error is the same as in Section 3.2, 0.08%, and is represented in the following plots by error bars.

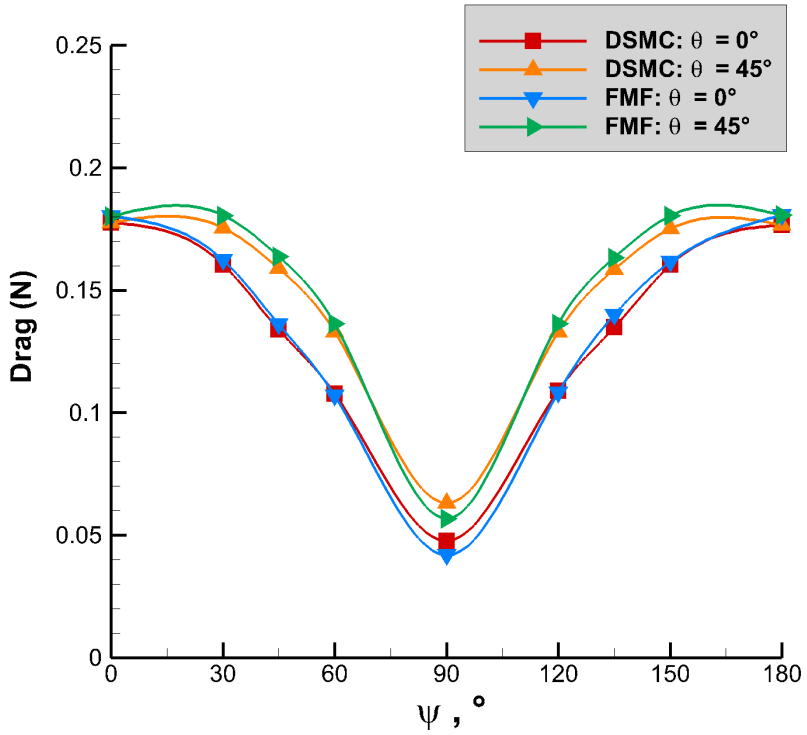

Figure 3.22: Drag calculated using DSMC and free-molecular (FMF) analytical models for all experiment orientations of the TBEx at a Knudsen number of 10.

Figure 3.22 shows that maximum drag values are achieved for $\psi = 0°$ and $\psi = 180°$, while minimum drag is achieved for $\psi = 0°$. The same features of this plot can be seen in Figure 3.15 in Section 3.2: the maxima and minimum values correspond to the maximum and minimum flow-exposed projected areas. When $\psi = 90°$, the rectangular body of the TBEx faces the oncoming flow. When $\psi = 0°$ or $\psi = 180°$, the flow encounters the deployed solar panels, increasing the pressure force on the body and subsequently increasing the drag. The $\theta = 45°$ drag values are increased due to increased exposed area: two sides of the rectangular body are exposed versus one for $\theta = 0°$.

The average drag calculated using the DSMC MONACO modeling results is $1.35 \times 10^{-1} \pm 1.08 \times 10^{-4}$ N, while the average drag calculated using the free-molecular analytical modeling

results is 1.37×10^{-1} N. The percentile difference between the averages is 1.03%. The normalized root-mean-square deviation between all the drag results across both models is 2.75%. Again, there is good agreement between both models at this Knudsen number as expected.

Figure 3.23 shows the calculated lift for all orientations using both methods. Similarly to results from Section 3.2, lift is two orders of magnitude smaller compared to drag due to the TBEx's near vertical symmetry. Resolved as described in Chapter 2, nearly all force applied to the TBEx body is attributed to drag.

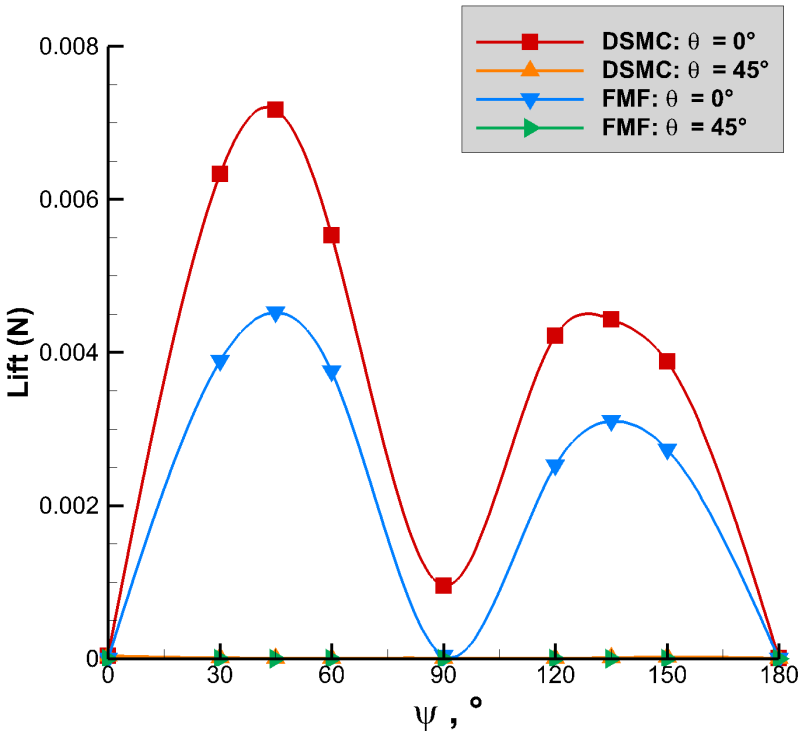

Figure 3.23: Lift calculated using DSMC and free-molecular (FMF) analytical models for all experiment orientations of the TBEx at a Knudsen number of 10.

The average lift calculated using the DSMC MONACO modeling results is $1.82 \times 10^{-3} \pm 1.46 \times 10^{-6}$ N, while the average lift calculated using the free-molecular analytical modeling results is 1.13×10^{-3} N. The normalized root-mean-square difference between all the lift results

across both models is 25.0%; this deviation normalizes using the range of lift, due to the lift values being very close to zero. Additionally, it is reasonable to assume that the shear stress and pressure are applied in opposing lift directions; and the errors in each are magnified by the summation, as in seen in Chapters 4 and 5. This normalized root mean square deviation is also elevated due to the relatively near-zero lift values, however, the deviations are a good way to understand free-molecular agreement with DSMC techniques as Knudsen number decreases. The deviation has increased by nearly a factor of 10 when compared with the results from $Kn = 100$ in Section 3.2. This deviation reflects what is seen visually in Figure 3.23, versus Figure 3.16: while the free-molecular model is very accurate for the larger drag force at this altitude, small differences in surface element macroscopic properties are causing differences in calculated lift as the Knudsen number decreases.

Figure 3.23 shows that maximum lift values are again achieved for $\theta = 0$, $\psi = 45°$ and $\psi = 135°$ for both modeling approaches. The reasons for these maxima and minima are described in Section 3.2. Noteworthy is the difference between the free-molecular and DSMC lift curves for $\theta = 0°$: the curves are more disparate than those in Figure 3.16. The shear-stress contribution to the lift is beginning to differ and effect results. The shear-stress calculations differ the most between the modeling approaches as described in Chapter 2. There is still good agreement between the free-molecular and DSMC models at this Knudsen number, but differences are becoming apparent.

For the drag and lift coefficients, free-stream density is again gathered from [9]. At 119 km, or TBEx's $Kn = 10$, the free-stream density $\rho = 1.81 \times 10^{-8}$ kg m^{-3}. The orbital velocity is the circular orbital speed used throughout the $Kn = 10$ results: $V = 7830$ m s^{-1}. The products of the aerodynamic coefficients and the flow-facing areas are calculated as described in Section 3.2. Figure 3.24 shows $C_D A$ and $C_L A$ calculated for all models and orientations for $Kn = 10$

experienced by the TBEx body.

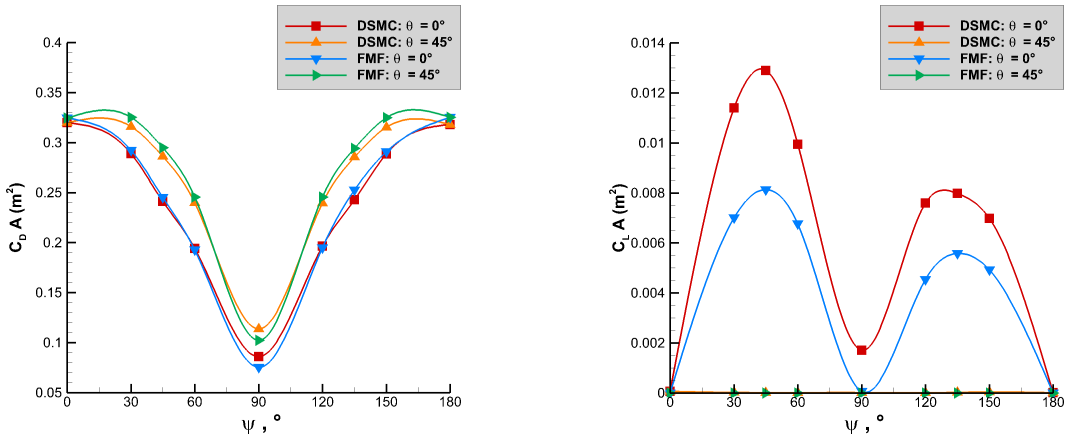

(a) (b)

Figure 3.24: Drag (a) and lift (b) coefficients calculated using DSMC and free-molecular (FMF) analytical models for all experiment orientations of the TBEx using both models for a Knudsen number of 10.

The average C_DA calculated using the DSMC MONACO modeling results is $2.44 \times 10^{-1} \pm 1.95 \times 10^{-4}$ m^2, while the average C_DA calculated using the free-molecular analytical modeling results is 2.46×10^{-1} m^2. The percent difference between the averages is 1.03%. The normalized root-mean-square deviation between all the C_DA results across both models is 2.75%. The average C_LA calculated using the DSMC MONACO modeling results is $3.27 \times 10^{-3} \pm 2.62 \times 10^{-6}$ m^2, while the average C_LA calculated using the free-molecular analytical modeling results is 2.03×10^{-3} m^2. The normalized root-mean-square difference between all the C_LA results across both models is 25.0%, and is elevated as discussed with the lift, due to the very small C_LA values, especially for $\theta = 45°$ orientations. Like the drag and lift results, the C_DA values show good agreement between models, while there is a larger difference between the C_LA values as Knudsen number drops.

3.3.2 $Kn = 10$: Moments and Angular Accelerations

The moments are taken about the TBEx body centroid as discussed in Section 3.2.2. The angular acceleration error again equates to: 2.73×10^{-5} radians s^{-2}, or 1.57×10^{-3} degrees s^{-2}. This is plotted as an error bar in any angular acceleration plots in this chapter.

Figure 3.25 displays the moment results produced by both models across all the TBEx body orientations about the three primary axes. Figure 3.25 mirrors the results seen in Figure 3.18 but at a larger scale, proportional to the larger forces induced on the body in less-rarefied flow at a higher orbital speed. As in Section 3.2, the aerodynamic moments about the Z-axis are smaller than those about the X- and Y-axes by three orders of magnitude due to the rotational near-symmetry of the TBEx about the Z-axis.

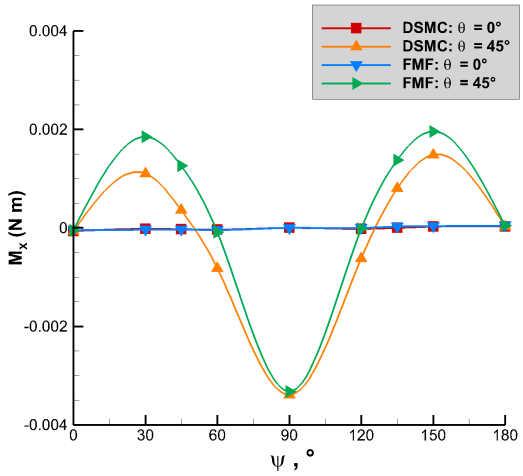

(a)

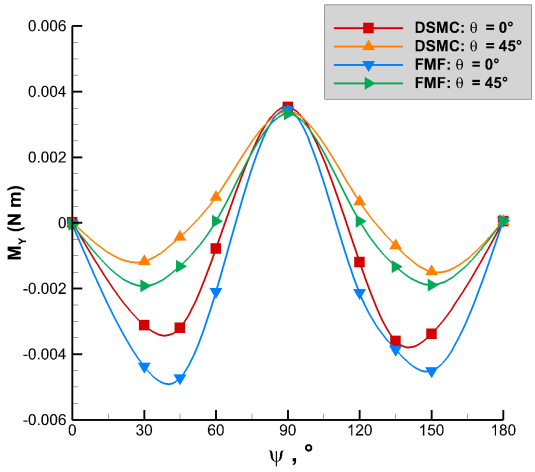

(b)

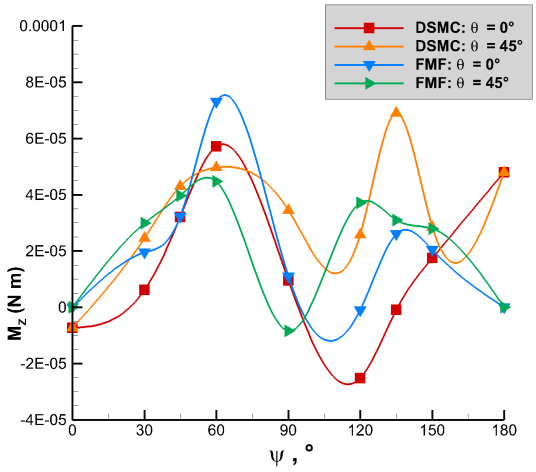

(c)

Figure 3.25: Moments calculated using DSMC and free-molecular (FMF) analytical models for all experiment orientations of the TBEx about the: (a) X axis; (b) Y axis; (c) Z axis, for a Knudsen number of 10.

As seen in Figure 3.25 (a), the aerodynamic moments about the X-axis are incurred when the θ value of the simulation is $45°$, due to the phenomena discussed in Section 3.2.

In Figure 3.25 (b), Y-moments are induced across both θ values. The same maxima and minima ψ values occur as in Section 3.2, for the same reasons. However, for both the X- and Y-moments

in Figure 3.25, a larger qualitative discrepancy can be seen between the free-molecular and DSMC results when compared to Figure 3.18.

The moment averages are sensitive due to the small magnitudes of the moment results and the sign changes as ψ changes. In order to compare the free-molecular and DSMC modeling approaches effectively, averages are taken according to θ value and are listed in Table 3.8. "FMF" in Table 3.8 refers to results from the free-molecular analytical model.

Table 3.8 portrays that the free-molecular and DSMC modeling approaches yield somewhat similar results for this Knudsen number. This reinforces what we see in Figure 3.25, where the curves are qualitatively close, but are further apart than the curves in Figure 3.18.

The sign differences between the DSMC and free-molecular results for the X- and Y- moments in Table 3.8, $\theta = 45°$ are due to the free-molecular results producing more-negative minima in the Y-moment, and more-positive maxima in the X-moments. Since the moments center around zero, these maxima and minima can pull the averages towards the negative or positive side of zero.

Table 3.8: Average moments calculated for a Knudsen number of 10 for the DSMC and free-molecular analytical modeling approaches for both θ values.

Average	θ **= 0°**		θ **= 45°**	
	FMF	**DSMC**	**FMF**	**DSMC**
$\mathbf{M}_X$ **(N m)**	-5.92×10^{-6}	-1.05×10^{-5} $\pm 8.40 \times 10^{-9}$	1.29×10^{-4}	-3.28×10^{-4} $\pm 2.62 \times 10^{-7}$
$\mathbf{M}_Y$ **(N m)**	-1.78×10^{-3}	-1.03×10^{-3} $\pm 8.24 \times 10^{-7}$	-1.29×10^{-4}	3.24×10^{-4} $\pm 2.59 \times 10^{-7}$
$\mathbf{M}_Z$ **(N m)**	2.07×10^{-5}	1.45×10^{-5} $\pm 1.16 \times 10^{-8}$	2.20×10^{-5}	3.45×10^{-5} $\pm 2.76 \times 10^{-8}$

The normalized root-mean-square deviation between the X-axes moments is 7.49%, the normalized root-mean-square deviation between the Y-axes moments is 9.45%, and the normalized root-mean-square deviation between the Z-axes moments is 28.8%. These deviations are affect by

the near-zero moments; particularly in the Z-moment case. These deviations indicate good agreement, as also seen for $Kn = 100$ in Section 3.2. Also as in Section 3.2, the Z-moments are three orders of magnitude smaller than the X- and Y- moments, and show noisy variation across θ and ψ values.

The moments incurred about the Y-axis are the largest and are non-zero for the DSMC and free-molecular models for both θ values, therefore this angular acceleration is examined. Figure 3.26 shows the calculated angular acceleration about the Y-axis for the TBEx body using both models across all orientations, with error bars as described in Section 3.2. The interpolated average angular accelerations about the Y-axis are -1.65×10^{-3} degrees s^{-2} using the DSMC method and -4.47×10^{-3} degrees s^{-2} using the free-molecular analytical method. These averages reflect what Figure 3.26 shows qualitatively: the free-molecular results yield more extreme minima than the DSMC results. This is due to the diffusive effect of the DSMC particle method on surface properties, as discussed in Section 3.2. DSMC is a particle method: particles interacting with each surface element create less extreme results when compared to the analytical model, as the analytical model calculates each surface element experiencing flow with the same normal vector as having identical surface properties. The normalized root-mean-square difference between the angular accelerations about the Y-axis is 9.45%.

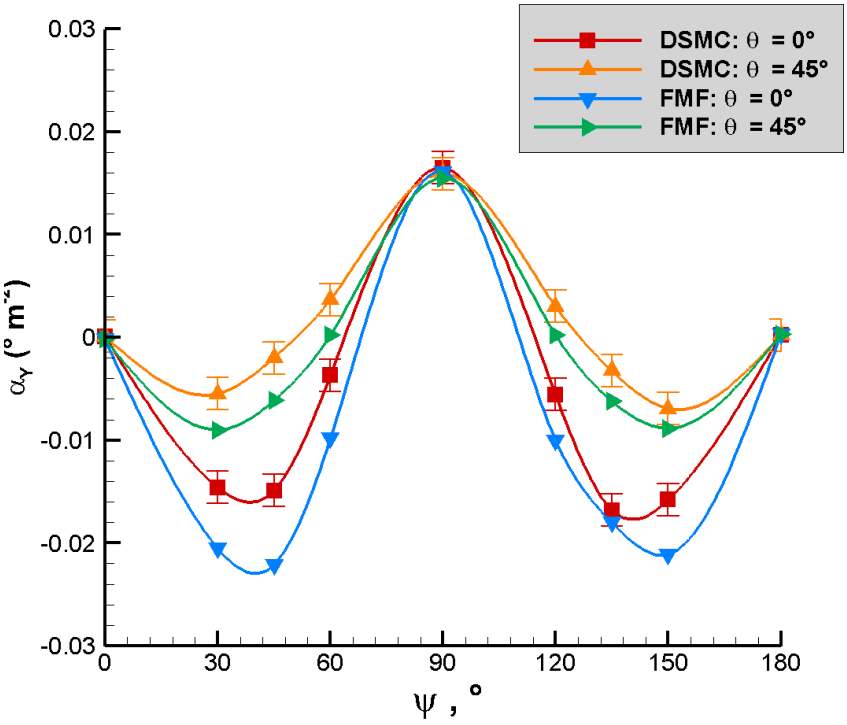

Figure 3.26: Angular acceleration about the Y-axis calculated using DSMC and free-molecular (FMF) analytical models for all experiment orientations of the TBEx, for a Knudsen number of 10. Error bars reflect the angular velocity uncertainty of 1.57×10^{-3} degrees s^{-2}.

3.4 Knudsen Number of 1

?? A Knudsen number of 1 is achieved for the TBEx body at 104 km of altitude. A Knudsen number of 1 is the limit of defined free-molecular flow [20]. In this regime, the flowfields will still be rarefied, but our expectation of good agreement between the models does not hold: particle collisions will matter at this Knudsen number. The circular orbital speed and atmospheric composition at this altitude are listed in Table 3.1. As already noted, MONACO is run with a time step of 1×10^7 s. 80,000 simulation time steps are conducted before sampling begins and 25,000 further steps are run for a total of 105,000 time steps. As an example, the $\theta = 0°$, $\psi = 135°$ orientation,

Orientation #7 in Table 3.2, is presented for the Knudsen number of 1 altitude. All slices of the flowfield are taken at $Y = 0.175$ m which is the center slice of the TBEx showing the X-Z plane. The TBEx body is represented by the white "cut-out" of the slice of the body.

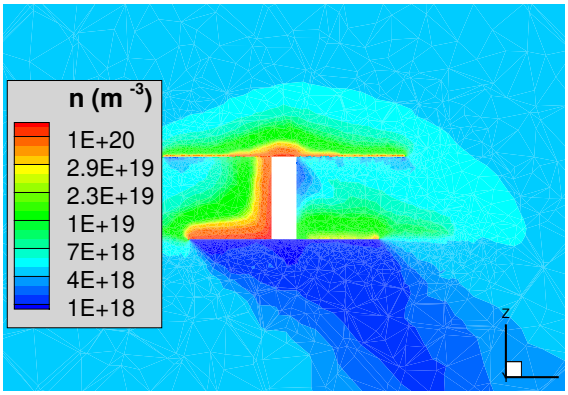

(a)

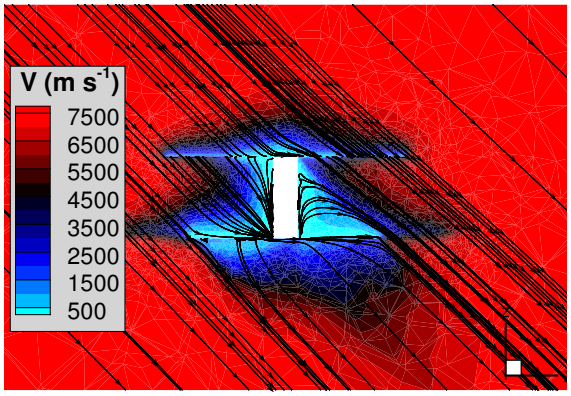

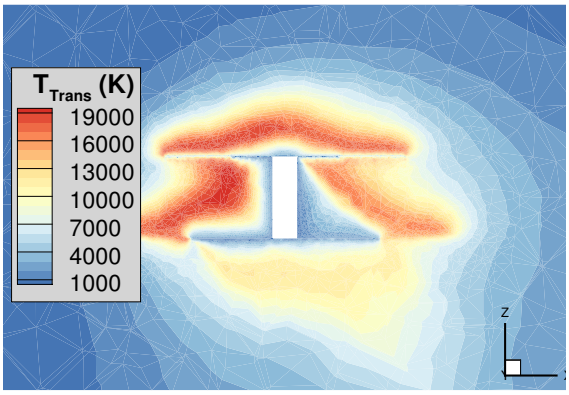

(b) (c)

Figure 3.27: Flowfield contours at $Kn = 1$, $\theta = 0°$ and $\psi = 135°$ (Orientation #7): (a) number density; (b) velocity; (c) translational temperature.

Figure 3.27 shows the flowfield contours of the $Kn = 1$, Orientation #7 case. Figure 3.27 shows a flowfield transitioning between the highly rarefied "bubble" formations found for $Kn = 100$ and 10 in Figures 3.13 3.20 and an expected shock upstream of the body in denser, high-speed

flow. The upstream disturbed flow has flattened out, and the low-dense flow in the TBEx's shadow can be seen in the number density contours in Figure 3.27 (a). Backflow that deflects off of the aft solar panels makes contact with the sides of the body. Since this backflow is not detected in the free-molecular model, these reflecting particles will be a source of disparity between the two models. In Figure 3.27 (b), the velocity streamlines are plotted, and the velocity ψ angle can be seen clearly by the direction of the streamlines.

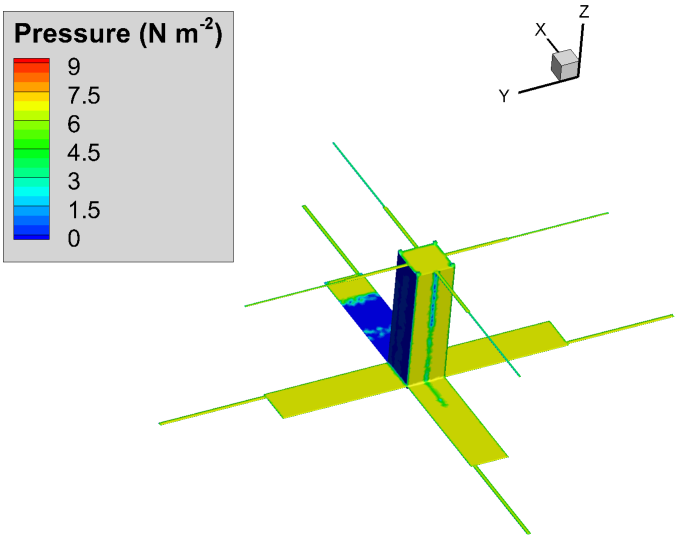

(a)

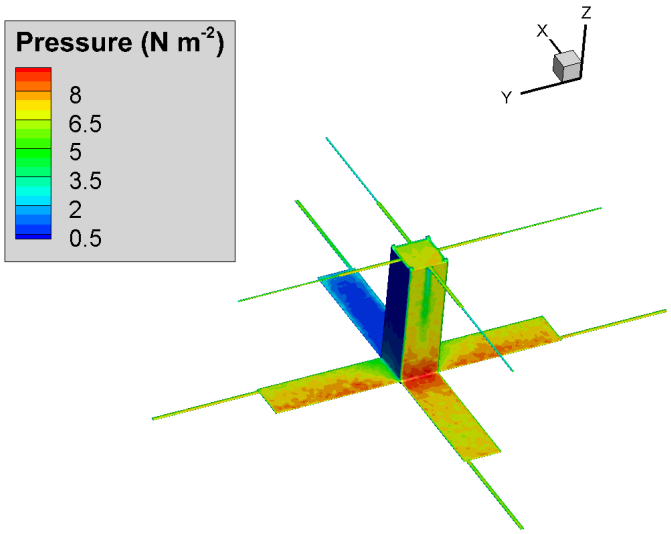

(b)

Figure 3.28: Pressure distribution at $Kn = 1$, $\theta = 0^\circ$ and $\psi = 135^\circ$ (Orientation #7): calculated using: (a) free molecular theory; (b) DSMC.

Figures 3.28 displays an example of the macroscopic properties (pressure, N m^{-2}) on the TBEx

surface for the $Kn = 1$, Orientation #7 case. Figure 3.28 clearly shows the diffuse effect of the particles impacting the surface as a result of the DSMC modeling approach versus the back-tracing blocked algorithm applied to the analytical equations used on the free-molecular model body. The antenna "shadow" is visible on the free-molecular image.

The pressure distributions from the two methods are similar: the average pressure experienced by the surface is calculated as 2.50 N m^{-2} using the free-molecular method. The average pressure experienced over the body calculated by using MONACO results is 2.59 $\pm 2.10 \times 10^{-3}$ N m^{-2}. The difference in average pressure experienced by the body at this orientation is 3.53%.

3.4.1 $Kn = 1$: Drag and Lift

The orientations are interpolated over as described in Section 3.2. Figure 3.29 shows the calculated drag for all orientations (including the projected #1 and #9 for $\theta = 45°$) using both models. The data points for the orientation simulation results are connected using splines to demonstrate the smooth transition of drag experienced as the body rotates. The curves are duplicated and repeated for $\psi = 180°$ to $\psi = 360°$ and for subsequent symmetric θ values. The interpolated average drag and lift over these two θ curves are taken as the average drag and lift experienced by the tumbling TBEx in orbit, as described in Section 3.2. The Poisson statistical error is the same as in Section 3.2, 0.08%, and is represented in the following plots by error bars.

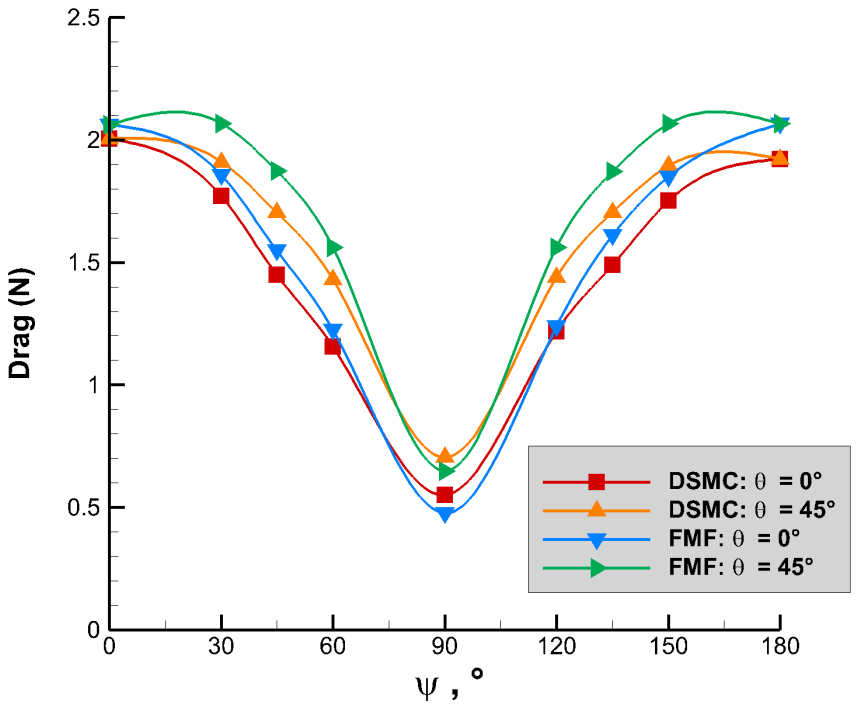

Figure 3.29: Drag calculated using DSMC and free-molecular (FMF) analytical models for all experiment orientations of the TBEx at a Knudsen number of 1.

Figure 3.29 shows that maximum drag values are achieved for $\psi = 0°$ and $\psi = 180°$, while minimum drag is achieved for $\psi = 0°$. The same features of this plot can be seen in Figure 3.15 and Figure 3.22: the maxima and minimum values correspond to the maximum and minimum flow-exposed projected areas. When $\psi = 90°$, the rectangular body of the TBEx faces the oncoming flow. When $\psi = 0°$ or $\psi = 180°$, the flow encounters the deployed solar panels, increasing the pressure force on the body and subsequently increasing the drag. The $\theta = 45°$ drag values are increased due to increased exposed area: two sides of the rectangular body are exposed versus one for $\theta = 0°$.

The average drag calculated using the DSMC MONACO modeling results is $1.48 \pm 1.12 \times 10^{-3}$ N, while the average drag calculated using the free-molecular analytical modeling results is 1.56

N. The percentile difference between the averages is 5.58%. The normalized root-mean-square deviation between all the drag results across both models is 7.07%. The differences between models at $Kn = 1$, compared to the more rarefied regimes, is clearly more evident. Particle collisions are having a larger effect on the flowfield. At $Kn = 1$, there are around 600 collisions in the flowfield per DSMC time step. This changes the flow before it impacts the TBEx surface which in turn changes the impacts the particles have with the TBEx surface. The energy of the flow is dissipated due to collisions, causing the DSMC pressure, and drag, to be lower overall. In addition, the particle collisions with the surface have a dissipative effect over the surface planes, in contrast with the free-molecular analytical method, which does not account for differing flowfield properties across the body. The differences in DSMC and free-molecular surface pressure are seen in Figure 3.28.

Figure 3.30 shows the calculated lift for all orientations using both methods. Lift is an order of magnitude smaller than the drag results due to the TBEx's near vertical symmetry. Resolved as described in Chapter 2, nearly all force applied to the TBEx is attributed to drag.

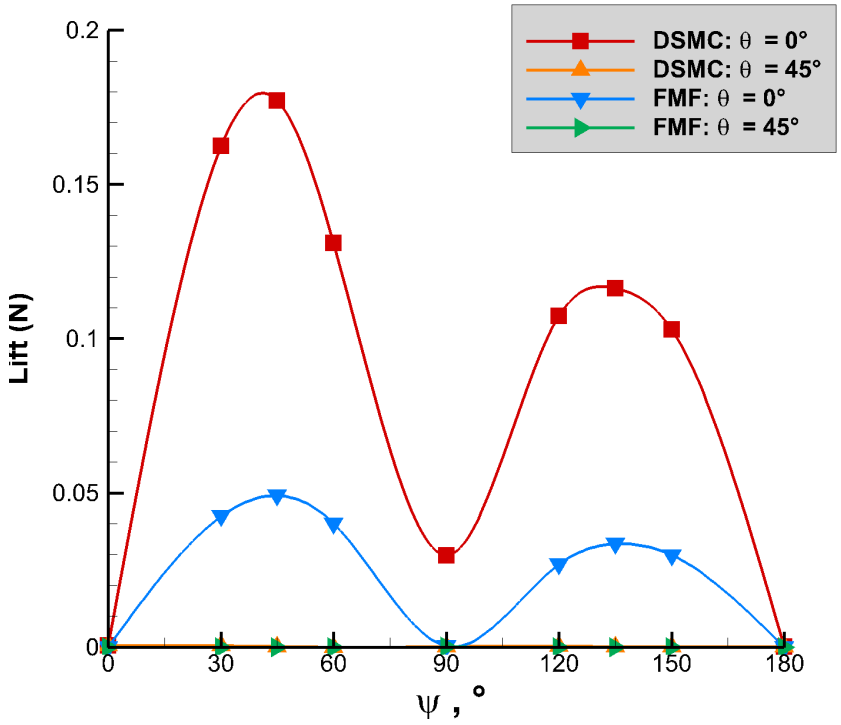

Figure 3.30: Lift calculated using DSMC and free-molecular (FMF) analytical models for all experiment orientations of the TBEx at a Knudsen number of 1.

The average lift calculated using the DSMC MONACO modeling results is $4.63 \times 10^{-2} \pm 3.70 \times 10^{-5}$ N, while the average lift calculated using the free-molecular analytical modeling results is 1.22×10^{-2} N. The normalized root-mean-square difference between all the lift results across both models is elevated due to the free-molecular results being close to zero, especially for the $\theta = 45°$ results. Using the DSMC range of lift to normalize yields a normalized root-mean-square deviation between the lift results of 32.2%; this reflects the differences between the $\theta = 0°$ seen in Figure 3.30. While the DSMC drag is less than the free-molecular drag at this Knudsen number, lift differs. Additionally, it is reasonable to assume that the shear stress and pressure are applied in opposing lift directions; and the errors in each are magnified by the summation, as in seen in Chapters 4 and 5. The DSMC lift results are consistently greater than the free molecular lift

results (see Figures 3.16, 3.23, and 3.30). This is due to the models' treatment of the shear stress on the surface. The DSMC model calculates shear stress from the tangential momentum transfer of particles hitting the surface elements, while the free-molecular model calculates analytical shear stress and distributes it in the cardinal X, Y, and Z directions based on the surface element's positioning, as described in Chapter 2. This treatment of the analytical shear stress yields less force in the lift-direction.

Figure 3.30 shows that maximum lift values are again achieved for $\theta = 0°$, $\psi = 45°$ and $\psi = 135°$ for both modeling approaches. The reasons for these maxima and minima are described in Section 3.2. The differences between the DSMC and free-molecular lift results are growing as Knudsen number lowers and the lift is the most magnifying way to visualize the differences. Qualitatively this is seen in Figures 3.16, 3.23, and 3.30.

For the drag and lift coefficients, free-stream density is again gathered from [9]. At 104 km, or TBEx's $Kn = 1$, the free-stream density $\rho = 2.07 \times 10^{-7}$ kg m^{-3}. The orbital velocity is the circular orbital speed used throughout the $Kn = 1$ results: $V = 7840$ m s^{-1}. The products of the aerodynamic coefficients and the flow-facing areas are calculated as described in Section 3.2. Figure 3.31 shows $C_D A$ and $C_L A$ calculated for all models and orientations for $Kn = 1$ experienced by the TBEx body.

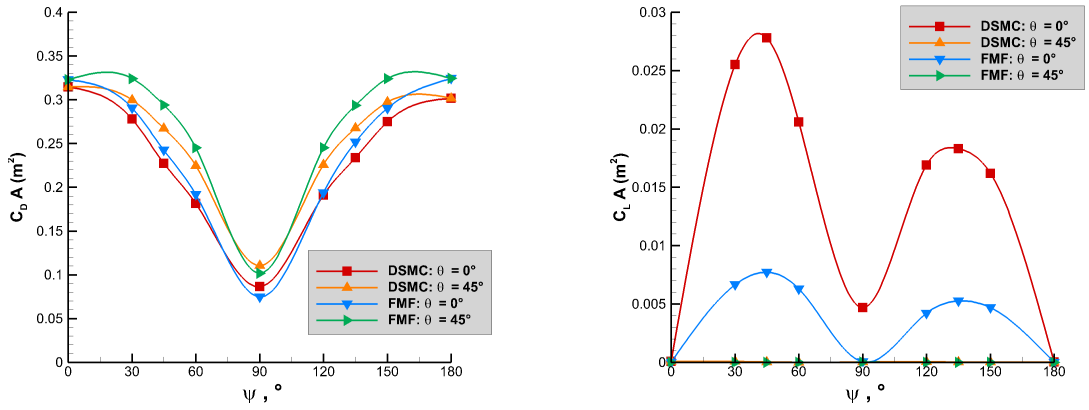

(a) (b)

Figure 3.31: Drag (a) and lift (b) coefficients calculated using DSMC and free-molecular (FMF) analytical models for all experiment orientations of the TBEx using both models for a Knudsen number of 1. Error bars reflect the 0.08% statistical DSMC error.

The average $C_D A$ calculated using the DSMC MONACO modeling results is $2.33 \times 10^{-1} \pm 1.86 \times 10^{-4}$ m^2, while the average $C_D A$ calculated using the free-molecular analytical modeling results is 2.45×10^{-1} m^2. The percent difference between the averages is 5.46%. The normalized root-mean-square difference between all the $C_D A$ results across both models is 7.02%. The average $C_L A$ calculated using the DSMC MONACO modeling results is $7.28 \times 10^{-3} \pm 5.82 \times 10^{-6}$ m^2, while the average $C_L A$ calculated using the free-molecular analytical modeling results is 1.91×10^{-3} m^2. The root-mean-square difference between all the $C_L A$ results across both models is 32.2%. The differences between modeling approach results for drag, lift, $C_D A$ and $C_L A$ are getting bigger when compared to Section 3.2 and 3.3: as Knudsen number is reduced, the free-molecular modeling approach becomes less physically applicable, and therefore less accurate.

3.4.2 $Kn = 1$: Moments and Angular Accelerations

The moments are taken about the TBEx body centroid as discussed in Section 3.2.2. The angular acceleration error again equates to: 2.73×10^{-5} radians s^{-2}, or 1.57×10^{-3} degrees s^{-2}.

Figure 3.32 displays the moment results yielded by both models across all the TBEx body orientations about the three primary axes. Figure 3.32 mirrors the results seen in Figures 3.25 and 3.18, but at a larger scale, proportional to the larger forces induced on the body in less-rarefied flow at a higher orbital speed. As in Section 3.2, the aerodynamic moments about the Z-axis are smaller than those about the X- and Y-axes by three orders of magnitude due to the rotational near-symmetry of the TBEx about the Z-axis.

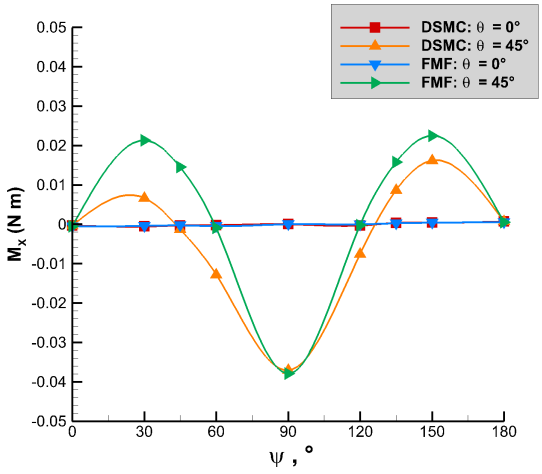

(a)

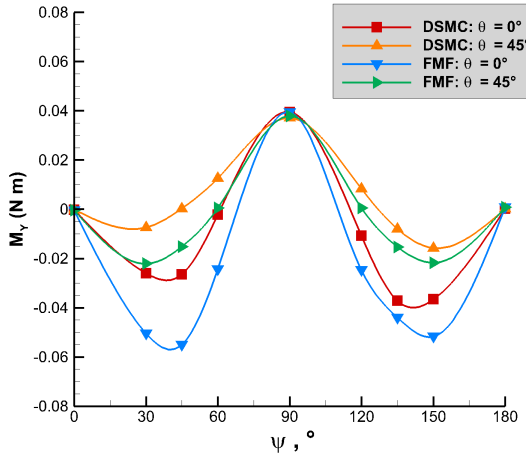

(b)

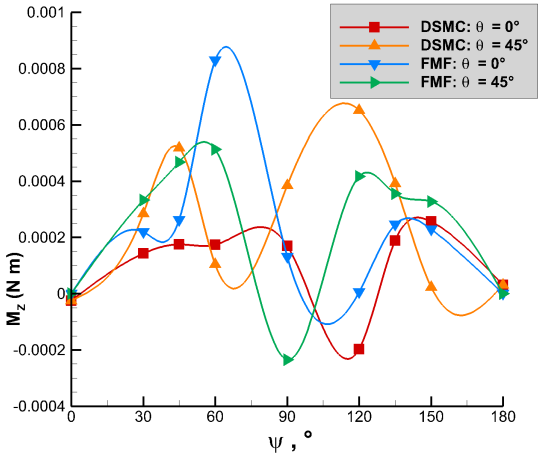

(c)

Figure 3.32: Moments calculated using DSMC and free-molecular (FMF) analytical models for all experiment orientations of the TBEx about the: (a) X axis; (b) Y axis; (c) Z axis, for a Knudsen number of 1.

As seen in Figure 3.32 (a), the aerodynamic moments about the X-axis are incurred when the θ value of the simulation is $45°$, due to the phenomena discussed in Section 3.2.

In Figure 3.32 (b), Y-moments are induced across both θ values. The same maxima and minima ψ values occur as in Section 3.2, for the same reasons. However, for both the X- and Y-moments

in Figure 3.32, a larger qualitative discrepancy can be seen between the free-molecular and DSMC results when compared to Figures 3.18 and 3.25.

The moment averages are sensitive due to the small magnitudes of the moment results and the sign changes as ψ changes about the Z-axis. In order to compare the free-molecular and DSMC modeling approaches effectively, averages are taken according to θ value and are listed in Table 3.9.

Table 3.9 portrays that the free-molecular and DSMC modeling approaches exhibit slight differences for this Knudsen number as compared to Tables 3.7 and 3.8 for Knudsen numbers of 100 and 10, respectively. The sign differences between the DSMC and free-molecular results for the X- and Y- moments in Table 3.9, $\theta = 45^\circ$ are due to the free-molecular results producing more-negative minima in the Y-moment, and more-positive maxima in the X-moments. Since the moments center around zero, these maxima and minima can pull the averages towards the negative or positive side of zero.

Table 3.9: Average moments calculated for a Knudsen number of 1 for the DSMC and free-molecular analytical modeling approaches for both θ values.

Average	θ **= 0°**		θ **= 45°**	
	FMF	**DSMC**	**FMF**	**DSMC**
$\mathbf{M}_X$ **(N m)**	-6.20×10^{-5}	-4.51×10^{-5} $\pm 3.61 \times 10^{-8}$	1.54×10^{-3}	-5.22×10^{-3} $\pm 4.18 \times 10^{-6}$
$\mathbf{M}_Y$ **(N m)**	-2.06×10^{-2}	-8.18×10^{-3} $\pm 6.54 \times 10^{-6}$	-1.55×10^{-3}	5.26×10^{-3} $\pm 4.21 \times 10^{-6}$
$\mathbf{M}_Z$ **(N m)**	2.24×10^{-4}	1.06×10^{-4} $\pm 8.48 \times 10^{-8}$	2.28×10^{-4}	2.73×10^{-4} $\pm 2.18 \times 10^{-7}$

The normalized root-mean-square deviation between the X-axes moments is 10.7%, the normalized root-mean-square deviation between the Y-axes moments is 14.0% N m, and the normalized root-mean-square deviation between the Z-axes moments is 24.3%. These normalized

root-mean-square deviations are normalized using the range of the free-molecular values so the relatively near-zero values don't overly inflate the deviations. These deviations indicate lessening agreement as the Knudsen number lowers; the error has increased between the models by about 5% from the more free-molecular altitudes. As in Section 3.2, the Z-moments are three orders of magnitude smaller than the X- and Y- moments, and show noisy variation across θ and ψ values; error between Z-moments is therefore not the most reliable way to measure differences between models as the Knudsen number lowers.

The moments incurred about the Y-axis are the largest and are non-zero for the DSMC and free-molecular models for both θ values, therefore this angular acceleration is examined. Figure 3.33 shows the calculated angular acceleration about the Y-axis for the TBEx body using both models across all orientations, with error bars as described in Section 3.2. The interpolated average angular accelerations about the Y-axis incurred are -6.82×10^{-3} degrees s^2 using the DSMC method and -5.16×10^{-2} degrees s^2 using the free-molecular analytical method. These averages reflect what Figure 3.33 shows qualitatively: the free-molecular results yield more extreme minima than the DSMC results. This is due to the diffusive effect of the DSMC particle method on surface properties, as discussed in Section 3.2. The normalized root-mean-square deviation between the angular accelerations about the Y-axis is 14.0%.

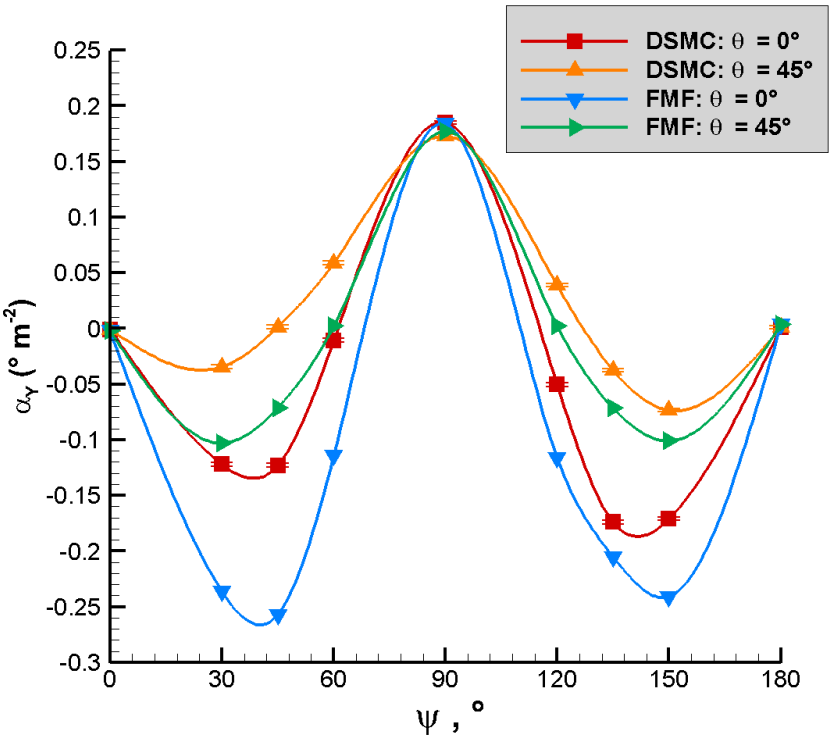

Figure 3.33: Angular acceleration about the Y-axis calculated using DSMC and free-molecular (FMF) analytical models for all experiment orientations of the TBEx, for a Knudsen number of 1. Error bars reflect the angular velocity uncertainty of 1.57×10^{-3} degrees s^{-2}.

3.5 Knudsen Number of 0.1

A Knudsen number of 0.1 is achieved for the TBEx body at 91 km of altitude. A Knudsen number of 0.1 is purely in the transitional regime [20]. In this regime, the flowfields are markedly less rarefied and an expectation of good agreement between the models should not hold. The circular orbital speed and atmospheric composition at this altitude are listed in Table 3.1. As already noted, MONACO is run with a time step of 1×10^{-7} s. 80,000 simulation time steps are conducted before sampling begins and 25,000 further steps are run for a total of 105,000 time steps. As an example, the $\theta = 45°$, $\psi = 60°$ orientation, Orientation #12 in Table 3.2, is presented for the Knudsen number of 0.1 altitude. All slices of the flowfield are taken the plane with the normal

vector: $X = 0.71$ m, $Y = -0.71$ m, $Z = 0.0$ m, which is the center slice of the TBEx showing the $45°$ plane . The TBEx body is represented by the white "cut-out" of the slice of the body.

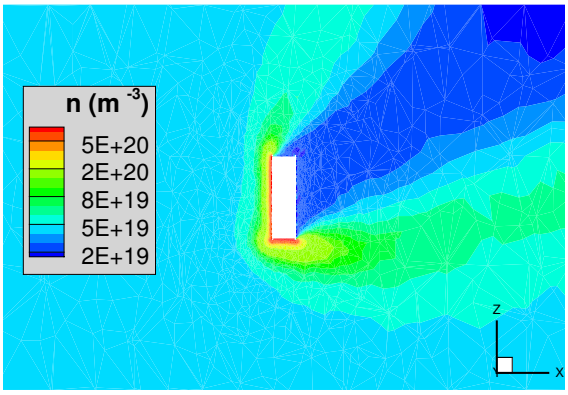

(a)

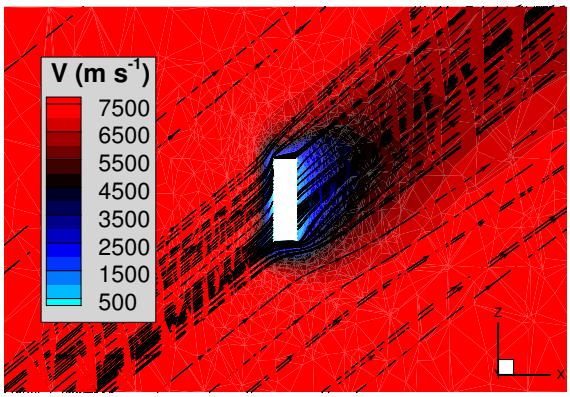

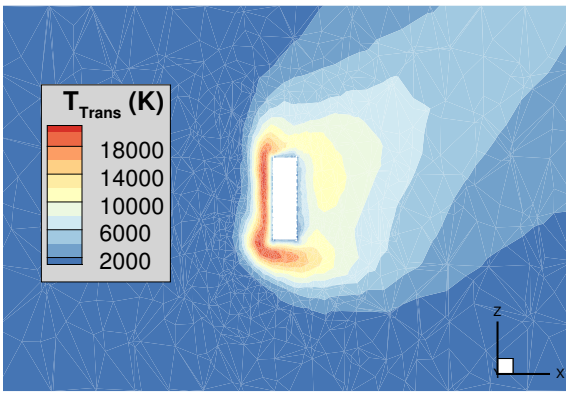

(b) (c)

Figure 3.34: Flowfield contours at $Kn = 1$, $\theta = 45°$ and $\psi = 60°$ (Orientation #12): (a) number density; (b) velocity; (c) translational temperature.

Figure 3.34 shows the flowfield contours of the $Kn = 0.1$, Orientation #12 case. In Figure 3.34, the flowfield is beginning to resemble a shock in front of the TBEx body: the "bubble" of disturbed flow upstream of the TBEx has been flattened out, and the disturbed flow has a narrower

profile that streams around the body. This is indicative of higher density, higher speed flow, as the regime moves from free-molecular into transitional flow that is dense enough to create a shock layer. In Figure 3.34 (b), the velocity streamlines are plotted, and the velocity ψ angle can be seen clearly by the direction of the streamlines.

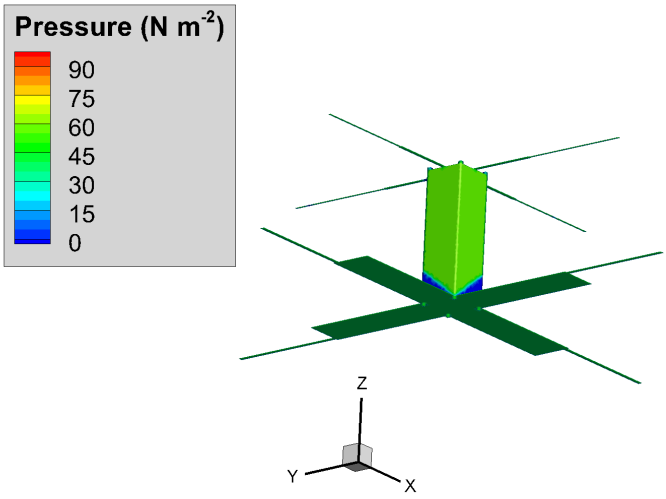

(a)

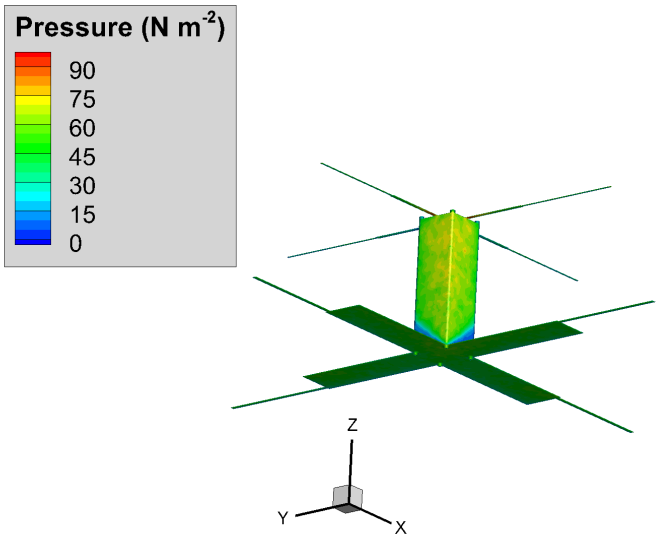

(b)

Figure 3.35: Pressure distribution at $Kn = 0.1$, $\theta = 45°$ and $\psi = 60°$ (Orientation #12): calculated using: (a) free molecular theory; (b) DSMC.

Figures 3.35 displays an example of the macroscopic properties (pressure, N m^{-2}) on the TBEx body wall for the $Kn = 0.1$, Orientation #12 case.

The pressure distributions are similar: the average pressure experienced by the surface elements is calculated as 21.0 N m^{-2} using the free-molecular method. The average pressure experienced over the body calculated by using MONACO results is 24.0 $\pm 1.92 \times 10^{-2}$ N m^{-2}. The difference in average pressure experienced by the body at this orientation is is 12.6%. Immediately, the difference in modeling approaches at this altitude is notable: collisions matter at this altitude and will greatly affect aerodynamic results.

3.5.1 $Kn = 0.1$: Drag and Lift

The orientations are interpolated over as illustrated in Section 3.2. Figure 3.36 shows the calculated drag for all orientations (including the projected #1 and #9 for $\theta = 45°$) using both models. The data points for the orientation simulation results are connected using splines to demonstrate the smooth transition of drag experienced as the body rotates. The curves are duplicated and repeated for $\psi = 180°$ to $\psi = 360°$ and for subsequent symmetric θ values. The interpolated average drag and lift over these two θ curves are taken as the average drag and lift experienced by the tumbling TBEx in orbit, as described in Section 3.2. The Poisson statistical error is the same as in Section 3.2, 0.08%, and is represented in the following plots by error bars.

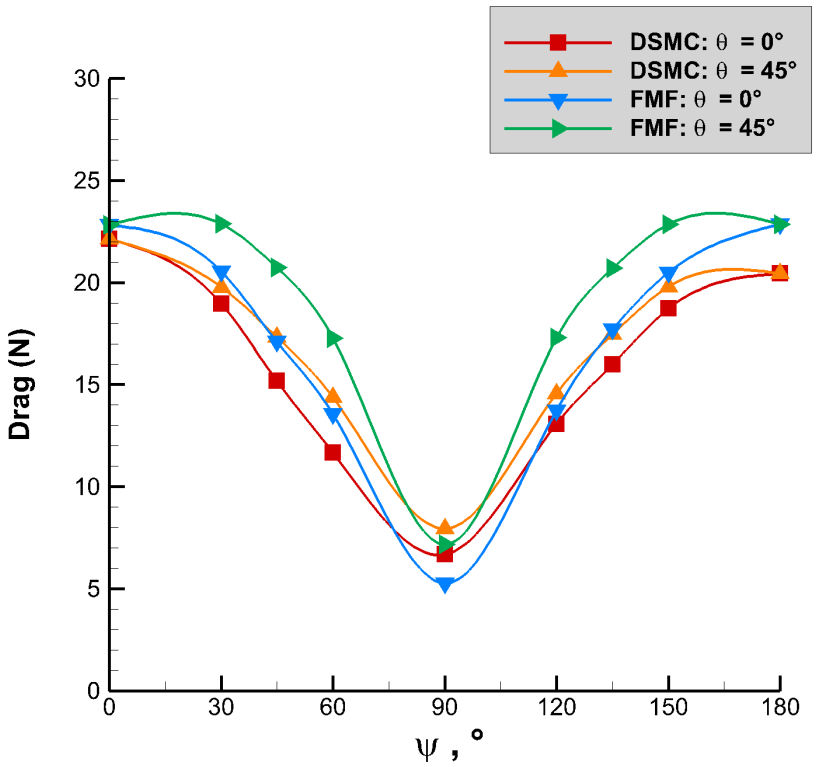

Figure 3.36: Drag calculated using DSMC and free-molecular (FMF) analytical models for all experiment orientations of the TBEx at a Knudsen number of 0.1.

Figure 3.36 shows that, again, maximum drag values are achieved for $\psi = 0°$ and $\psi = 180°$, while minimum drag is achieved for $\psi = 0°$. The same features of this plot can be seen in Figures 3.15, 3.22, and 3.29: the maxima and minimum values correspond to the maximum and minimum flow-exposed projected areas. When $\psi = 90°$, the rectangular body of the TBEx faces the oncoming flow. When $\psi = 0°$ or $\psi = 180°$, the flow encounters the deployed solar panels, increasing the pressure force on the body and subsequently increasing the drag. The $\theta = 45°$ drag values are increased due to increased exposed area: two sides of the rectangular body are exposed versus one for $\theta = 0°$.

In Figure 3.36, the free-molecular and DSMC results are diverging. The free-molecular curves are more extreme when compared to the DSMC drag curves, and the distance between the $\theta = 0°$

and 45° free-molecular and DSMC results are increased when compared to Figures 3.15, 3.22, and 3.29. This flow regime is no longer free-molecular because it is much less rarefied. This invalidates the collisionless assumption made in the free-molecular analytical method and causes the differences in these results.

The average drag calculated using the DSMC MONACO modeling results is 15.70 $\pm 1.26 \times 10^{-2}$ N, while the average drag calculated using the free-molecular analytical modeling results is 17.31 N. The percentile difference between the averages is 10.3%. The normalized root-mean-square deviation between all the drag results across both models is 12.1%. The differences between models continues increasing as Knudsen number lowers.

Figure 3.37 shows the calculated lift for all orientations using both methods. As in previous sections, lift is smaller than drag. For $Kn = 0.1$, lift is one order of magnitude smaller than drag. Nearly all force is resolved in the drag direction due to the TBEx's near vertical symmetry.

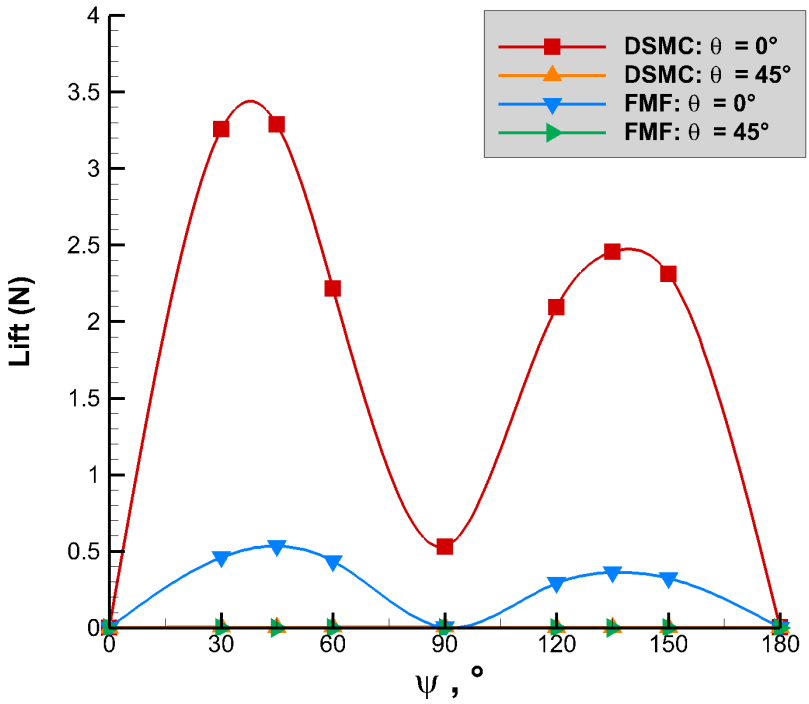

Figure 3.37: Lift calculated using DSMC and free-molecular (FMF) analytical models for all experiment orientations of the TBEx at a Knudsen number of 0.1.

The average lift calculated using the DSMC MONACO modeling results is $9.03 \times 10^{-1} \pm 7.22 \times 10^{-4}$ N, while the average lift calculated using the free-molecular analytical modeling results is 1.32×10^{-1} N. The normalized root-mean-square deviation between all the lift results across both model, normalized with the free-molecular range of lift, is 39.6%. It is reasonable to assume that the shear stress and pressure are applied in opposing lift directions; and the errors in each are magnified by the summation, as in seen in Chapters 4 and 5. However, the normalized root-mean-square deviations keep increasing as Knudsen numbers decreases, so comparing the deviations is useful for examining where the free-molecular approach fails. There is over 10 times the deviation between lift yielded by the models for a Knudsen number of 0.1 compared with that experienced for a Knudsen number of 100!

Figure 3.37 shows that maximum lift values are again achieved for $\theta = 0°$, $\psi = 45°$ and $\psi = 135°$ for both modeling approaches. The reasons for these maxima and minima are described in Section 3.2. The differences between the DSMC and free-molecular lift results can be seen increasing as Knudsen number lowers. Qualitatively this is seen in Figures 3.16, 3.23, 3.30 and 3.37.

For the drag and lift coefficients, free-stream density is again gathered from [9]. At 91 km, or TBEx's $Kn = 0.1$, the free-stream density $\rho = 2.29 \times 10^{-6}$ kg m^{-3}. The orbital velocity used is the circular orbital speed used throughout the $Kn = 0.1$ results: $V = 7850$ m s^{-1}. The products of the aerodynamic coefficients and the flow-facing areas are calculated as described in Section 3.2. Figure 3.38 shows C_DA and C_LA calculated for all models and orientations for $Kn = 0.1$ experienced by the TBEx body.

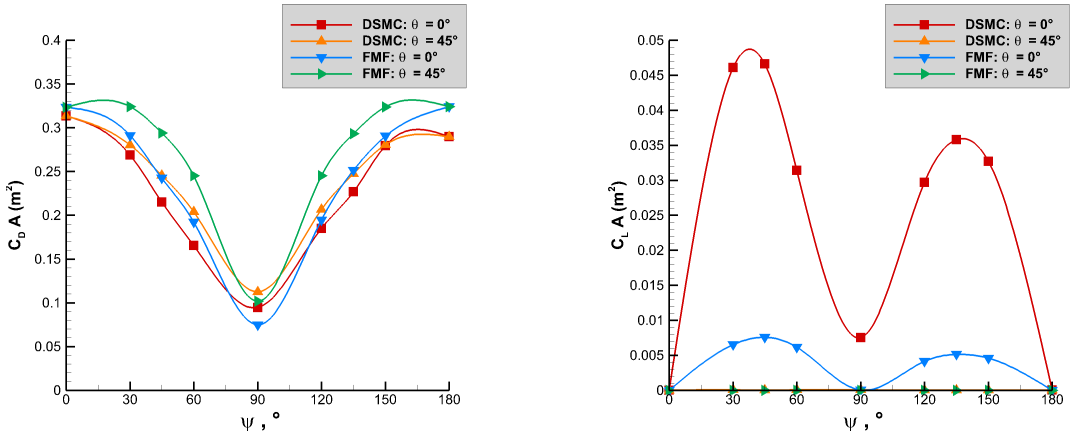

(a) (b)

Figure 3.38: Drag (a) and lift (b) coefficients calculated using DSMC and free-molecular (FMF) analytical models for all experiment orientations of the TBEx using both models for a Knudsen number of 0.1.

The average C_DA calculated using the DSMC MONACO modeling results is $2.23 \times 10^{-1} \pm 1.78 \times 10^{-4}$ m^2, while the average C_DA calculated using the free-molecular analytical modeling

results is 2.45×10^{-1} m^2. The percent difference between the averages is 13.9%. The normalized root-mean-square deviance between all the C_DA results across both models is 12.0%. The average C_LA calculated using the DSMC MONACO modeling results is $1.28\times10^{-2}\pm1.00\times10^{-5}$ m^2, while the average C_LA calculated using the free-molecular analytical modeling results is 1.87×10^{-3} m^2. The normalized root-mean-square deviation between all the C_LA results across both models is 39.6%. The normalized root-mean-square deviations and percent differences are growing as the Knudsen number decreases (see Sections 3.2, 3.3, **??**). Again, collisions matter in this flow regime, causing the free-molecular collisionless assumption to break down, making the free-molecular results less and less accurate.

3.5.2 $Kn = 0.1$: Moments and Angular Accelerations

The moments are taken about the TBEx body centroid as discussed in Section 3.2.2. The angular acceleration error again equates to: 2.73×10^{-5} radians s^{-2}, or 1.57×10^{-3} degrees s^{-2}.

Figure 3.39 displays the moment results yielded by both models across all the TBEx body orientations about the three primary axes. Figure 3.39 mirrors the results seen in Figures 3.25, 3.18, and 3.25, but at a larger scale, proportional to the larger forces induced on the body in less-rarefied flow at a higher orbital speed. As in Section 3.2, the aerodynamic moments about the Z-axis are smaller than those about the X- and Y-axes by three orders of magnitude due to the rotational near-symmetry of the TBEx about the Z-axis.

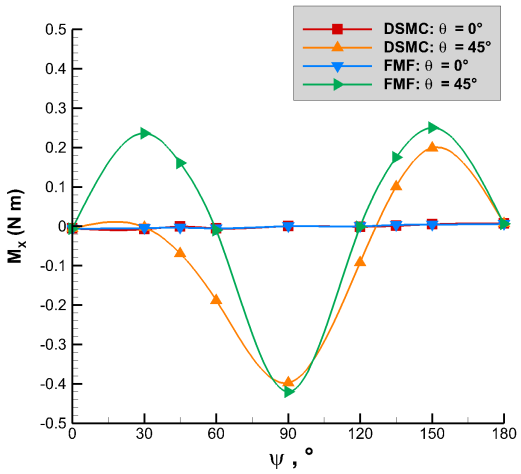

(a)

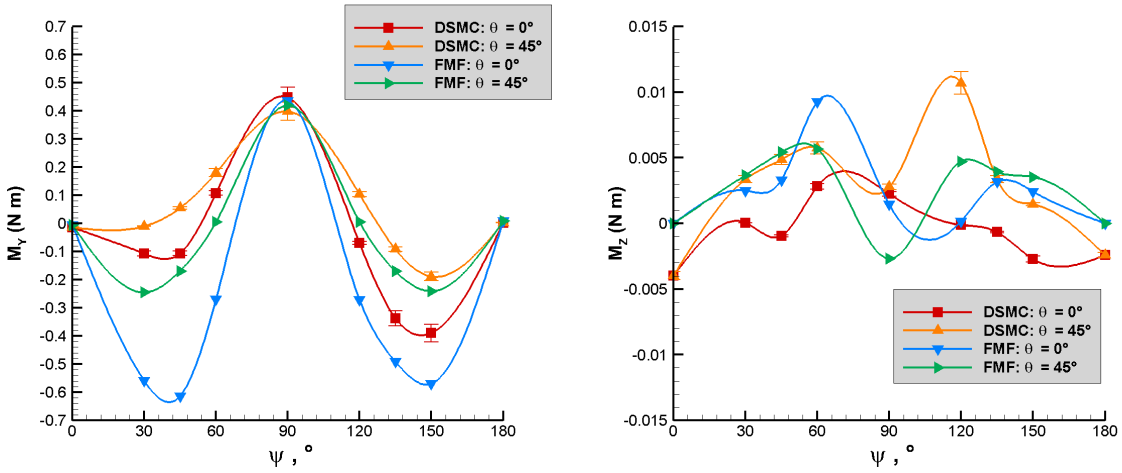

(b) (c)

Figure 3.39: Moments calculated using DSMC and free-molecular (FMF) analytical models for all experiment orientations of the TBEx about the: (a) X axis; (b) Y axis; (c) Z axis, for a Knudsen number of 0.1.

As seen in Figure 3.39 (a), the aerodynamic moments about the X-axis are incurred when the θ value of the simulation is $45°$, due to the phenomena discussed in Section 3.2.

In Figure 3.39 (b), Y-moments are induced across both θ values. The same maxima and minima ψ values occur as in Section 3.2, for the same reasons. However, for both the X- and Y-moments

in Figure 3.39, a larger qualitative discrepancy can be seen between the free-molecular and DSMC results when compared to Figures 3.18, 3.25, and 3.32.

The moment averages are sensitive due to the small magnitudes of the moment results and the sign changes as ψ changes about the Z-axis. In order to compare the free-molecular and DSMC modeling approaches effectively, averages are taken according to θ value and are listed in Table 3.10.

Table 3.10 portrays that the free-molecular and DSMC modeling approaches exhibit larger differences for this Knudsen number as compared to Tables 3.7, 3.8, and 3.9 for Knudsen numbers of 100, 10, and 1, respectively. The sign differences between the DSMC and free-molecular results for the X- and Y- moments in Table 3.9, $\theta = 45^\circ$ are due to the free-molecular results producing more-negative minima in the Y-moment, and more-positive maxima in the X-moments. Since the moments center around zero, these maxima and minima can pull the averages towards the negative or positive side of zero.

Table 3.10: Average moments calculated for a Knudsen number of 0.1 for the DSMC and free-molecular analytical modeling approaches for both θ values.

Average	θ **= 0°**		θ **= 45°**	
	FMF	**DSMC**	**FMF**	**DSMC**
$\mathbf{M}_X$ **(N m)**	-7.15×10^{-4}	-8.99×10^{-4} $\pm 7.19 \times 10^{-7}$	1.73×10^{-2}	-7.39×10^{-2} $\pm 5.90 \times 10^{-5}$
$\mathbf{M}_Y$ **(N m)**	-2.28×10^{-1}	-2.07×10^{-2} $\pm 1.70 \times 10^{-5}$	-1.73×10^{-2}	7.30×10^{-2} $\pm 5.84 \times 10^{-5}$
$\mathbf{M}_Z$ **(N m)**	2.58×10^{-3}	-2.88×10^{-4} $\pm 2.30 \times 10^{-7}$	2.54×10^{-3}	3.27×10^{-3} $\pm 2.62 \times 10^{-6}$

The normalized root-mean-square deviations between the moments again use the range of the DSMC results to normalized to address the exacerbated error caused by the near-zero free-molecular results. The normalized root-mean-square deviation between the X-axes moments is

15.7%. The normalized root-mean-square deviation between the Y-axes moments is 26.0%. The normalized root-mean-square deviation between the Z-axes moments is 23.9%. The normalized root-mean-square deviations have increased by over 5% from a Knudsen number of 1; and by over 10% from a Knudsen number of 100. These increased differences confirm the fact that the free-molecular modeling approach is not accurate for this regime.

The moments incurred about the Y-axis are the largest and are non-zero for the DSMC and free-molecular models for both θ values, therefore this angular acceleration is examined. Figure 3.40 shows the calculated angular acceleration about the Y-axis for the TBEx body using both models across all orientations, with error bars as described in Section 3.2. The interpolated average angular accelerations about the Y-axis are $1.22 \times 10^{-1} \pm 9.76 \times 10^{-5}$ degrees s^2 using the DSMC method and -5.73×10^{-1} degrees s^2 using the free-molecular analytical method. These averages reflect what Figure 3.40 shows qualitatively: the free-molecular results yield more extreme minima than the DSMC results. This is due to the diffusive effect of the DSMC particle method on surface properties, as discussed in Section 3.2. The diffusive factor as well as the importance of flowfield collisions is causing the DSMC results to differ more from the free-molecular results in this regime. The normalized root-mean-square deviation between the angular accelerations about the Y-axis is 26.0%.

Comparing Figures 3.19, 3.26, 3.33, and 3.40, it is clear that the effect of the uncertainty of the angular velocity of the TBEx impacts results less as Knudsen number decreases. Moments and forces are larger as flowfield density increases. Intuitively, it can be assumed that as the TBEx descends in altitude, the angular velocity will increase due to these aerodynamic moments, and tumbling will occur more rapidly in lower altitudes.

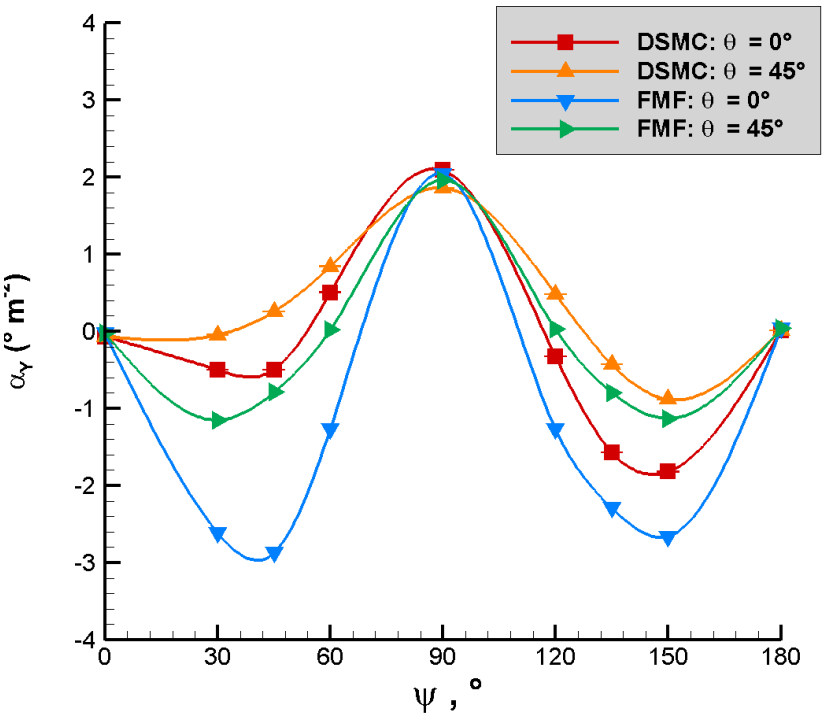

Figure 3.40: Angular acceleration about the Y-axis calculated using DSMC and free-molecular (FMF) analytical models for all experiment orientations of the TBEx, for a Knudsen number of 0.1. Error bars reflect the angular velocity uncertainty of 1.57×10^{-3} degrees s^{-2}.

3.6 Orbital Decay Analyses

The orbital decay model developed in Section 2.3 is applied to the interpolated coefficients of drag and lift ($C_D A$ and $C_L A$) to analyze the impact of the model used; as well as the impact of addressing tumbling motion on lifetime predictions. The aerodynamic coefficients, as before, are calculated across the entire projected TBEx body accounting for all variations of θ and ψ.

In order to project realistic orbital decay, the tumbling of the TBEx is assumed, and the average $C_D A$ and $C_L A$ values discussed in Sections 3.2-3.5 are used. To measure how the tumbling assumption affects the orbital decay, two different sets of aerodynamic coefficients are used: the

interpolated average coefficients, and the $\theta = 0°$, $\psi = 0°$ (Orientation #1) coefficient results. These results are representative of a typical approach to estimating aerodynamic coefficients, with only one flow-facing area used. This method was used to estimate the TBEx experiment orbital lifetimes prior to launch, as discussed in Section 2.3.5.2. The estimated C_DA was 2.32. The maximum projected area, corresponding to an orientation of $\theta = 0°$, $\psi = 0°$ (Orientation #1), is 0.13 m^2. This yields an estimated C_DA of 3.02×10^{-1} m^2. The minimum projected area, corresponding to an orientation of $\theta = 0°$, $\psi = 90°$ (Orientation #5), is 3.56×10^{-2} m^2. This yields an estimated C_DA of 8.25×10^{-2} m^2.

Though the TBEx has an elliptical mission orbit of about 850 km by 300 km, the orbital decay comparisons in this work are projected to an altitude of 147 km, or a Knudsen number of 10 for the TBEx. This is an appropriate assumption to make because as orbits degrade over time they become more and more circular, therefore experiencing such an orbit is highly probable for the TBEx once it experiences the prerequisite orbital decay. The initial orbit is a circular orbit with an altitude of 147 km and angular orbital elements (Ω, i, and ω_p) of 0°.

Table 3.11 contains the weighted average coefficients and the $\theta = 0°$, $\psi = 0°$ coefficients yielded from each modeling approach at each altitude used to model the TBEx's orbital decay. Statistical error is not included in Table 3.11 because it very small, and is not included in the orbital decay projections.

The coefficients of drag and lift are interpolated to yield coefficients experienced throughout the TBEx's orbital decay. The DSMC averaged and $\theta = 0°$, $\psi = 0°$ results are fitted using a quadratic. Linear interpolations are used for all other modeling modes. Figure 3.41 plots the drag coefficients used to estimate orbital lifetime pre-launch of the TBEx experiment from [7], drag coefficients listed in Table 3.11, and the interpolated fits of each of the drag coefficients, across the

Table 3.11: Coefficients of lift and drag, resulting from the DSMC and FMF modeling approaches, used to project orbital decay of the TBEx.

Average Coefficients					
		DSMC		**FMF**	
Kn	**Alt (km)**	C_DA **(m^2)**	C_LA **(m^2)**	C_DA **(m^2)**	C_LA **(m^2)**
100	147	2.50×10^{-1}	2.34×10^{-3}	2.46×10^{-1}	2.24×10^{-3}
10	119	2.44×10^{-1}	3.27×10^{-3}	2.46×10^{-1}	2.03×10^{-3}
1	104	2.33×10^{-1}	7.28×10^{-3}	2.45×10^{-1}	1.91×10^{-3}
0.1	91	2.23×10^{-1}	1.28×10^{-2}	2.45×10^{-1}	1.87×10^{-3}
$\theta = 0^\circ, \psi = 0^\circ$ **Coefficients**					
		DSMC		**FMF**	
Kn	**Alt (km)**	C_DA **(m^2)**	C_LA **(m^2)**	C_DA **(m^2)**	C_LA **(m^2)**
100	147	3.25×10^{-1}	2.79×10^{-6}	3.25×10^{-1}	9.67×10^{-7}
10	119	3.20×10^{-1}	6.60×10^{-5}	3.25×10^{-1}	1.19×10^{-7}
1	104	3.15×10^{-1}	7.26×10^{-5}	3.23×10^{-1}	9.06×10^{-8}
0.1	91	3.14×10^{-1}	9.17×10^{-6}	3.23×10^{-1}	1.00×10^{-7}

altitudes experienced in the modeled orbital decay. The flight data drag coefficients are multiplied by the respective minimum and maximum projected areas, as discussed previously.

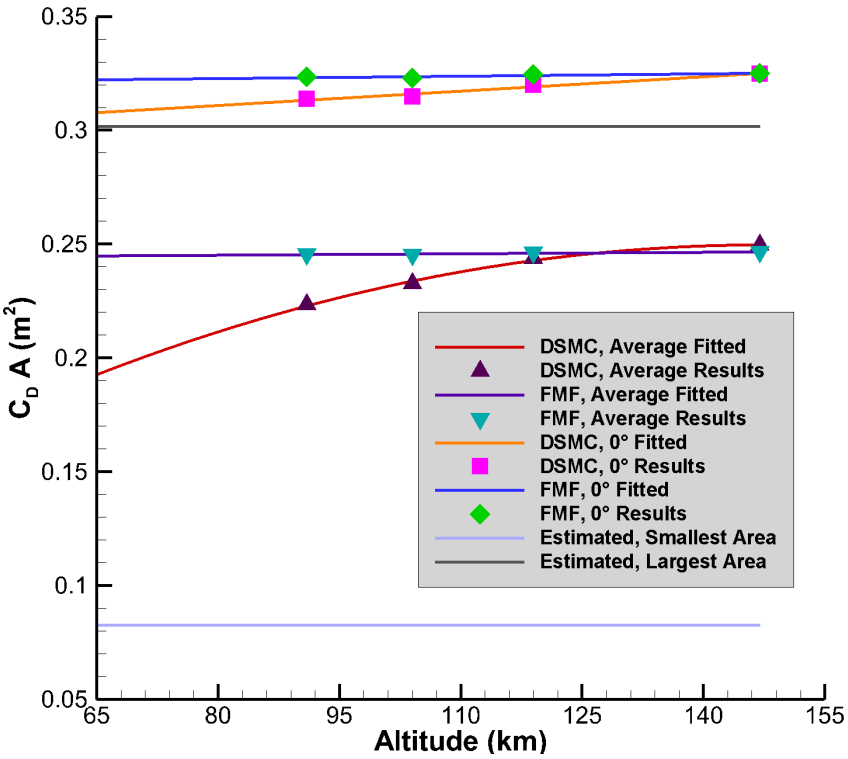

Figure 3.41: The drag coefficients used to estimate the orbital lifetime of the TBEx experiment pre-launch from [7], plotted with the weighted drag coefficient results and the $\theta = 0°$, $\psi = 0°$ drag coefficient results from both the free-molecular and DSMC approaches across the orbital decay altitudes modeled.

Figure 3.41 displays that the estimated drag coefficient using the largest area agrees with the modeled $\theta = 0°$, $\psi = 0°$ coefficients for both the DSMC and free-molecular models, as expected. The averaged drag coefficients are lower. There is excellent visual agreement between the DSMC and free-molecular models at 147 km ($Kn = 100$), good agreement at 119 km ($Kn = 10$), and weakening agreement at lower altitudes. The DSMC coefficient of drag results decrease with altitude; while the free-molecular results stay consistent across altitude. The DSMC results decreasing with altitude reflect that the "Mach" number of the TBEx is increasing as altitude decreases, the TBEx gains speed, and the temperature drops as the TBEx exits the thermosphere [30]. Though the thermosphere is not assumed dense enough to exhibit a true speed of sound, effects of an in-

creasing Mach can be seen in the flowfields as the Knudsen number drops: shocks begin to form around $Kn = 0.1$. It is known that above a critical Mach number, drag coefficient decreases; therefore as the TBEx travels through atmosphere dense enough to form a shock in front of the body and continues to speed up, the drag coefficient is expected to decrease [31]. In addition, there is published work establishing the decrease of coefficient of drag as altitude decreases, so the DSMC modeling results reflect this phenomenon [32]. The free-molecular analytical model applies the same assumptions to all the altitudes, increasing the drag as density increases, and not accounting for the atmosphere particles forming a shock in front of the body. Therefore the free-molecular analytical results are expected to be consistent for drag coefficient which is normalized by flow density.

The estimated smallest area drag coefficient is much lower than the average or $\theta = 0°$, $\psi = 0°$ drag coefficients. Any orientation change from the minimum flow facing-area increases the drag by a large amount due to the prescience of the solar panels which would experience direct pressure.

Figure 3.42 plots the lift coefficients listed in Table 3.11, and the linear interpolations of the lift coefficients, across the altitudes experienced in the modeled orbital decay. The lift coefficients were not estimated pre-launch of the TBEx experiment, as lift is usually assumed as zero for satellites in LEO.

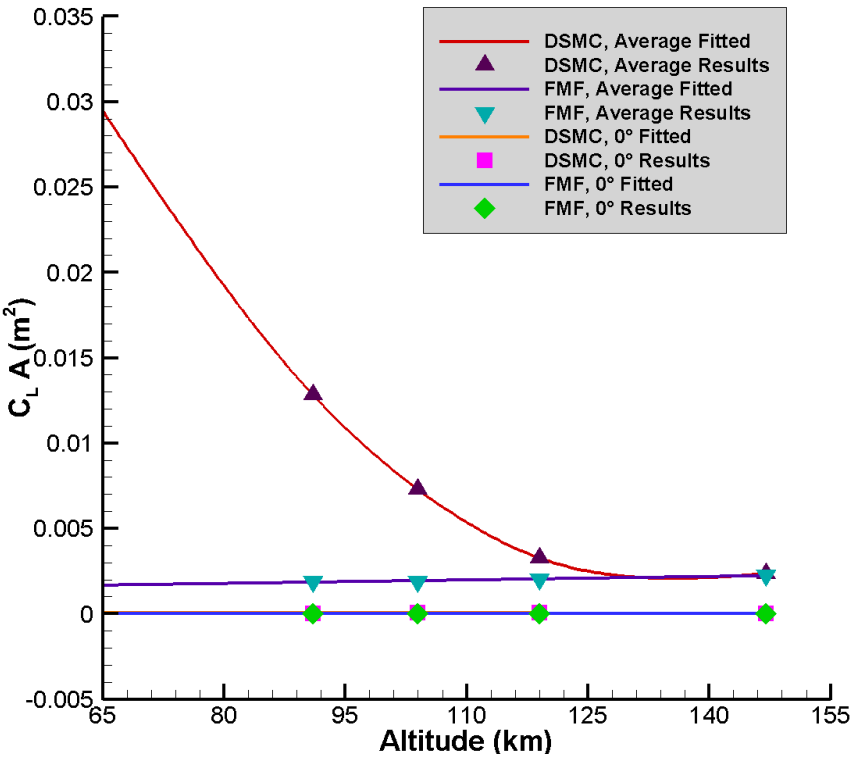

Figure 3.42: The average lift coefficient results and the $\theta = 0°$, $\psi = 0°$ lift coefficient results from both the free-molecular and DSMC approaches across the orbital decay altitudes modeled; and the linear interpolations of each set of coefficients.

Figure 3.42 is useful to contextualize how the models differ, and how the approach to rotational motion yields different lift values. Using average $C_L A$ values increases the lift coefficients, as differing orientations will incur slight pressure gradients in the lift direction. The $\theta = 0°$, $\psi = 0°$ results are very near-zero as enumerated in Table 3.6, and match relatively well across all Knudsen numbers. The average lift coefficients are matched excellently at 147 km ($Kn = 100$) and well at 119 km ($Kn = 10$) in Figure 3.42. As altitude decreases, the DSMC model yields the appropriate backflow by following the particles, and generates higher lift. The free-molecular results stay consistent and near-zero regardless of altitude. Therefore there is disagreement between the models by 104 km, of $Kn = 1$, and the disagreement grows as the altitude and Knudsen number decrease further.

Figure 3.43 displays the orbital decay from the starting altitude of 147 km ($Kn = 10$), projected using the linearly interpolated coefficients for each model according to the current altitude; and the constant pre-launch drag coefficient estimates for the minimum and maximum areas. Qualitatively, Figure 3.43 shows that the $\theta = 0°$, $\psi = 0°$ results for the free-molecular and DSMC approaches match relatively well, and both match with the orbital decay using the pre-launch estimated largest area drag coefficient for the TBEx. The orbital decay using the free-molecular and DSMC averages diverge quite a bit from the $\theta = 0°$, $\psi = 0°$ orbital decay; and there is separation between the free-molecular and DSMC orbital decay using the coefficient averages as the altitude lowers. The orbital decay using the pre-launch estimated smallest area is vastly different from all other modeling modes, and is an effective outlier.

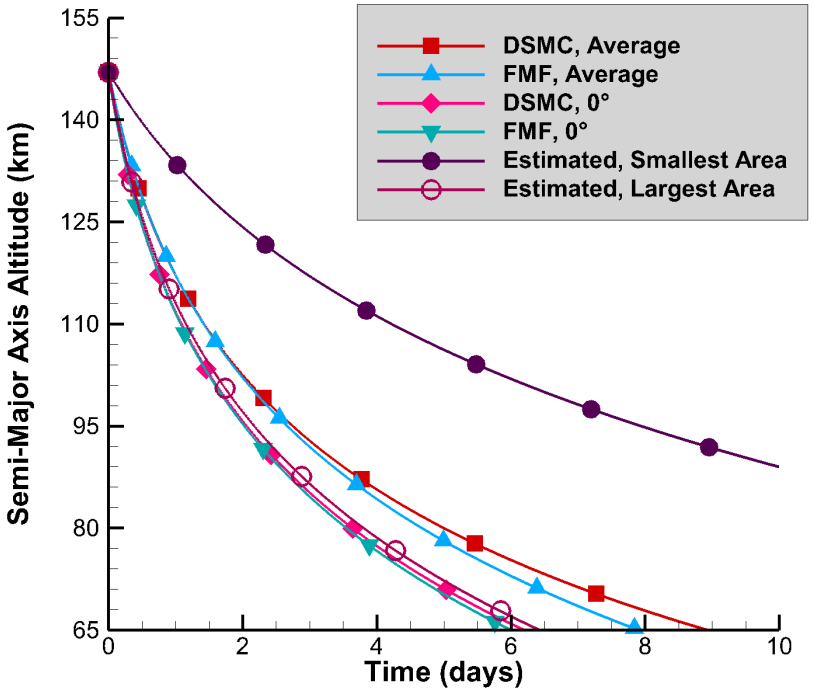

Figure 3.43: Orbital decay estimated from an altitude corresponding to $Kn = 10$ using the pre-launch estimates for drag coefficient; and the average drag and lift coefficients and $\theta = 0°$, $\psi = 0°$ drag and lift coefficients from both the free-molecular and DSMC results.

The orbital decay model is run until the TBEx achieves an altitude of 65 km for all modeling modes. Table 3.12 displays the time the TBEx takes to achieve 65 km of altitude using each modeling approach (DSMC; free-molecular; and pre-launch estimates) and each orientation scheme (averages for both coefficients, or $\theta = 0°$, $\psi = 0°$ coefficients only). Table 3.13 contains the root-mean-square differences over the orbital decay and the percent deviation in time-to-reenter between all modeling modes.

Table 3.12: Time for the TBEx to achieve reentry altitude (or time-to-reenter) according to each modeling mode.

Modeling Mode	**Time-to-Reenter (days)**
DSMC, Averages	8.94
DSMC, $\theta = 0°$**,** $\psi = 0°$	6.20
FMF, Averages	7.91
FMF, $\theta = 0°$**,** $\psi = 0°$	6.01
Estimated, Largest Area	6.42
Estimated, Smallest Area	23.5

Table 3.13: Root-mean-square differences, in kilometers, over the TBEx orbital decay, and time-to-reenter deviation between models and tumbling approaches and estimated pre-flight drag coefficients..

Root-Mean-Square Differences Over Orbital Decay				
	DSMC, Averages	**DSMC,** $\theta, \psi = 0°$	**FMF, Averages**	**FMF,** $\theta, \psi = 0°$
DSMC, Averages	-	7.44 km	1.73 km	-
FMF, Averages	1.73 km	-	-	6.89 km
Est. Large Area	6.36 km	1.21 km	5.16 km	1.79 km
Est. Small Area	24.0 km	30.1 km	25.1 km	30.4 km
Time-to-Reenter Deviations				
	DSMC, Averages	**DSMC,** $\theta, \psi = 0°$	**FMF, Averages**	**FMF,** $\theta, \psi = 0°$
DSMC, Averages	-	30.7%	11.5%	-
FMF, Averages	11.5%	-	-	24.0%
Est. Large Area	28.1%	3.64%	18.8%	6.87%
Est. Small Area	61.0%	73.6%	66.4%	74.4%

The choice of using average coefficients about different body orientations affects the orbital decay predictions more than the choice of model, but both choices have consequences when mod-

eling orbital decay. There is a day or less time-to-reenter difference between the free-molecular and DSMC approaches applied to the orbital decay. The free-molecular drag coefficients are elevated across lower altitudes and produce more rapid orbital decay. There is about a two day difference between the $\theta = 0°$, $\psi = 0°$ stagnant approach versus the average, accounting for rotational motion, approach applied to either model's coefficients used in the orbital decay model. When using the minimum area stagnant approach, there is a difference in reentry prediction of over two weeks! This indicates that in order to have a realistic picture of decay, more than one orientation should be taken into account.

A concern with reentering space debris is safety: if large debris reenters, pieces do survive and impact the Earth, posing a threat to people and property. Knowing impact locations is also important for spacecraft intended for reuse [33]. Small changes in predicting reentry time changes projected debris impact by a large amount. If reentry projections are off by one minute, impact location can change by as much as 480 km [34]. A simple transformation of the information on time-to-reenter differences in Table 3.12 using the average rotation of the Earth ($4.18 \times 10^{-3} \circ \text{s}^{-1}$) yields an estimate in differences in ground footprint projection of impact: these differences are up to 600,000 km. Large differences in impact location are projected because a small change in time-to-reenter involves differences of many orbits around the Earth. This highlights the importance of choosing accurate aerodynamic coefficients in projecting orbital lifetimes. In order to measure these differences in a more precise way, more accurate orbital decay modeling will need to be used with the aerodynamic coefficients, but this gives a general idea of how large differences in orbital lifetimes impact reentry crash landing predictions.

3.7 TBEx: Summary and Conclusions

In this chapter, the TBEx body was used to compare force and moment results across the free-molecular and the DSMC models for four Knudsen numbers: 100, 10, 1, and 0.1. These Knudsen numbers represent different flow regimes from very free-molecular ($Kn = 100$) to transitional flow ($Kn = 0.1$). Coefficients of drag and lift calculated using both modeling approaches were interpolated over and used to compare how the choice of model affects orbital lifetime predictions. The orbital decay predictions using free-molecular calculated aerodynamic coefficients differed from those using the DSMC-calculated aerodynamic coefficients by about 12%.

Table 3.14 enumerates the normalized root-mean-square deviations between the models for the calculated drag, lift, and y-moments. The lift and Y-moment errors are elevated due to the Y-moment averages being relatively close to zero, but are included as a comparison metric to track how differences in aerodynamic rotational motion increase as Knudsen number decreases. There is also an expectation that because of lift being a summation between conflicting directional surface elements of pressure and shear stress, errors in the calculations are magnified; this phenomenon is examined in close detail in Chapters 4 and 5. Table 3.14 shows that for free-molecular Knudsen numbers; the differences between the DSMC and free-molecular results for drag and Y-moment are small. This indicates that the free-molecular model performs consistently well for free-molecular Knudsen numbers. However, the lift error is nearly a factor of 10 worse for $Kn = 10$. Lift is very small for satellites and differences are not expected to lead to much effect on orbital decay. The lift error increasing is the only recognizable difference for $Kn = 10$ indicating that the flow has become more dense at this altitude; only a few particle collisions with certain surface elements can produce a big difference in a small value like lift. All the errors are larger for $Kn = 1$, and become

more significant once $Kn = 0.1$ is achieved.

Table 3.14: Normalized root-mean-square deviations between the free-molecular and DSMC results for the TBEx across all orientations for each Knudsen number for drag, lift, and Y-moments.

	Force or Moment Compared		
Knudsen Number	**Drag**	**Lift**	**Y-Moment**
100	2.23%	3.22%	9.65%
10	2.75%	25.0%	9.45%
1	7.07%	32.2%	14.0%
0.1	12.1%	39.6%	26.0%

Table 3.15 lists the average core-hours required to run each model for one orientation at each Knudsen number, and the total core-hours to run all 16 simulations for every orientation of the TBEx at each Knudsen number. The free-molecular model's computational cost scales with the number of surface elements in the mesh used due to the blocking algorithm it employs. The DSMC core-hours are dependent on several factors, such as: the mesh size and the number of particles used as well as the time step, and number of time steps in the simulation.

Table 3.15: Average computational cost in core-hours for one simulation and total core-hours for simulating all 16 orientations of the TBEx using each model at each Knudsen number.

	C-Hs for One Simulation		**C-Hs for all orientations simulated**	
Knudsen Number	**FMF**	**DSMC**	**FMF**	**DSMC**
100	1.6×10^{-1}	35	2.6	570
10	1.5×10^{-1}	31	2.5	490
1	1.6×10^{-1}	32	2.6	520
0.1	1.6×10^{-1}	36	2.5	570

Tables 3.14 and 3.15 together lead to interesting conclusions about where the use of each model is appropriate. For a Knudsen number of 100, the free-molecular model saves hundreds of core-hours over simulating 16 orientations of the TBEx; and the drag calculated using the free-molecular model agrees with the DSMC results within 3%. The lift and Y-moment free-molecular results are within 10% of the DSMC results at this Knudsen number as well, indicating good agreement for

relatively small values of lift and moments about the Y-axis. At this Knudsen number, over 200 free-molecular orientations can be run for the cost of one DSMC simulation. This indicates that at Knudsen numbers of 100 and higher, the free-molecular model is desirable to determine drag, and perhaps other forces and moments, in order to save computational cost; especially for bodies where rotational motion is of interest. In addition, due to the low cost of the free-molecular model and the differences in modeling the orbital decay with a constant estimate of coefficient of drag versus an averaged coefficient that accounts for the tumbling motion of a small satellite, it is worth it to conduct several free-molecular analytical simulations on small satellites in high-altitude orbit in order to obtain a realistic picture of induced drag.

The same is true for a Knudsen number of 10: the cost is low; and the drag is very accurate. The only reason to pursue DSMC simulations at this Knudsen number is if very precise lift is necessary; otherwise, free-molecular modeling is recommended.

For a Knudsen number of 1, the errors are more elevated, with free-molecular drag now only within 10% of DSMC drag. The free-molecular Y-moment is accurate to the DSMC Y-moment to about 15%. This indicates that for very accurate lift or moment information, DSMC should be used at a Knudsen number of 1. However, because the free-molecular computational cost is so much lower than the DSMC computational cost at this Knudsen number, it may be desirable to run preliminary free-molecular analyses to get an idea of drag, lift, and moments, before conducting costly DSMC simulations.

When the Knudsen number drops to and below 0.1, the free-molecular model becomes much less accurate. The free-molecular drag differs from the DSMC drag by 12%, indicating that for accurate drag, DSMC must be used.

The orbital decay results reinforce these ideas of where the free-molecular modeling is ap-

propriate. The orbital decay results also reveal that the differences in projected orbital decay and impact are large when tumbling motion is accounted for versus a constant flow-facing area approach to the aerodynamic forces. Accounting for tumbling led to differences in time-to-reenter of about 2 days for both the free-molecular and DSMC approaches. For satellites in LEO, known to have tumbling motion along their orbits, these results indicate that rotational motion should be accounted for when estimating drag in mission planning.

CHAPTER 4

Analysis of the REBR Capsule

REBR is the Reentry Breakup Recorder, a device developed by the Aerospace Corporation in the early 2000s, for the purposes of capturing data during the reentry and breakup phases of a satellite [15]. Reentry data is important in order to obtain a better understanding of potential hazards to people and property that reentering large space debris poses [15]. One launch of the REBR was successfully flight-tested and returned data collected throughout reentry: this REBR was attached to the Japanese HTV2 supply vehicle, ejected from the International Space Station (ISS) in 2011 [10].

REBR is a small, aerodynamically stable device that records data related to the reentry of space debris, such as temperature, acceleration, and rotational rate. REBR is designed to release from a larger host vehicle during its breakup process, aerodynamically stabilize, and uplink recorded data to the Iridium network for downlink to a ground station. Recovery of the REBR vehicle is not required due to the data transmission [10].

The REBR body is chosen for analysis because of existing data from the launch of REBR attached to HTV2 in 2011, and due to the fact that the design of REBR resembles many prevalent reentry vehicle designs. REBR refers to the experimental body used for this research.

The REBR shape is based on the NASA Mars Microprobe, and resembles many typical reentry

vehicle designs. It uses a $45°$-angled forebody with a spherical segment aftbody with a maximum diameter of 0.31 m and a maximum length of 0.25 m. Figure 4.1 displays the outline of the REBR. Figure 4.2 is a photograph of the REBR used in the HTV2 successful launch.

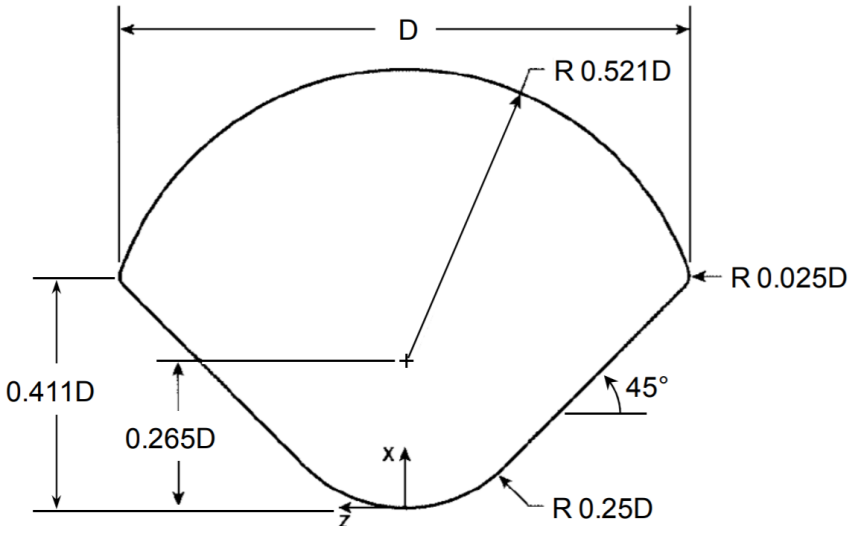

Figure 4.1: REBR diagram. For the launched REBR attached to HTV2, D $= 0.310$ m, from [10].

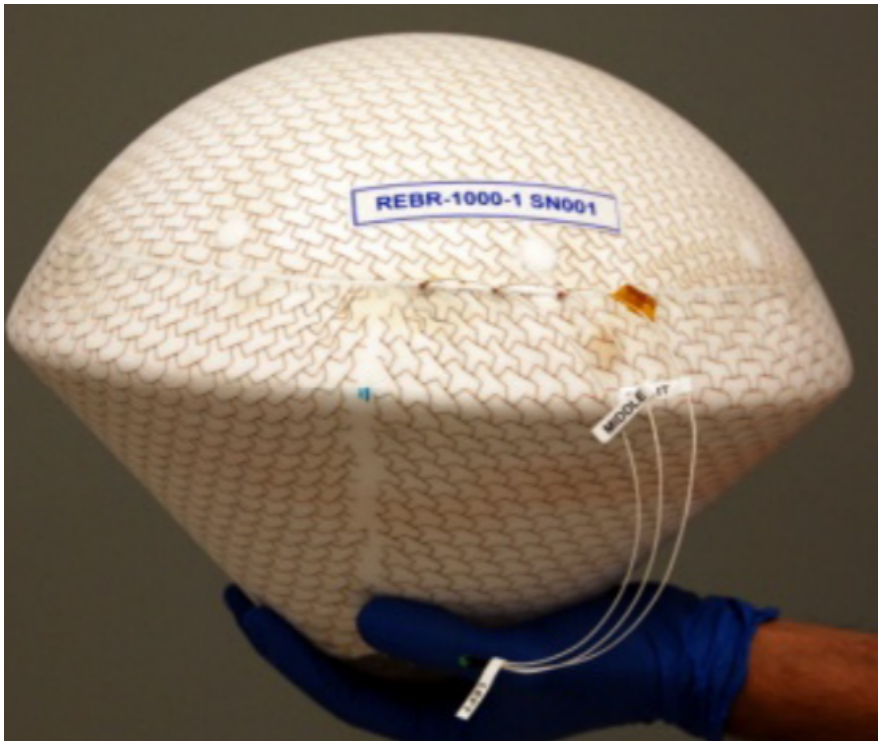

Figure 4.2: Photo of REBR used on HTV2 reentry in 2011, from [10].

4.1 REBR Body Experiment Design

In order to replicate the launched REBR shape for use with MONACO at different altitudes and the free molecular model, meshes are generated using Pointwise. Different meshes are generated to use with MONACO in order to refine the length of cells on the body to less than the local mean free path. The parameters of the different meshes used are described in the sections below.

In meshing a representation of the body, the symmetrical nature of the REBR is taken advantage of to reduce the computational cost. The REBR is symmetrical about the longitudinal axis which is assigned as the Z-axis in meshing the body. Therefore, the body is divided, and the X-Z plane is declared as a plane of symmetry in MONACO simulations. Assuming symmetry about the X-Z plane does implicate that any moments that would turn the vehicle out of this plane are not significant. When examining the turning rates, the turning rate about the symmetrical, longitudinal, or Z-axis represents the motion of spinning like a top. The moment about the normal to the symmetrical axis, the latitudinal, or the Y-axis, changes the total angle of attack of the body. Therefore, assuming symmetry about the X-Z plane does allow for thorough examination of the normal axis, which is the moment that changes the flow-facing area of the body. Figure 4.3 shows the mesh representation of the REBR.

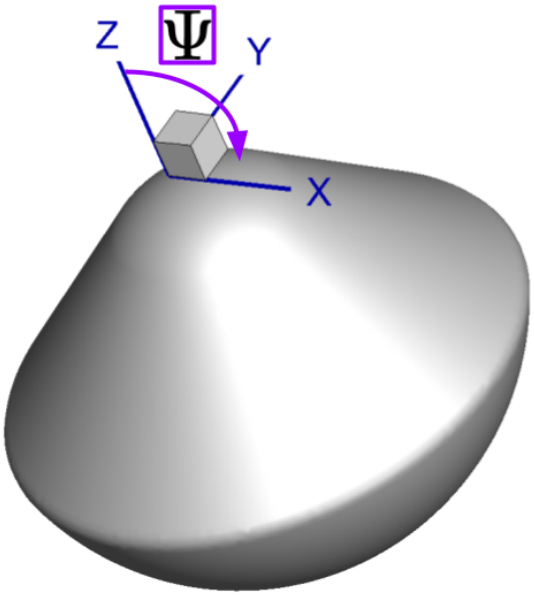

Figure 4.3: The REBR body as used for mesh representation. Axis represent the body axes used and show the X-Z plane used as the plane of symmetry. Ψ is the angle projected from the positive Z-axis in the X-Z plane of symmetry used in this work.

One primary goal of this thesis is to establish Knudsen numbers where a free molecular analytical approach to gathering aerodynamic force and moment information is no longer acceptable for desired accuracy. In order to evaluate the effect of Knudsen number on model results, altitudes must be chosen where there is a marked difference in Knudsen number as the flow regime moves from free molecular to transitional and even into continuum for any body tested. The REBR launched with HTV2 in 2011 achieved a trajectory of reentry beginning at just under 80 km, reentering within a half-hour and impacting the Earth. The reconstructed trajectory of the successful launch of the REBR is plotted in Figure 4.4, along with the Knudsen number of the REBR versus altitude [10]. The Knudsen numbers in Figure 4.4 are calculated using the U.S. Standard Atmosphere from 1976 estimates for mean free path [12]. The characteristic length used for calculating the Knudsen numbers is the average between the maximum diameter and length: $L = 0.28$ m. An average characteristic length is used to account for the REBR's changing orientations in projected

orbits due to any tumbling motions.

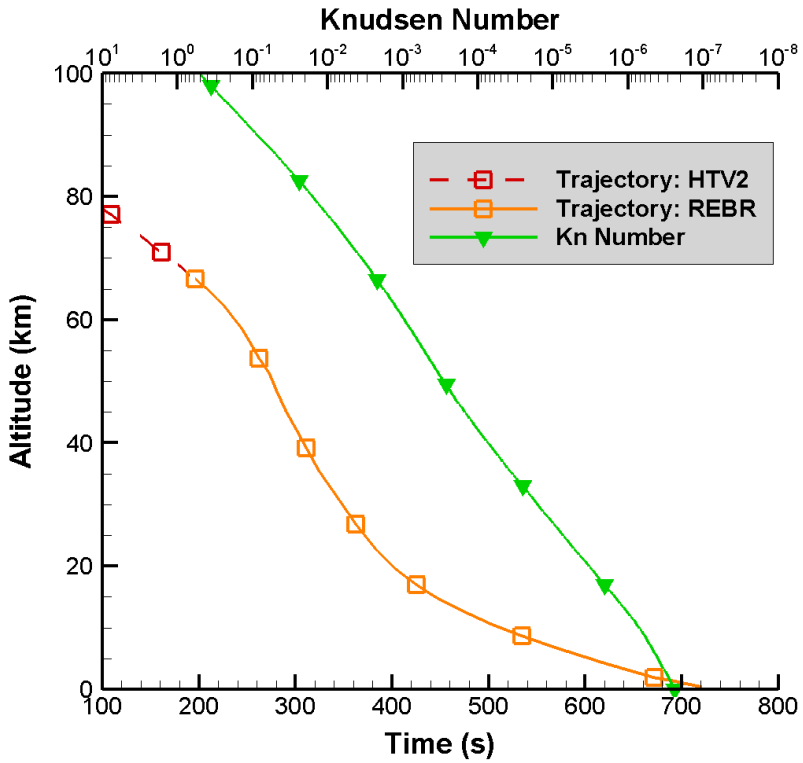

Figure 4.4: Reconstructed reentry trajectory of the HTV2 and REBR after separation from the HTV2 [10] plotted against the Knudsen number of the REBR body over altitude.

Examining Figure 4.4, along its trajectory, the REBR experiences only very dense transitional and continuum flow ($Kn \leq 0.01$). However, this thesis work is concerned with comparing modeling approaches at rarefied regimes. Some reentry capsules are designed for higher-altitude injections in order to gather more data on reentry processes [15], and several real reentry capsules, such as NASA's Orion and SpaceX's Dragon, are designed to enter from orbital altitudes [35] [33]. Therefore, the REBR trajectory is projected to higher altitudes in order to test both the DSMC and free-molecular models performance on the REBR shape.

The REBR's small size and symmetry allow for extreme surface cell refinement. The minimum average surface element size length used is 2.5×10^{-4} m. At an altitude of 77 km, the free-stream

mean free path is 2.8×10^{-3} m; compression by a factor of 10 yields the local mean free path near the body surface of 2.8×10^{-4} m. The Knudsen number of the REBR at the altitude of 77 km is 0.01, which is the limit between transitional and continuum flow. Knudsen numbers chosen for study for the REBR are: 0.01, 0.1, 1, and 10. A Knudsen number of 10 is chosen as the "control" case, as free molecular analytical approaches are expected to yield accurate (and therefore matching DSMC results) results in this regime.

Atmospheric composition is an important factor for achieving accurate results. The atmospheric composition modeled on the REBR is the same as that for the TBEx, described in Chapter 3. Figure 3.6 displays the neutral atmosphere composition from [9]. Based on molar composition, the primary atmospheric constituents are used to compose the flowfield for both models.

The atmospheric properties of each of the chosen altitudes are listed in Table 4.1. The REBR body experiences the same Knudsen number altitudes as the TBEx for $Kn = 10$, 1, and 0.1, because their characteristic lengths are similar (see Table 3.1). At the altitudes used in modeling the REBR, the orbit would be decayed to the point of becoming circular [6]. The orbital speed, V, is then calculated using a circular orbit assumption. Monatomic oxygen is not used at lower altitudes where its mole fraction falls below 1×10^{-6}. In Table 4.1, "Alt" refers to altitude of the satellite's orbit.

Table 4.1: Atmospheric properties for the REBR conditions analyzed [9] [12].

				Number Density (m^{-3})			
Kn	**Alt (km)**	**V ($m\ s^{-1}$)**	**T (K)**	**N_2**	**O_2**	**O**	**Ar**
10	119	7830	384	2.94×10^{17}	4.18×10^{16}	7.95×10^{16}	1.53×10^{15}
1	104	7840	200	3.44×10^{18}	6.92×10^{17}	3.24×10^{17}	3.20×10^{16}
0.1	91	7850	187	3.80×10^{19}	9.15×10^{18}	2.81×10^{17}	4.40×10^{17}
0.01	77	7860	215	3.33×10^{20}	8.59×10^{19}	-	3.97×10^{18}

To narrow the scope of this thesis work, wall temperature for the body of the REBR is assigned

to be 300 K, as in Chapter 3 for the TBEx. Similarly, the accommodation coefficient used to model the REBR is $\alpha = 1$, simulating fully diffuse reflections of particles impacting the REBR surface. One application of future work is comparison of models using differing accommodation coefficients and surface temperatures.

To understand the effect tumbling has on the experienced aerodynamic forces and moments, the REBR launch data is taken into consideration. Figure 4.5 displays the absolute angle between the REBR logitudinal axis of symmetry (the Z-axis) and the incoming flow vector, called the total angle of attack, over the time from the HTV2 launch. The time on the X-axis in Figure 4.5 corresponds to the time from launch in Figure 4.4. Until 196 seconds, the REBR is housed within the HTV2, and experiences large oscillations in angle of attack. After 200 seconds, the REBR has stabilized with oncoming flow facing its nose cone. The REBR then oscillates around 5° angle of attack [10].

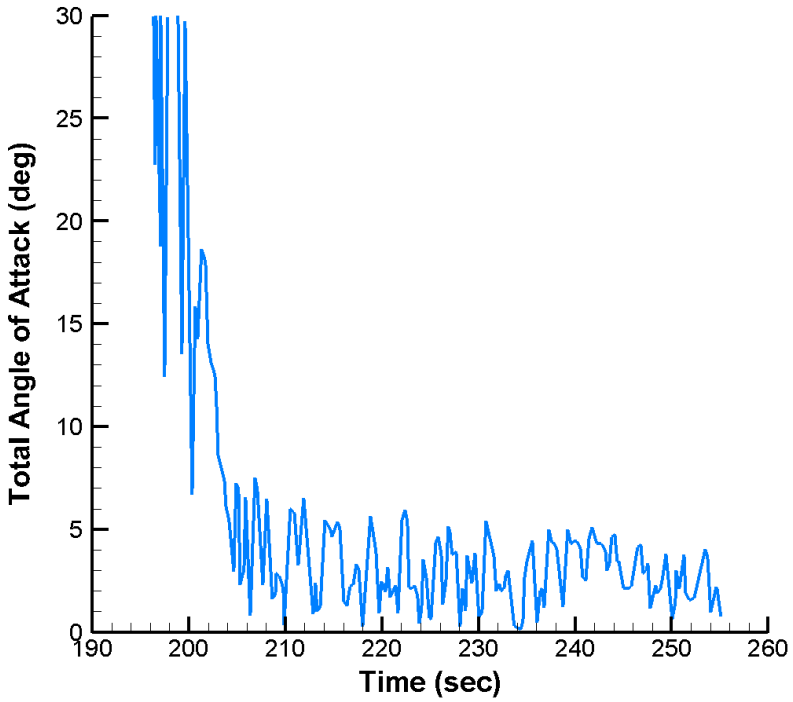

Figure 4.5: Total angle of attack between the longitudinal axis of symmetry for the REBR and the relative velocity vector of the incoming flow from the HTV2 launch data [10].

The REBR stabilizes with oncoming flow facing the nose-cone and experiences rotational tumbling about the symmetric axis and normal axis (the Z- and Y-axes, respectively). The angle of attack analysis plotted in Figure 4.5 displays the oscillatory behavior of the reentering REBR experiences flow in different orientations.

Since in this thesis work, the orbit of the simulated REBR is projected to higher altitudes, more orientations than the relative total angle of attacks experienced in Figure 4.5 are desired for analysis. Understanding effects of the REBR "flipping over" to experience flow on its spherical heat-shield aftbody are desired for analysis.

In order to interpolate average drag and lift experienced, several Ψ angles in the X-Z plane of the REBR's symmetry are chosen to model using both DSMC and the free-molecular approach.

More orientations are modeled with the nose cone of the REBR facing in the incoming flow to correspond to the stabilizing of the REBR discussed previously, but the spherical aft-body facing the flow is modeled as well. Ψ is taken from the positive Z-direction, as pictured in Figure 4.3. More information about the modeled orientations can be found in Appendix B.

The last variable defined for modeling the REBR is the number of sampling steps for use in MONACO simulations. A simple case study is set up to determine the effect increasing the number of sampling steps has on the aerodynamic coefficients C_D and C_L and what difference this causes in orbital decay. For the REBR simulations, sampling begins after 80,000 time steps. After 80,000 time steps, all simulations have reached their steady-state number of particles in the flowfield.

For every REBR simulation the VHS model is used for collisions. 1×10^{-7} seconds is used for the time step. The VHS reference temperature is again 273 K and the viscosity temperature exponent is 0.75 across all simulations. Table 3.3 in Chapter 3 contains the properties for the molecular species utilized. Again, none of the included species are ionized. For more information on these inputs used with MONACO, refer to [20], [22], and [23].

Table 5.3 contains the reference particle weights (the number of real particles represented by one model particle) used in each MONACO simulation for differing Knudsen numbers. The particle weights are chosen to keep the total steady-state number of particles consistently between 4 and 6 $\times 10^6$ as the Knudsen number changes. More particles raise computational cost.

Table 4.2: Reference particle weights used in MONACO REBR simulations at each Knudsen number.

Knudsen Number	**Reference Particle Weight (N_{Real}/N_{Model})**
10	1×10^{11}
1	1×10^{12}
0.1	1×10^{13}
0.01	1.3×10^{14}

The number of sampling steps is varied from 25,000 to 500,000 steps. The Knudsen number used in this sampling study is $Kn = 0.1$. Table 4.3 display the MONACO aerodynamic coefficients for each simulation set up as described above and the number of core-hours (C-Hs) each simulation took. Understanding computational cost needed to impact solutions is an important part of this thesis work. Table 4.3 displays the sampling steps study results for the $\Psi = 0^{\circ}$ case. The aerodynamic coefficients in Table 4.3 are calculated using a projected area of $A = 7.55 \times 10^{-2}$ m^2. The drag and lift forces yield by the MONACO simulations are multiplied by two to account for the symmetric half missing in the meshed representation, as shown in Figure **??**.

Table 4.3: $\Psi = 0^{\circ}$: sampling steps results for coefficient of drag and lift and total core-hours to run simulation.

Sampling Steps	C_D	C_L	**C-Hs**
25000	1.62	2.13×10^{-1}	67.9
50000	1.62	2.14×10^{-1}	83.4
75000	1.62	2.14×10^{-1}	98.4
100000	1.62	2.14×10^{-1}	118
200000	1.62	2.14×10^{-1}	190
300000	1.62	2.14×10^{-1}	258
400000	1.62	2.14×10^{-1}	337
500000	1.62	2.14×10^{-1}	400

The result in Table 4.3 are used in the orbital decay model described in Section 2.3 in order to understand how large of an effect the number of time steps has on orbital decay projections. The difference in orbital decay projections is measured using a RMSD between each methods' loss-of-altitude in kilometers over the time steps taken to project the decay. The RMSD between the 500,000 sampling step simulation orbital decay and the 25,000 sampling steps simulation orbital decay is 2.63×10^{-5} km. The time-to-reenter difference percentage between the 500,000 step simulation and the 25,000 sampling steps simulation is 9.8×10^{-2} %. Based on this analysis, 25,000 sampling steps is chosen for all REBR simulations.

4.2 Knudsen Number of 10

As stated above, a Knudsen number of 10 is achieved for the REBR body at 119 km of altitude. A Knudsen number of 10 is in the free-molecular regime so well-matched results between the MONACO results and the free-molecular model results are expected. The circular orbital speed and atmospheric composition at this altitude are listed in Table 5.3. The REBR surface elements used at this altitude have a side length average of 6.70×10^{-3} m in order to be smaller than the free-stream mean free path compressed by a factor of 10 (2.94×10^{-1} m), and to capture the curvature of the REBR shape. This refinement yields 4.45×10^{4} volume cells in the flowfield, and 2700 surface elements. As an example, the $\Psi = 0^{\circ}$ orientation is presented. All slices of the flowfield are taken at $X = 0$ m, which is the center slice of the REBR showing the Y-Z plane. The REBR body is represented by the white "cut-out" of the slice of the body.

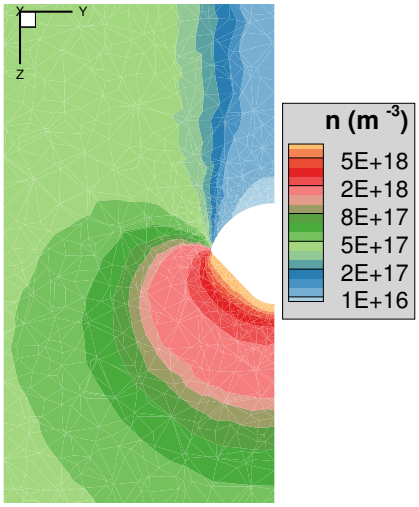

(a)

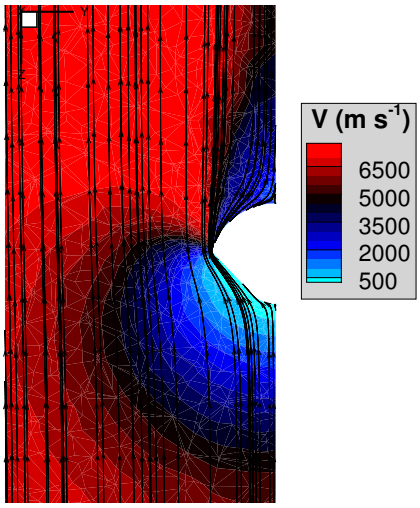

(b)

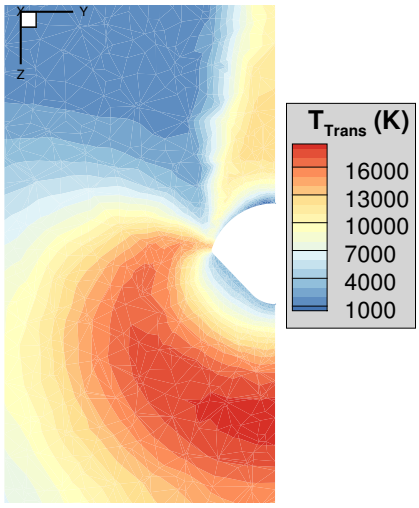

(c)

Figure 4.6: Flowfield contours at $Kn = 10$, $\Psi = 0°$: (a) number density; (b) velocity; (c) translational temperature.

Figure 4.6 shows the flowfield contours. Figure 4.6 depicts the flow phenomena expected when an object disturbs rarefied high-speed flow: instead of a shock wave, a large "bubble" of slowed-down, high-temperature flow forms in front of the object. Additionally, the object, or in this case, the REBR, blocks the incoming flow, so low density flow is seen directly behind the REBR. In Figure 4.6 (b), the velocity streamlines are plotted, and the velocity Ψ angle of $0°$ can be seen

clearly by the direction of the streamlines.

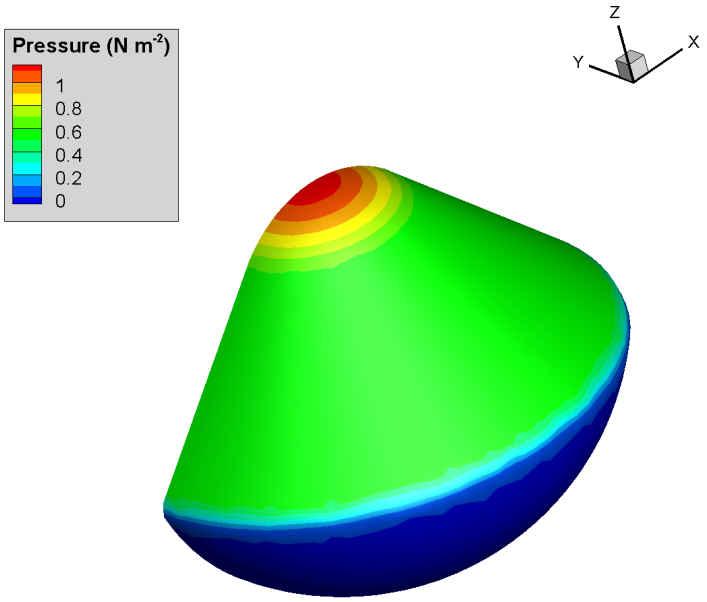

(a)

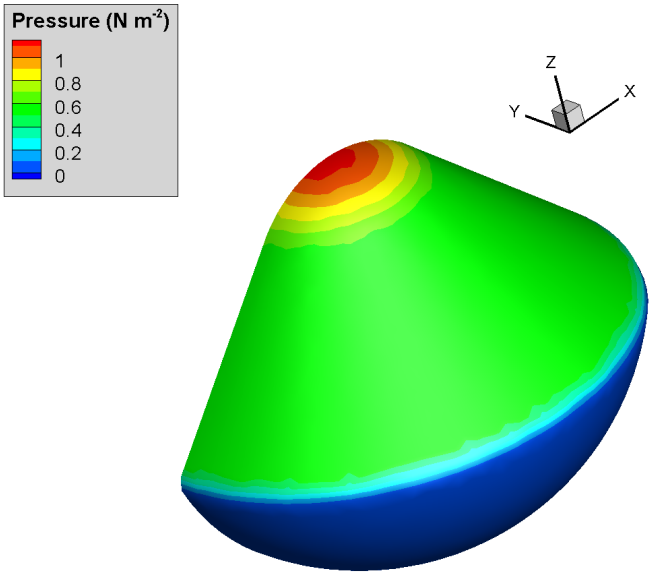

(b)

Figure 4.7: Pressure distribution at $Kn = 10$, $\Psi = 0°$: calculated using: (a) free molecular theory; (b) DSMC.

Figures 4.7 displays an example of the surface pressure on the REBR for the $\Psi = 0^{\circ}$ case. The pressure distributions are very similar: the average pressure experienced by the surface is calculated as 2.78×10^{-1} N m^{-2} using the free-molecular method. This average is calculated by accounting for the pressure on each surface element over the entire body, weighting with respect to surface area, for this orientation. The average pressure experienced over the body calculated by using MONACO results is $2.77 \times 10^{-1} \pm 1.52 \times 10^{-4}$ N m^{-2}, and is calculated similarly. The statistical error for the DSMC pressure calculation is due to the Poisson statistical error of the DSMC results due to the number of hits experienced by the body per surface element per time step and is enumerated in the next section. The difference in average pressure experienced by the body at this orientation is 0.36%. For all percentage differences, as in Chapter 3, the DSMC MONACO results are taken as the more-accurate results, therefore the percentile difference is how much the free-molecular analytical calculation differs from the more-accurate DSMC simulation.

4.2.1 $Kn = 10$: Drag and Lift

Now the drag and lift experienced over the body are compared between the two models. Note that the drag and lift forces plotted and discussed in this section apply to only the half of the REBR that is meshed and simulated. For use in other models (such as the orbital decay model), the forces are duplicated to represent the entire body.

In order to compare models, the drag and lift forces gathered for each modeled orientation are interpolated over all values of Ψ to yield an average value. The average forces over all angles of the body may be an important metric to use with other models such as orbital decay models. The average is also taken as another metric to compare how the models approximate average drag over

a fully revolving body. Though for this particular case of the REBR, a different average is taken for use in the orbital decay model based on flight data, the average taken over all the Ψ values is an important comparison metric to show the weakness or strength of the free-molecular approach in evaluating forces at the current Knudsen number.

Figure 4.8 shows the calculated drag for all orientations using both approaches. The data points for individual simulation results are connected using splines to demonstrate the smooth transition of drag experienced as body rotation would occur.

The Poisson statistical error due to the number of hits experienced by the body per surface element per time step for MONACO DSMC simulations is calculated as in Equation 3.1. Using Equation 3.1, the average hits per sampling time step per surface element across the REBR at this Knudsen number is 4.59×10^{-2}, the total number of surface elements is 2700, and using 25,000 sampling steps: the Poisson statistical error of aerodynamic DSMC results is 0.06%. Error bars are not shown in the following figures because the statistical error is very small.

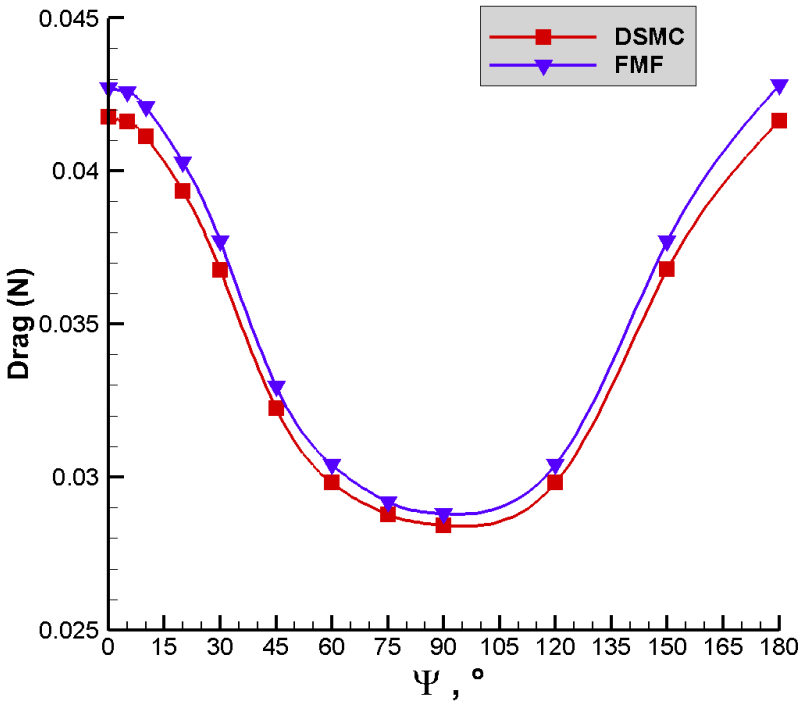

Figure 4.8: Drag calculated using DSMC and free-molecular (FMF) analytical models for all orientations analyzed of the REBR at a Knudsen number of 10.

Figure 4.8 shows that maximum drag values are achieved for $\Psi = 0°$ and $\Psi = 180°$, while minimum drag is achieved for $\Psi = 90°$. These maxima and minimum values correspond to the maximum and minimum flow-exposed projected areas (the projected area of the circle of maximum diameter is 7.55×10^{-2} m^2, the projected area of the side-facing cone and half circle is 5.12×10^{-2} m^2). When $\Psi = 0°$ or $\Psi = 180°$, the flow encounters either the spherical heat shield or the incident nose cone, exposing the entire circular projected area to the incoming flow. When $\Psi = 90°$, the flow encounters the conical "side" of the REBR, and a half-circle section of the semispherical heat shield.

The average drag calculated using the MONACO results interpolated across all orientations is $3.39 \times 10^{-2} \pm 1.90 \times 10^{-5}$ N. The average drag calculated using the free-molecular results is

3.46×10^{-2} N. The percent difference between the averages is 2.06%. The normalized root-mean-square deviation between all the drag results across both models is 2.27%. These results match what is expected: good agreement between the free-molecular analytical and the DSMC results.

Figure 4.9 shows the calculated lift for all orientations using both methods. The lift displayed in Figure 4.9 is translated into an Earth-centric frame, which yields positive lift values. Lift is an order of magnitude smaller compared to drag because REBR is nearly spherical. Spheres experience zero lift at all angles, so the REBR has very low lift. Resolved as described in Chapter 2, nearly all force applied to the REBR body is attributed to drag. Unless a pressure gradient in a normal direction to the oncoming velocity is created by the body's geometry, drag will be the dominating force.

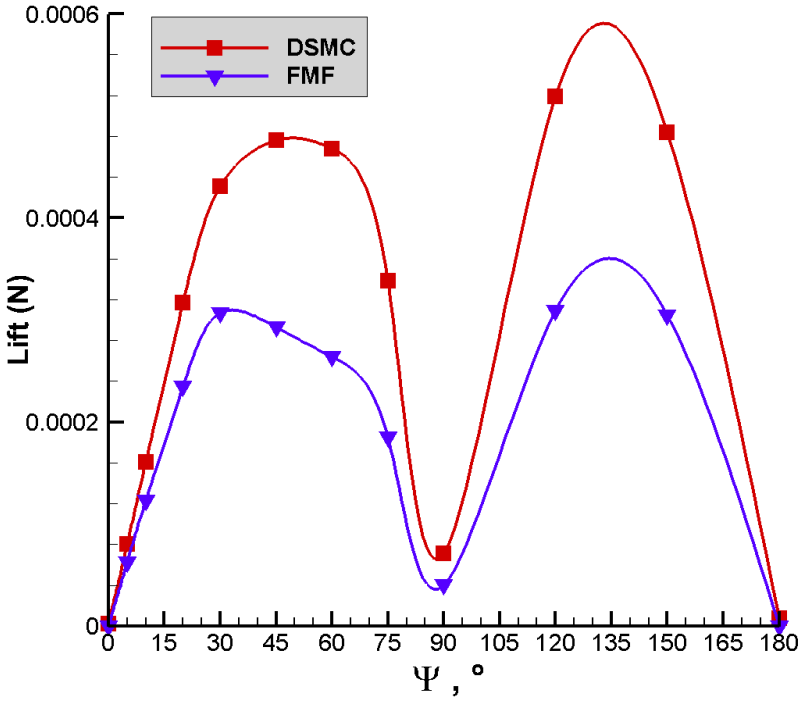

Figure 4.9: Lift calculated using DSMC and free-molecular (FMF) analytical models for all orientations of the REBR at a Knudsen number of 10.

Qualitatively, it is evident that the lift curves in Figure 4.9 are further apart than for drag as

shown in Figure 4.8. At this Knudsen number, good agreement between DSMC and free-molecular results is expected, therefore this lift discrepancy is examined in further detail.

The forces on the body, as discussed in Chapter 2, are the sum of contributions of a pressure force and a shear stress force in the direction desired. In order to examine the modeling differences, both pressure and shear stress contributions to the lift force are inspected below. Figure 4.10 displays the pressure contribution to the lift force for both models, while Figure 4.11 displays the shear stress contribution to the lift force for both models.

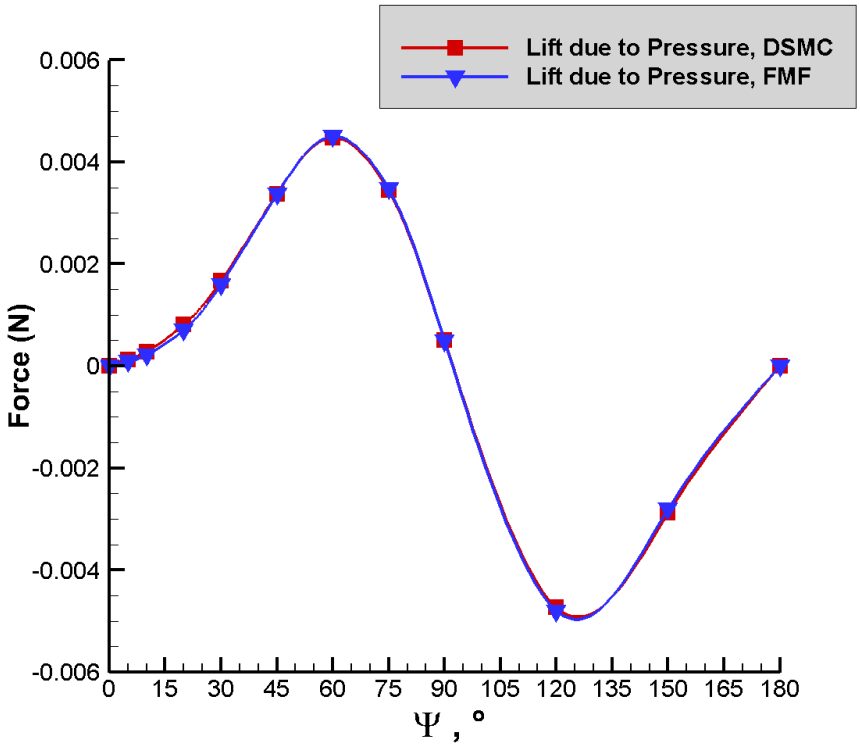

Figure 4.10: Lift due to pressure on the REBR, calculated using DSMC and free-molecular (FMF) analytical models for all orientations at a Knudsen number of 10.

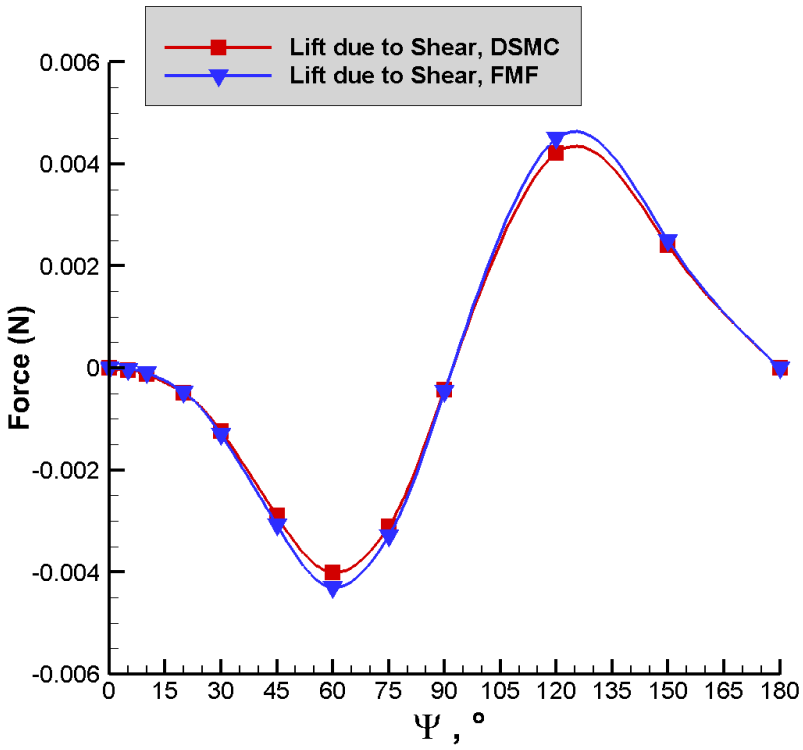

Figure 4.11: Lift due to shear stress on the REBR, calculated using DSMC and free-molecular (FMF) analytical models for all orientations at a Knudsen number of 10.

Figures 4.10 and 4.11 qualitatively display the agreement expected at this Knudsen number between the modeling approaches. The shear stress free-molecular results are more extreme due to the DSMC modeling of particles, which create a more diffusive shear stress across the body, but the models still show good agreement. Quantitatively, the normalized root-mean-square deviation between all the lift due to pressure results across both models is 2.87%. The normalized root-mean-square deviation between all the lift due to shear stress results across both models is 8.65%. These error results are also inflated due to the data points at $\Psi = 0°$ and $180°$ being close to zero, but an order of magnitude apart; and because the average lift due to shear is very close to zero. Data points of interest are enumerated in Table 4.4.

This good agreement reflects that the modeling approaches are matching in calculating these

Table 4.4: Lift due to shear stress on the REBR at specific Ψ values for a Knudsen number of 10.

Lift due to Shear Stress (N)		
	FMF	**DSMC**
$\Psi = 0°$	1.61×10^{-7}	2.14×10^{-6} $\pm 1.28 \times 10^{-9}$
$\Psi = 180°$	-2.26×10^{-7}	-3.13×10^{-6} -1.88×10^{-9}

surface properties and distributing them in the lift direction.

To take the total lift across the body, the lift due to pressure and the lift due to shear stress are summed. This results in lift values very close to zero; and small discrepancies in both contributing forces are magnified; yielding the curves in Figure 4.9. Because the lift is so small, the differences between models will not greatly change any orbital decay results. As Knudsen number is decreased, the lift differences are expected to increase, for both the total lift force as well as each contribution component.

In order to calculate coefficients of drag and lift for use in the orbital decay model, a free-stream density is taken from [9]. At 119 km, where for REBR $Kn = 10$, the free-stream density $\rho = 1.81 \times 10^{-8}$ kg m^{-3}. The orbital velocity is the circular orbital speed used throughout the $Kn = 10$ results: $V = 7830$ m s^{-1}. The aerodynamic coefficients are calculated for a full-body (not half, or meshed representation of) REBR, and include the area as in Chapter 3, for use in the orbital decay modeling. The modeled force is multiplied by two to get the total force on the body: Total Drag $= 2\times$ Modeled Drag. The total drag is then input into the equation for C_DA: $C_DA = 2\times$ Total Drag $\times(\rho V^2)^{-1}$. The lift coefficient is calculated similarly.

Figure 4.12 shows C_DA and C_LA calculated for all models and orientations for $Kn = 10$ experienced by the REBR body.

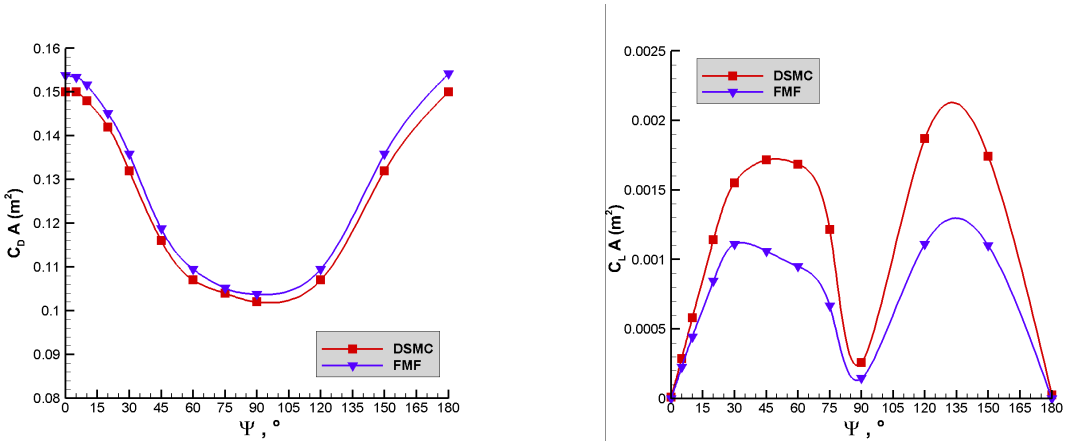

(a) (b)

Figure 4.12: Drag (a) and lift (b) coefficients calculated using DSMC and free-molecular (FMF) analytical models for all experiment orientations of the REBR using both models for a Knudsen number of 10.

The average $C_D A$ calculated using the DSMC MONACO modeling results is $1.22 \times 10^{-1} \pm 7.00 \times 10^{-5}$ m^2, while the average $C_D A$ calculated using the free-molecular analytical modeling results is 1.25×10^{-1} m^2. The percent difference between the averages is 2.46%. The normalized root-mean-square deviation between all the $C_D A$ results across both models is 2.27%. The average $C_L A$ calculated using the DSMC MONACO modeling results is $1.67 \times 10^{-3} \pm 1.49 \times 10^{-6}$ m^2, while the average $C_L A$ calculated using the free-molecular analytical modeling results is 1.07×10^{-3} m^2. The same higher-than-expected discrepancy is seen qualitatively between the coefficient of lift curves in Figure 4.12 (b), and the error between them is exponentially elevated due to the phenomena discussed above. The error percentage between the modeling approaches for the lift coefficient is therefore not a good metric to judge agreement between models.

4.2.2 $Kn = 10$: Moments and Angular Accelerations

The moments are taken about the geometric REBR body centroid: $X = -6.14 \times 10^{-4}$ m, $Y = 0$ m, $Z = -7.78 \times 10^{-3}$ m. The moments of inertia about the whole REBR's primary axes are $I_{XX} = 1.02 \times 10^{-1}$ kg m^2, $I_{YY} = 1.17 \times 10^{-1}$ kg m^2, and $I_{ZZ} = 1.10 \times 10^{-1}$ kg m^2.

Due to the symmetrical modeling of the half-REBR, there is a reflected point across the Y-axis for every point on the modeled REBR. These reflected points experience the same X and Z direction forces, but reflected Y-forces due to the flow being deflected in the opposite direction of the meshed REBR over the nose cone or spherical heat shield. The modeled point's moments are given in Equation 4.1. The subscript M refers to the modeled meshed points and moments. The X, Y, and Z subscripts in Equation 4.1 refer to the component of the moment taken about that axis. r is the position coordinate of the points.

$$\begin{aligned} M_{X,M} &= r_{Y,M}F_{Z,M} - r_{Z,M}F_{Y,M} \\ M_{Y,M} &= r_{Z,M}F_{X,M} - r_{X,M}F_{Z,M} \\ M_{Z,M} &= r_{X,M}F_{Y,M} - r_{Y,M}F_{X,M} \end{aligned} \tag{4.1}$$

The reflected point's moments are given in Equation 4.2. The subscript R refers to the non-modeled, reflected points.

$$M_{X,R} = r_{Y,R}F_{Z,R} - r_{Z,R}F_{Y,R}$$
$$M_{Y,R} = r_{Z,R}F_{X,R} - r_{X,R}F_{Z,R} \tag{4.2}$$
$$M_{Z,R} = r_{X,R}F_{Y,R} - r_{Y,R}F_{X,R}$$

Applying the symmetry of the modeled REBR: $r_{X,M} = r_{X,R}$, $r_{Z,M} = r_{Z,R}$, $F_{X,M} = FX, R$, and $F_{Z,M} = F_{X,M}$. For the Y-axis: $r_{Y,R} = -r_{Y,M}$ and $F_{Y,R} = -F_{Y,M}$. Applying this to Equations 4.1 and 4.2, and summing for total moments, the X- and Z- moments cancel out across the body, and the Y-moments double. The Y-moments correspond to the rotation about the lateral (normal to the symmetrical) axis in Figure 4.3.

Though the X- and Z- moments cancel across the body, the yielded moments on half the body are studied in this section in order to compare models. Note that the Y-moments are not doubled when plotted.

Figure 4.13 displays the moment results about the three primary axes yielded by both models across all the REBR orientations.

The aerodynamic moments about the X-axis are an order of magnitude larger than those modeled about the Y- and Z- axes. This is because the flow-facing area changes are large as the relative velocity vector moves across the X-axis. Though the X- and Z- moments cancel out when projecting results to the entire body, Figure 4.13 shows the good agreement of the DSMC and free-molecular approaches expected at this Knudsen number.

As seen in Figure 4.13 (a), the maximum aerodynamic moments about the X-axis are incurred when Ψ is 0° or 180°, concentrated on one side of the REBR, and "pushing" the half-REBR to

spin about the X-axis. When $\Psi = 90°$, the oncoming flow is applied in a near-symmetric way about the X-axis. The opposite of this phenomenon happens about the Z-axis in Figure 4.13 (c): the flow is symmetric about the Z-axis for $\Psi = 0°$ and $180°$. At $90°$, the pressure distribution is unsymmetrical, and "pushes" the REBR to spin about the Z-axis.

In Figure 4.13 (b), the Y-moments experience two local maxima at $\Psi = 45°$ and $120°$. Minima occur when the flow is applied to a symmetric configuration, at $\Psi = 0°$ and $180°$. The maxima correspond to an uneven flow distribution across the nose cone or spherical heat shield.

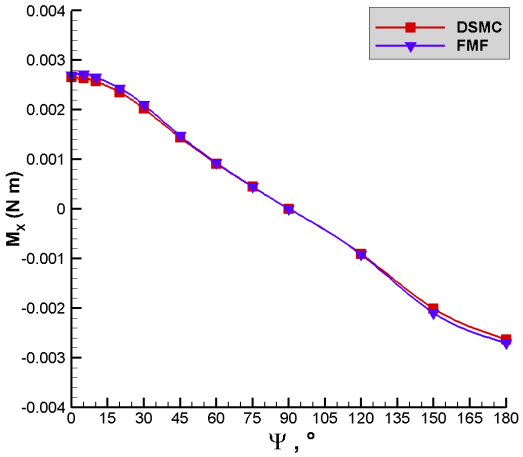

(a)

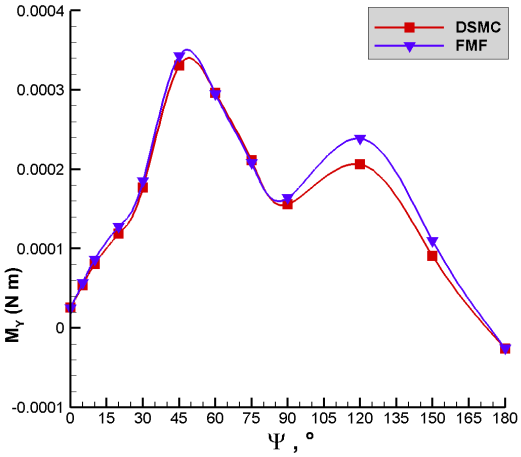

(b)

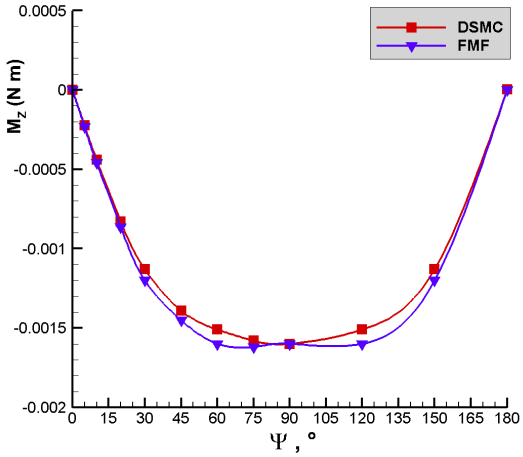

(c)

Figure 4.13: Moments calculated using DSMC and free-molecular (FMF) analytical models for all experiment orientations of the REBR about the: (a) X axis; (b) Y axis; (c) Z axis, for a Knudsen number of 10.

The moment averages are listed in Table 4.5. Table 4.5 portrays clearly that the free-molecular and DSMC modeling approaches yield similar results for this Knudsen number.

The normalized root-mean-square deviation between all the X-axes moments is 3.58%. The normalized root-mean-square deviation between the Y-axes moments is 7.94%. The normalized

Table 4.5: Average moments calculated for a Knudsen number of 10 for the DSMC and free-molecular analytical modeling approaches across all Ψ values.

Average	FMF	DSMC
$\mathbf{M}_X$ **(N m)**	1.45×10^{-5}	1.65×10^{-5} $\pm 9.37 \times 10^{-9}$
$\mathbf{M}_Y$ **(N m)**	1.73×10^{-4}	1.61×10^{-4} $\pm 9.65 \times 10^{-8}$
$\mathbf{M}_Z$ **(N m)**	-1.21×10^{-3}	-1.16×10^{-3} $\pm 6.59 \times 10^{-7}$

root-mean-square deviation between the Z-axes moments is 5.21%. The moment results reflect good agreement between the free-molecular and DSMC methods at this Knudsen number.

Because the Y-moments are the only ones that are non-zero across the whole REBR body, the angular acceleration about the Y-axis is examined more thoroughly here. While a statistical error of 0.06% still applies to the DSMC results, in this section angular acceleration uncertainty is plotted and discussed. This is both because it is larger, and more importantly, plotting the angular rotational uncertainty gives an intuitive picture of where aerodynamic moments would affect the overall motion of the body.

The angular acceleration uncertainty is treated the same way as in Chapter 3, using Equation 3.2's Y-component. Applying the data from the REBR flight, and seen in Figure 4.5, the maximum stable rates of rotation about the Y- and Z-axes are 5 degrees s^{-1}. Using the moments of inertia enumerated previously, the angular acceleration uncertainty about the Y-axis is 2.98×10^{-2} radians s^{-2}, or 1.71 degrees s^{-2}. This is plotted as an error bar in all of the angular acceleration plots in this chapter to understand the effect aerodynamic moments would have on a body that has already achieved an angular velocity through some pre-applied force.

Figure 4.14 shows the calculated angular acceleration about the Y-axis for the REBR body using both models across all orientations, with error bars as described previously. In Figure 4.14,

the Y-moments across the orientations have been doubled, then divided by I_{YY}, to represent the moments incurred by the entire REBR body. The interpolated average angular accelerations about the Y-axis incurred are $1.57 \times 10^{-1} \pm 8.90 \times 10^{-5}$ degrees s^{-2} using the DSMC method and 1.69×10^{-1} degrees s^{-2} using the free-molecular analytical method. The normalized root-mean-square deviation between the angular accelerations about the Y-axis is 7.94%. Again, there is good agreement between the models, as expected since angular acceleration results are proportional to the Y-moment results.

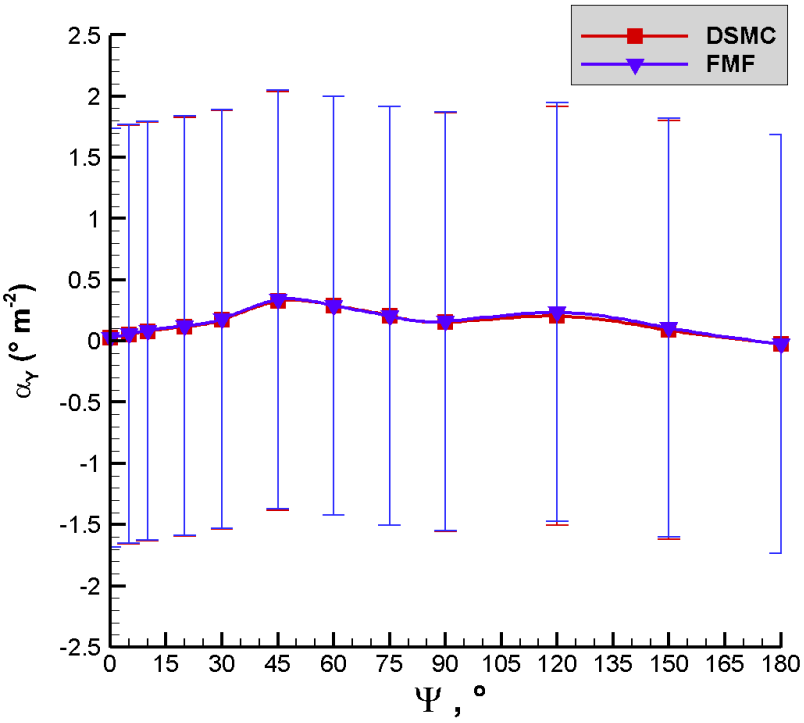

Figure 4.14: Angular acceleration about the Y-axis calculated using DSMC and free-molecular (FMF) analytical models for all experiment orientations of the REBR, for a Knudsen number of 10. Error bars reflect the angular velocity uncertainty of 1.71 degrees s^{-2}.

The error bars in Figure 4.14 illustrate the effect the aerodynamic Y-moment has on the tumbling behavior of the REBR. If the REBR has an angular velocity about the Y-axis of 5 degrees s^{-1}, the effect of aerodynamic moments will be small compared to the effect of the established

tumbling motion. This is expected since the REBR is designed to be aerodynamically stable.

4.3 Knudsen Number of 1

A Knudsen number of 1 is achieved for the REBR body at 104 km of altitude. A Knudsen number of 1 is the limit of defined free-molecular flow [20]. In this regime, the flowfields will still be rarefied, but the expectation of good agreement between the models does not hold: particle collisions will matter at this Knudsen number. The circular orbital speed and atmospheric composition at this altitude are listed in Table 4.1.

The same mesh used in Section 4.2 is used for this altitude. The REBR surface elements used at this altitude have a side length average of 6.70×10^{-3} m in order to be smaller than the free-stream mean free path compressed by a factor of 10 (2.84×10^{-2} m), and to capture the curvature of the REBR shape. This refinement yields 4.45×10^{4} volume cells in the flowfield, and 2700 surface elements. As an example, the $\Psi = 20^{\circ}$ orientation is presented. All slices of the flowfield are taken at $X = 0$ m, which is the center slice of the REBR showing the Y-Z plane. The REBR body is represented by the white "cut-out" of the slice of the body.

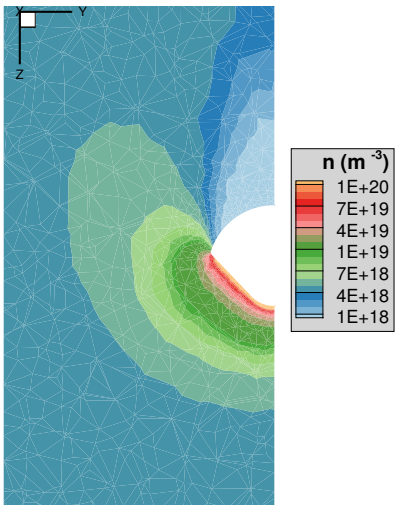

(a)

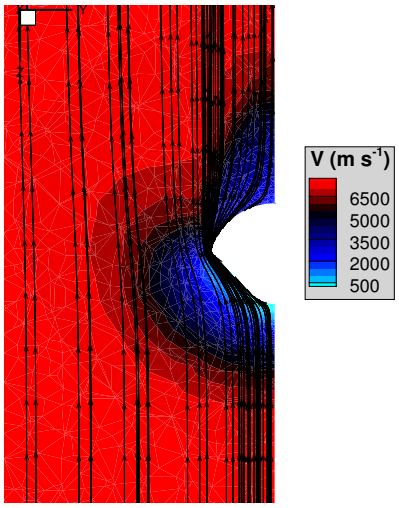

(b)

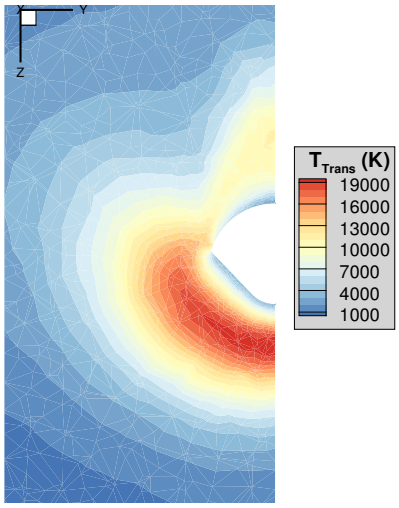

(c)

Figure 4.15: Flowfield contours at $Kn = 1$, $\Psi = 20°$: (a) number density; (b) velocity; (c) translational temperature.

Figure 4.15 shows the flowfield contours. Figure 4.15 depicts the flow phenomena expected when an object disturbs rarefied high-speed flow. Similarly to at the higher altitude of $Kn = 10$, instead of a shock wave, a projected area of slowed-down, high-temperature flow forms in front of the object. The REBR blocks the incoming flow: low density flow is seen directly behind the REBR. In Figure 4.15 (b), the velocity streamlines are plotted. The velocity Ψ value of $20°$

cannot be immediately seen from the streamlines due to the position of the flowfield slice plane. The velocity Ψ deflection is out-of-frame of the slice taken; this slice is taken to demonstrate the half-REBR modeled body and flowfield.

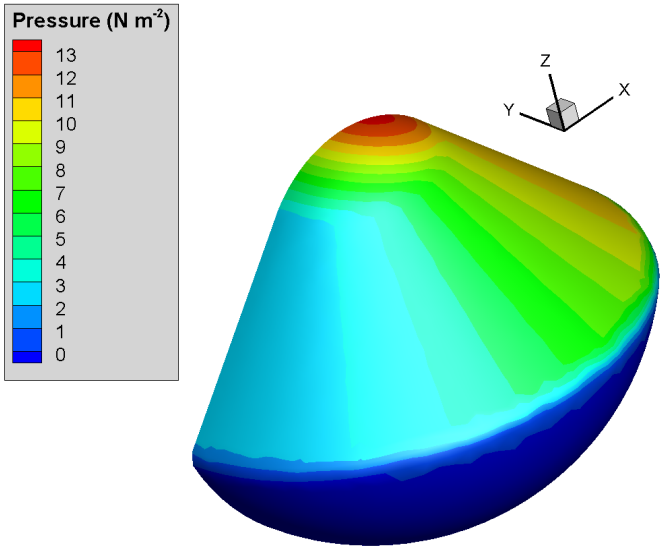

(a)

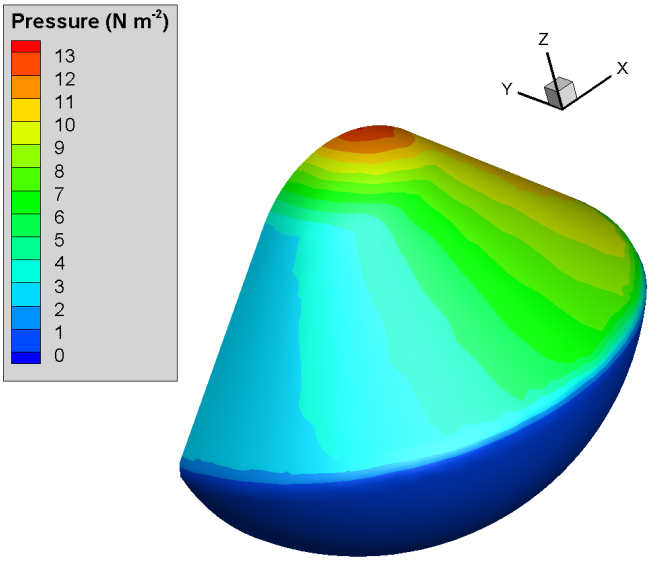

(b)

Figure 4.16: Pressure distribution at $Kn = 1$, $\Psi = 20°$, calculated using: (a) free molecular theory; (b) DSMC.

Figures 4.16 displays an example of the surface pressure on the REBR for the $\Psi = 20^{\circ}$ case. Figure 4.16 shows the diffuse nature of the particles impacting the surface as a result of the DSMC modeling approach versus free-molecular analytical approach which applies the same macroscopic quantities to every cell experiencing flow with identical normal vectors. The influence of particles is evident on the spherical heat-shield section of REBR. The free-molecular method does not detect particles impacting the surface, therefore the spherical heat-shield side of REBR experiences zero pressure in Figure 4.16 (a) as it is not exposed to the flow. The DSMC method is a particle method, and therefore tracks the few collisions that the flow has with the "underside" of the REBR: Figure 4.16 (b) displays this very low pressure on the spherical heat-shield portion of the REBR.

The pressure distributions from the two methods are similar: the average pressure experienced by the surface is calculated as 3.02 N m^{-2} using the free-molecular method. The average pressure experienced over the body calculated by using MONACO results is 3.00 $\pm 1.40 \times 10^{-3}$ N m^{-2}. The average is calculated the same way as in Section 4.2 and is weighed by each surface element area. The statistical error for the DSMC pressure calculation is due to the Poisson statistical error of the DSMC results due to the number of hits experienced by the body per surface element per time step and is enumerated in the next section. The difference in average pressure experienced by the body at this orientation is 0.60%.

4.3.1 $Kn = 1$: Drag and Lift

Now the drag and lift experienced over the body are compared between the two models. Note that the drag and lift forces plotted and discussed in this section apply to only the half of the REBR that is meshed and simulated. For use in other models (such as the orbital decay model), the forces

are duplicated to represent the entire body.

In order to compare models, the drag and lift forces gathered for each modeled orientation are interpolated over all values of Ψ to yield an average value. A different average is taken for use in the orbital decay model and is discussed in later sections.

Figure 4.17 shows the calculated drag for all orientations using both approaches. The data points for individual simulation results are connected using splines to demonstrate the smooth transition of drag experienced as body rotation would occur.

The Poisson statistical error due to the number of hits experienced by the body per surface element per time step for MONACO DSMC simulations is calculated as in Equation 3.1. Using Equation 3.1, the average hits per sampling time step per surface element across the REBR at this Knudsen number is 6.37×10^{-2}, the total number of surface elements is 2700, and using 25,000 sampling steps: the Poisson statistical error of aerodynamic DSMC results is 0.05%. Error bars are not shown in the following figures because the statistical error is very small.

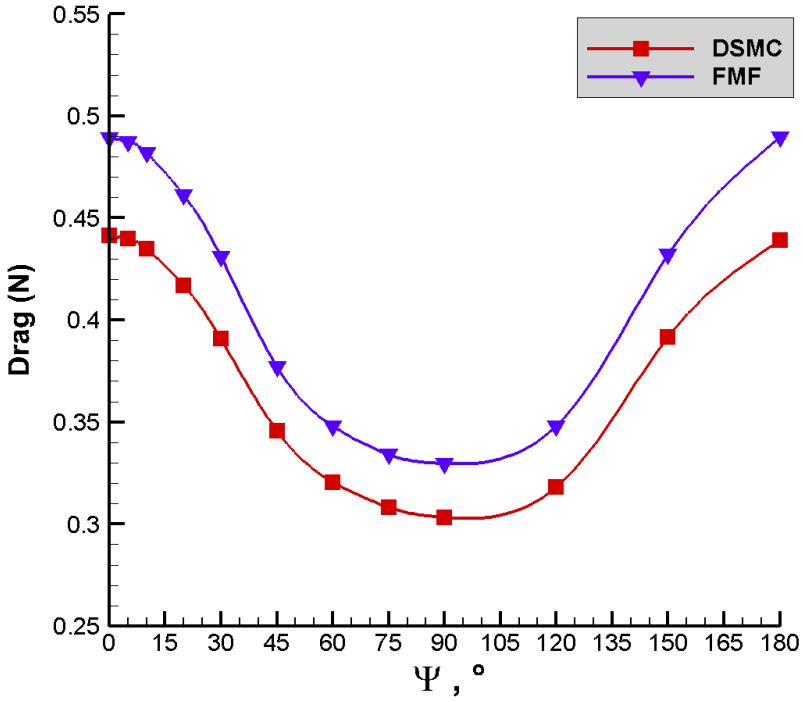

Figure 4.17: Drag calculated using DSMC and free-molecular (FMF) analytical models for all orientations analyzed of the REBR at a Knudsen number of 1.

Figure 4.17 shows that maximum drag values are achieved for $\Psi = 0°$ and $\Psi = 180°$, while minimum drag is achieved for $\Psi = 90°$. The same features of this plot can be seen in Figure 4.8: the maxima and minima correspond to the maximum and minimum flow-exposed projected areas. When $\Psi = 0°$ or $\Psi = 180°$, the flow encounters either the spherical heat shield or the incident nose cone, exposing the entire circular projected area to the incoming flow. When $\Psi = 90°$, the flow encounters the conical "side" of the REBR, and a half-circle section of the semispherical heat shield.

The average drag calculated using the MONACO results interpolated across all orientations is $3.61 \times 10^{-1} \pm 1.74 \times 10^{-4}$ N. The average drag calculated using the free-molecular results is 3.96×10^{-1} N. The percent difference between the averages is 9.84%. The normalized root-

mean-square deviation between all the drag results across both models is 9.40%. This reflects the degrading level of agreement between the modeling approaches as Knudsen number decreases.

Figure 4.18 shows the calculated lift for all orientations using both methods. The lift displayed in Figure 4.18 is translated into an Earth-centric frame, yielding positive lift. Lift is an order of magnitude smaller compared to drag due to the REBR's sphere-like body, as discussed in Section 4.2. Resolved as described in Chapter 2, nearly all force applied to the REBR body is attributed to drag. Unless a pressure gradient in a normal direction to the oncoming velocity is created by the body's geometry, drag will be the dominating force.

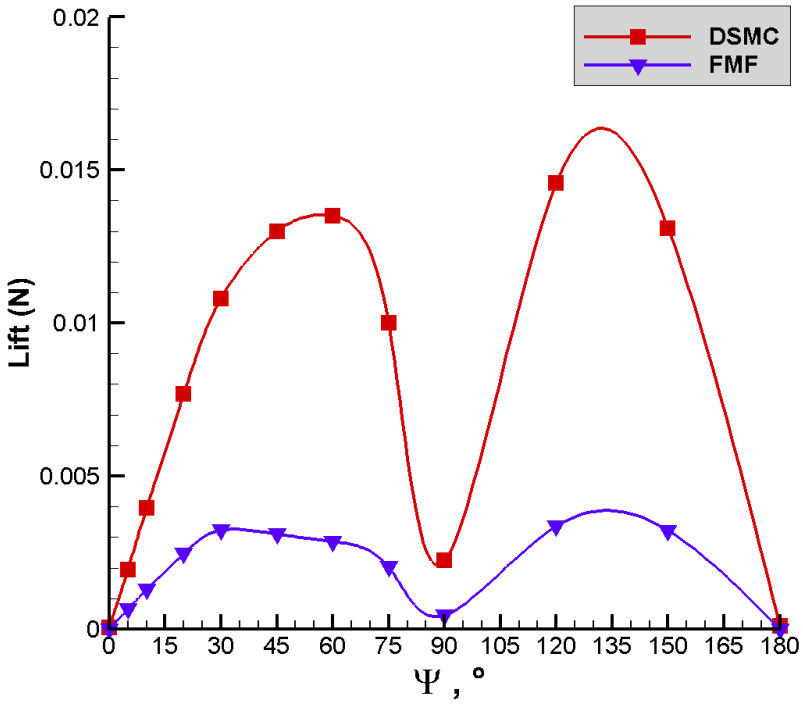

Figure 4.18: Lift calculated using DSMC and free-molecular (FMF) analytical models for all orientations of the REBR at a Knudsen number of 1.

Qualitatively, it is evident that the lift curves in Figure 4.18 are further apart than for drag as shown in Figure 4.17. As in Section 4.2, this discrepancy is examined in further detail to

understand the differences between the modeling approaches.

To examine the modeling differences, both pressure and shear stress contributions to the lift force are inspected below. Figure 4.19 displays the pressure contribution to the lift force for both models, while Figure 4.20 displays the shear stress contribution to the lift force for both models.

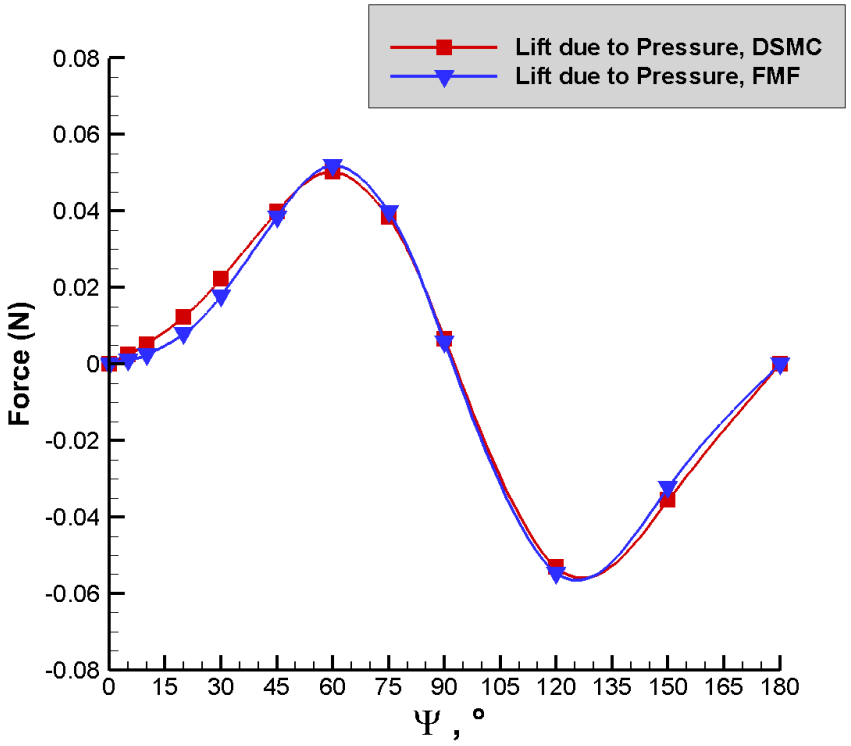

Figure 4.19: Lift due to pressure on the REBR, calculated using DSMC and free-molecular (FMF) analytical models for all orientations at a Knudsen number of 1.

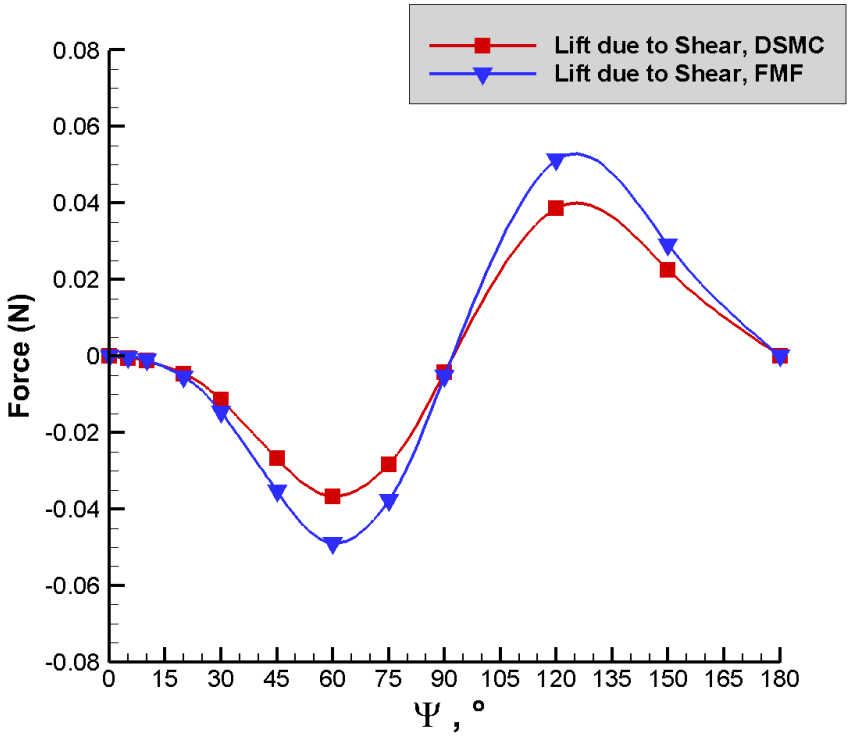

Figure 4.20: Lift due to shear stress on the REBR, calculated using DSMC and free-molecular (FMF) analytical models for all orientations at a Knudsen number of 1.

Figures 4.19 and 4.20 display much better agreement between the modeling approaches than Figure 4.18. Once again, the contributions are canceling out in a way that magnifies the differences between the models. Figure 4.20 shows the more extreme differences in the shear stress yields of both models; as discussed in Section 4.2, the free-molecular modeling of the shear stress is more extreme because the particles are not modeled individually and there is no diffusion in particle momentum across the planes of the body. While Figures 4.19 and 4.20 display some agreement between the models at this Knudsen number, comparisons with Figures 4.10 and 4.11 clearly show the weakening of the free-molecular assumption as Knudsen number lowers.

Quantitatively, the normalized root-mean-square deviation between all the lift due to pressure results across both models is 11.5%. The normalized root-mean-square deviation between all the

lift due to shear stress results across both models is 34.7%. These error results are also inflated due to the data points at $\Psi = 0°$ and $180°$ being close to zero, but an order of magnitude apart. These data points are enumerated in Table 4.6.

Table 4.6: Lift due to pressure and shear stress on the REBR at specific Ψ values for a Knudsen number of 1.

Lift due to Pressure (N)		
	FMF	**DSMC**
$\Psi = 0°$	-1.72×10^{-6}	-1.61×10^{-5} $\pm -8.05 \times 10^{-9}$
$\Psi = 180°$	2.63×10^{-6}	-1.05×10^{-5} -5.23×10^{-9}
Lift due to Shear Stress (N)		
	FMF	**DSMC**
$\Psi = 0°$	1.85×10^{-6}	1.11×10^{-4} $\pm 5.53 \times 10^{-8}$
$\Psi = 180°$	-2.60×10^{-6}	-4.51×10^{-5} -2.26×10^{-8}

To take the total lift across the body, the lift due to pressure and the lift due to shear stress are summed. This results in lift values very close to zero; and small discrepancies in both contributing forces are magnified; yielding the curves in Figure 4.18. Because the lift is so small when compared to drag results, the differences between models will not greatly change any orbital decay results. These differences in lift and lift contribution forces are expected to increase further as Knudsen number decreases.

In order to calculate coefficients of drag and lift for use in the orbital decay model, a free-stream density is taken from [9]. At 104 km, where for REBR $Kn = 1$, the free-stream density $\rho = 2.07 \times 10^{-7}$ kg m^{-3}. The orbital velocity is the circular orbital speed used throughout the $Kn = 1$ results: $V = 7840$ m s^{-1}. The aerodynamic coefficients are calculated as described in Section 4.2.

Figure 4.21 shows C_DA and C_LA calculated for all models and orientations for $Kn = 1$ experienced by the REBR body.

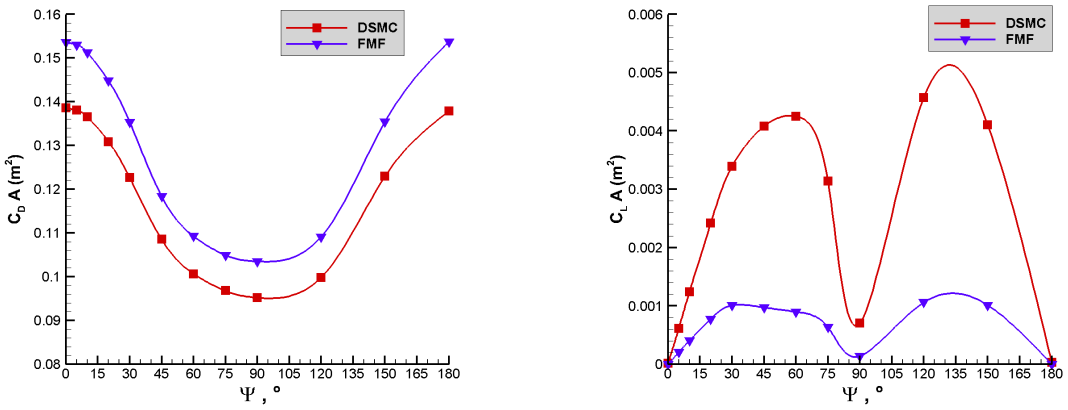

(a) (b)

Figure 4.21: Drag (a) and lift (b) coefficients calculated using DSMC and free-molecular (FMF) analytical models for all experiment orientations of the REBR using both models for a Knudsen number of 1.

The average C_DA calculated using the MONACO results is $1.13 \times 10^{-1} \pm 5.50 \times 10^{-5}$ m^2, while the average C_DA calculated using the free-molecular results is 1.24×10^{-1} m^2. The percent difference between the averages is 9.80%. The normalized root-mean-square deviation between all the C_DA results across both models is 9.40%. The average C_LA calculated using the DSMC MONACO modeling results is $3.97 \times 10^{-3} \pm 1.93 \times 10^{-6}$ m^2, while the average C_LA calculated using the free-molecular analytical modeling results is 1.00×10^{-3} m^2. The same higher-than-expected discrepancy is seen qualitatively between the coefficient of lift curves in Figure 4.21 (b), and the error between them is exponentially elevated due to the problems discussed above. The differences between modeling approach results for drag, lift, C_DA and C_LA are getting bigger when compared to Section 4.2. At this Knudsen number, collisions are becoming much more important and are effecting results in an evident way.

4.3.2 $Kn = 1$: Moments and Angular Accelerations

Moments are treated in the same way as detailed in Section 4.2.2. The angular acceleration uncertainty again equates to: 2.98×10^{-2} radians s^{-2}, or 1.71 degrees s^{-2}. This uncertainty is projected from the findings of the REBR launch.

Figure 4.22 displays the moment results about the three primary axes yielded by both models across all the REBR body orientations. Figure 4.22 mirrors the results seen in Figures 4.13, but at a larger scale, proportional to the larger forces induced on the body in less-rarefied flow at a higher orbital speed. There is one exception: for $\Psi = 120^{\circ}$, the DSMC method does not yield another maxima moment about the Y-axis (see Figure 4.22). As Knudsen number lowers, the second maxima in the moment about the Y-axis "smooths" out, as seen in further sections. As the flow becomes more continuum-like, the aerodynamic shape of the REBR yields a smaller moment at that orientation.

Besides this data point, Figure 4.22 behaves like Figure 4.13; with proportionally larger moments as the forces are larger at this Knudsen number, and slightly bigger differences in the curves due to the lower Knudsen number invalidating the free-molecular collisionless assumption.

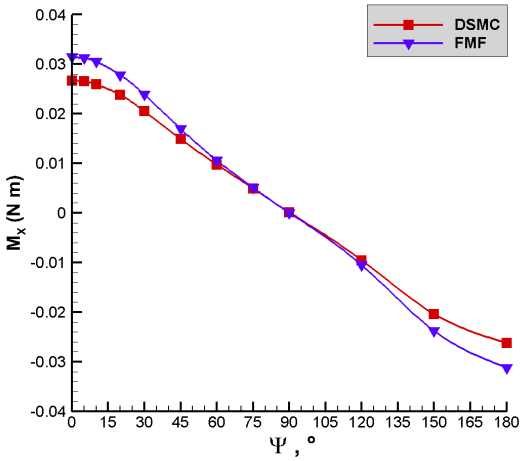

(a)

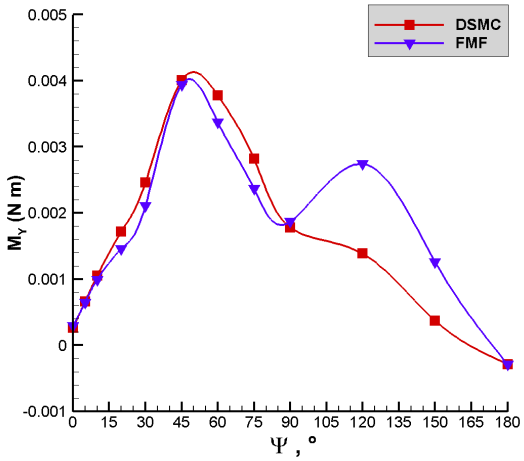

(b)

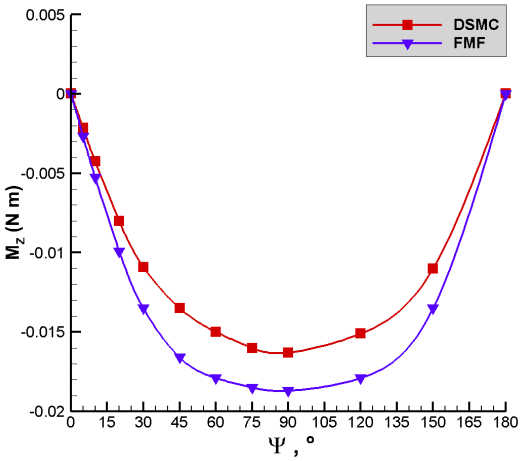

(c)

Figure 4.22: Moments calculated using DSMC and free-molecular (FMF) analytical models for all experiment orientations of the REBR about the: (a) X axis; (b) Y axis; (c) Z axis, for a Knudsen number of 1.

The moment averages are listed in Table 4.7. Table 4.7 portrays that the free-molecular and DSMC modeling approaches yield similar results for this Knudsen number, however, there are more noticeable differences than the results for a Knudsen number of 10 in Section 4.2.

The normalized root-mean-square deviation between all the X-axes moments is 16.6%. The

Table 4.7: Average moments calculated for a Knudsen number of 1 for the DSMC and free-molecular analytical modeling approaches across all Ψ values.

Average	FMF	DSMC
$\mathbf{M}_X$ **(N m)**	1.92×10^{-4}	2.43×10^{-4} $\pm 1.22 \times 10^{-7}$
$\mathbf{M}_Y$ **(N m)**	1.97×10^{-3}	1.71×10^{-3} $\pm 8.53 \times 10^{-7}$
$\mathbf{M}_Z$ **(N m)**	-1.38×10^{-2}	-1.15×10^{-2} $\pm -5.77 \times 10^{-6}$

normalized root-mean-square deviation between the Y-axes moments is 29.0%. The normalized root-mean-square deviation between the Z-axes moments is 19.4%. There is decent agreement at these Knudsen numbers; especially when comparing very small moments. However, differences between the models are immediately larger than those at a Knudsen number of 10.

Because the Y-moments are the only ones that are non-zero across the whole REBR body, the angular acceleration about the Y-axis is examined more thoroughly here. While a statistical error of 0.05% still applies to the DSMC results, in this section angular acceleration uncertainty is plotted and discussed. This is both because it is larger, and more importantly, plotting the angular rotational uncertainty gives an intuitive picture of where aerodynamic moments would affect the overall motion of the body. The Y-axis angular acceleration uncertainty is treated the same way as in Chapter 3 and is 2.98×10^{-2} radians s^{-2}, or 1.71 degrees s^{-2}, plotted as an error bar in all of the angular acceleration plots in this chapter. This is to visualize the effect aerodynamic moments would have on the tumbling motion of the REBR body with a previously imposed angular velocity.

Figure 4.23 shows the calculated angular acceleration about the Y-axis for the REBR body using both models across all orientations, with error bars as described previously. In Figure 4.23, the Y-moments across the orientations have been doubled, then divided by I_{YY}, to represent the moments incurred by the entire REBR body, and not the meshed half. The interpolated average

angular accelerations about the Y-axis incurred are $1.67 \pm 8.06 \times 10^{-4}$ degrees s^{-2} using the DSMC method and 1.93 degrees s^{-2} using the free-molecular analytical method. The normalized root-mean-square deviation between the angular accelerations about the Y-axis is 29%. These results reflect the decaying accuracy of the free-molecular assumption as Knudsen number lowers, as the differences between models are increasing when compared to results at $Kn = 10$.

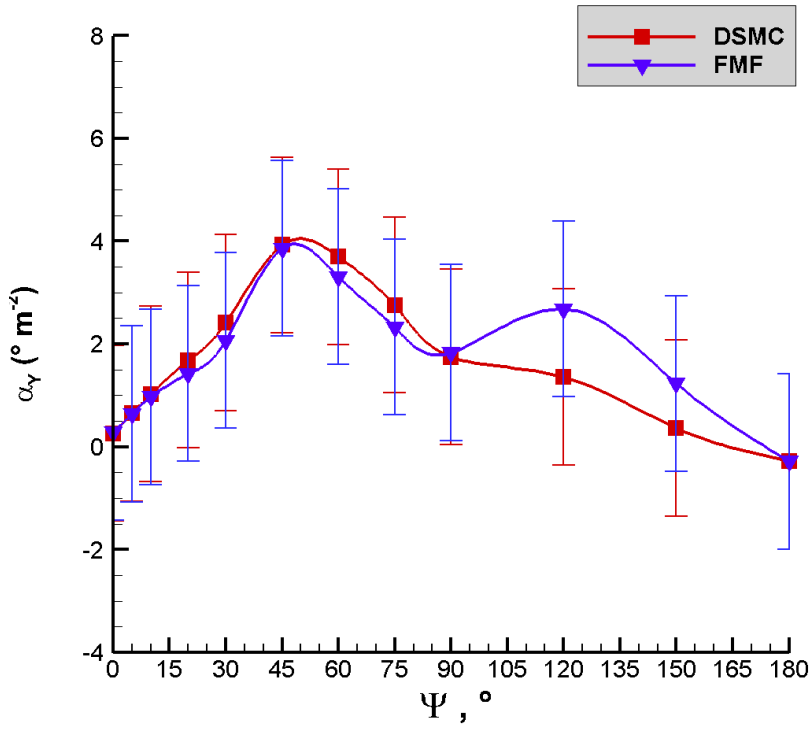

Figure 4.23: Angular acceleration about the Y-axis calculated using DSMC and free-molecular (FMF) analytical models for all experiment orientations of the REBR, for a Knudsen number of 1. Error bars reflect the angular velocity uncertainty of 1.71 degrees s^{-2}.

The error bars in Figure 4.23 illustrate the effect the aerodynamic Y-moment has on the tumbling behavior of the REBR. If the REBR has an angular velocity about the Y-axis of 5 degrees s^{-1}, the aerodynamic moments at this altitude will have an effect, changing the angular acceleration by a few degrees.

4.4 Knudsen Number of 0.1

A Knudsen number of 0.1 is achieved for the REBR body at 91 km of altitude. A Knudsen number of 0.1 is purely in the transitional regime [20]. In this regime, the flowfields are markedly less rarefied and an expectation of good agreement between the models should not hold. The circular orbital speed and atmospheric composition at this altitude are listed in Table 4.1. A different mesh is used for this altitude in order to achieve cell sizes with side lengths smaller than the mean free path.

The REBR surface elements used at this altitude have a side length average of 8.94×10^{-4} m in order to be smaller than the free-stream mean free path compressed by a factor of 10 (2.83×10^{-3} m). This refinement yields 9.88×10^{5} volume cells in the flowfield, and 1.49×10^{5} surface elements. As an example, the $\Psi = 75^{\circ}$ orientation is presented. All slices of the flowfield are taken at $X = 0$ m, which is the center slice of the REBR showing the Y-Z plane. The REBR body is represented by the white "cut-out" of the slice of the body.

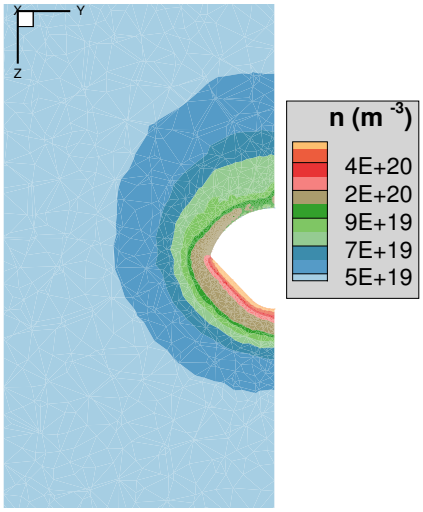

(a)

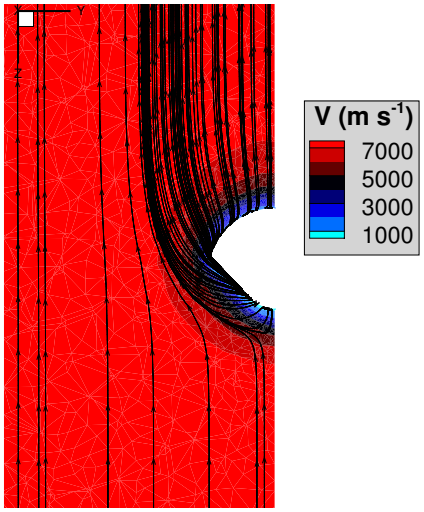

(b)

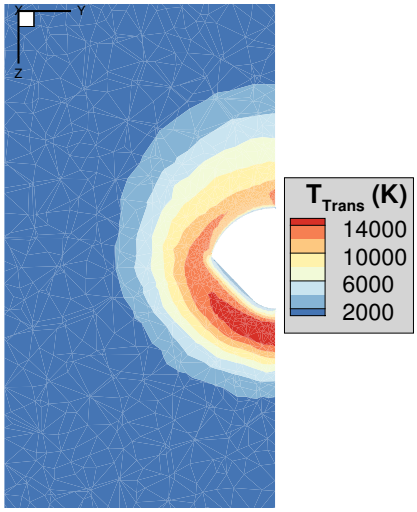

(c)

Figure 4.24: Flowfield contours at $Kn = 0.1$, $\Psi = 75°$: (a) number density; (b) velocity; (c) translational temperature.

Figure 4.24 shows the flowfield contours. In Figure 4.24 (b), the velocity streamlines are plotted. The velocity Ψ value of $75°$ cannot be immediately seen from the streamlines but is noticeable in differences in qualitative appearance of flowfield disturbances when compared to Figures 4.6 and 4.15. The velocity Ψ deflection is out-of-frame of the slice taken; this slice is taken to demonstrate the half-REBR modeled body and flowfield.

In Figure 4.24, the flowfield is beginning to resemble a shock in front of the REBR body: the "bubble" of disturbed flow upstream of the REBR is reduced in area when compared to results from higher Knudsen numbers. This is indicative of higher density, higher speed flow, as the regime moves from free-molecular to transitional flow that is dense enough to create a shock layer.

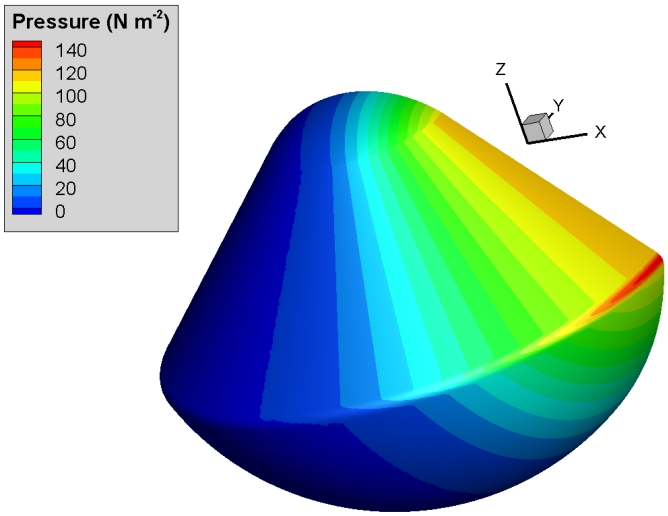

(a)

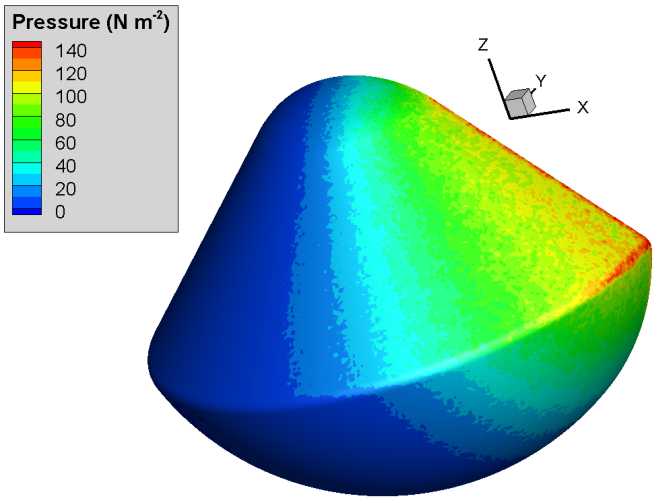

(b)

Figure 4.25: Pressure distribution at $Kn = 0.1$, $\Psi = 75°$: calculated using: (a) free molecular theory; (b) DSMC.

Figures 4.25 display an example of the surface pressure on the REBR for the $\Psi = 75^{\circ}$ case.

The pressure distributions are as such: the average pressure experienced by the surface elements is calculated as 21.5 N m^{-2} using the free-molecular method. The average pressure experienced over the body calculated by using MONACO results is 22.8 $\pm 1.14 \times 10^{-2}$ N m^{-2}. Again, the average is calculated the same way as in Section 4.2 and is weighed by each surface element area. The difference in average pressure experienced by the body at this orientation is is 5.71%. Immediately, the difference in modeling approaches at this altitude is notable: collisions matter at this altitude and will effect aerodynamic results to a high degree.

4.4.1 $Kn = 0.1$: Drag and Lift

Now the drag and lift experienced over the body are compared between the two models. As in Section 4.2, the drag and lift forces plotted and discussed in this section apply to only the half of the REBR that is meshed and simulated. For use in realistic projections, such as the orbital decay model, the forces are duplicated to represent the entire body.

The forces are treated in the same was as in Section 4.2 and 4.3: to compare models, the drag and lift forces gathered for each modeled orientation in Table B.1 are interpolated over all values of Ψ to yield an average value in this section. For the orbital decay model, a weighted average is applied.

Figure 4.26 shows the calculated drag for all orientations using both approaches. The data points for individual simulation results are connected using splines to demonstrate the smooth transition of drag experienced as body rotation would occur. The Poisson statistical error for MONACO DSMC simulations is calculated as in Equation 3.1. Using Equation 3.1, the average

hits per sampling time step per surface element across the REBR at this Knudsen number is 1.19×10^{-3}, the total number of surface elements is 1.49×10^{5}, and using 25,000 sampling steps: the Poisson statistical error of aerodynamic DSMC results is 0.05%. Again, this error is small enough that it is not plotted in the following figures.

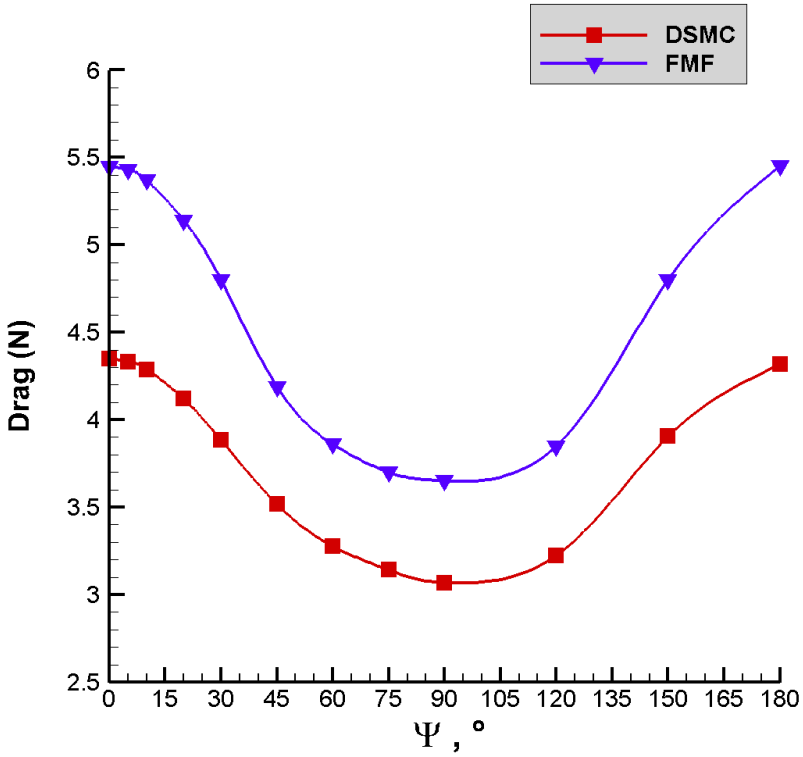

Figure 4.26: Drag calculated using DSMC and free-molecular (FMF) analytical models for all orientations analyzed of the REBR at a Knudsen number of 0.1.

Figure 4.26 shows that maximum drag values are achieved for $\Psi = 0°$ and $\Psi = 180°$, while minimum drag is achieved for $\Psi = 90°$. The same features of this plot can be seen in Figures 4.8 and 4.17: the maxima and minima correspond to the maximum and minimum flow-exposed projected areas. When $\Psi = 0°$ or $\Psi = 180°$, the flow encounters either the spherical heat shield or the incident nose cone, exposing the entire circular projected area to the incoming flow. When $\Psi = 90°$, the flow encounters the conical "side" of the REBR, and a half-circle section of the

semispherical heat shield.

Qualitatively, Figure 4.26 portrays the growing differences in the forces yielded by the DSMC and free-molecular modeling approaches. The free-molecular model yields much higher drag as it applies a constant pressure to every surface element experiencing flow with the same normal vector. The DSMC method, in using particles, models real-world diffusive effects of particles colliding with the surface, and therefore yields less pressure and therefore less drag. For shear stress, the DSMC tracking of the collisions' transfer of tangential momentum to the surface actually yields an increase in the resulting lift, versus the free-molecular analytical model.

The average drag calculated using the MONACO results interpolated across all orientations is $3.62 \pm 1.70 \times 10^{-3}$ N. The average drag calculated using the free-molecular results is 4.40 N. The percent difference between the averages is 21.6%. This reflects the fact that the free-molecular assumption is failing at this altitude, as the margin of error between the free-molecular analytical model and the DSMC model grows. The normalized root-mean-square deviation between all the drag results across both models is 19.0%, reflecting the disagreement between the models.

The differences between models at $Kn = 0.1$, compared to more rarefied regimes, is evident. Particle collisions are having a quantifiable effect on the flowfield. At $Kn = 0.1$, there are around 5500 collisions in the flowfield per DSMC time step. The number of collisions is non-negligable, and changes the flow before the flow impacts the REBR surface. The energy of the flow is dissipated due to collisions, causing the DSMC pressure, and drag, to be lower overall. In addition, the particle collisions with the surface have a dissipative effect over the surface planes, in contrast with the free-molecular analytical method, which does not account for differing flowfield properties across the body.

Figure 4.27 shows the calculated lift for all orientations using both methods. The lift displayed

in Figure 4.27 is translated into an Earth-centric frame, yielding positive lift. Lift is at least an order of magnitude smaller compared to drag due to the REBR's resemblance to a sphere. Resolved as described in Chapter 2, nearly all force applied to the REBR body is attributed to drag. Unless a pressure gradient in a normal direction to the oncoming velocity is created by the body's geometry, drag will be the dominating force.

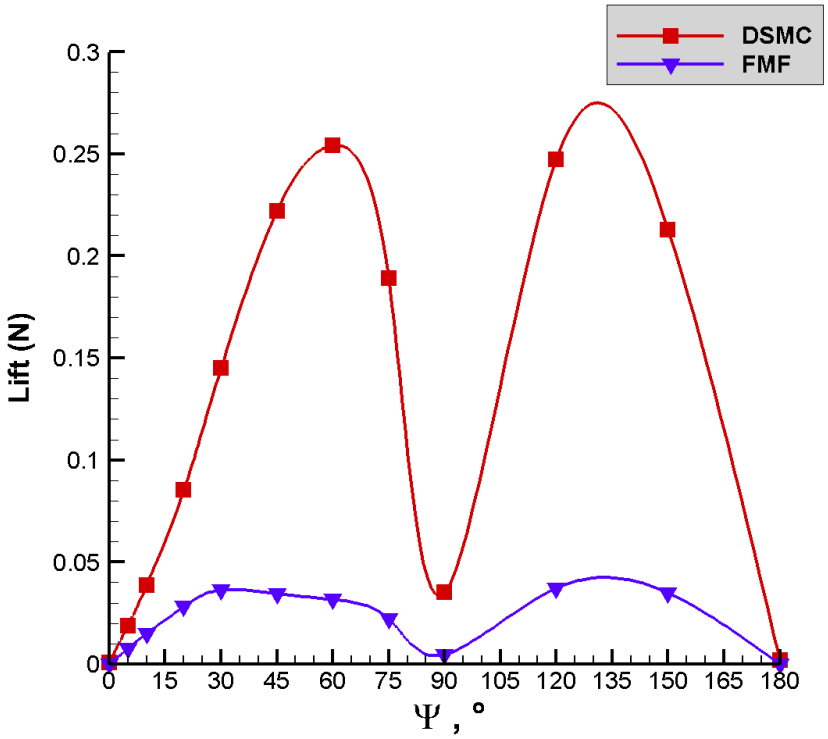

Figure 4.27: Lift calculated using DSMC and free-molecular (FMF) analytical models for all orientations of the REBR at a Knudsen number of 0.1.

Qualitatively, it is evident that the lift curves in Figure 4.27 are further apart than for drag as shown in Figure 4.26. As in Section 4.2, this discrepancy is examined in further detail to understand the differences between the modeling approaches.

To examine the modeling differences, both pressure and shear stress contributions to the lift force are inspected below. Figure 4.28 displays the pressure contribution to the lift force for both

models, while Figure 4.29 displays the shear stress contribution to the lift force for both models.

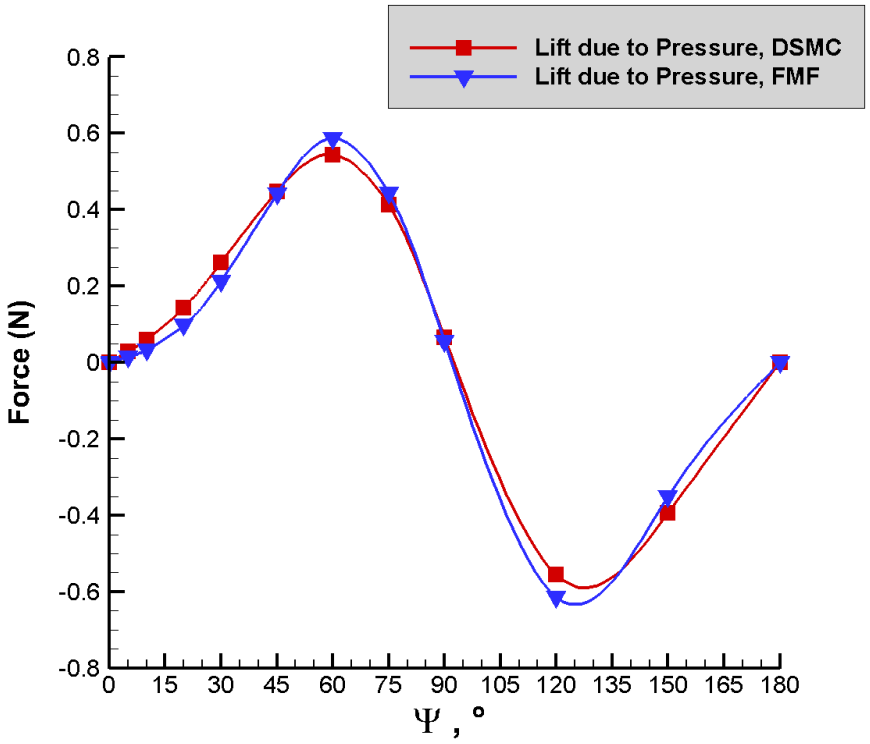

Figure 4.28: Lift due to pressure on the REBR, calculated using DSMC and free-molecular (FMF) analytical models for all orientations at a Knudsen number of 0.1.

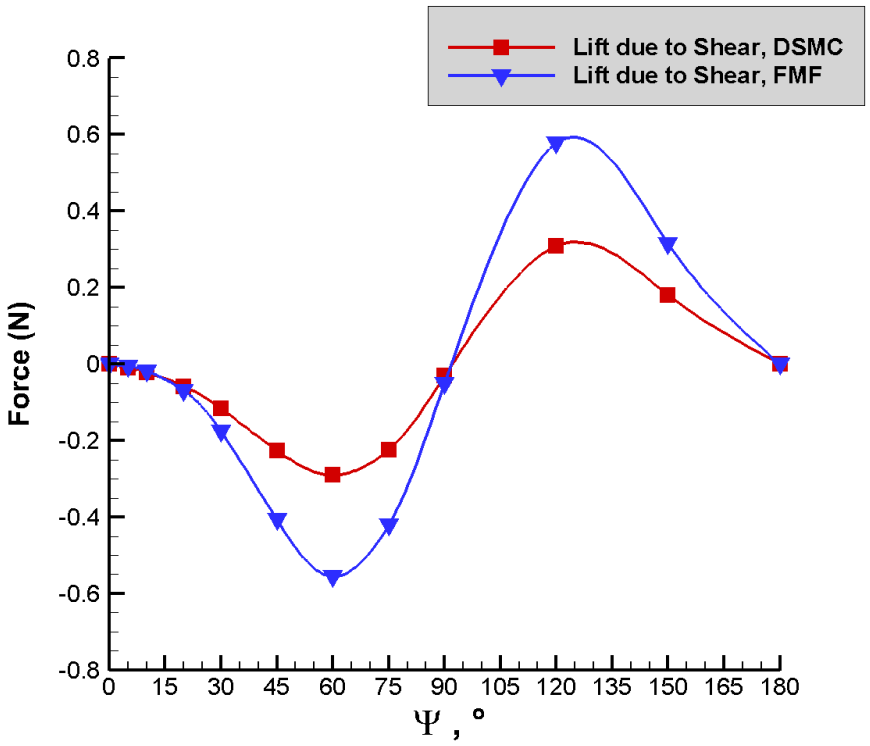

Figure 4.29: Lift due to shear stress on the REBR, calculated using DSMC and free-molecular (FMF) analytical models for all orientations at a Knudsen number of 0.1.

Figures 4.28 and 4.29 display much better agreement between the modeling approaches than Figure 4.27. Contributions to the lift are canceling out in a way that magnifies the differences between the models. Figure 4.29 shows the more extreme differences in the shear stress yields of both models; as discussed in Section 4.2, the free-molecular modeling of the shear stress is more extreme because the particles are not modeled individually and there is no diffusion in particle momentum across the planes of the body. While Figures 4.28 and 4.29 display some agreement between the models at this Knudsen number, comparisons with Figures 4.10, 4.11, 4.19, and 4.20 clearly show that the free molecular assumption is weaker at this Knudsen number and resulting in significant differences from the DSMC model.

Quantitatively, the normalized root-mean-square deviation between all the lift due to pressure

results across both models is 14.3%. The normalized root-mean-square deviation between all the lift due to shear stress results across both models is 64.9%. These error results are also inflated due to the data points at $\Psi = 0^\circ$ and 180° being close to zero, but orders of magnitude apart, sometimes even with sign differences. These data points are enumerated in Table 4.8. Only a few surface elements need to be influenced by shear stress in order to cause a result so close to zero to "flip" signs. The free-molecular results at these Ψ values are consistent with those a Knudsen number of 1, showing the consistent results that the free-molecular analytical model yields.

Table 4.8: Lift due to pressure and shear stress on the REBR at specific Ψ values for a Knudsen number of 0.1.

Lift due to Pressure (N)		
	FMF	**DSMC**
$\Psi = 0^\circ$	-6.39×10^{-6}	1.11×10^{-3} $\pm 5.53 \times 10^{-7}$
$\Psi = 180^\circ$	-3.52×10^{-6}	-4.53×10^{-4} -2.27×10^{-7}
Lift due to Shear Stress (N)		
	FMF	**DSMC**
$\Psi = 0^\circ$	5.88×10^{-6}	6.36×10^{-4} $\pm 3.18 \times 10^{-7}$
$\Psi = 180^\circ$	1.48×10^{-6}	-4.54×10^{-4} -2.27×10^{-7}

To take the total lift across the body, the lift due to pressure and the lift due to shear stress are summed. This results in lift values close to zero when compared with drag values; and the discrepancies in both contributing forces are magnified; yielding the curves in Figure 4.27. Because the lift is small when compared to drag results, the differences between models will not greatly change any orbital decay results. These differences in lift and lift contribution forces are expected to increase further as Knudsen number decreases.

In order to calculate coefficients of drag and lift for use in the orbital decay model, a free-

stream density is taken from [9]. At 91 km, where for REBR $Kn = 0.1$, the free-stream density $\rho = 2.29 \times 10^{-6}$ kg m^{-3}. The orbital velocity is the circular orbital speed used throughout the $Kn = 0.1$ results: $V = 7850$ m s^{-1}. The aerodynamic coefficients are calculated as described in Section 4.2.

Figure 4.30 shows $C_D A$ and $C_L A$ calculated for all models and orientations for $Kn = 0.1$ experienced by the REBR body.

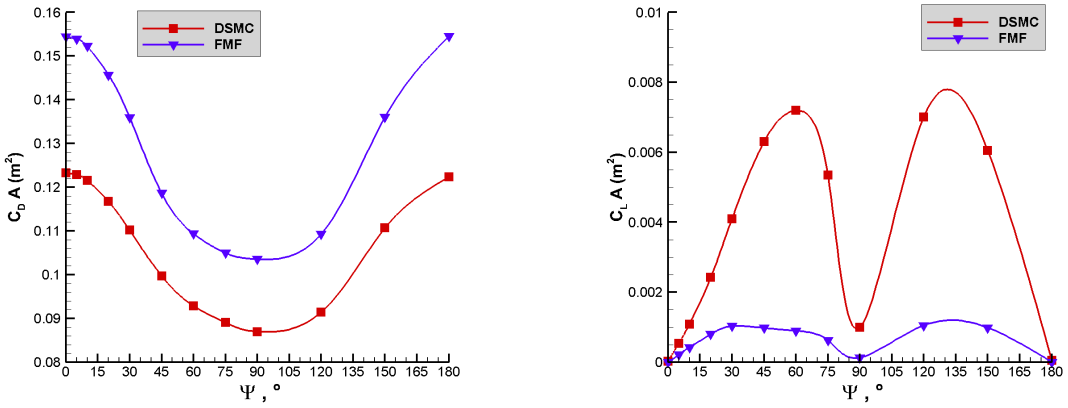

(a) (b)

Figure 4.30: Drag (a) and lift (b) coefficients calculated using DSMC and free-molecular (FMF) analytical models for all experiment orientations of the REBR using both models for a Knudsen number of 0.1.

The average $C_D A$ calculated using the DSMC MONACO modeling results is $1.03 \times 10^{-1} \pm 4.87 \times 10^{-5}$ m^2, while the average $C_D A$ calculated using the free-molecular analytical modeling results is 1.25×10^{-1} m^2. The percent difference between the averages is 21.6%. The normalized root-mean-square deviation between all the $C_D A$ results across both models is 19.0%. The average $C_L A$ calculated using the DSMC MONACO modeling results is $5.96 \times 10^{-3} \pm 2.83 \times 10^{-6}$ m^2, while the average $C_L A$ calculated using the free-molecular analytical modeling results is 9.93×10^{-4} m^2. The root-mean-square difference between all the $C_L A$ results across both models is 7.08×10^{-3}

m^2. The same higher-than-expected discrepancy is seen qualitatively between the coefficient of lift curves in Figure 4.30 (b), and the error between them is exponentially elevated due to the problems discussed above. The differences between modeling approach results for drag, lift, C_DA and C_LA are much bigger when compared to Sections 4.2 and 4.3. At this Knudsen number, collisions are important, and are effecting results that will have bigger implications when examining other models, such as orbital decay.

4.4.2 $Kn = 0.1$: Moments and Angular Accelerations

Moments are treated in the same way as determined in Section 4.2.2. The angular acceleration uncertainty again equates to: 2.98×10^{-2} radians s^{-2}, or 1.71 degrees s^{-2}

Figure 4.31 displays the moment results about the three primary axes yielded by both models across all the REBR orientations. Figures 4.31 (a) and (c) mirror the results seen in Figures 4.13 (a) and (c) and 4.22 (a) and (c), but at a larger scale, proportional to the larger forces induced on the body in less-rarefied flow at a higher orbital speed.

Figure 4.31 (b) displays the "smoothing out" of the second maxima when applying the DSMC model. The free-molecular model continues to oscillate about zero, while the DSMC results give a strong Y-moment at $\Psi = 45°$ and $60°$, and a small negative moment at $\Psi = 120°$ and $150°$. The aerodynamic shape of the REBR's domed heat shield does not yield a moment as the flow becomes more dense and continuum-like.

All these differences qualitatively reinforce the fact that the free-molecular modeling approach is becoming less adequate at this Knudsen number: the differences are visible.

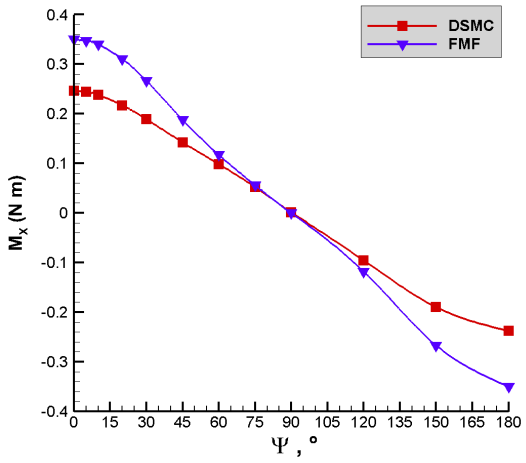

(a)

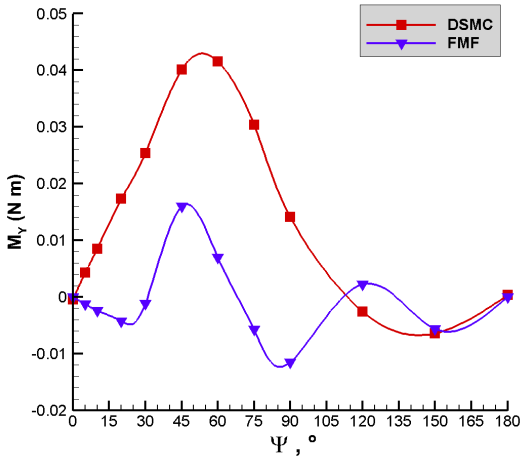

(b)

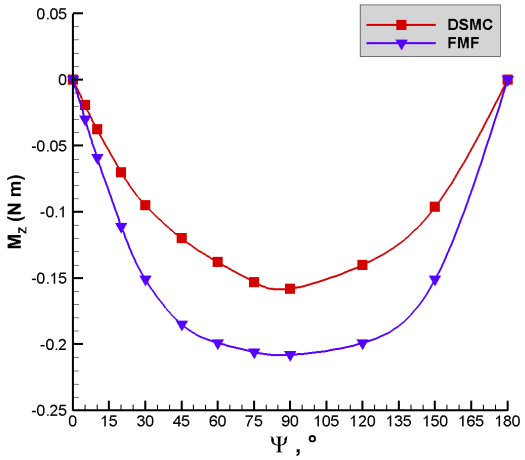

(c)

Figure 4.31: Moments calculated using DSMC and free-molecular (FMF) analytical models for all experiment orientations of the REBR about the: (a) X axis; (b) Y axis; (c) Z axis, for a Knudsen number of 0.1.

The moment averages are listed in Table 4.9.

The sign difference between the Y-moment interpolated averages in Table 4.9 is explained by examining Figure 4.31. The free-molecular method yields oscillatory moments about zero, while the DSMC results have a large positive maxima which pushes the average positive. The free-

Table 4.9: Average moments calculated for a Knudsen number of 0.1 for the DSMC and free-molecular analytical modeling approaches across all Ψ values.

Average	FMF	DSMC
$\mathbf{M}_X$ **(N m)**	1.17×10^{-3}	2.41×10^{-3} $\pm 1.15 \times 10^{-6}$
$\mathbf{M}_Y$ **(N m)**	-1.02×10^{-3}	1.28×10^{-2} $\pm 6.41 \times 10^{-6}$
$\mathbf{M}_Z$ **(N m)**	-1.53×10^{-1}	-1.06×10^{-1} $\pm 5.03 \times 10^{-5}$

molecular average is much closer to zero, and negative due to the minima at $\Psi = 90^{\circ}$.

The normalized root-mean-square deviation between all the X-axes moments is 33.3%. The normalized root-mean-square deviation between the Y-axes moments is 42.9%. The normalized root-mean-square deviation between the Z-axes moments is 36.7%. These deviation's clearly show the lack of agreement between the models at this Knudsen number.

Because the Y-moments are the only ones that are non-zero across the whole REBR body, the angular acceleration about the Y-axis is examined more thoroughly here. In this section angular acceleration uncertainty is plotted and discussed. As stated in previous sections, plotting the angular rotational uncertainty gives an intuitive picture of where aerodynamic moments would affect the overall motion of the body. The Y-axis angular acceleration uncertainty is treated the same way as in Chapter 3 and is 2.98×10^{-2} radians s^{-2}, or 1.71 degrees s^{-2}, plotted as an error bar in all of the angular acceleration plots in this chapter.

Figure 4.32 shows the calculated angular acceleration about the Y-axis for the REBR body using both models across all orientations, with error bars as described previously. In Figure 4.32, the Y-moments across the orientations have been doubled, then divided by I_{YY}, to represent the moments incurred by the entire REBR body. The interpolated average angular accelerations about the Y-axis incurred are $12.6 \pm 6.00 \times 10^{-3}$ degrees s^{-2} using the DSMC method and -0.99 degrees

s^{-2} using the free-molecular analytical method. The reason for the sign change is the same as the reason for the sign change between the average Y-moments. The oscillatory nature of the free-molecular results yields an average close to zero; while the maxima of the DSMC results yields a positive average.

The normalized root-mean-square deviation between the angular accelerations about the Y-axis is 42.9%. These results reflect the inaccuracy of the free-molecular assumption as Knudsen number lowers, as the differences between models are increasing when compared to results at $Kn = 10$ or $Kn = 1$.

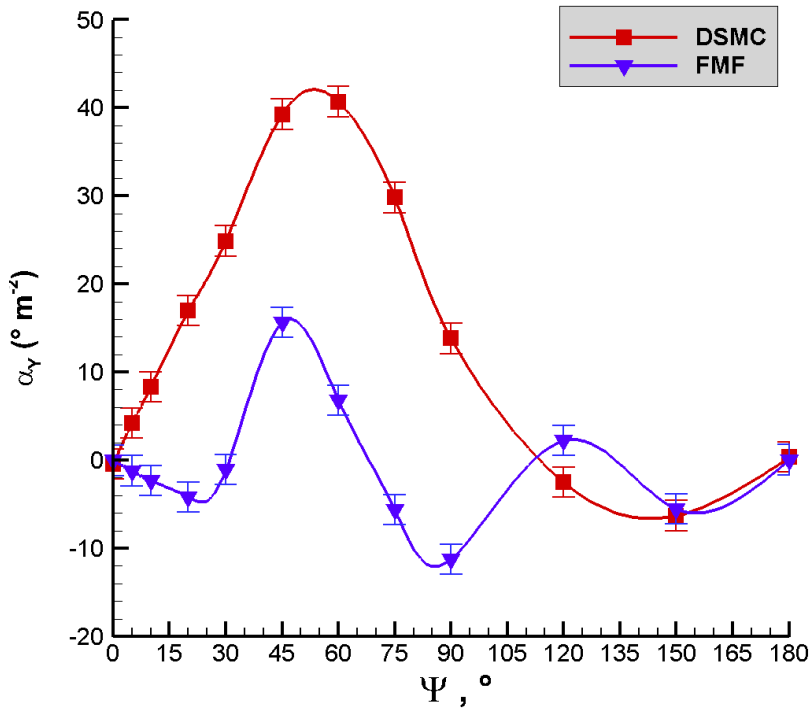

Figure 4.32: Angular acceleration about the Y-axis calculated using DSMC and free-molecular (FMF) analytical models for all experiment orientations of the REBR, for a Knudsen number of 0.1. Error bars reflect the angular velocity uncertainty of 1.71 degrees s^{-2}.

The error bars in Figure 4.32 illustrate the effect the aerodynamic Y-moment has on the tumbling behavior of the REBR. The effect of the moments, whose magnitudes are large because the

forces at this Knudsen number are large, outsize the effect of an imposed angular velocity of 5 degrees s^{-1}.

4.5 Knudsen Number of 0.01

A Knudsen number of 0.01 is achieved for the REBR body at 77 km of altitude. A Knudsen number of 0.01 is the limit of defined transitional flow, at lower altitudes than this, the continuum approximation can apply [20]. At this Knudsen number, the flowfield is dense, and much less rarefied. The free-molecular model is expected to fail at this altitude and yield exceedingly different results when compared to DSMC results, due to particle collisions. The circular orbital speed and atmospheric composition at this altitude are listed in Table 4.1. A different surface mesh is used for this altitude, in the DSMC method, in order to achieve cell sizes with side lengths smaller than the mean free path.

The REBR surface elements used at this altitude have a side length average of 2.5×10^{-4} m in order to be smaller than the free-stream mean free path compressed by a factor of 10 (2.80×10^{-4} m). This refinement yields 4.82×10^{6} volume cells in the flowfield, and 7.82×10^{5} surface elements. As an example, the $\Psi = 5^{\circ}$ orientation is presented. All slices of the flowfield are taken at $X = 0$ m, which is the center slice of the REBR showing the Y-Z plane. The REBR body is represented by the white "cut-out" of the slice of the body.

For the free-molecular method, the surface mesh defined in Section 4.4 is used. The free-molecular method is applied using MATLAB, and the wall time for a surface mesh of 7.82×10^{5} cells is undesirable, as MATLAB is only parallel-capable up to the compatibility of an individual desktop, commonly a maximum of eight cores. The computational time of checking if each of

7.82×10^5 cells is blocked by any of the other 7.82×10^5 cells is exceptional. Additionally, the free-molecular method results do not change to a detectable level according to surface cell refinement as long as the shape of the body is represented [36]. This is because the free-molecular analytical application applying the same surface properties to any surface element that experiences flow with the same surface normal. Therefore, it is appropriate and desirable to use the $Kn = 0.1$ surface mesh for use in the free-molecular approach, with 1.49×10^5 cells.

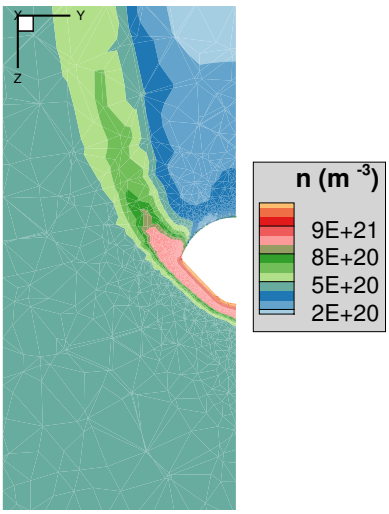

(a)

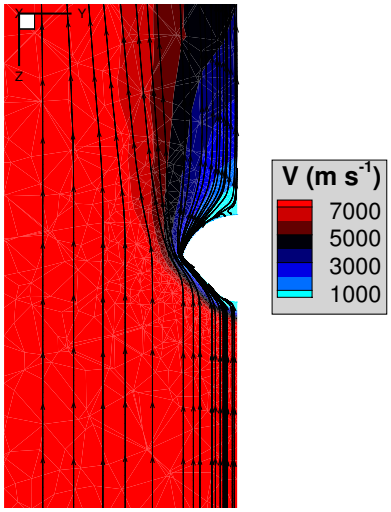

(b)

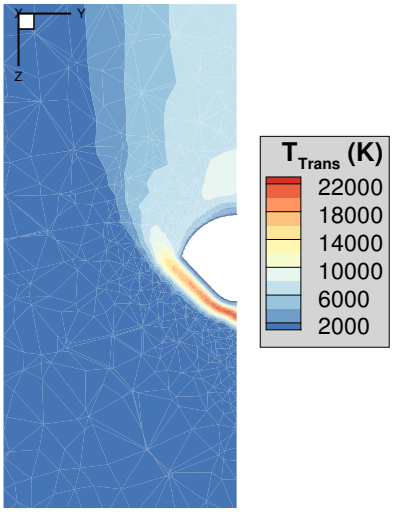

(c)

Figure 4.33: Flowfield contours at $Kn = 0.01$, $\Psi = 5°$: (a) number density; (b) velocity; (c) translational temperature.

Figure 4.33 shows the flowfield contours. In Figure 4.33 (b), the velocity streamlines are plotted, and the Ψ value of $5°$ is not immediately noticeable; as it is a slight deflection off-plane. However, when compared to Figure 4.6 (b), which display a $\Psi = 0°$ streamlines, a slight difference can be noted, due to the $5°$ deflection. Figure 4.33 shows a fully-developed shock layer which forms since the regime is denser than the previous Knudsen number regimes examined. Figure

4.33 (a) displays the compressed density post-shock directly upstream of the REBR; with very low-density flow behind the REBR as it blocks the oncoming flow. Similarly, Figure 4.33 (c) displays the super-heated temperature post-shock, and the relatively cooler air downstream of the REBR.

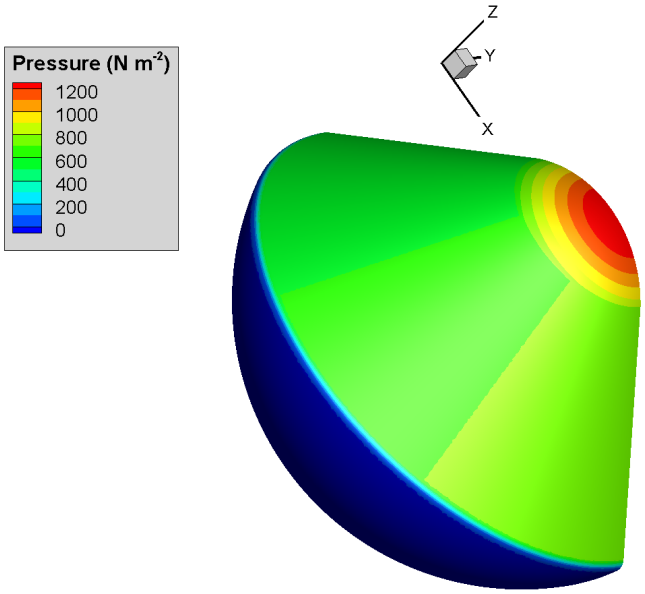

(a)

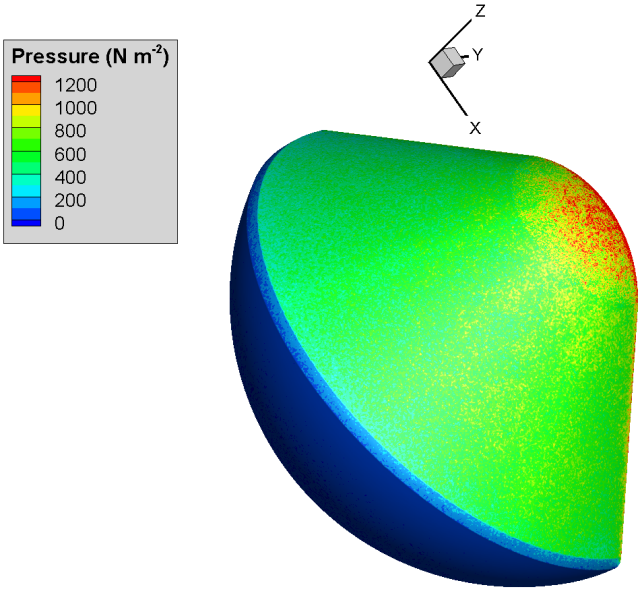

(b)

Figure 4.34: Pressure distribution at $Kn = 0.01$, $\Psi = 5°$: calculated using: (a) free molecular theory; (b) DSMC.

Figures 4.34 display an example of the surface pressure on the REBR for the $\Psi = 5^{\circ}$ case.

The pressure distributions are differing, which can be qualitatively seen in Figure 4.34. The DSMC method yields a diffusive pressure distribution, while the free-molecular analytical equations yield a consistent lessening of pressure over the sphere surface according to the curvature change. In addition, the maximum pressure is vastly different: the maximum pressure on a surface element yielded by the DSMC method is 2620 $\pm$ 1.88 N m^{-2}. The maximum pressure yielded by the free-molecular analytical method is 1310 N m^{-2}. This a 50% difference in maximum pressure!

Again, the average is calculated the same way as in Section 4.2 and is weighed by each surface element area. The average pressure experienced by the surface elements is calculated as 318 N m^{-2} using the free-molecular method. The average pressure experienced over the body calculated by using MONACO results is 279 $\pm$0.17 N m^{-2}. The difference in average pressure experienced by the body at this orientation is is 13.9%. This margin of error reflects what is shown qualitatively in Figure 4.34: the free-molecular analytical model fails at this Knudsen number due to the importance of collisions in the flowfield.

4.5.1 $Kn = 0.01$: Drag and Lift

Now the drag and lift experienced over the body are compared between the two models. As in Section 4.2, the drag and lift forces plotted and discussed in this section apply to only the half of the REBR that is meshed and simulated. For use in realistic projections, such as the orbital decay model, the forces are duplicated to represent the entire body.

The forces are treated in the same was as in Section 4.2, 4.3, and 4.4: to compare models, the drag and lift forces gathered for each modeled orientation in Table B.1 are interpolated over

all values of Ψ to yield an average value in this section. For the orbital decay model, a weighted average is applied.

Figure 4.35 shows the calculated drag for all orientations using both approaches. The data points for individual simulation results are connected using splines to demonstrate the smooth transition of drag experienced as body rotation would occur. In Figure 4.35, the error bars are the Poisson statistical error of the DSMC results due to the number of hits experienced by the body per surface element per time step. The Poisson statistical error for MONACO DSMC simulations is calculated as in Equation 3.1. Using Equation 3.1, the average hits per sampling time step per surface element across the REBR at this Knudsen number is 2.49×10^{-4}, the total number of surface elements is 7.82×10^{5}, and using 25,000 sampling steps: the Poisson statistical error of aerodynamic DSMC results is 0.05%. Again this is not plotted in the following figures because it is so small.

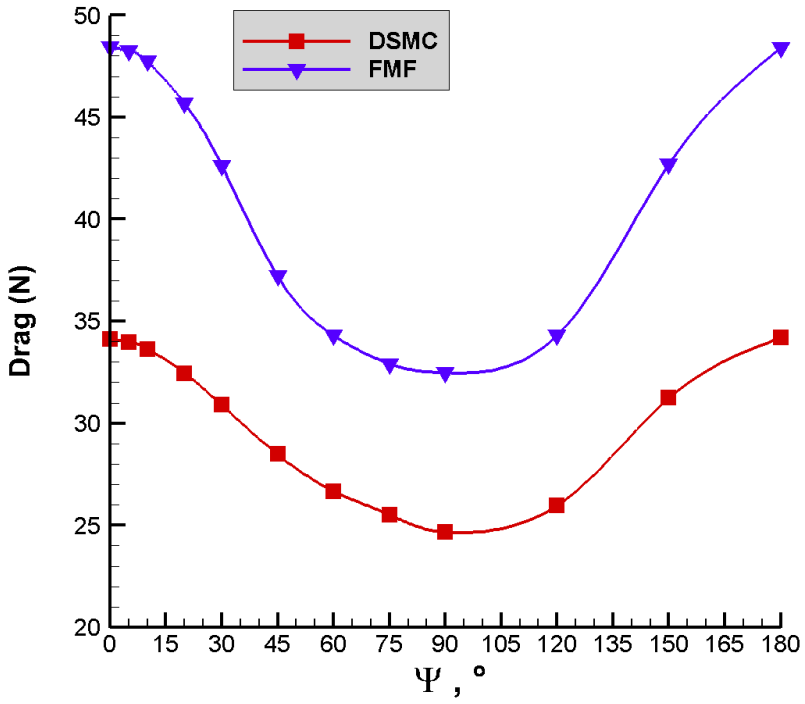

Figure 4.35: Drag calculated using DSMC and free-molecular (FMF) analytical models for all orientations analyzed of the REBR at a Knudsen number of 0.01.

Figure 4.35 shows that maximum drag values are achieved for $\Psi = 0°$ and $\Psi = 180°$, while minimum drag is achieved for $\Psi = 90°$. The same features of this plot can be seen in Figures 4.8, 4.17, and 4.26: the maxima and minima correspond to the maximum and minimum flow-exposed projected areas. When $\Psi = 0°$ or $\Psi = 180°$, the flow encounters either the spherical heat shield or the incident nose cone, exposing the entire circular projected area to the incoming flow. When $\Psi = 90°$, the flow encounters the conical "side" of the REBR, and a half-circle section of the semispherical heat shield.

Figure 4.26 portrays the nearly 15 N difference in the drag forces yielded by the DSMC and free-molecular models. The free-molecular model yields much higher drag as it applies a constant pressure to every surface element experiencing flow with the same normal vector. At this Knud-

sen number, the free-molecular assumption breaks down completely, yielded free-molecular drag results that are up to 50% higher than the DSMC results. The DSMC method, in using particles, models real-world diffusive effects of particles colliding with the surface, and therefore yields less pressure and therefore less drag. For shear stress, the DSMC tracking of the collisions' transfer of tangential momentum to the surface actually yields and increase in the resulting lift, versus the free-molecular analytical model.

The average drag calculated using the MONACO results interpolated across all orientations is $29.0 \pm 1.31 \times 10^{-2}$ N. The average drag calculated using the free-molecular results is 39.1 N. The percent difference between the averages is 35.1%. This reflects the fact that the free-molecular assumption fails at this altitude, as the margin of error between the free-molecular analytical model and the DSMC model is large. The normalized root-mean-square deviation between all the drag results across both models is 27.8%.

The differences between models at $Kn = 0.01$, compared to rarefied regimes, is evident. Particle collisions are extremely important at this Knudsen number, and change the flowfield handily. The shock layer in Figure 4.34 as opposed to Figures 4.7, 4.16, and 4.25, is evident of the flowfield changing significantly before impacting the surface. At $Kn = 0.01$, there are around 39500 collisions in the flowfield per DSMC time step. The number of collisions every time step is large, and changes the flow before the flow impacts the REBR surface. The nature of collisions with the surface matters too; yielding the difference in things such as maximum pressure experienced on the surface.

Figure 4.36 shows the calculated lift for all orientations using both methods. The lift displayed in Figure 4.36 is translated into an Earth-centric frame, yielding positive lift. Lift is over an order of magnitude smaller compared to drag due to the REBR resembling a sphere, which would ex-

perience no lift at all angles. Resolved as described in Chapter 2, nearly all force applied to the REBR body is attributed to drag. Unless a pressure gradient in a normal direction to the oncoming velocity is created by the body's geometry, drag will be the dominating force.

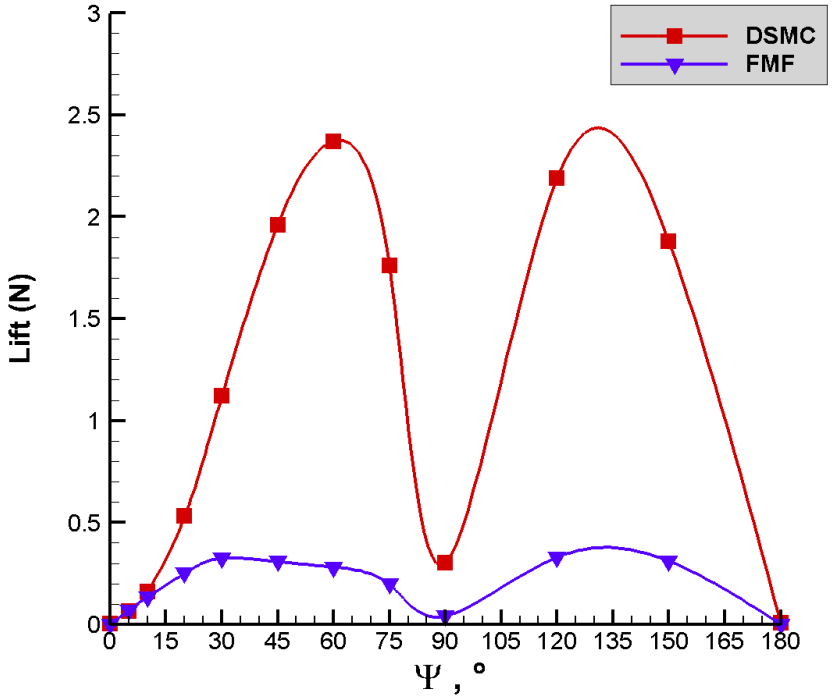

Figure 4.36: Lift calculated using DSMC and free-molecular (FMF) analytical models for all orientations of the REBR at a Knudsen number of 0.01.

Qualitatively, it is evident that the lift curves in Figure 4.36 are further apart than for drag as shown in Figure 4.35. As in the previous sections, this discrepancy is examined in further detail to understand the differences between the modeling approaches.

To examine the modeling differences, both pressure and shear stress contributions to the lift force are inspected below. Figure 4.37 displays the pressure contribution to the lift force for both models, while Figure 4.38 displays the shear stress contribution to the lift force for both models.

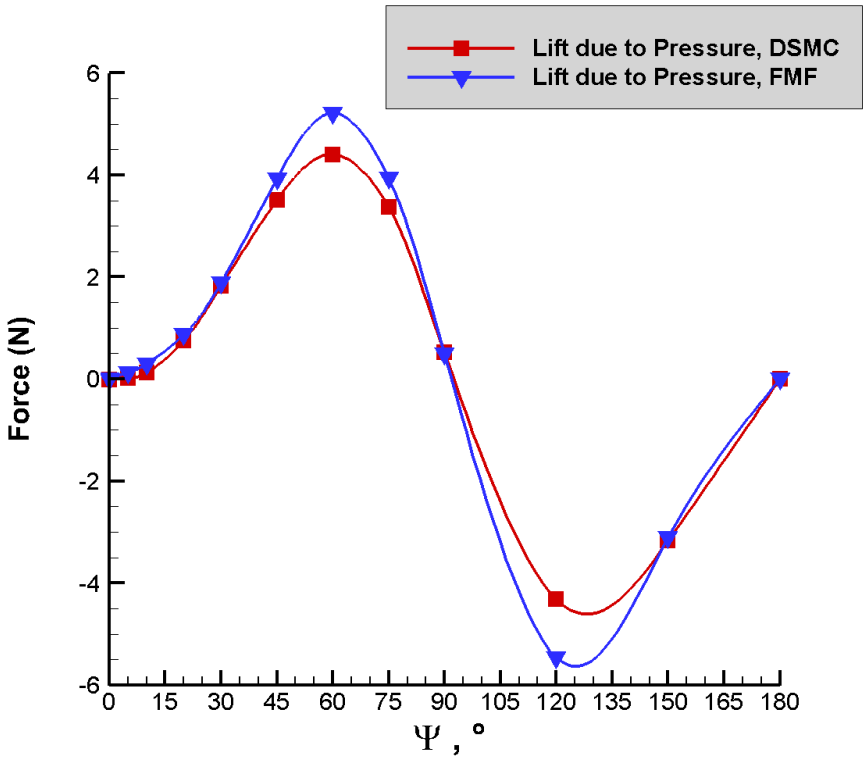

Figure 4.37: Lift due to pressure on the REBR, calculated using DSMC and free-molecular (FMF) analytical models for all orientations at a Knudsen number of 0.01.

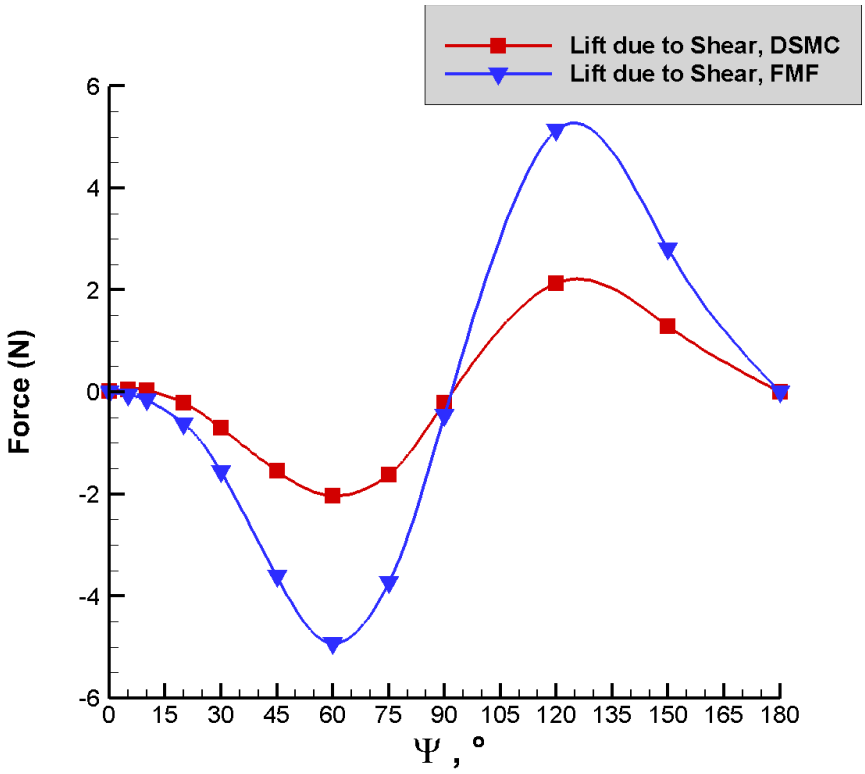

Figure 4.38: Lift due to shear stress on the REBR, calculated using DSMC and free-molecular (FMF) analytical models for all orientations at a Knudsen number of 0.01.

Figures 4.37 and 4.38 display much better agreement between the modeling approaches than Figure 4.36. Contributions to the lift are canceling out in a way that magnifies the differences between the models. Figure 4.38 shows the more extreme differences in the shear stress yields of both models; as discussed in Section 4.2, the free-molecular modeling of the shear stress is more extreme because the particles are not modeled individually and there is no diffusion in particle momentum across the planes of the body. While Figure 4.37 displays some tentative agreement between the models at this Knudsen number, Figure 4.38 clearly shows drastic differences between the modeling approaches. Additionally, comparisons with Figures 4.10, 4.11, 4.19, 4.20, and 4.28, and 4.29 show that the free molecular assumption is inadequate for modeling this non-rarefied Knudsen number.

Quantitatively, the normalized root-mean-square deviation between all the lift due to pressure results across both models is 21.6%. The normalized root-mean-square deviation between all the lift due to shear stress results across both models is 81.5%. These error results are also inflated due to the data points at $\Psi = 0^\circ$ and 180° being close to zero, but orders of magnitude apart, sometimes even with sign differences. These data points are enumerated in Table 4.10. Only a few surface elements need to be influenced by shear stress in order to cause a result so close to zero to "flip" signs. The free-molecular results at these Ψ values are consistent with those at higher Knudsen numbers, showing the consistent results that the free-molecular analytical model yields.

Table 4.10: Lift due to pressure and shear stress on the REBR at specific Ψ values for a Knudsen number of 0.01.

Lift due to Pressure (N)		
	FMF	**DSMC**
$\Psi = 0^\circ$	-5.58×10^{-5}	6.46×10^{-3} $\pm 3.23 \times 10^{-6}$
$\Psi = 180^\circ$	-3.25×10^{-5}	-1.38×10^{-2} -6.89×10^{-6}
Lift due to Shear Stress (N)		
	FMF	**DSMC**
$\Psi = 0^\circ$	5.21×10^{-4}	-8.28×10^{-4} $\pm -4.14 \times 10^{-7}$
$\Psi = 180^\circ$	1.34×10^{-5}	9.28×10^{-3} 4.64×10^{-6}

To take the total lift across the body, the lift due to pressure and the lift due to shear stress are summed. This results in lift values close to zero when compared with drag values; and the discrepancies in both contributing forces are magnified; yielding the curves in Figure 4.36. Because the lift is small when compared to drag results, the differences between models will not greatly change any orbital decay results. The differences in lift, though magnified, still show that the free-molecular results significantly differs from the DSMC results at this Knudsen number.

In order to calculate coefficients of drag and lift for use in the orbital decay model, a free-stream density is taken from [9]. At 77 km, where for REBR $Kn = 0.01$, the free-stream density $\rho = 2.03 \times 10^{-5}$ kg m^{-3}. The orbital velocity is the circular orbital speed used throughout the $Kn = 0.01$ results: $V = 7860$ m s^{-1}. The aerodynamic coefficients are calculated as described in Section 4.2.

Figure 4.39 shows C_DA and C_LA calculated for all models and orientations for $Kn = 0.10$ experienced by the REBR body.

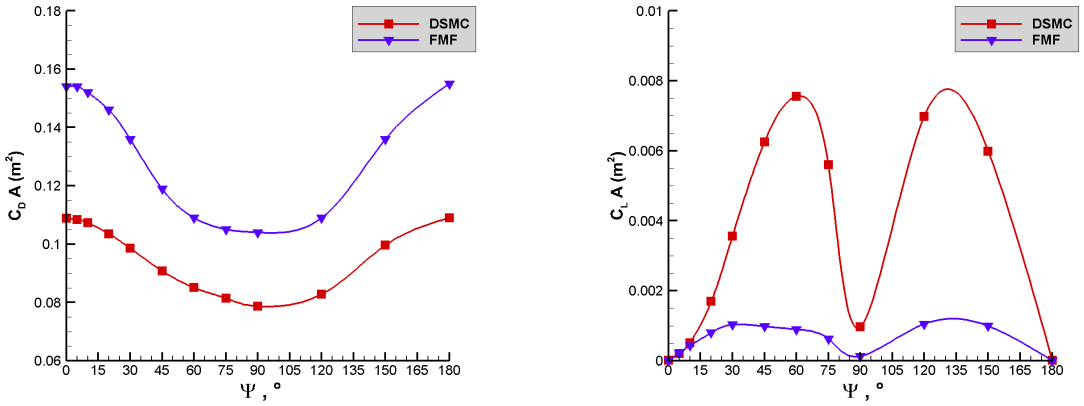

(a) (b)

Figure 4.39: Drag (a) and lift (b) coefficients calculated using DSMC and free-molecular (FMF) analytical models for all experiment orientations of the REBR using both models for a Knudsen number of 0.01.

The average C_DA calculated using the DSMC MONACO modeling results is $9.24 \times 10^{-2} \pm 4.18 \times 10^{-5}$ m^2, while the average C_DA calculated using the free-molecular analytical modeling results is 1.25×10^{-1} m^2. The percent difference between the averages is 35.1%. The normalized root-mean-square deviation between all the C_DA results across both models is 27.8%. The average C_LA calculated using the DSMC MONACO modeling results is $5.95 \times 10^{-3} \pm 2.70 \times 10^{-6}$ m^2, while the average C_LA calculated using the free-molecular analytical modeling results is 9.95×10^{-4}

m^2. The same higher-than-expected discrepancy is seen qualitatively between the coefficient of lift curves in Figure 4.30 (b), and the error between them is exponentially elevated due to the problems discussed above.

The differences between modeling approach results for drag, lift, C_DA and C_LA are bigger when compared to Sections 4.2, 4.3, and 4.4 . At this Knudsen number, collisions are necessary to model an accurate flowfield, and therefore effect surface properties and net forces. The free-molecular modeling approach is invalidated at this Knudsen number.

4.5.2 $Kn = 0.01$: Moments and Angular Accelerations

Moments are treated in the same way as determined in Section 4.2.2. Figure 4.40 displays the moment results about the three primary axes yielded by both models across all the REBR body orientations. Figures 4.40 mirrors the results seen in Figure 4.31, but at a larger scale, proportional to the larger forces induced on the body in less-rarefied flow at a higher orbital speed.

Figure 4.40 (b) displays no second maximum at $\Psi = 120°$. This phenomena of a second maximum seems apply to a free-molecular treatment of the flowfield, and lessens as the altitude decreases (see Figures 4.13, 4.22, 4.31, 4.40 (b)). The free-molecular model continues to oscillate about zero, while the DSMC results give a strong Y-moment at $\Psi = 45°$ and $60°$, and a small negative moment at $\Psi = 120°$ and $150°$. The aerodynamic shape of the REBR's domed heat shield does not yield a moment as the flow becomes more dense and continuum-like.

All these differences qualitatively reinforce the fact that the free-molecular modeling approach is not adequate at this Knudsen number.

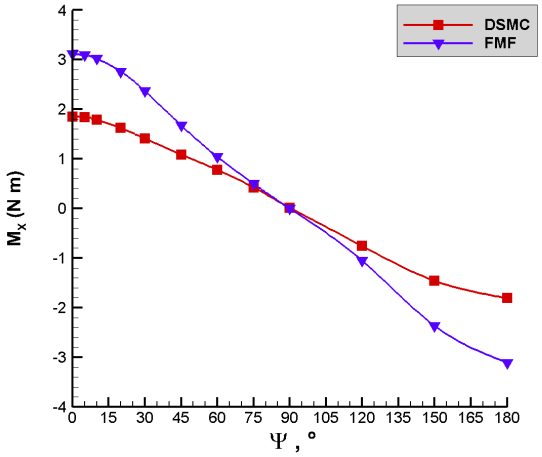

(a)

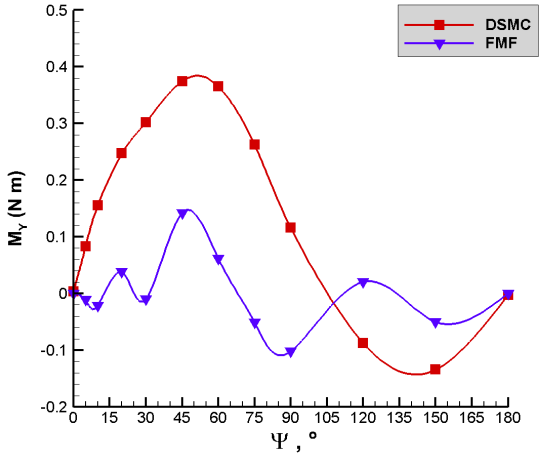

(b)

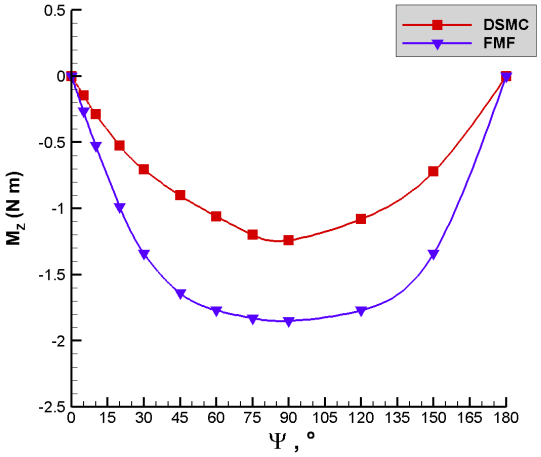

(c)

Figure 4.40: Moments calculated using DSMC and free-molecular (FMF) analytical models for all experiment orientations of the REBR about the: (a) X axis; (b) Y axis; (c) Z axis, for a Knudsen number of 0.01. Error bars reflect the 0.05% statistical DSMC error.

The moment averages are listed in Table 4.11.

The normalized root-mean-square deviation between all the X-axes moments is 45.3%. The normalized root-mean-square deviation between the Y-axes moments is 48.2%. The normalized root-mean-square deviation between the Z-axes moments is 47.6%. These deviation's reflect the

Table 4.11: Average moments calculated for a Knudsen number of 0.01 for the DSMC and free-molecular analytical modeling approaches across all Ψ values.

Average	FMF	DSMC
$\mathbf{M}_X$ **(N m)**	1.17×10^{-2}	1.12×10^{-2} $\pm 5.06 \times 10^{-6}$
$\mathbf{M}_Y$ **(N m)**	-4.76×10^{-3}	1.04×10^{-1} $\pm 4.73 \times 10^{-5}$
$\mathbf{M}_Z$ **(N m)**	-1.36	-8.13×10^{-1} $\pm 3.68 \times 10^{-4}$

lack of agreement between the models, expected at this Knudsen number, where the free-molecular assumption is not appropriate.

Because the Y-moments are the only ones non-zero across the whole REBR body, the angular acceleration about the Y-axis is examined more thoroughly here. As stated in previous sections, plotting the angular rotational uncertainty gives an intuitive picture of where aerodynamic moments would affect the overall motion of the body. The Y-axis angular acceleration uncertainty is treated the same way as in Chapter 3 and is 2.98×10^{-2} radians s^{-2}, or 1.71 degrees s^{-2}, plotted as an error bar in all of the angular acceleration plots in this chapter.

Figure 4.41 shows the calculated angular acceleration about the Y-axis for the REBR body using both models across all orientations, with error bars as described previously. In Figure 4.41, the Y-moments across the orientations have been doubled, then divided by I_{YY}, to represent the moments incurred by the entire REBR body. The interpolated average angular accelerations about the Y-axis incurred are $102 \pm 4.63 \times 10^{-2}$ degrees s^{-2} using the DSMC method and 4.67 degrees s^{-2} using the free-molecular analytical method. The reason for the sign change is the same as the reason for the sign change between the average Y-moments in Section 4.4. The oscillatory nature of the free-molecular results yields an average close to zero; while the maxima of the DSMC results yields a positive average.

The normalized root-mean-square deviation between the angular accelerations about the Y-axis is 53.16%. These results reflect the inaccuracy of the free-molecular assumption as Knudsen number lowers, as the differences between models are increasing when compared to results at higher altitudes.

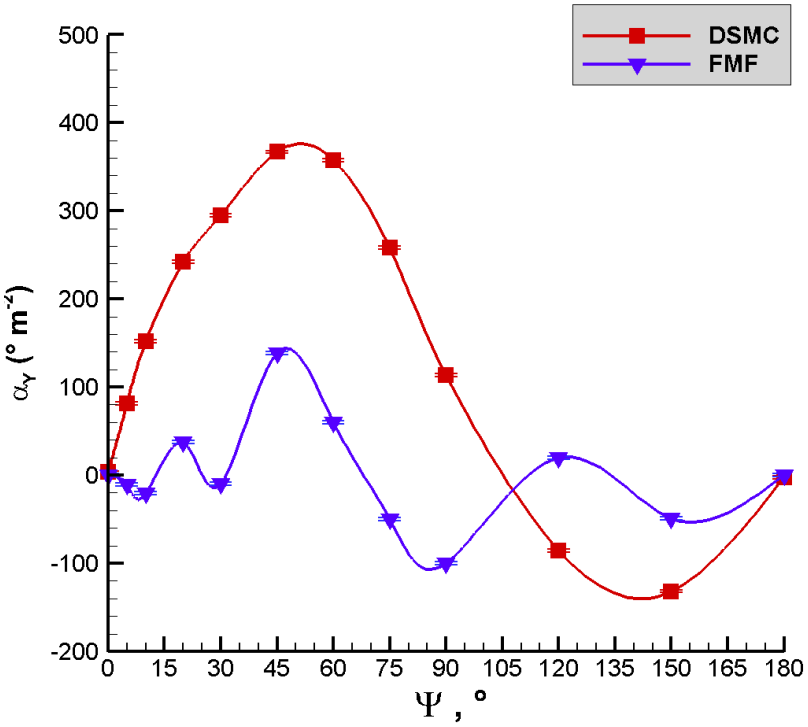

Figure 4.41: Angular acceleration about the Y-axis calculated using DSMC and free-molecular (FMF) analytical models for all experiment orientations of the REBR, for a Knudsen number of 0.01. Error bars reflect the angular velocity uncertainty of 1.71 degrees s^{-2}.

The error bars in Figure 4.32 illustrate the effect the aerodynamic Y-moment has on the tumbling behavior of the REBR. The effect of the moments, whose magnitudes are large because the forces at this Knudsen number are large, again outsize the effect of an imposed angular velocity of 5 degrees s^{-1}.

4.6 Orbital Decay Analyses

The orbital decay model developed in Section 2.3 is applied to the interpolated coefficients of drag and lift (C_DA and C_LA) to analyze the impact of the model used; as well as the impact of addressing tumbling motion on lifetime orbital predictions. The aerodynamic coefficients, as before, are calculated across the entire projected REBR body, a result of doubling the drag and lift forces calculated on the simulated half-REBR.

In order to project realistic reentry, the aerodynamic stability of the REBR is taken into account. The flight data from [10] shows that the REBR maintained a stable configuration of the nose cone facing incoming flow, with a total angle of attack oscillating between -5° and 5°, when it was flying free of its housing. For this work, the oscillations are estimated to be sinusoidal, with the REBR spending approximately equal time at $\Psi = 5°$, $-5°$, and $0°$. The $\Psi = 5°$ orientation results are representative of the $-5°$. Therefore, the average aerodynamic coefficients used to calculate the orbital decay and reentry are weighted averages of the results from the Ψ values of 5° and 0°. The weighing scheme is two-to-one, with the $\Psi = 5°$ results receiving the higher weighting.

Two different sets of aerodynamic coefficients are used: the weighted average of the $\Psi = 0°$ and $5°$ coefficients, and the $\Psi = 0°$ coefficient results. The $\Psi = 0°$ results represent a typical approach to estimating aerodynamic coefficients, with only one flow-facing area used.

Though the trajectory of the REBR did not experience orbit until 67 km of altitude (where the REBR has a Knudsen number of 2.35×10^{-3}, much less than the modeled Knudsen numbers in this thesis) the aerodynamic stability is projected upwards to a theoretical orbit decay starting at an altitude of 119 km, or a Knudsen number of 10 for the REBR. The initial orbit is a circular orbit with an altitude of 119 km and angular orbital elements (Ω, i, and ω_p) of 0°.

Table 4.12 contains the weighted average coefficients and the $\Psi = 0^\circ$ coefficients yielded from each modeling approach at each altitude used to model the REBR's orbital decay. Statistical error is not included in Table 4.12 because it very small, and is not included in the orbital decay projections.

Table 4.12: Coefficients of lift and drag, resulting from the DSMC and FMF modeling approaches, used to project orbital decay of the REBR.

Weighted Average Coefficients					
		DSMC		**FMF**	
Kn	**Alt (km)**	C_DA **(m^2)**	C_LA **(m^2)**	C_DA **(m^2)**	C_LA **(m^2)**
10	119	1.50×10^{-1}	1.95×10^{-4}	1.54×10^{-1}	1.50×10^{-4}
1	104	1.38×10^{-1}	4.13×10^{-4}	1.53×10^{-1}	1.37×10^{-4}
0.1	91	1.23×10^{-1}	3.67×10^{-4}	1.54×10^{-1}	1.44×10^{-4}
0.01	77	1.09×10^{-1}	1.42×10^{-4}	1.54×10^{-1}	1.45×10^{-4}
$\Psi = 0^\circ$ **Coefficients**					
		DSMC		**FMF**	
Kn	**Alt (km)**	C_DA **(m^2)**	C_LA **(m^2)**	C_DA **(m^2)**	C_LA **(m^2)**
10	119	1.50×10^{-1}	8.90×10^{-6}	1.54×10^{-1}	1.17×10^{-8}
1	104	1.39×10^{-1}	1.74×10^{-5}	1.54×10^{-1}	1.13×10^{-8}
0.1	91	1.23×10^{-1}	2.57×10^{-5}	1.54×10^{-1}	5.78×10^{-8}
0.01	77	1.09×10^{-1}	1.44×10^{-5}	1.54×10^{-1}	6.10×10^{-8}

The coefficients of drag and lift are interpolated to yield coefficients experienced throughout the REBR's orbital decay. Linear interpolations are used for both models and both the weighted and $\Psi = 0^\circ$ only free-molecular results. The DSMC results are fitted with a spliend combination of two linear fits that levels off at a C_DA of 1.54×10^{-1} to reflect the free-molecular theoretical result. Figure 4.42 plots the drag coefficient data from the REBR flight [10], drag coefficients listed in Table 4.12, and the linear interpolations of the drag coefficients, across the altitudes experienced in the modeled orbital decay. The flight data drag coefficients are multiplied by a projected front-facing area of 0.75 m^2. This area corresponds with the spherical projection of the REBR.

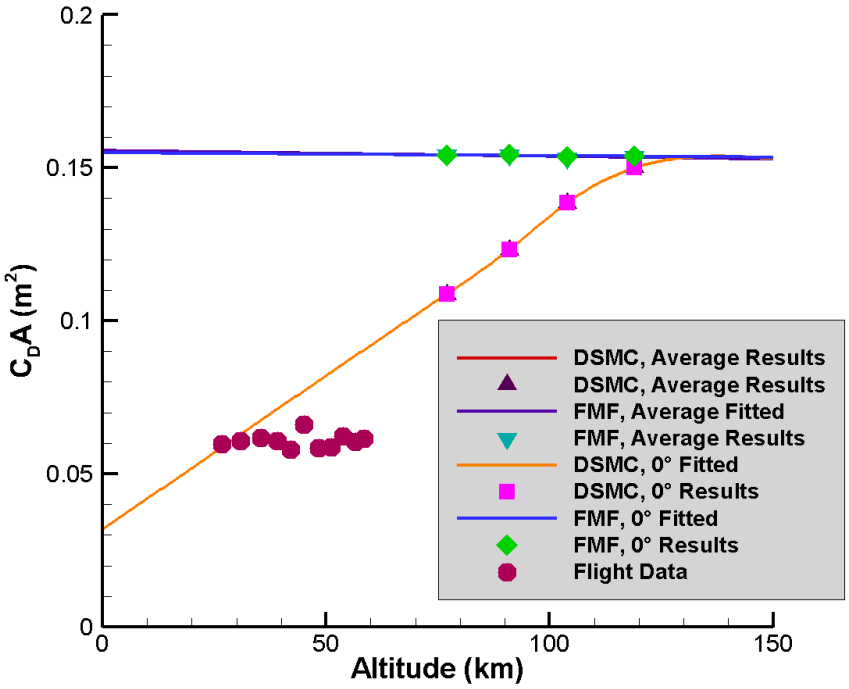

Figure 4.42: The drag coefficients reconstructed from the REBR flight data ([10]) plotted with the weighted drag coefficient results and the $\Psi = 0°$ drag coefficient results from both the free-molecular and DSMC approaches across the orbital decay altitudes modeled.

The REBR flight occurred at altitudes corresponding to the continuum regime, and therefore out of the scope of this thesis work. However, Figure 4.42 is useful to contextualize which models are appropriate at which altitudes. The free-molecular approach yields nearly identical drag coefficients regardless of altitude or Knudsen number. When divided by a front-facing area of 0.75 m^2, the free-molecular results across all Knudsen numbers yield a drag coefficient of about 2: the theoretical hypersonic drag coefficient for a sphere. That is consistent with the REBR shape with its spherical heat shield and circular projected area. The DSMC results for drag decrease linearly as altitude decreases. This matches more closely with the flight data. In Figure 4.42, the lowest-altitude flight data corresponds with the linearly fitted DSMC results. Although it looks like the DSMC drag coefficient estimate could be high for the higher-altitude flight data, it is pos-

sible that CFD, a more suitable approach to modeling continuum aerodynamics, would yield the appropriately low drag coefficient at that dense altitude.

The $\Psi = 0°$ data and linear interpolations in Figure 4.42 are nearly indistinguishable from the averaged data. This is due to the weighted averages use data pulled from near the $0°$ orientation. Comparing the stagnant REBR approach to the oscillating REBR approach, however, is useful for measuring if multiple simulations of such a body would improve upon orbital lifetime estimates.

Figure 4.43 plots the lift coefficients listed in Table 4.12, and the linear interpolations of the lift coefficients, across the altitudes experienced in the modeled orbital decay. There is no flight data on the lift coefficients the REBR experienced.

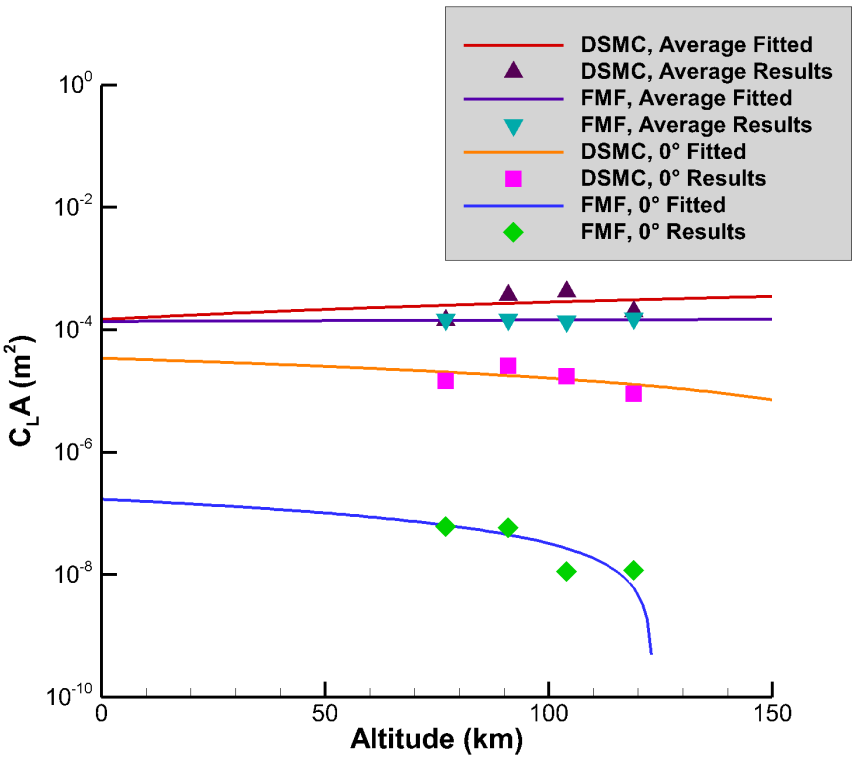

Figure 4.43: The weighted lift coefficients results and the $\Psi = 0°$ lift coefficient results from both the free-molecular and DSMC approaches across the orbital decay altitudes modeled.

Figure 4.43 is useful to contextualize how the models differ, and how the approach to rotational

motion yields different lift values. The weighted average data and linear fits are much larger and closer than the $\Psi = 0°$ only data and fits. Again, at $\Psi = 0°$, the REBR behaves like a sphere. Therefore, the lift is much closer to zero than even a small angle of attack creates.

Figure 4.44 displays the orbital decay from the starting altitude of 119 km ($Kn = 10$), projected using the linearly interpolated coefficients for each model according to the current altitude. The orbital decay models diverge as the altitude lowers, reflecting the changing coefficients of drag, which is the dominant factor affecting the speed of the orbital decay.

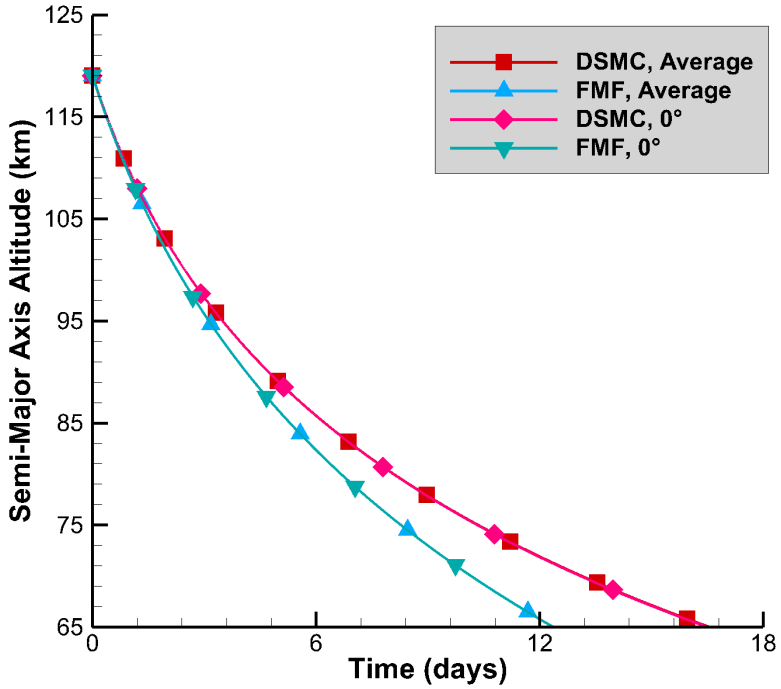

Figure 4.44: Orbital decay estimated from an altitude corresponding to $Kn = 10$ using weighted drag and lift coefficients, and $\Psi = 0°$ drag and lift coefficients, from results obtained using both methods.

The orbital decay model is run until the REBR achieves an altitude of 65 km for all modeling modes. Table 4.13 displays the time the REBR took to achieve 65 km of altitude using each modeling approach (DSMC and free-molecular) and each orientation scheme (weighted averages

for both coefficients, or $\Psi = 0^\circ$ coefficients only). Table 4.14 contains the root-mean-square differences over the orbital decay and the percent deviation in time-to-reenter between all modeling modes. Due to the weighting scheme used for the average coefficients, there is not much difference between using the $\Psi = 0^\circ$ coefficients and the weighted coefficients. This is seen qualitatively in Figure 4.44 as well: the $\Psi = 0^\circ$ orbital decay modeling is identical to the weighted average modeling for each approach.

The choice of model between DSMC and free-molecular affects the orbital decay predictions much more. The time-to-reenter differences are about four days between the free-molecular and DSMC approaches. The free-molecular drag coefficients are consistent even as altitude drops; which is not the case for the DSMC drag coefficients, as seen in Figure 4.42. These elevated drag coefficients significantly speed up the decay and cause a 25% reduction in orbital lifetime predictions.

Table 4.13: Time for the REBR to achieve reentry altitude (or time-to-reenter) according to each modeling mode.

Modeling Mode	**Time-to-Reenter (days)**
DSMC, Averages	16.6
DSMC, $\Psi = 0^\circ$	16.5
FMF, Averages	12.4
FMF, $\Psi = 0^\circ$	12.4

Table 4.14: Root-mean-square differences over the orbital decay and time-to-reenter deviation between models and tumbling approaches for the REBR.

Root-Mean-Square Differences Over Orbital Decay				
	DSMC, Averages	**DSMC,** $\Psi = 0^\circ$	**FMF, Averages**	**FMF,** $\Psi = 0^\circ$
DSMC, Averages	-	0.04 km	3.81 km	-
FMF, Averages	3.81 km	-	-	0.02 km
Time-to-Reenter Deviations				
	DSMC, Averages	**DSMC,** $\Psi = 0^\circ$	**FMF, Averages**	**FMF,** $\Psi = 0^\circ$
DSMC, Averages	-	0.31%	25.3%	-
FMF, Averages	25.3%	-	-	0.03%

Figure 4.42 reinforces a general approach to modeling these forces: at a Knudsen number of 10, the free-molecular model is highly accurate and much less expensive; therefore free-molecular modeling should be used at altitudes at or above a Knudsen number of 10. At a Knudsen number of 1, free-molecular modeling can be used for a first approximation, but DSMC is more accurate and should be used if highly accurate lift or moment information is desired. At Knudsen numbers of 0.1 or 0.01, DSMC must be used to obtain accurate drag information.

Again, as in Section 3.6, an estimate is conducted to approximate how the changes in time-to-reenter translate to ground impact. Small changes in predicting reentry time changes projected debris impact by a large amount. A simple transformation of the information on time-to-reenter differences in Table 4.13 using the average rotation of the Earth ($4.18 \times 10^{-3} \circ s^{-1}$) yields an estimate in differences in ground footprint projection of impact. For the REBR, the impact location is changed by up to 200,000 km. Again, small changes in time-to-reenter cause spacecraft to complete many additional orbits around the Earth; orbital periods are short, and the rotational motion of the Earth is fast. Therefore, modeling every contributing factor in the reentry process has a large affect on the impact location; accurate aerodynamic information is very important. Choice of model for the aerodynamic coefficients can have extremely large affects on the impact location prediction for a reentering spacecraft. Even though the weighted averages are very close to the constant coefficients, the difference in time-to-reenter causes a significant distance difference in ground impact location. As stated before, for future work, more accurate orbital decay modeling will need to be used with the aerodynamic coefficients, but this gives a general idea of how differences in orbital lifetimes impact reentry crash landing predictions.

4.7 REBR: Summary and Conclusions

In this chapter, the REBR body was used to compare force and moment results across the free-molecular and the DSMC models for four Knudsen numbers: 10, 1, 0.1, and 0.01. These Knudsen numbers represent different flow regimes from firmly free-molecular ($Kn = 10$) to the limit of continuum flow ($Kn = 0.01$). Coefficients of drag and lift calculated using both modeling approaches were interpolated over and used to compare how the choice of model affects orbital lifetime predictions. The orbital decay predictions using free-molecular calculated aerodynamic coefficients differed from those using the DSMC-calculated aerodynamic coefficients by 25%.

Table 4.15 enumerates the normalized root-mean-square deviations between the models for the calculated drag, lift due to pressure, and y-moments. The lift due to shear and total lift aren't included because their errors are inflated by the average values being so close to zero. The Y-moment errors are elevated for this reason too, but are included as a comparison metric to track how differences in aerodynamic rotational motion increase as Knudsen number decreases. Table 4.15 shows that the free-molecular approach yields results similar to the DSMC approach for a Knudsen number of 10. The errors are bigger for $Kn = 1$, and become significantly larger once $Kn = 0.1$ is achieved.

Table 4.15: Normalized root-mean-square deviations between the free-molecular and DSMC results for the REBR across all orientations for each Knudsen number for drag, lift due to pressure, and Y-moments.

	Force or Moment Compared		
Knudsen Number	**Drag**	**Lift due to Pressure**	**Y-Moment**
10	2.27%	2.87%	7.94%
1	9.40%	11.5%	29.0%
0.1	19.0%	14.3%	42.9%
0.01	27.8%	21.6%	48.2%

Table 4.16 lists the average core-hours required to run each model for one orientation at each Knudsen number, and the total core-hours to run all 12 simulations for every orientation at each Knudsen number. The free-molecular model's computational cost scales with the number of surface elements in the mesh used due to the blocking algorithm it employs. The DSMC core-hours are dependent on several factors, such as: the mesh size and the number of particles used as well as the time step, and number of time steps in the simulation.

Table 4.16: Average computational cost in core-hours for one simulation and total core-hours for simulating all 12 orientations of the REBR using each model at each Knudsen number.

	C-Hs for One Simulation		**C-Hs for all orientations simulated**	
Knudsen Number	**FMF**	**DSMC**	**FMF**	**DSMC**
10	4.8×10^{-3}	36	5.8×10^{-2}	430
1	8.2×10^{-3}	34	9.8×10^{-2}	410
0.1	13	66	160	660
0.01	13	170	160	1900

Tables 4.15 and 4.16 together make interesting conclusions about where each model is appropriate. For a Knudsen number of 10, the free-molecular model saves hundreds of core-hours over simulating 12 orientations of the REBR; and the drag calculated using the free-molecular model is accurate to the DSMC results within 3%. The lift and y-moment free-molecular results are within 10% of the DSMC results at this Knudsen number as well, indicating decent agreement for relatively small values of lift and moments about the Y-axis. At this Knudsen number, over 7000 free-molecular orientations can be run for the cost of one DSMC simulation. This indicates that at Knudsen numbers of 10 and higher, the free-molecular model is desirable to measure drag, and perhaps other forces and moments, in order to save computational cost.

For a Knudsen number of 1, the errors are more elevated, with free-molecular drag within 10% of DSMC drag. The free-molecular Y-moment is only accurate to the DSMC Y-moment within

30%. This indicates that for very accurate lift or moment information, DSMC should be used at a Knudsen number of 1. However, because the free-molecular computational cost is so low at this Knudsen number, it may be desirable to run preliminary free-molecular analyses to get an idea of drag, lift, and moments, before conducting costly DSMC simulations. When the Knudsen number drops to and below 0.1, the free-molecular model becomes much less appropriate. The free-molecular drag differs from the DSMC drag by about 20%, indicating that for accurate drag, DSMC must be used.

The orbital decay results reinforce these ideas of where the free-molecular modeling is appropriate. For the aerodynamically stable configuration of the REBR, there are not large differences in the orbital decay projections between the constant coefficient estimates and the averaged coefficient estimates. However, even slight time-to-reenter differences cause large differences in impact location projections. There are larger differences between the DSMC and free-molecular modes of modeling orbital decay, indicating that DSMC is necessary for projecting orbital decay of objects that experience mostly low-Knudsen number orbits and reentry.

CHAPTER 5

Analysis of the Star48B Rocket Motor

The Star48 rocket motor is a third-stage solid rocket motor developed by Thiokol Production and now produced by Northrop Grumman Innovation Systems [11] [37]. It is commonly used as an upper stage to launch vehicles into space. The Star48B is chosen for study for a couple of reasons: one, it is a good example of large space debris regularly left in orbit, and two, there is some reconstructed reentry data available for a specific Star48B that crash landed in Saudi Arabia in 2001 [13]. This shows that the Star48B is large enough to survive reentry and impact the Earth, making it an important and interesting case study for safety reasons.

The Star48B rocket motor has a maximum diameter of 1.24 m and a maximum length of 2.03 m including the nozzle. The total mass of the Star48B at burnout is 117 kg and the rocket motor outside casing is made of the titanium alloy Ti-6Al-4V. The exit nozzle inside is coated with a thermal protection carbon phenolic material which ablates throughout firing. The exit nozzle thickness at burnout is estimated at 6.35 mm [38]. Figure 5.1 is a photograph of a Star48B taken from the ATK catalog [11].

Figure 5.1: Photo of Star48B as given in the ATK catalog, from [11].

5.1 Star48B Body Numerical Experiment Design

Meshes are generated based on the body shape of the Star48B using CAD and Pointwise. The meshed shape is simplified to reduce computational time as much as possible: small changes on a body require surface element refinement even if the local mean free path does not require it. The ridges, which are flanges designed to attach the Star48B body to its housing, on the near-spherical forebody are not meshed. Additionally, the inlet pipes that flank the exit nozzle in Figure 5.1 are not meshed.

The symmetrical nature of the Star48B is taken advantage of to reduce the computational cost of the simulations. This is necessary when meshing the body because of its relatively large size. The larger the body is, the more cells are needed to refine the surface to be appropriate for DSMC simulations experiencing certain local mean free paths.

The Star48B is cylindrically symmetrical about the longitudinal axis which is assigned as the X-axis in meshing the body. Therefore, the body is divided, and the X-Y plane is declared as

a plane of symmetry in MONACO simulations. Assuming symmetry about the X-Y plane does imply that any moments that would turn the vehicle out of this plane are not significant. There is no data on the rotational motion of a Star48b left in orbit, so this assumption is made to reduce computational cost and allow simulations of the Star48B at lower Knudsen numbers. The assumption of symmetry about the X-Y plane does allow for thorough examination of the normal (or Z-) axis, which is one moment that changes the flow-facing area of the body. Figure 5.2 shows a mesh representation of the Star48B. Different mesh refinements are used for different Knudsen numbers. Additionally, mesh refinement limits the wall depth achievable for the nozzle cone. The nozzle wall thickness for all meshes is 10 mm.

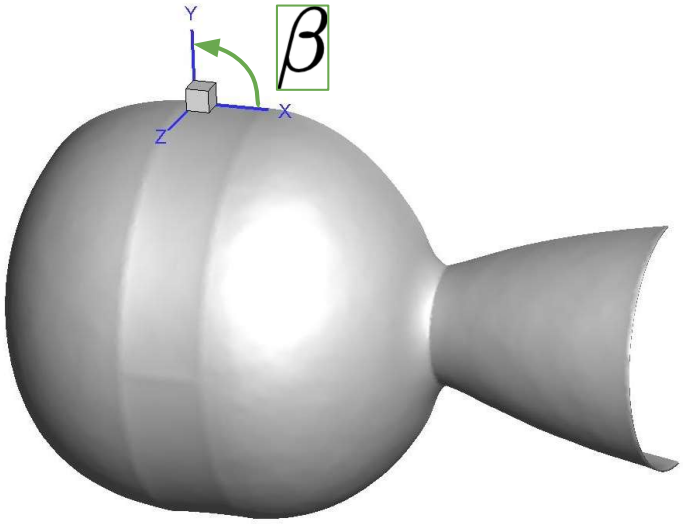

Figure 5.2: The Star48B body as used for mesh representation. Axis represent the body axes used and show the X-Y plane used as the plane of symmetry. β is the angle projected from the positive X-axis in the X-Y plane of symmetry used in this work.

One primary goal of this thesis is to establish Knudsen numbers where a free molecular analytical approach to gathering aerodynamic force and moment information is no longer acceptable

for desired accuracy. In order to evaluate the effect of Knudsen number on model results, altitudes must be chosen where there is a marked difference in Knudsen number as the flow regime moves from free molecular to transitional and even into continuum. The Star38b that crash-landed in Saudi Arabia in 2001 was originally left in an elliptical orbit of 180 km by 20,300 km after launching a GPS satellite into LEO in May 1993. After staying in orbit for several years, the Star48b orbit had decayed to 145 km by 800 km by January 1, 2001 [39]. In January the stage quickly went through catastrophic decay and crash-landed on January 12, 2001. Ailor et al. reconstructed the reentry trajectory of the Star48b stage through its breakup phase at 71.8 km using available sensor data [13]. The orbital elements of the Star48b reconstructed trajectory prior to and at breakup are listed in Table 5.1. In Table 5.1, the Star48B is orbiting with a negative perigee. This would put the imaginary orbital perigee inside of the radius of the Earth, and indicates that within that orbit, the Star48B will crash land on the Earth.

Table 5.1: Reconstructed orbital state vectors for the Star48b prior to and at breakup, from [13].

	Prior to Breakup	**At Breakup**
Epoch	1/12/2001	1/12/2001
Time (hms), GMT	16:37:00	16:38:38.7
Altitude (km)	81.6	71.8
Relative Velocity (m/s)	7420	6200
Apogee (km)	98.2	74.4
Perigee (km)	-105	-2910
Argument of Perigee (ω_p, °)	179	217
Inclination (i, °)	34.6	34.4
RAAN (Ω, °)	7.45	7.11
True Anomaly (θ, °)	215	184
Longitude (° **East**)	35.2	41.0
Geodetic Latitude (°)	18.7	21.8

A projected orbital decay and reentry of the Star48B is plotted in Figure 5.3 starting from the perigee altitude on January 1, 2001 of 145 km. The orbital decay is projected using the orbital

decay model elaborated on in Chapter 2. The starting orbital elements are those listed in the "prior to breakup" column of Table 5.1, excepting the apogee, perigee, and inclination. The starting apogee is 20,300 km, the starting perigee 180 km, and the starting inclination is 34.9° [39]. These changes in the orbit are made in order to project the orbital decay from the initial; elliptical orbit that the Star48B is left in, in 1993. The orbital elements from Table 5.1 are projected to this initial altitude in order to approximate what Knudsen numbers the Star48B experiences.

The Knudsen number of the Star48B across these altitudes is also plotted in Figure 5.3. The Knudsen numbers in Figure 5.3 are calculated using the U.S. Standard Atmosphere from 1976 estimates for mean free path [12]. The characteristic length used for calculating the Knudsen numbers is the average between the maximum diameter and length: $L = 1.64$ m. An average characteristic length is used to account for modeling of the Star48B's changing orientations in projected orbits due to any tumbling motions.

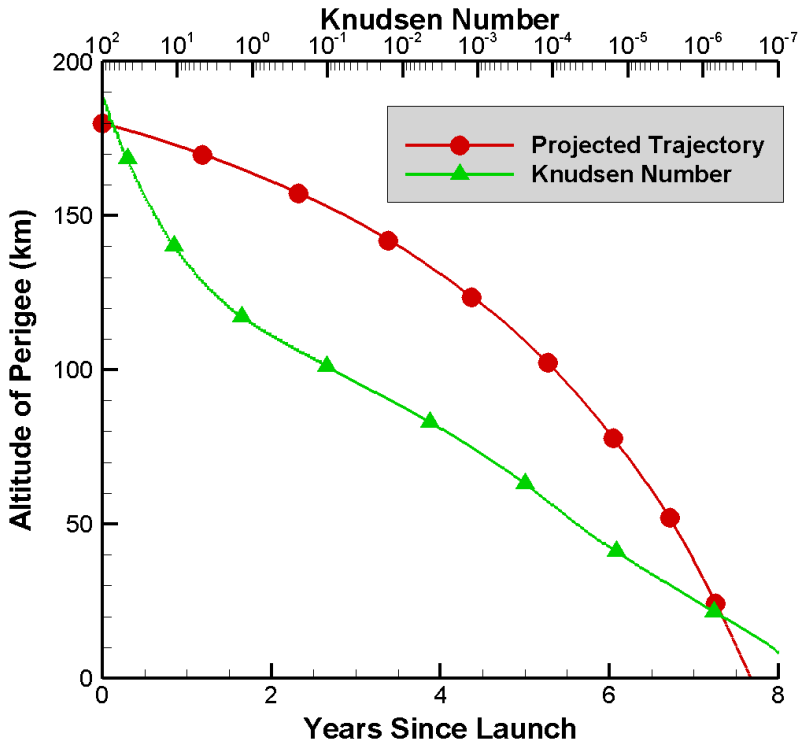

Figure 5.3: Projected orbital decay of the Star48B after January 1, 2001, plotted against the Knudsen number of the Star48B body over altitude.

Figure 5.3 displays that the breakup event of the Star48B occurs in continuum regime flow, which is outside the scope of this work. However, the Star48B experiences a lot of its orbital decay, even the January 2001 catastrophic orbital decay, in free-molecular and transitional flow. Knudsen numbers are picked in order to compare and contrast modeling approaches dealing with a rocket stage shape and size undergoing orbital decay and the beginning of reentry.

The Star48B is relatively large. The surface element refinement achievable limits the lowest Knudsen number possible for modeling the Star48B. The minimum average surface element size length used is 6.87×10^{-3} m. At an altitude of 97 km, the free-stream mean free path is 8.29×10^{-2} m; compression by a factor of 10 yields the local mean free path near the body surface of 8.29×10^{-3} m. The Knudsen number of the Star48B at the altitude of 97 km is 0.05, in transitional

flow. Knudsen numbers chosen for study for the Star48B are: 0.05, 0.1, 1, and 10. A Knudsen number of 10 is chosen as the "control" case, as free molecular analytical approaches are expected to yield accurate (and therefore matching DSMC results) results in this regime.

Atmospheric composition is an important factor for achieving accurate results. The atmospheric composition modeled on the Star48B is the same as that for the TBEx, described in Chapter 3. Figure 3.6 displays the neutral atmosphere composition from [9]. Based on molar composition, the primary atmospheric constituents are used to compose the flowfield for both models.

The atmospheric properties of each of the chosen altitudes are listed in Table 5.2. Though the Star48B begins in a highly elliptical orbit, a circular orbit approximation is used to study the Star48B body. This assumption is made in order to standardize the velocities used in this numerical experiment. The orbital speed, V, is calculated using a circular orbit assumption. It is appropriate to use a circular orbit approximation for the orbital velocity because orbital degradation results in circular orbits just before reentry and impact [6]. Therefore the Star48B would experience circular orbits on its reentry path. In Table 5.2, "Alt" refers to altitude of the satellite's orbit.

Table 5.2: Atmospheric properties for the Star48B conditions analyzed [9] [12].

				Number Density (m^{-3})			
Kn	**Alt (km)**	**V ($m\ s^{-1}$)**	**T (K)**	**N_2**	**O_2**	**O**	**Ar**
10	139	7820	622	5.15×10^{16}	4.87×10^{15}	2.55×10^{16}	1.53×10^{14}
1	115	7840	322	5.06×10^{17}	7.91×10^{16}	1.13×10^{17}	3.06×10^{15}
0.1	101	7840	185	6.20×10^{18}	1.32×10^{18}	4.06×10^{17}	6.28×10^{16}
0.05	97	7850	179	1.33×10^{19}	3.01×10^{18}	4.59×10^{17}	1.46×10^{17}

To narrow the scope of this thesis work, wall temperature for the body of the Star48B is assigned to be 300 K, as in Chapter 3 for the TBEx. Similarly, the accommodation coefficient used to model the Star48B is $\alpha = 1$, simulating fully diffuse reflections of particles impacting the Star48B surface. One application of future work is comparison of models using differing accommodation

coefficients and surface temperatures.

There is no tumbling or rotational data available for a reentering Star48B. However, it's known that spacecraft tumble and rotate throughout their orbits, and in LEO, spacecraft are known to tumble with a revolution rate of about 4 rpm [19]. Space debris such as rocket stages begin to tumble after orbital insertion due to factors such as the expulsion of remaining propellant. The evolution of these tumbling motions due to aerodynamically imposed torques is not well understood, and is one of the interests of this work.

Another objective is to obtain average aerodynamic forces experienced over one revolution of the body in order to simulate deorbiting of the spacecraft. Several orientations of the Star48B must be examined in order to understand average forces the body would be subjected to as it deorbits. Because the body exhibits very different flow-facing areas as β in Figure 5.2 is changed, 13 different β angles are chosen to understand how the forces and moments change as the entire body turns. The β angles are evenly distributed from 0° to 180° at intervals of 15°. β is taken from the positive X-direction, and is in the X-Y plane, as pictured in Figure 5.2, in order to adequately use the defined plane of symmetry.

The last variable defined for modeling the Star48B is the number of sampling steps for use in MONACO simulations. A simple case study is set up to determine the effect increasing the number of sampling steps has on the aerodynamic coefficients C_D and C_L and what difference this causes in orbital decay. For the Star48B simulations, sampling begins after 80,000 time steps. After 80,000 time steps, all simulations have reached their steady-state number of particles in the flowfield.

For every Star48B simulation the VHS model is used for collisions. For this sampling study, 1×10^{-7} seconds is used for the time step. The VHS reference temperature is again 273 K and the

viscosity temperature exponent is 0.75 across all simulations. Table 3.3 in Chapter 3 contains the properties for the molecular species utilized. Again, none of the included species are ionized. For more information on these inputs used with MONACO, refer to [20], [22], and [23].

Table **??** contains the reference particle weights (the number of real particles represented by one model particle) and time steps used in each MONACO simulation for differing Knudsen numbers. The particle weights are chosen to keep the total steady-state number of particles consistently between 5 and 7 $\times 10^6$ as the Knudsen number changes. More particles raise computational cost. The time step is chosen to reach steady state in 80,000 steps for the size of the Star48B mesh and to minimize the number of collisions with probability greater than one.

Table 5.3: Reference particle weights and time steps used in MONACO Star48B simulations at each Knudsen number.

Knudsen Number	**Reference Particle Weight (N_{Real}/N_{Model})**	**Time Step (s)**
10	3×10^{12}	1×10^{-6}
1	2.4×10^{13}	1×10^{-6}
0.1	3×10^{14}	1×10^{-6}
0.01	6×10^{14}	1×10^{-7}

The number of sampling steps is varied from 25,000 to 500,000 steps. The Knudsen number used in this sampling study is $Kn = 0.05$. Table 5.4 displays the MONACO aerodynamic coefficients for each simulation set up as described above and the number of core-hours (C-Hs) each simulation takes. Understanding computational cost needed to impact solutions is an important part of this thesis work. Table 5.4 displays the sampling steps study results for the $= 0^\circ$ case. The aerodynamic coefficients in Table 5.4 are calculated using a projected area of $A = 1.21$ m^2. The drag and lift forces yielded by the MONACO simulations are multiplied by two to account for the symmetric half missing in the meshed representation, as shown in Figure 5.2.

The results in Table 5.4 are used in the orbital decay model described in Section 2.3 in order to

Table 5.4: $\beta = 0°$: sampling steps results for coefficient of drag and lift and total core-hours to run simulation.

Sampling Steps	C_D	C_L	**C-Hs**
25000	1.83	2.74×10^{-1}	58.0
50000	1.83	2.74×10^{-1}	75.1
75000	1.83	2.74×10^{-1}	87.8
100000	1.83	2.74×10^{-1}	101
200000	1.83	2.73×10^{-1}	167
300000	1.83	2.73×10^{-1}	272
400000	1.83	2.73×10^{-1}	296
500000	1.83	2.73×10^{-1}	385

understand how large of an effect the number of time steps has on orbital decay projections. The difference in orbital decay projections is measured using a RMSD between each methods' loss-of-altitude in kilometers over the time steps taken to project the decay. The RMSD between the 500,000 sampling step simulation orbital decay and the 25,000 sampling steps simulation orbital decay is 3.88×10^{-2} km. The time-to-reenter difference percentage between the 500,000 step simulation and the 25,000 sampling steps simulation is 0.23%. Based on this analysis, 25,000 sampling steps is chosen for all Star48B simulations.

5.2 Knudsen Number of 10

As stated above, a Knudsen number of 10 is achieved for the Star48B body at 139 km of altitude. A Knudsen number of 10 is in the free-molecular regime so well-matched results between the MONACO results and the free-molecular model results are expected. The circular orbital speed and atmospheric composition at this altitude are listed in Table 5.2. The Star48B surface elements used at this altitude have a side length average of 1.65×10^{-2} m in order to be smaller than the free-stream mean free path compressed by a factor of 10 (1.70 m), and to capture the curvature of

the Star48B shape. This refinement yields 2.29×10^5 volume cells in the flowfield, and 32,200 surface elements. As an example, the $\beta = 0^\circ$ orientation is presented. All slices of the flowfield are taken at $Z = 3.67 \times 10^{-2}$ m, which is close to the X-Y plane, the plane of symmetry. This slice is chosen in order to show both the fore spherical shape of the body as well as the aft nozzle cone of the body experiencing flow. The Star48B body is represented by the white "cut-out" of the slice of the body.

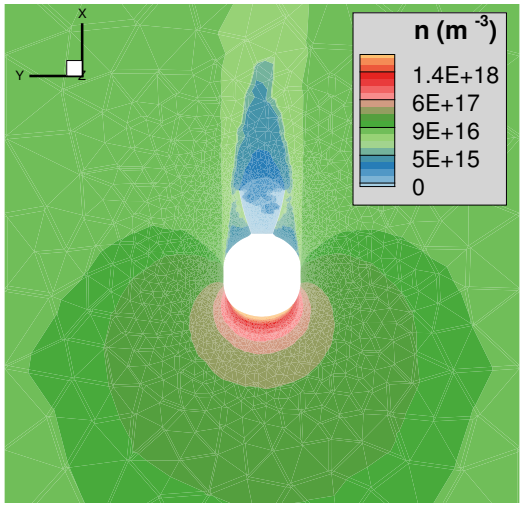

(a)

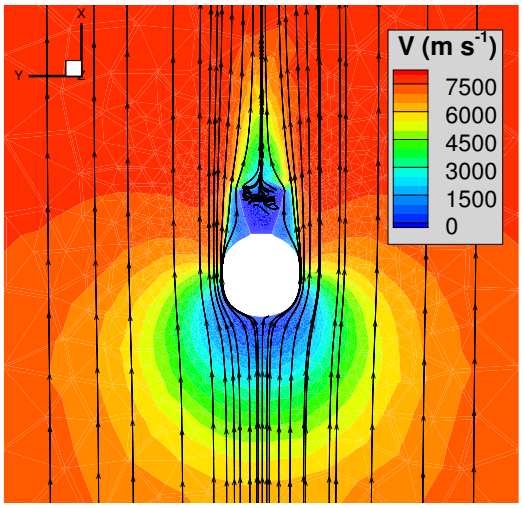

(b)

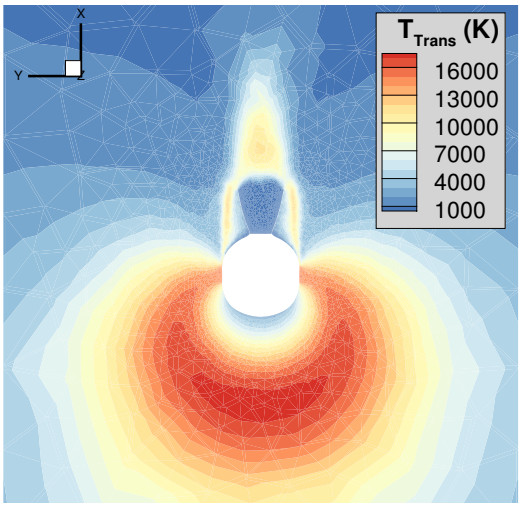

(c)

Figure 5.4: Flowfield contours at $Kn = 10$, $\beta = 0°$: (a) number density; (b) velocity; (c) translational temperature.

Figure 5.4 shows the flowfield contours computed using MONACO. All three contour plots show flow phenomena expected when an object disturbs rarefied high-speed flow: instead of a defined shock layer, a large volume of heated, slowed-down flow forms in front of the object. Figure 5.4 (a) displays the number density contours, which explicitly shows the backflow that effects the nozzle cone. Part of the nozzle cone does not experience any flow penetration. In

Figure 5.4 (b) the velocity streamlines are plotted. The β angle can be clearly seen in the direction of these streamlines. Again, there is interesting disturbed flow behavior in the nozzle cone, from backflow that reflects off the nozzle walls and exits the nozzle cone again. Figure 5.4 (c) displays the translational temperature; in collisionless flow, indicative of where populations of freestream and reflected particles are located. In the temperature contours, the particles reflected off of the surface appear as the "hot" particles. Figure 5.4 (c) shows population of reflected particles stream off the surface after impacting the spherical aft body.

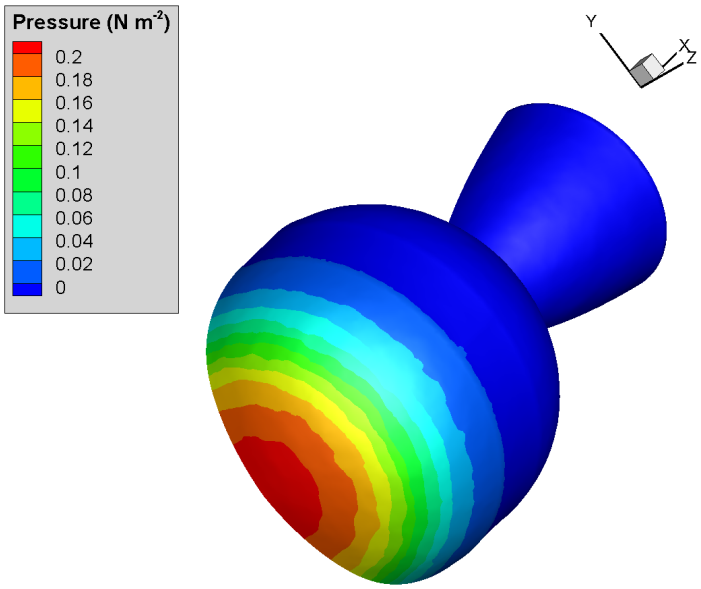

(a)

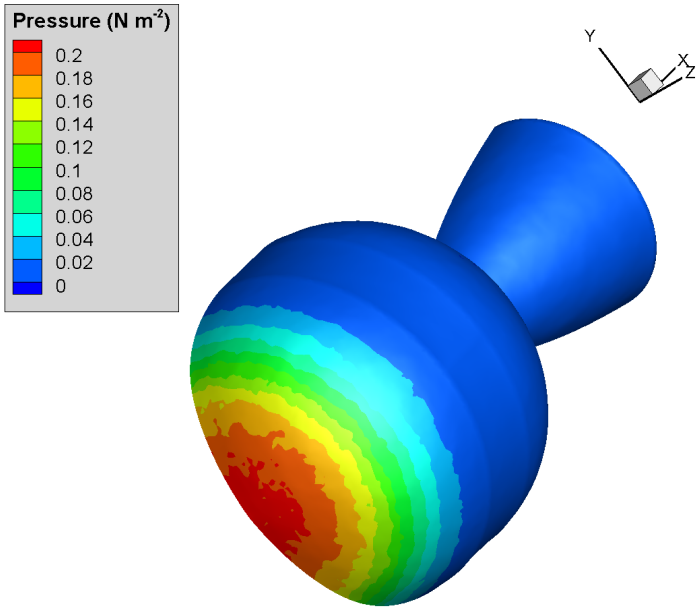

(b)

Figure 5.5: Pressure distribution at $Kn = 10$, $\beta = 0°$: calculated using: (a) free molecular theory; (b) DSMC.

Figures 5.5 displays an example of the surface pressure on the Star48B for the $\beta = 0^{\circ}$ case. It is evident when comparing Figures 5.5 (a) and (b) that the backflow experienced via simulation using DSMC is affecting the pressure distribution. The free-molecular analytical approach detects when cells directly experience flow; because it does not track particles, no pressure is seen on the backside of the Star48B in Figure 5.5 (a). Still, the pressure distributions are similar: the average pressure experienced by the surface is calculated as 2.36×10^{-2} N m^{-2} using the free-molecular method. This average is calculated by accounting for the pressure on each surface element over the entire body, weighting with respect to surface area, for this (the $\beta = 0^{\circ}$) orientation. The average pressure experienced over the body calculated by using MONACO results is $2.36 \times 10^{-2} \pm 1.18 \times 10^{-5}$ N m^{-2}, and is calculated similarly. The statistical error for the DSMC pressure calculation is due to the Poisson statistical error of the DSMC results due to the number of hits experienced by the body per surface element per time step and is enumerated in the next section. There is no difference (0%) in average pressure experienced by the body for up to three significant figures. For all percentage differences, as in Chapter 3, the DSMC MONACO results are taken as the more-accurate results, therefore the percentile difference is how much the free-molecular analytical calculation differs from the more-accurate DSMC simulation.

5.2.1 $Kn = 10$: Drag and Lift

Now the drag and lift experienced over the body are compared between the two models. Note that the drag and lift forces plotted and discussed in this section apply to only the half of the Star48B that is meshed and simulated. For use in other models (such as the orbital decay model), the forces are doubled to represent the entire body.

In order to compare models, the drag and lift forces gathered for each modeled orientation are interpolated over all values of β to yield an average value.

Figure 5.6 shows the calculated drag for all orientations using both approaches. The data points for individual simulation results are connected using splines to demonstrate the smooth transition of drag experienced as body rotation would occur.

The Poisson statistical error due to the number of hits experienced by the body per surface element per time step for MONACO DSMC simulations is calculated as in Equation 3.1. Using Equation 3.1, the average hits per sampling time step per surface element across the Star48B at this Knudsen number is 4.18×10^{-3}, the total number of surface elements is 32,200, and using 25,000 sampling steps: the Poisson statistical error of aerodynamic DSMC results is 0.05%. Error bars are not shown in the following figures because the statistical error is very small.

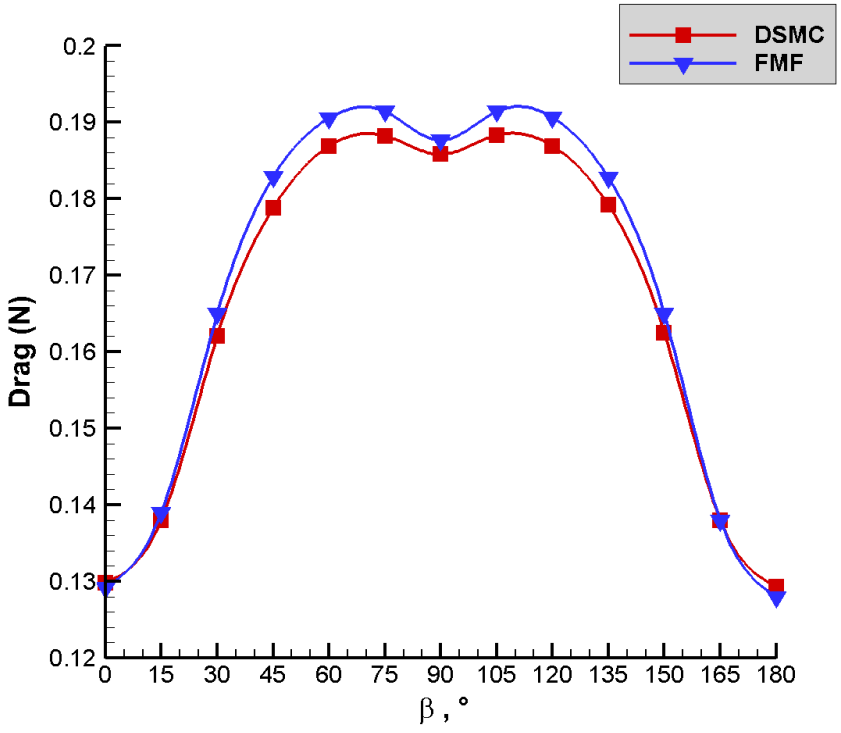

Figure 5.6: Drag calculated using DSMC and free-molecular (FMF) analytical models for all orientations analyzed of the Star48B at a Knudsen number of 10.

Figure 5.6 shows that maximum drag values are achieved for $\beta = 75^\circ$ and $\beta = 105^\circ$. At these orientations, the maximum spherical body area and the maximum nozzle cone area are exposed to the oncoming flow. The small dip at $\beta = 90^\circ$ is because at this angle of attack, less area of the nozzle cone is exposed to the flow. The nozzle has a smaller diameter near the spherical body and flares out, so when more of the flared area is exposed to the flow, the drag is increased. Minimum drag is achieved for $\beta = 0^\circ$ and $\beta = 180^\circ$. At these orientations, a minimal area is exposed to the flow: approximately at both angles, a semicircular area projection is exposed to direct pressure.

The average drag calculated using the MONACO results interpolated across all orientations is $1.69 \times 10^{-1} \pm 8.45 \times 10^{-5}$ N. The average drag calculated using the free-molecular results is 1.71×10^{-1} N. The percent difference between the averages is 1.41%. The normalized root-mean-square deviance between all the drag results across both models is 1.65%. These results match what is expected: good agreement between the free-molecular analytical and the DSMC results.

Figure 5.7 shows the calculated lift for all orientations using both methods. The lift displayed in Figure 5.7 is translated into an Earth-centric frame, which yields positive lift values. Lift is two orders of magnitude smaller compared to drag due to the Star48B's symmetry. The similarity to a sphere also affects the lift; spheres experience no lift, so the resemblance of the forebody to a sphere minimizes lift. Resolved as described in Chapter 2, nearly all force applied to the Star48B body is attributed to drag. Unless a pressure gradient in a normal direction to the oncoming velocity is created by the body's geometry, drag will be the dominating force.

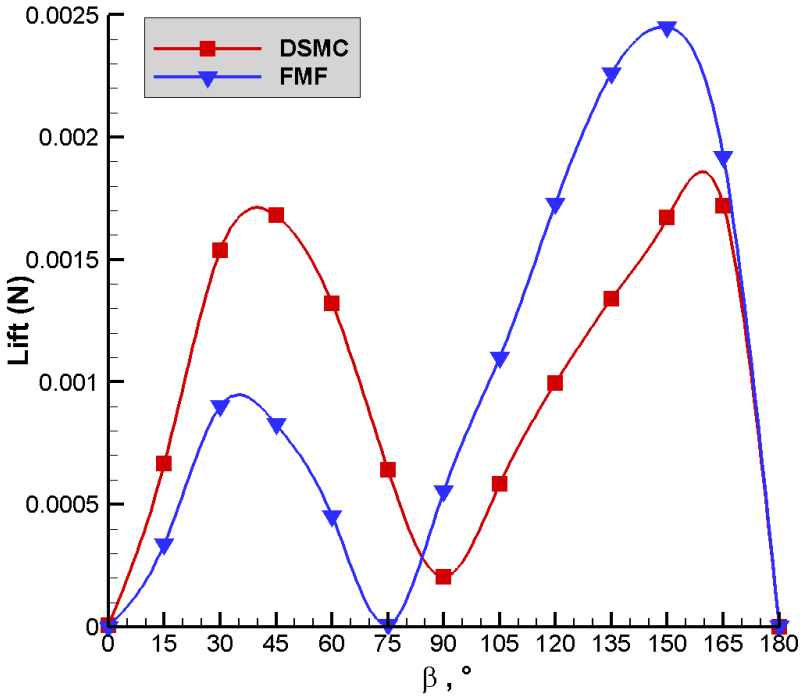

Figure 5.7: Lift calculated using DSMC and free-molecular (FMF) analytical models for all orientations of the Star48B at a Knudsen number of 10.

The average lift calculated using the MONACO results interpolated across all orientations is $1.03 \times 10^{-3} \pm 5.15 \times 10^{-7}$ N. The average lift calculated using the free-molecular results is 1.05×10^{-3} N. The percent difference between the averages is 1.49%. The normalized root-mean-square deviance is affected by the averages being so close to zero, and is not a good metric to judge the agreement between models.

Qualitatively, it is evident that the lift curves in Figure 5.7 are further apart than in Figure 5.6; showing differences between the models. At this Knudsen number, good agreement between DSMC and free-molecular results is expected, therefore this lift discrepancy is examined in further detail.

The forces on the body, as discussed in Chapter 2, are the sum of contributions of a pressure

force and a shear stress force in the direction desired. In order to examine the modeling differences, both pressure and shear stress contributions to the lift force are inspected below. Figure 5.8 displays the pressure contribution to the lift force for both models, while Figure 5.9 displays the shear stress contribution to the lift force for both models.

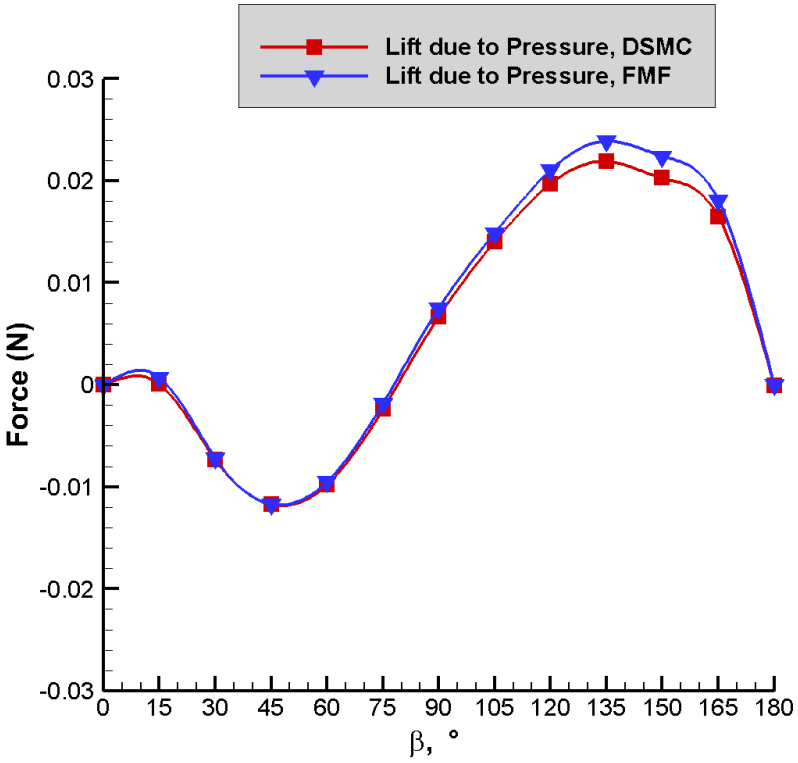

Figure 5.8: Lift due to pressure on the Starb48B, calculated using DSMC and free-molecular (FMF) analytical models for all orientations at a Knudsen number of 10.

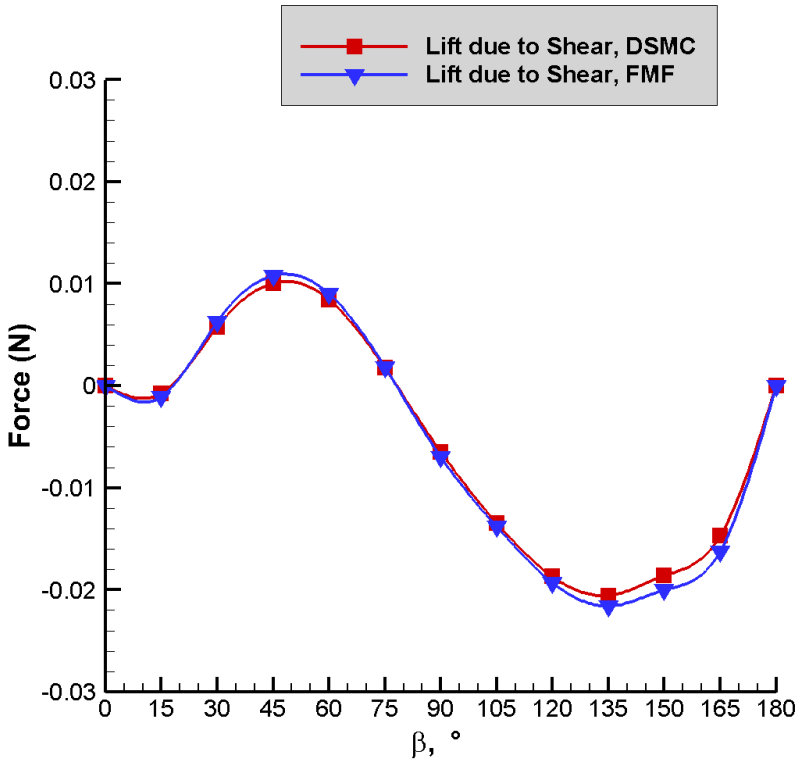

Figure 5.9: Lift due to shear stress on the Star48B, calculated using DSMC and free-molecular (FMF) analytical models for all orientations at a Knudsen number of 10.

Figures 5.8 and 5.9 display the agreement expected at this Knudsen number between the modeling approaches. The shear stress free-molecular results are slightly more extreme due to the DSMC modeling of particles, which create a more diffusive shear stress across the body, but the models still show good agreement. Quantitatively, the normalized root-mean-square deviance between all the lift due to pressure results across both models is 10.2%. The normalized root-mean-square deviance between all the lift due to shear stress results across both models is 7.67%. These error results are also inflated due to the data points at $\beta = 0°$ and $15°$ being close to zero, but orders of magnitude apart, sometimes even with sign differences. These data points are enumerated in Table 5.5. Only a few surface elements need to be influenced by pressure in order to cause a result so close to zero to "flip" signs.

Table 5.5: Lift due to pressure and shear stress on the Starb48B at specific β values for a Knudsen number of 10.

Lift due to Pressure (N)		
	FMF	**DSMC**
$\beta = 0°$	1.02×10^{-5}	-4.78×10^{-7} $\pm - 2.39 \times 10^{-10}$
$\beta = 15°$	7.30×10^{-4}	6.89×10^{-5} $\pm 3.44 \times 10^{-8}$
Lift due to Shear Stress (N)		
	FMF	**DSMC**
$\beta = 0°$	-9.62×10^{-6}	-4.76×10^{-6} $\pm - 4.14 \times 10^{-7}$
$\beta = 15°$	-1.07×10^{-3}	-7.37×10^{-4} $\pm - 3.69 \times 10^{-7}$

To take the total lift across the body, the lift due to pressure and the lift due to shear stress are summed. This results in lift values very close to zero; and small discrepancies in both contributing forces are magnified; yielding the curves in Figure 5.7. Because the lift is so small, the differences between models will not greatly change any orbital decay results, especially for a large piece of space debris as the 117 kg Star48B. As Knudsen number is decreased, the lift differences are expected to increase, for both the total lift force as well as each contribution component.

In order to calculate coefficients of drag and lift for use in the orbital decay model, a free-stream density is taken from [9]. At 139 km, where for Star48B $Kn = 10$, the free-stream density $\rho = 3.34 \times 10^{-9}$ kg m^{-3}. The orbital velocity is the circular orbital speed used throughout the $Kn = 10$ results: $V = 7820$ m s^{-1}. The aerodynamic coefficients are calculated for a full-body (not half, or meshed representation of) Star48B, and include the area as in Chapter 3, for use in the orbital decay modeling. The modeled force is multiplied by two to get the total force on the body. The lift coefficient is calculated similarly.

Figure 5.10 shows $C_D A$ and $C_L A$ calculated for all models and orientations for $Kn = 10$

experienced by the Star48B body.

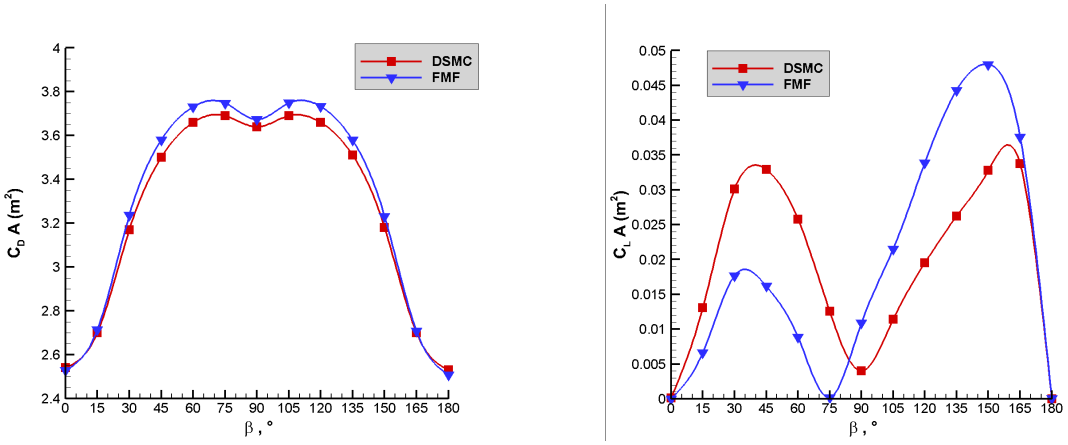

(a) (b)

Figure 5.10: Drag (a) and lift (b) coefficients calculated using DSMC and free-molecular (FMF) analytical models for all experiment orientations of the Star48B using both models for a Knudsen number of 10.

The average $C_D A$ calculated using the DSMC results is $3.30 \pm 1.65 \times 10^{-3}$ m^2, while the average $C_D A$ calculated using the free-molecular results is 3.35 m^2. The percent difference between the averages is 1.52%. The normalized root-mean-square deviation between all the $C_D A$ results across both models is 1.65%. The average $C_L A$ calculated using the DSMC results is $2.02 \times 10^{-2} \pm 1.01 \times 10^{-5}$ m^2, while the average $C_L A$ calculated using the free-molecular analytical modeling results is 2.05×10^{-2} m^2. The percent difference between the averages is 1.53%. The same higher-than-expected discrepancy is seen qualitatively between the coefficient of lift curves in Figure **??** (b), and the normalized root-mean-square error between them is exponentially elevated due to the phenomena discussed above, as well as the average value being very close to zero. The error percentage between the modeling approaches for the lift coefficient is therefore not a good metric to judge agreement between models.

5.2.2 $Kn = 10$: Moments and Angular Accelerations

The moments are taken about the geometric Star48B body centroid: $X = 9.67 \times 10^{-1}$ m, $Y = 1.12 \times 10^{-3}$ m, $Z = 0.00 \times 10^{-3}$ m. The moments of inertia about the whole STAR48B's primary axes are $I_{XX} = 26.1$ kg m^2, $I_{YY} = 50.5$ kg m^2, and $I_{ZZ} = 51$ kg m^2.

Due to the symmetrical modeling of the half-Star48B, there is a reflected point across the Z-axis for every point on the modeled Star48B. These reflected points experience the same X and Y direction forces, but reflected Z-forces due to the flow being deflected in the opposite direction of the meshed Star48B over the spherical forebody or nozzle cone aftbody. The modeled point's moments are given in Equation 5.1. The subscript M refers to the modeled meshed points and moments. The X, Y, and Z subscripts in Equation 5.1 refer to the component of the moment taken about that axis. r is the position coordinate of the points.

$$\begin{aligned} M_{X,M} &= r_{Y,M}F_{Z,M} - r_{Z,M}F_{Y,M} \\ M_{Y,M} &= r_{Z,M}F_{X,M} - r_{X,M}F_{Z,M} \\ M_{Z,M} &= r_{X,M}F_{Y,M} - r_{Y,M}F_{X,M} \end{aligned} \tag{5.1}$$

The reflected point's moments are given in Equation 5.2. The subscript R refers to the non-modeled, reflected points.

$$
\begin{aligned}
M_{X,R} &= r_{Y,R}F_{Z,R} - r_{Z,R}F_{Y,R} \\
M_{Y,R} &= r_{Z,R}F_{X,R} - r_{X,R}F_{Z,R} \\
M_{Z,R} &= r_{X,R}F_{Y,R} - r_{Y,R}F_{X,R}
\end{aligned}
\tag{5.2}
$$

Applying the symmetry of the modeled Star48B: $r_{X,M} = r_{X,R}$, $r_{Y,M} = r_{Y,R}$, $F_{X,M} = FX, R$, and $F_{Y,M} = F_{Y,M}$. For the Z-axis: $r_{Z,R} = -r_{Z,M}$ and $F_{Z,R} = -F_{Z,M}$. Applying this to Equations 5.1 and 5.2, and summing for total moments, the X- and Y- moments cancel out across the body, and the Z-moments double. The Z-moments correspond to one mode of rotation of the Star48B which would change the area exposed to the flow.

Though the X- and Y- moments cancel across the body, the yielded moments on half the body are studied in this section in order to compare models. Note that the Z-moments are not doubled when plotted.

Figure 5.11 displays the moment results about the three primary axes yielded by both models across all the Star48B orientations.

The aerodynamic moments about the X- and Y-axes are an order of magnitude larger than those modeled about the Z-axis. This is because the flow-facing area changes are large as the relative velocity vector moves across the X-Y plane. Though the X- and Y- moments cancel out when projecting results to the entire body, Figure 5.11 shows the good agreement of the DSMC and free-molecular approaches expected at this Knudsen number.

As seen in Figure 5.11 (a), the maximum aerodynamic moment about the X-axis is incurred when β is $90°$. Flow is distributed across the differing areas of the spherical forebody and nozzle

cone aftbody and the differences in area cause a force distribution that pushes the Star48B. When $\beta = 0°$ or $180°$, the oncoming flow is applied symmetrically about the X-axis, causing the X-moment minima. In Figure 5.11 (b), the Y-moment has absolute maximas of around 0.04 N m for $\beta = 30°$ and $\beta = 150°$. At $\beta = 30°$, the flow impacts a large part of the spherical aftbody in an angled way, and only some of the nozzle cone experiences non-negligible applied pressure, and vice-versa for $\beta = 150°$. The pressure and area difference creates the maxmimum moments. The minimum Y-moment occurs for $\beta = 0°$, where the flow is distributed evenly across the Y-axis.

For the Z-axis, in Figure 5.11 (c), the moment is minimized when $\beta = 0°$ and $\beta = 180°$. The incoming flow at these angles again impacts a near-circular area which is even across the Z-axis, therefore a moment is not incurred. The local maxima at $\beta = 15°$, $90°$, and $165°$ occur because the pressure force is not distributed evenly between the impacted spherical forebody and nozzle cone aftbody. The local minima at $\beta = 45°$ and $\beta = 135°$ occur because the pressure distribution between the differing areas of the body is minimized at these angles. More of the nozzle cone is experiencing pressure, and less of the spherical forebody is experiencing pressure, which equalizes the moment about the Z-axis.

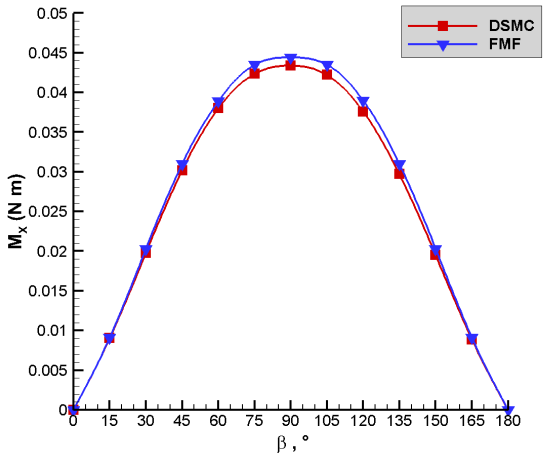

(a)

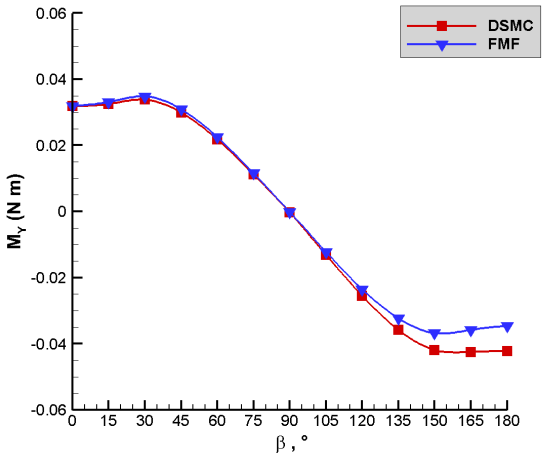

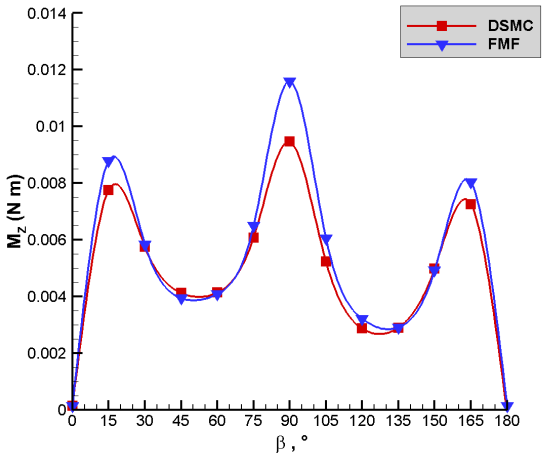

(b) (c)

Figure 5.11: Moments calculated using DSMC and free-molecular (FMF) analytical models for all experiment orientations of the Star48B about the: (a) X axis; (b) Y axis; (c) Z axis, for a Knudsen number of 10.

The moment averages are listed in Table 5.6. Table 5.6 portrays clearly that the free-molecular and DSMC modeling approaches yield similar results for this Knudsen number.

Qualitatively, Figure 5.11 displays good agreement between the DSMC results and the free-molecular results, for all three moments. In Table 5.6, the Y-moments do not appear to agree.

Table 5.6: Average moments calculated for a Knudsen number of 10 for the DSMC and free-molecular analytical modeling approaches across all β values.

Average	FMF	DSMC
$\mathbf{M}_X$ **(N m)**	2.75×10^{-2}	2.67×10^{-2} $\pm 1.34 \times 10^{-5}$
$\mathbf{M}_Y$ **(N m)**	-7.64×10^{-4}	-2.92×10^{-3} $\pm -1.46 \times 10^{-6}$
$\mathbf{M}_Z$ **(N m)**	5.50×10^{-3}	5.05×10^{-3} $\pm 2.53 \times 10^{-6}$

This is due to the average Y-moment being very close to zero. In Figure 5.11 (b), there is good agreement between the models with some small deviance at the end. The small deviance is caused by the blocking algorithm yielding zero pressure in the blocked zones for the free-molecular model, while the DSMC model follows particles. The nozzle cone geometry exacerbates these differences, which causes the deviance around $\beta = 180°$. However, there is still good agreement between the models. This is not reflected in the averages because the DSMC average is pulled negative due to the more-negative results near $\beta = 180°$. The normalized root-mean-square deviance is also affected by the near-zero average.

The normalized root-mean-square deviance between all the X-axes moments is 3.38%. The normalized root-mean-square deviance between the Y-axes moments is 12.9%. The normalized root-mean-square deviance between the Z-axes moments is 14.9%. Both the Y- and Z-moment normalized root-mean-square deviations are affected by the averages being so near-zero; they are inflated beyond what is qualitatively seen in Figure 5.11 as good agreement. The moment results overall reflect good agreement between the free-molecular and DSMC methods at this Knudsen number, as expected.

Because the Z-moments are the only ones that are non-zero across the whole Star48B body, the angular acceleration about the Z-axis is examined more thoroughly here. There is no data on

the rotational behavior of the Star48B so there are no uncertainty error bars applied. The angular acceleration is examined to visually inspect on what scale would aerodynamic moments induce rotational motion in the Star48B at this altitude.

Figure 5.12 shows the calculated angular acceleration about the Z-axis for the Star48B body using both models across all orientations. In Figure 5.12, the Z-moments across the orientations have been doubled, then divided by I_{ZZ}, to represent the moments incurred by the entire Star48B.

The interpolated average angular accelerations about the Z-axis incurred are $1.13 \times 10^{-2} \pm 5.65 \times 10^{-6}$ degrees s^{-2} using the DSMC method and 1.24×10^{-2} degrees s^{-2} using the free-molecular analytical method. The normalized root-mean-square deviance between the angular accelerations about the Z-axis is 14.9%. Again, this in inflated because the averages are very near zero.

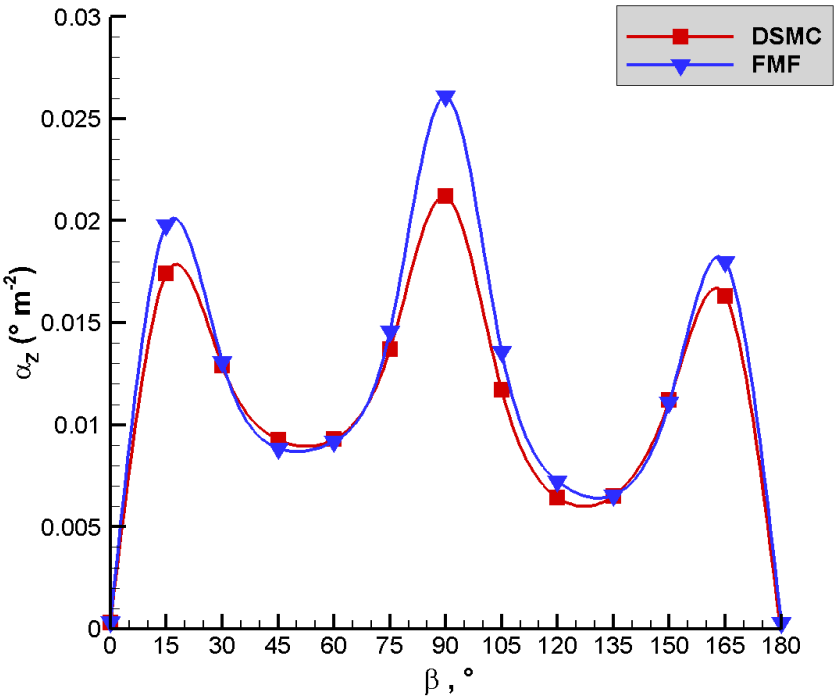

Figure 5.12: Angular acceleration about the Z-axis calculated using DSMC and free-molecular (FMF) analytical models for all experiment orientations of the Star48B, for a Knudsen number of 10.

The angular accelerations caused aerodynamically at this Knudsen number are very small. This makes sense: the Star48B is a relatively large, heavy piece of space debris, and a large force that is distributed unevenly is needed to cause a significant change in angular motion. At this altitude, the aerodynamic forces are not large enough to make much of a difference. An average rotation rate of 4 rpm, or 24 degrees s^{-1}, would only be changed by about 0.05% if an angular acceleration of 1.2×10^{-2} degrees s^{-2} was applied for a second. The aerodynamic moments are expected to increase, and become a more dominant influence on rotational behavior, as Knudsen number decreases at lower altitudes.

5.3 Knudsen Number of 1

A Knudsen number of 1 is achieved for the Star48B body at 115 km of altitude. As discussed for other bodies, a Knudsen number of 1 is the limit of defined free-molecular flow [20]. In this regime, the flowfields will still be rarefied, but the expectation of good agreement between the models does not hold: particle collisions will matter at this Knudsen number. The circular orbital speed and atmospheric composition at this altitude are listed in Table 5.2. The Star48B surface elements used at this altitude have a side length average of 1.65×10^{-2} m in order to be smaller than the free-stream mean free path compressed by a factor of 10 (0.18 m), and to capture the curvature of the Star48B shape. This refinement yields 2.29×10^{5} volume cells in the flowfield, and 32,200 surface elements. As an example, the $\beta = 90^{\circ}$ orientation is presented. All slices of the flowfield are taken at $Z = 3.67 \times 10^{-2}$ m, which is close to the X-Y plane, the plane of symmetry. This slice is chosen in order to show both the fore spherical shape of the body as well as the aft nozzle cone of the body experiencing flow. The Star48B body is represented by the white "cut-out" of the slice of the body.

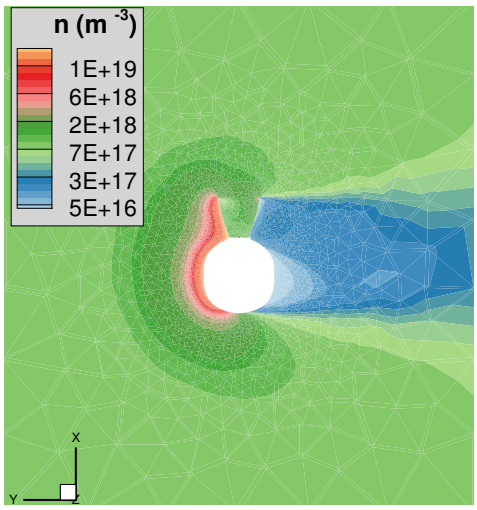

(a)

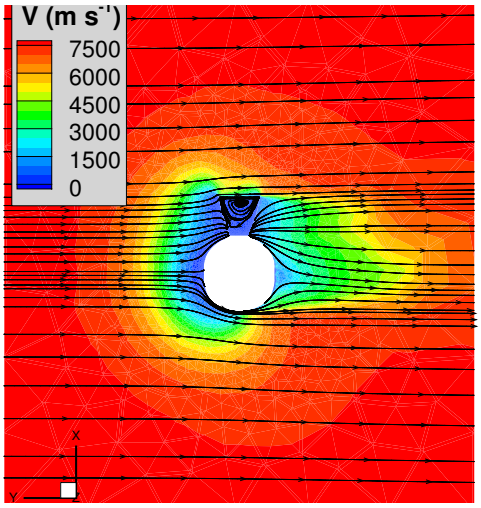

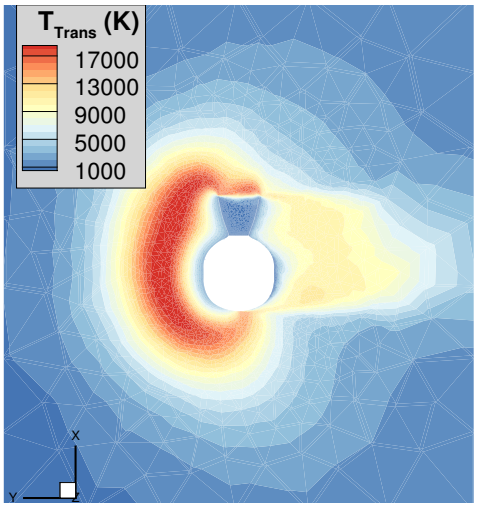

(b) (c)

Figure 5.13: Flowfield contours at $Kn = 1$, $\beta = 90°$: (a) number density; (b) velocity; (c) translational temperature.

Figure 5.13 shows the flowfield contours computed using MONACO. All three contour plots show flow phenomena expected when an object disturbs rarefied high-speed flow: instead of a defined shock layer, a large volume of slowed-down flow forms in front of the object. Figure 5.13 (a) displays the number density contours, which explicitly show the backflow enter. Part of the nozzle cone does not experience any flow penetration. In Figure 5.13 (b) the velocity streamlines

are plotted. The β angle can be clearly seen in the direction of these streamlines. Again, there is interesting disturbed flow behavior in the nozzle cone, from backflow that reflects off the nozzle walls and exits the nozzle cone again. Figure 5.13 (c) displays the translational temperature. The temperature is not raised in the nozzle cone, as that flow is more accommodated to the surface temperature of 300 K from contact with the nozzle walls.

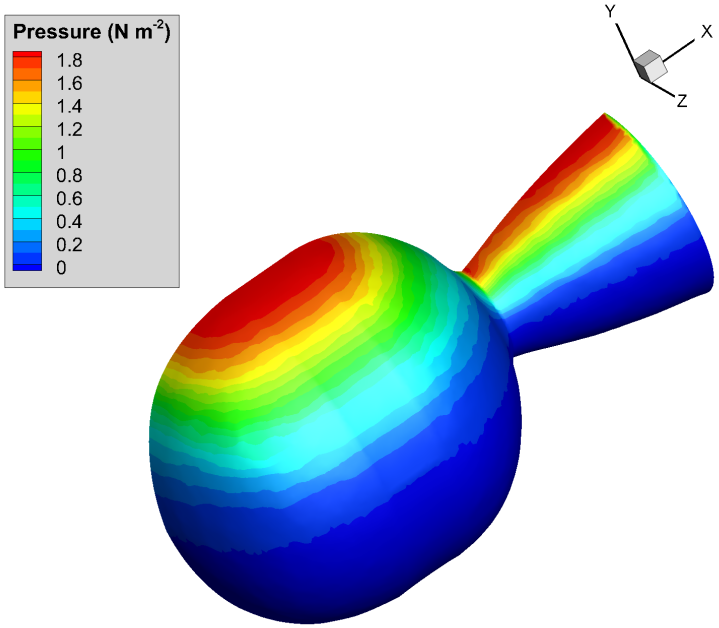

(a)

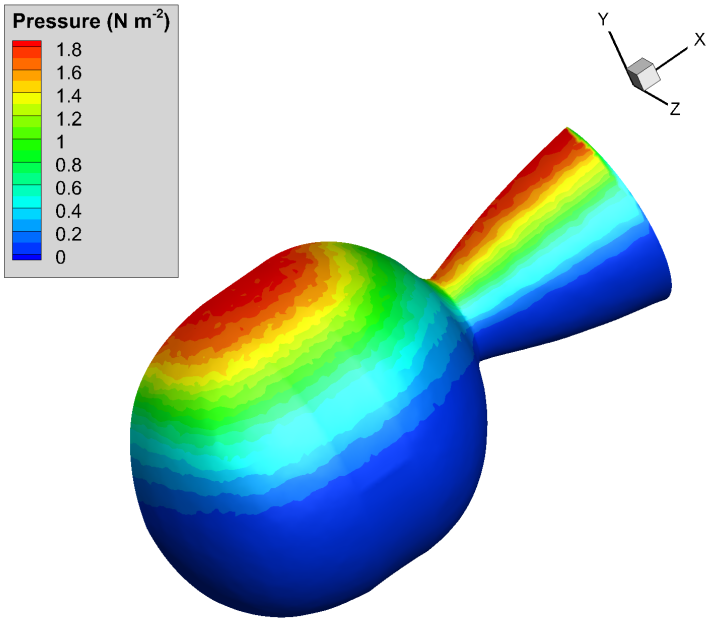

(b)

Figure 5.14: Pressure distribution at $Kn = 1$, $\beta = 90°$: calculated using: (a) free molecular theory; (b) DSMC.

Figures 5.14 displays an example of the surface pressure on the Star48B for the $\beta = 90^{\circ}$ case. It is evident when comparing Figures 5.14 (a) and (b) that the backflow experienced via simulation using DSMC is affecting the pressure distribution; as is the case for $Kn = 10$ in Section 5.2. The free-molecular analytical approach detects when cells directly experience flow; because it does not track particles, no pressure is seen on the underside of the Star48B in Figure 5.14 (a). The pressure distributions are still similar: the average pressure experienced by the surface is calculated as 3.15×10^{-1} N m^{-2} using the free-molecular method. This average is calculated by accounting for the pressure on each surface element over the entire body, weighting with respect to surface area, for this (the $\beta = 90^{\circ}$) orientation. The average pressure experienced over the body calculated by using MONACO results is $3.25 \times 10^{-1} \pm 1.30 \times 10^{-4}$ N m^{-2}, and is calculated similarly. The statistical error for the DSMC pressure calculation is the Poisson statistical error of the DSMC results caused by the number of hits experienced by the body per surface element per time step and is enumerated in the next section. The difference in average pressure experienced by the body at this orientation is 3.18%.

5.3.1 $Kn = 1$: Drag and Lift

Now the drag and lift experienced over the body are compared between the two models. The drag and lift forces plotted and discussed in this section apply to only the half of the Star48B that is meshed and simulated. For use in other models (such as the orbital decay model), the forces are doubled to represent the entire body.

In order to compare models, the drag and lift forces gathered for each modeled orientation are interpolated over all values of β to yield an average value.

Figure 5.15 shows the calculated drag for all orientations using both approaches. The data points for individual simulation results are connected using splines to demonstrate the smooth transition of drag experienced as body rotation would occur.

The Poisson statistical error due to the number of hits experienced by the body per surface element per time step for MONACO DSMC simulations is calculated as in Equation 3.1. Using Equation 3.1, the average hits per sampling time step per surface element across the Star48B at this Knudsen number is 7.74×10^{-3}, the total number of surface elements is 32,200, and using 25,000 sampling steps: the Poisson statistical error of aerodynamic DSMC results is 0.04%. Error bars are not shown in the following figures because the statistical error is very small.

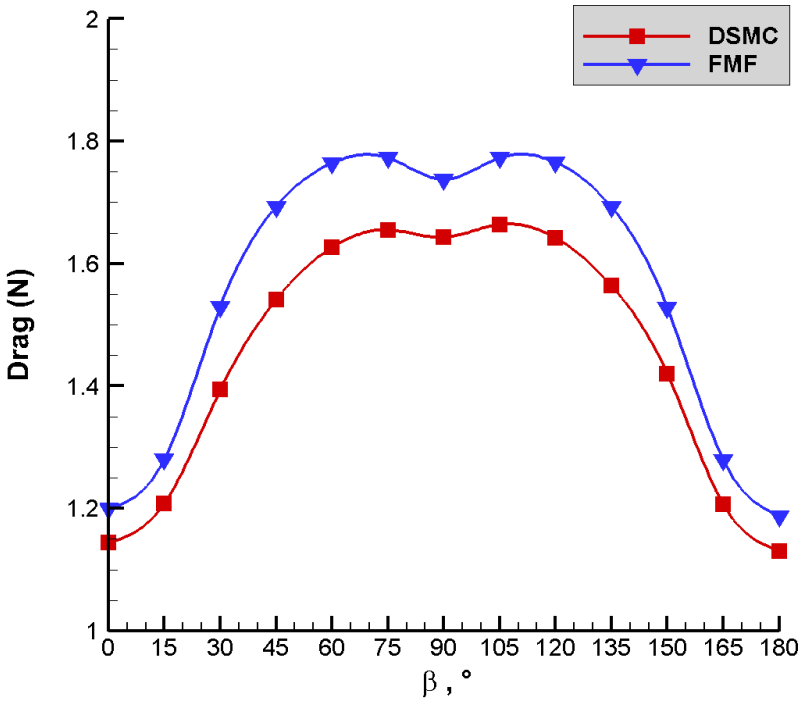

Figure 5.15: Drag calculated using DSMC and free-molecular (FMF) analytical models for all orientations analyzed of the Star48B at a Knudsen number of 1.

Figure 5.15 shows that maximum drag values are achieved for $\beta = 75°$ and $\beta = 105°$. The

same phenomena described in Section 5.2, for $Kn = 10$, happens for $Kn = 1$: for $\beta = 75°$ and $105°$, the maximum spherical body area and the maximum nozzle cone area are exposed to the oncoming flow. The small dip at $\beta = 90°$ is because less area of the nozzle cone is exposed to the flow. The nozzle has a smaller diameter near the spherical body and flares out, so when more of the flared area is exposed to the flow, the drag is increased. Minimum drag is achieved for $\beta = 0°$ and $\beta = 180°$. At these orientations, a minimal area is exposed to the flow: approximately at both angles, a semicircular area projection is exposed to direct pressure.

The average drag calculated using the MONACO results interpolated across all orientations is $1.48 \pm 5.90 \times 10^{-4}$ N. The average drag calculated using the free-molecular results is 1.58 N. The percent difference between the averages is 7.39%. The normalized root-mean-square deviance between all the drag results across both models is 7.05%. There results indicate that even though there is some agreement at this Knudsen number, the free-molecular assumption is weaker than at $Kn = 10$ where the drag error was less than 2%. The drag results match within 10%, and the drag at this altitude is small, so there is some agreement, but the free-molecular approach is becoming less appropriate as the Knudsen number lowers.

Figure 5.16 shows the calculated lift for all orientations using both methods. The lift displayed in Figure 5.16 is translated into an Earth-centric frame, which yields positive lift values. Lift is two orders of magnitude smaller compared to drag due to the Star48B's symmetry. The similarity to a sphere also affects the lift; spheres experience no lift, so the resemblance of the forebody to a sphere minimizes lift. Resolved as described in Chapter 2, nearly all force applied to the Star48B body is attributed to drag. Unless a pressure gradient in a normal direction to the oncoming velocity is created by the body's geometry, drag will be the dominating force.

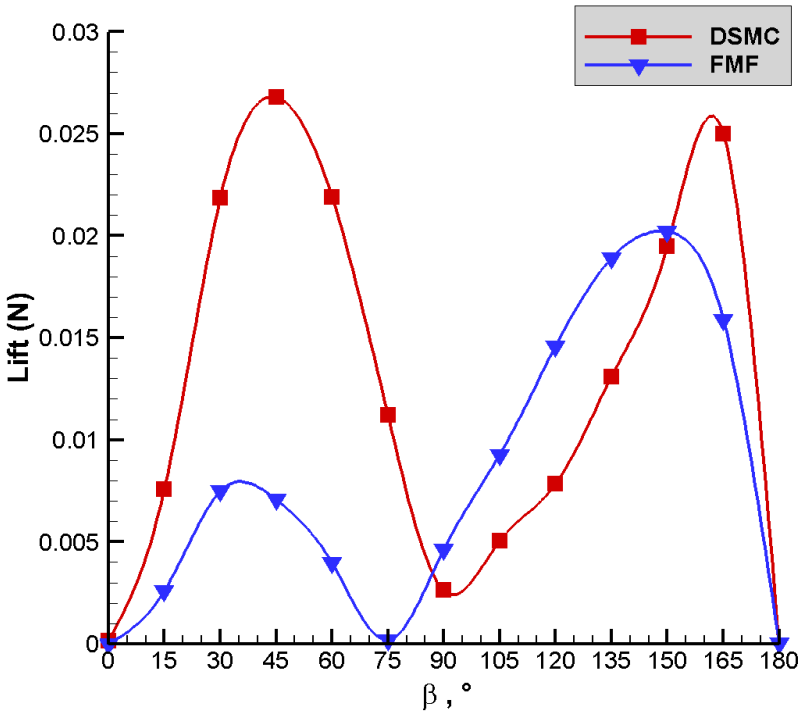

Figure 5.16: Lift calculated using DSMC and free-molecular (FMF) analytical models for all orientations of the Star48B at a Knudsen number of 1.

The average lift calculated using the MONACO results interpolated across all orientations is $1.35 \times 10^{-2} \pm 5.41 \times 10^{-6}$ N. The average lift calculated using the free-molecular results is 8.73×10^{-3} N. The percent difference between the averages is 35.5%. The normalized root-mean-square deviance is affected by the averages being so close to zero, and is not a good metric to judge the agreement between models.

Qualitatively, it is evident that the lift curves in Figure 5.16 are further apart than in Figure 5.15; showing differences between the models. Additionally, 35.5% error between the lift averages is much higher than expected from the differences in the drag forces. Therefore the lift is examined in more detail, as in Section 5.2.

In order to examine the modeling differences, both pressure and shear stress contributions to

the lift force are inspected below. Figure 5.17 displays the pressure contribution to the lift force for both models, while Figure 5.18 displays the shear stress contribution to the lift force for both models.

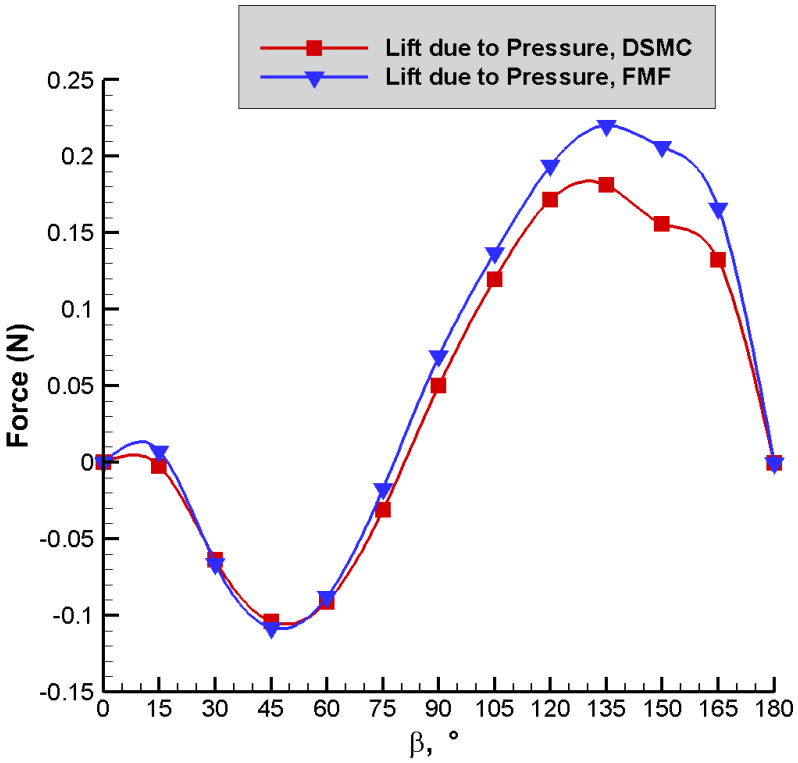

Figure 5.17: Lift due to pressure on the Starb48B, calculated using DSMC and free-molecular (FMF) analytical models for all orientations at a Knudsen number of 1.

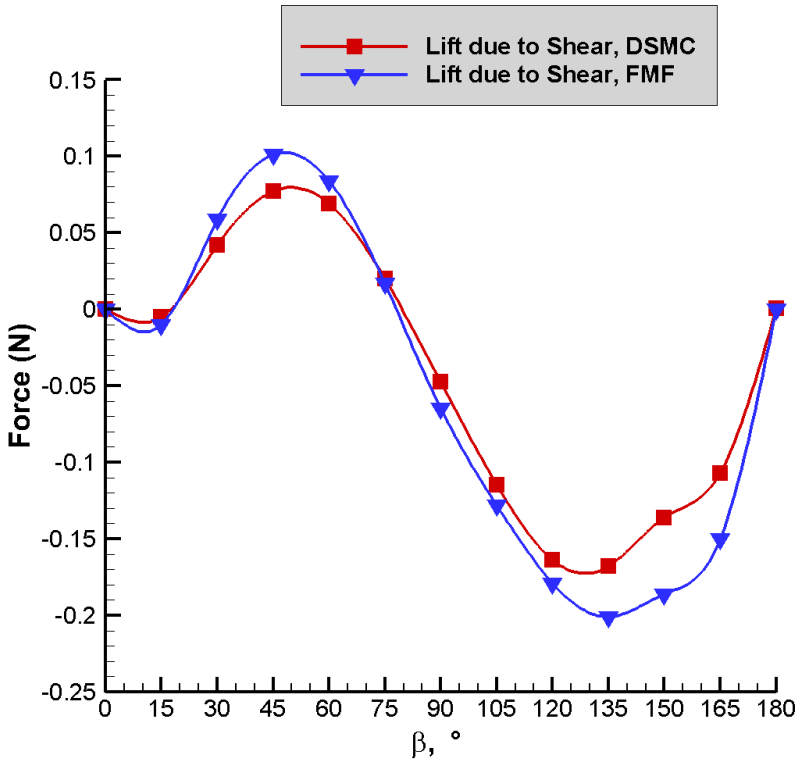

Figure 5.18: Lift due to shear stress on the Star48B, calculated using DSMC and free-molecular (FMF) analytical models for all orientations at a Knudsen number of 1.

Figures 5.17 and 5.18 display much better agreement than in Figure 5.16. For this Knudsen number, the pressure contribution differences are more extreme, as the backflow pressure experienced in the DSMC simulations effects the overall pressure force by minimizing it. This creates a smaller DSMC lift due to pressure force than the same calculated using the free-molecular method, as seen in Figure 5.17. Quantitatively, the normalized root-mean-square deviance between all the lift due to pressure results across both models is 23.1%. The normalized root-mean-square deviance between all the lift due to shear stress results across both models is 26.0%. These error results are also inflated due to the data points at $\beta = 0°$ and $\beta = 15°$ being close to zero, but relatively far apart, sometimes even with sign differences. These data points are enumerated in Table 5.7. Only a few surface elements need to be influenced by pressure in order to cause a result so

close to zero to "flip" signs. The average values being close to zero also inflate the error differences between the lift force contribution.

Table 5.7: Lift due to pressure and shear stress on the Starb48B at specific β values for a Knudsen number of 1.

Lift due to Pressure (N)		
	FMF	**DSMC**
$\beta = 0°$	9.48×10^{-5}	-1.54×10^{-4} $\pm - 6.16 \times 10^{-8}$
$\beta = 15°$	7.35×10^{-3}	-2.54×10^{-3} $\pm - 1.02 \times 10^{-6}$
Lift due to Shear Stress (N)		
	FMF	**DSMC**
$\beta = 0°$	-8.93×10^{-5}	1.02×10^{-5} $\pm 4.07 \times 10^{-9}$
$\beta = 15°$	-9.94×10^{-3}	-5.01×10^{-3} $\pm - 2.01 \times 10^{-6}$

To take the total lift across the body, the lift due to pressure and the lift due to shear stress are summed. This results in lift values very close to zero; and small discrepancies in both contributing forces are magnified; yielding the curves in Figure 5.16. Because the lift is so small, the differences between models will not greatly change any orbital decay results, especially for a large piece of space debris as the 117 kg Star48B. When compared to lift contribution results from $Kn = 10$, in Section 5.2, the differences between the modeling approaches have increased from around 10% to around 25%, showing the growing inadequacy of the free-molecular model to match DSMC results as Knudsen number lowers.

In order to calculate coefficients of drag and lift for use in the orbital decay model, a free-stream density is taken from [9]. At 115 km, where for Star48B $Kn = 1$, the free-stream density $\rho = 3.09 \times 10^{-8}$ kg m^{-3}. The orbital velocity is the circular orbital speed used throughout the $Kn = 1$ results: $V = 7840$ m s^{-1}. The aerodynamic coefficients are calculated for a full-body

(not half, or meshed representation of) Star48B, and include the area as in Chapter 3, for use in the orbital decay modeling. The modeled force is multiplied by two to get the total force on the body. The lift coefficient is calculated similarly.

Figure 5.19 shows C_DA and C_LA calculated for all models and orientations for $Kn = 1$ experienced by the Star48B body.

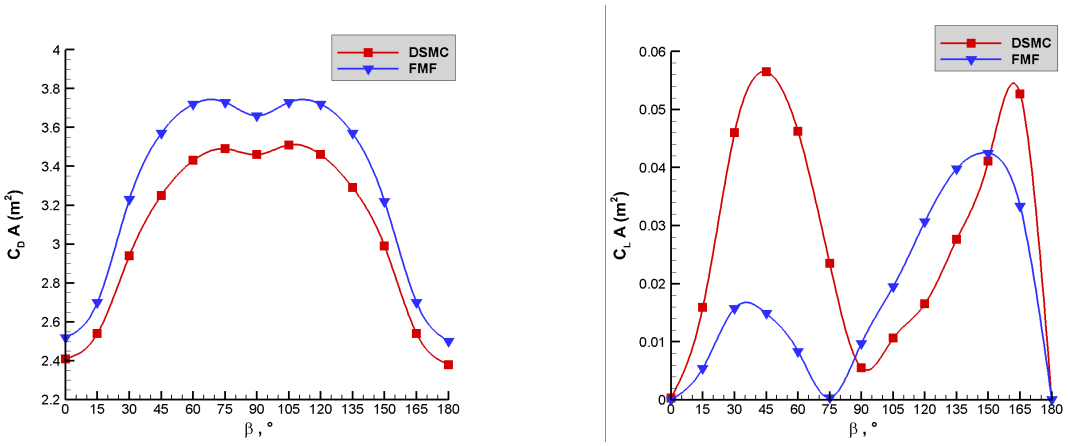

(a) (b)

Figure 5.19: Drag (a) and lift (b) coefficients calculated using DSMC and free-molecular (FMF) analytical models for all experiment orientations of the Star48B using both models for a Knudsen number of 1.

The average C_DA calculated using the DSMC results is $3.11 \pm 1.24 \times 10^{-3}$ m^2, while the average C_DA calculated using the free-molecular results is 3.34 m^2. The percent difference between the averages is 7.41%. The normalized root-mean-square deviation between all the C_DA results across both models is 7.05%. The average C_LA calculated using the DSMC results is $2.85 \times 10^{-2} \pm 1.14 \times 10^{-5}$ m^2, while the average C_LA calculated using the free-molecular analytical modeling results is 1.84×10^{-2} m^2. The percent difference between the averages is 35.5%. The same higher-than-expected discrepancy is seen qualitatively between the coefficient of lift curves in Figure 5.19 (b), and the normalized root-mean-square error between them is exponentially ele-

vated due to the phenomena discussed above, as well as the average value being very close to zero. The error percentage between the modeling approaches for the lift coefficient is therefore not a good metric to judge agreement between models.

5.3.2 $Kn = 1$: Moments and Angular Accelerations

Moments are treated in the same way as detailed in Section 5.2.2. Figure 5.20 displays the moment results about the three primary axes yielded by both models across all the Star48B orientations.

The aerodynamic moments about the X- and Y-axes are an order of magnitude larger than those modeled about the Z-axis. This is because the flow-facing area changes are large as the relative velocity vector moves across the X-Y plane. Though the X- and Y- moments cancel out when projecting results to the entire body, Figure 5.20 shows the decent agreement of the DSMC and free-molecular approaches expected at this Knudsen number.

The same phenomena that create maximized and minimized moments for a Knudsen number of 10 happen at a Knudsen number of 1. In Figure 5.20 (a), the maximum aerodynamic moment about the X-axis is incurred when β is $90°$. Flow is distributed across the differing areas of the spherical forebody and nozzle cone aftbody and the differences in area cause a force distribution that pushes the Star48B. When $\beta = 0°$ or $180°$, the oncoming flow is applied symmetrically about the X-axis, causing the X-moment minima. In Figure 5.20 (b), the Y-moment has absolute maximas of around 0.4 N m for $\beta = 30°$ and $\beta = 150°$. At $\beta = 30°$, the flow impacts a large part of the spherical aftbody in an angled way, and only some of the nozzle cone experiences non-negligible applied pressure, and vice-versa for $\beta = 150°$. The pressure and area difference creates the maxmimum

moments. The minimum Y-moment occurs for $\beta = 0°$, where the flow is distributed evenly across the Y-axis.

For the Z-axis, in Figure 5.20 (c), the moment is minimized when $\beta = 0°$ and $\beta = 180°$. The incoming flow at these angles again impacts a near-circular area which is even across the Z-axis, therefore a moment is not incurred. The local maxima at $\beta = 15°$, $90°$, and $165°$ occur because the pressure force is not distributed evenly between the impacted spherical forebody and nozzle cone aftbody. The local minima at around $\beta = 45°$ and $\beta = 120°$ occur because the pressure distribution between the differing areas of the body is minimized at these angles. More of the nozzle cone is experiencing pressure, and less of the spherical forebody is experiencing pressure, which equalizes the moment about the Z-axis.

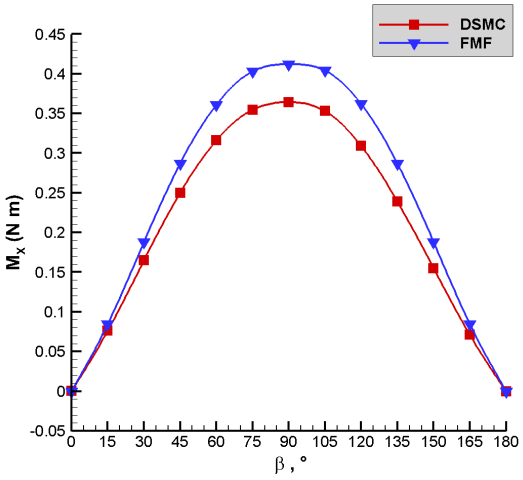

(a)

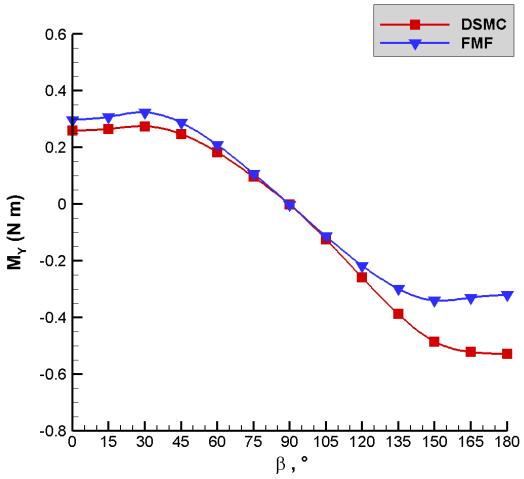

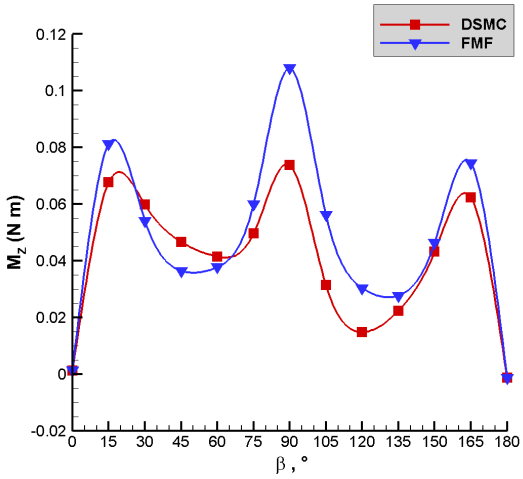

(b) (c)

Figure 5.20: Moments calculated using DSMC and free-molecular (FMF) analytical models for all experiment orientations of the Star48B about the: (a) X axis; (b) Y axis; (c) Z axis, for a Knudsen number of 1.

The moment averages are listed in Table 5.8. Table 5.8 portrays clearly that the free-molecular and DSMC modeling approaches yield similar results for this Knudsen number.

Qualitatively, Figure 5.20 displays relatively good agreement between the DSMC results and the free-molecular results, for the X- and Z- moments. In Table 5.8, the Y-moments are over an

Table 5.8: Average moments calculated for a Knudsen number of 1 for the DSMC and free-molecular analytical modeling approaches across all β values.

Average	**FMF**	**DSMC**
$\mathbf{M}_X$ **(N m)**	2.55×10^{-1}	2.21×10^{-1} $\pm 8.84 \times 10^{-5}$
$\mathbf{M}_Y$ **(N m)**	-6.29×10^{-3}	-7.08×10^{-2} $\pm -2.83 \times 10^{-5}$
$\mathbf{M}_Z$ **(N m)**	5.11×10^{-2}	4.28×10^{-2} $\pm 1.71 \times 10^{-5}$

order of magnitude apart, indicating unexpectedly large differences in the modeling approaches. This is due to the average Y-moment being very close to zero and the DSMC Y-moments becoming more negative as β approaches $180°$. In Figure 5.20 (b), there is agreement between the models with increasing deviance at the end. The deviance is caused by the blocking algorithm yielding zero pressure in the blocked zones for the free-molecular model, while the DSMC model follows particles. The nozzle cone geometry exacerbates these differences, which causes the deviance around $\beta = 180°$. However, there is still some agreement between the models. This is not reflected in the averages because the DSMC average is pulled negative due to the more-negative results near $\beta = 180°$. The normalized root-mean-square deviance is also affected by the near-zero average.

The normalized root-mean-square deviance between all the X-axes moments is 15.7%. The normalized root-mean-square deviance between the Y-axes moments is 39.5%. The normalized root-mean-square deviance between the Z-axes moments is 30.1%. Both the Y- and Z-moment normalized root-mean-square deviations are affected by the averages being so near-zero; but do reflect the degrading accuracy of the free-molecular analytical model as Knudsen number decreases.

Because the Z-moments are the only ones that are non-zero across the whole Star48B body, the angular acceleration about the Z-axis is examined more thoroughly here. There is no data on the rotational behavior of the Star48B so there are no uncertainty error bars applied. The angular

acceleration is examined to visually inspect on what scale would aerodynamic moments induce rotational motion in the Star48B at this altitude.

Figure 5.21 shows the calculated angular acceleration about the Z-axis for the Star48B body using both models across all orientations. In Figure 5.21, the Z-moments across the orientations have been doubled, then divided by I_{ZZ}, to represent the moments incurred by the entire Star48B.

The interpolated average angular accelerations about the Z-axis incurred are $9.61 \times 10^{-2} \pm 3.85 \times 10^{-5}$ degrees s^{-2} using the DSMC method and 1.15×10^{-1} degrees s^{-2} using the free-molecular analytical method. The normalized root-mean-square deviance between the angular accelerations about the Z-axis is 19.3%. Again, this in inflated because the averages are near zero.

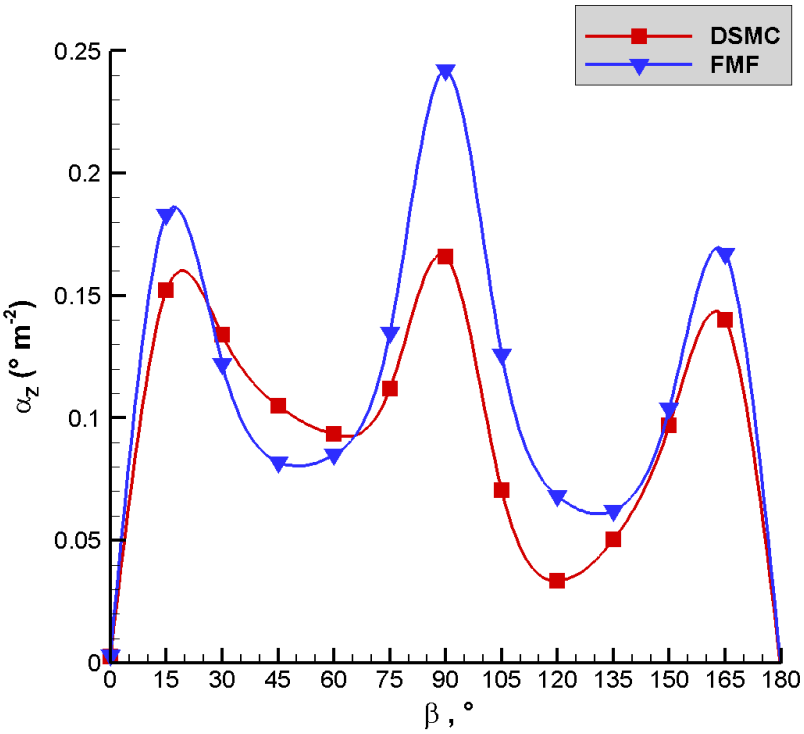

Figure 5.21: Angular acceleration about the Z-axis calculated using DSMC and free-molecular (FMF) analytical models for all experiment orientations of the Star48B, for a Knudsen number of 1.

The angular accelerations caused aerodynamically at this Knudsen number are small. This

makes sense: the Star48B is a relatively large, heavy piece of space debris, and a large force that is distributed unevenly is needed to cause a significant change in angular motion. Again at this altitude, the aerodynamic forces are not large enough to make much of a difference. An average rotation rate of 4 rpm, or 24 degrees s^{-1}, would only be changed by about 0.5% if an angular acceleration of 1.2×10^{-1} degrees s^{-2} was applied for a second. The aerodynamic moments are expected to increase, and become a more dominant influence on rotational behavior, as Knudsen number decreases at lower altitudes.

5.4 Knudsen Number of 0.1

A Knudsen number of 0.1 is achieved for the Star48B body at 101 km of altitude. A Knudsen number of 0.1 is purely in the transitional regime [20]. In this regime, the flowfields are markedly less rarefied and an expectation of good agreement between the models should not hold. The circular orbital speed and atmospheric composition at this altitude are listed in Table 5.2. A different mesh is used for this altitude in order to achieve cell sizes with side lengths smaller than the mean free path.

The Star48B surface elements used at this altitude have a side length average of 6.88×10^{-3} m in order to be smaller than the free-stream mean free path compressed by a factor of 10 (1.69×10^{-2} m), and to capture the curvature of the Star48B shape. This refinement yields 1.25×10^{6} volume cells in the flowfield, and 1.98×10^{5} surface elements. As an example, the $\beta = 180°$ orientation is presented. All slices of the flowfield are taken at $Z = 3.67 \times 10^{-2}$ m, which is close to the X-Y plane, the plane of symmetry. This slice is chosen in order to show both the fore spherical shape of the body as well as the aft nozzle cone of the body experiencing flow. The Star48B body is

represented by the white "cut-out" of the slice of the body.

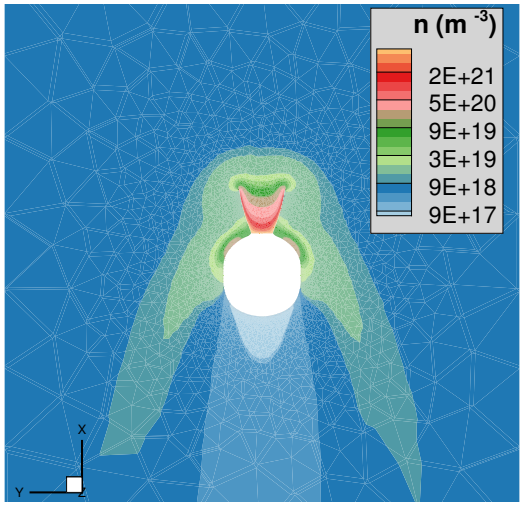

(a)

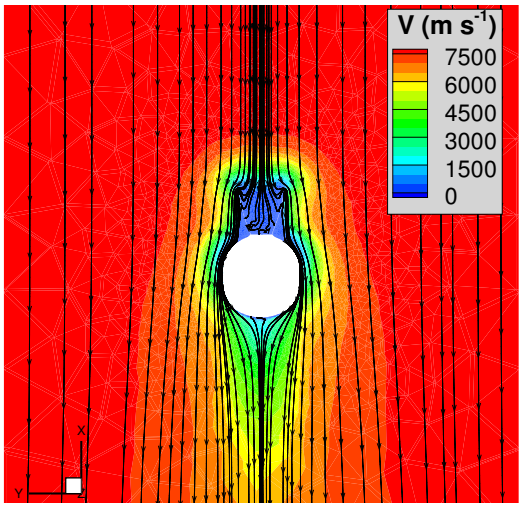

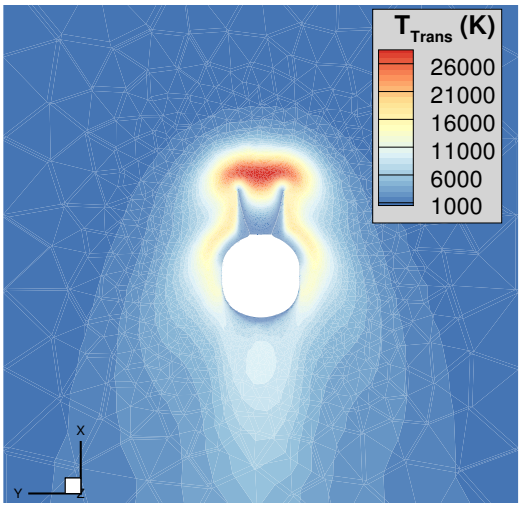

(b) (c)

Figure 5.22: Flowfield contours at $Kn = 0.1$, $\beta = 180°$: (a) number density; (b) velocity; (c) translational temperature.

Figure 5.23 shows the flowfield contours computed using MONACO. The contours show that as Knudsen number drops, a shock begins to form upstream of the body. The shock contour is interesting due to the concave nozzle cone. Figure 5.23 (a) displays the number density contours, which demonstrate the shock-like disturbance of the flow in front of the nozzle cone. There is

backflow which comes into contact with the spherical side of the Star48B, but the number density downstream of the Star48B demonstrates how the flow is blocked by the body. In Figure 5.22 (b) the velocity streamlines are plotted. The β angle can be clearly seen in the direction of these streamlines. There is interesting disturbed flow behavior in the nozzle cone that is demonstrated by the streamlines. The flow is deflected off the nozzle cone; inside the nozzle some flow is stagnant. Figure 5.22 (c) displays the translational temperature. The shock-like behavior of the flowfield can be seen upstream of the nozzle cone in the temperature contour.

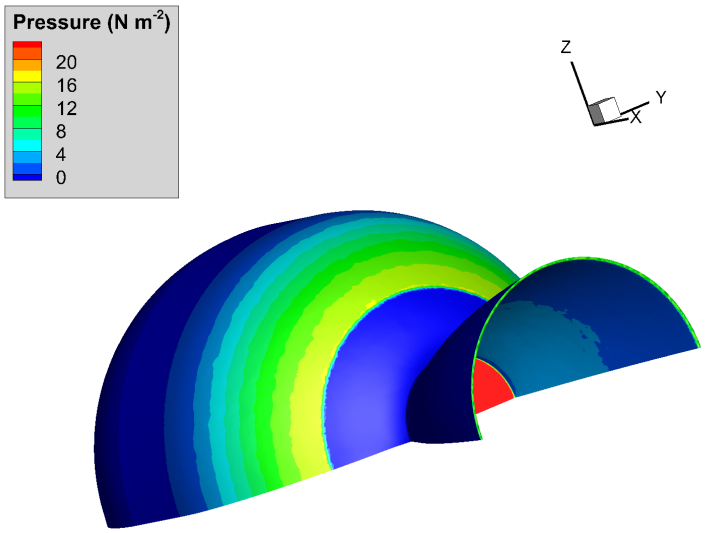

(a)

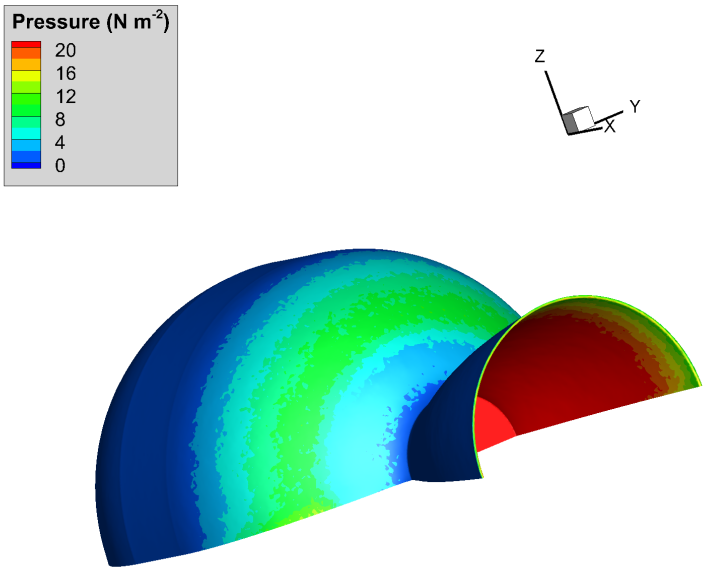

(b)

Figure 5.23: Pressure distribution at $Kn = 0.1$, $\beta = 180°$: calculated using: (a) free molecular theory; (b) DSMC.

Figures 5.23 displays an example of the surface pressure on the Star48B for the $\beta = 180°$ case. There are several differences in the surface pressure distributions. In Figure 5.23 (a), the maximum pressure is only applied to surface elements with the velocity orthogonal to their normal vectors; as described in Chapter 2, so the inside surface of the nozzle cone does not experience maximum pressure. In Figure 5.23 (b), many particle collisions of the nozzle-trapped flow impart high pressure on the inside of the nozzle cone walls. In Figure 5.23 (a), the "shadow" of the Star48B is noticeable in the sections of the surface that exhibit zero pressure. Figure 5.23 (b) exhibits backflow and flow that is deflected off of the outside of the nozzle cone, as nearly none of the visible surface experiences zero pressure. These visual differences are reflected in the average pressures. The average pressure experienced by the surface is calculated as 1.59 N m^{-2} using the free-molecular method. This average is calculated by accounting for the pressure on each surface element over the entire body, weighting with respect to surface area, for this (the $\beta = 180°$) orientation. The average pressure experienced over the body calculated by using MONACO results is $4.82 \pm 9.64 \times 10^{-4}$ N m^{-2}, and is calculated similarly. The statistical error for the DSMC pressure calculation is the Poisson statistical error of the DSMC results caused by the number of hits experienced by the body per surface element per time step and is enumerated in the next section. The difference in average pressure experienced by the body at this orientation is 67.0%. This error is extremely high, and shows how treatment of the surface using the free-molecular method is weak at this Knudsen number for this orientation.

5.4.1 $Kn = 0.1$: Drag and Lift

Now the drag and lift experienced over the body are compared between the two models. The drag and lift forces plotted and discussed in this section apply to only the half of the Star48B that is meshed and simulated. For use in other models (such as the orbital decay model), the forces are doubled to represent the entire body.

In order to compare models, the drag and lift forces gathered for each modeled orientation are interpolated over all values of β to yield an average value.

Figure 5.24 shows the calculated drag for all orientations using both approaches. The data points for individual simulation results are connected using splines to demonstrate the smooth transition of drag experienced as body rotation would occur.

The Poisson statistical error due to the number of hits experienced by the body per surface element per time step for MONACO DSMC simulations is calculated as in Equation 3.1. Using Equation 3.1, the average hits per sampling time step per surface element across the Star48B at this Knudsen number is 6.51×10^{-3}, the total number of surface elements is 1.98×10^{5}, and using 25,000 sampling steps: the Poisson statistical error of aerodynamic DSMC results is 0.02%. Error bars are not shown in the following figures because the statistical error is very small.

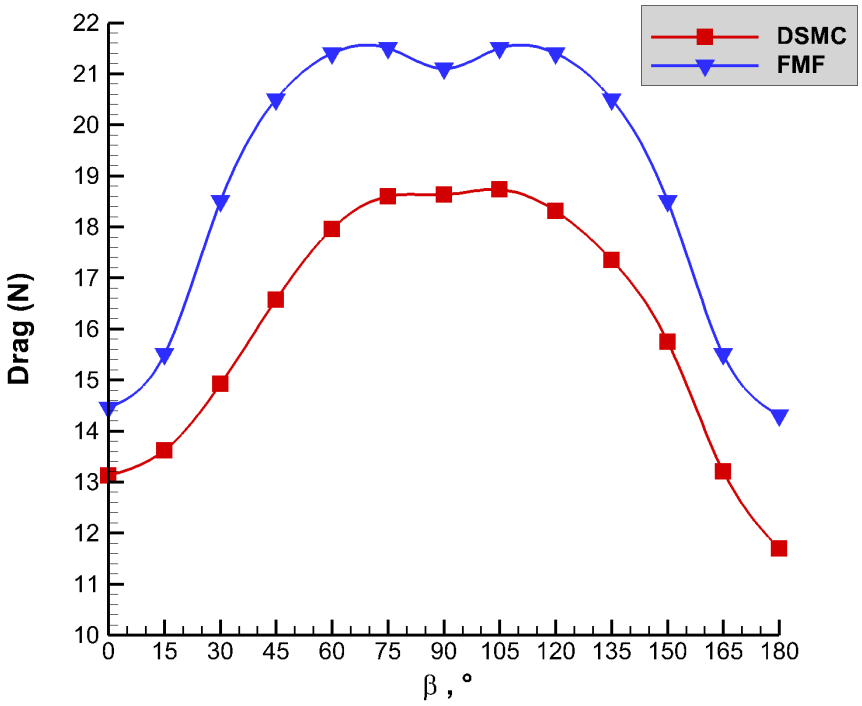

Figure 5.24: Drag calculated using DSMC and free-molecular (FMF) analytical models for all orientations analyzed of the Star48B at a Knudsen number of 0.1.

Figure 5.24 shows that maximum drag values are achieved for $\beta = 75°$ and $\beta = 105°$. The same phenomena described in Section 5.2 and Section 5.3 happens for $Kn = 0.1$ in the free-molecular curve: for $\beta = 75°$ and $105°$, the maximum spherical body area and the maximum nozzle cone area are exposed to the oncoming flow. The small dip at $\beta = 90°$ is because less area of the nozzle cone is exposed to the flow. The nozzle has a smaller diameter near the spherical body and flares out, so when more of the flared area is exposed to the flow, the drag is increased.

The DSMC curve is more bell-shaped, and actually has one maximum at $\beta = 105°$; drag experienced at $\beta = 90°$ is larger than at $\beta = 75°$ by a few hundredths of a Newton. The DSMC results differ from the free-molecular results in this way because there are more particles interacting with each and with the surface. At $\beta = 105°$, the flow catches on some of the inside of the nozzle

cone, increasing the drag to its maximum.

Minimum drag is achieved for $\beta = 0°$ and $\beta = 180°$. At these orientations, a minimal area is exposed to the flow: approximately at both angles, a semicircular area projection is exposed to direct pressure. For the DSMC curve, the extreme minimum is located at $\beta = 180°$; more flow is trapped inside the nozzle cone. The trapped flow collides with particles and the surface much more than at lower Knudsen numbers or other orientations. This trapped flow carries less momentum than free-stream flow, and therefore lowers the drag.

The average drag calculated using the MONACO results interpolated across all orientations is $16.3 \pm 3.27 \times 10^{-3}$ N. The average drag calculated using the free-molecular results is 19.2 N. The percent difference between the averages is 17.5%. The normalized root-mean-square deviance between all the drag results across both models is 15.3%. The error has increased by about 10% from the error experienced at a Knudsen number of 1. The free-molecular treatment is not performing well at this Knudsen number, as collisions between particles are much more important in this regime. Qualitatively, the drag curves are moving further and further apart as Knudsen number decreases, reflecting the disagreement between the models.

Figure 5.25 shows the calculated lift for all orientations using both methods. The lift displayed in Figure 5.25 is translated into an Earth-centric frame, which yields positive lift values. Lift is two orders of magnitude smaller compared to drag due to the Star48B's symmetry and resemblance to a sphere; as spheres produce no lift, the geometry of the Star48B minimizes the lift. Resolved as described in Chapter 2, nearly all force applied to the Star48B body is attributed to drag. Unless a pressure gradient in a normal direction to the oncoming velocity is created by the body's geometry, drag will be the dominating force.

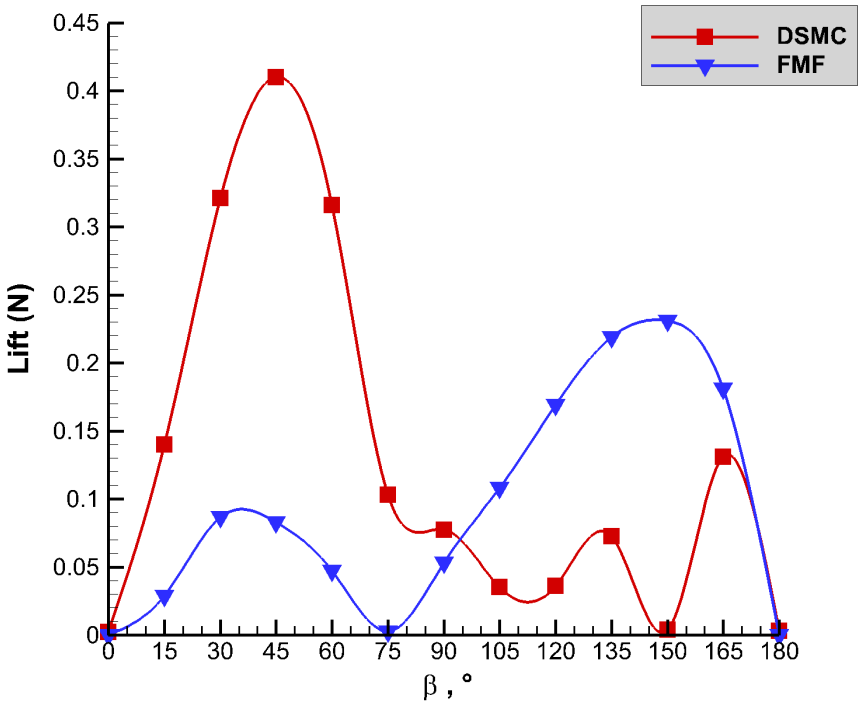

Figure 5.25: Lift calculated using DSMC and free-molecular (FMF) analytical models for all orientations of the Star48B at a Knudsen number of 0.1.

The average lift calculated using the MONACO results interpolated across all orientations is $1.37 \times 10^{-1} \pm 2.75 \times 10^{-5}$ N. The average lift calculated using the free-molecular results is 1.01×10^{-1} N. The percent difference between the averages is 26.6%. This seems contradictory; as the error percentage has gone down from that experienced at a Knudsen number of 1. The error is minimized not because there is agreement between the models, but because the lift curves have opposing shapes that cancel out error between them when taking the averages. The normalized root-mean-square deviance is affected by the averages being close to zero, and is not a good metric to judge the agreement between models.

Examining the lift force contributions is a better metric to judge the agreement or disagreement between the free-molecular and DSMC results. Qualitatively, it is evident that the lift curves in

Figure 5.25 are further apart than in Figure 5.16; showing growing differences between the models expected as the Knudsen number decreases. Therefore the lift is examined in more detail, as in Sections 5.2 and 5.3.

In order to examine the modeling differences, both pressure and shear stress contributions to the lift force are inspected below. Figure 5.26 displays the pressure contribution to the lift force for both models, while Figure 5.27 displays the shear stress contribution to the lift force for both models.

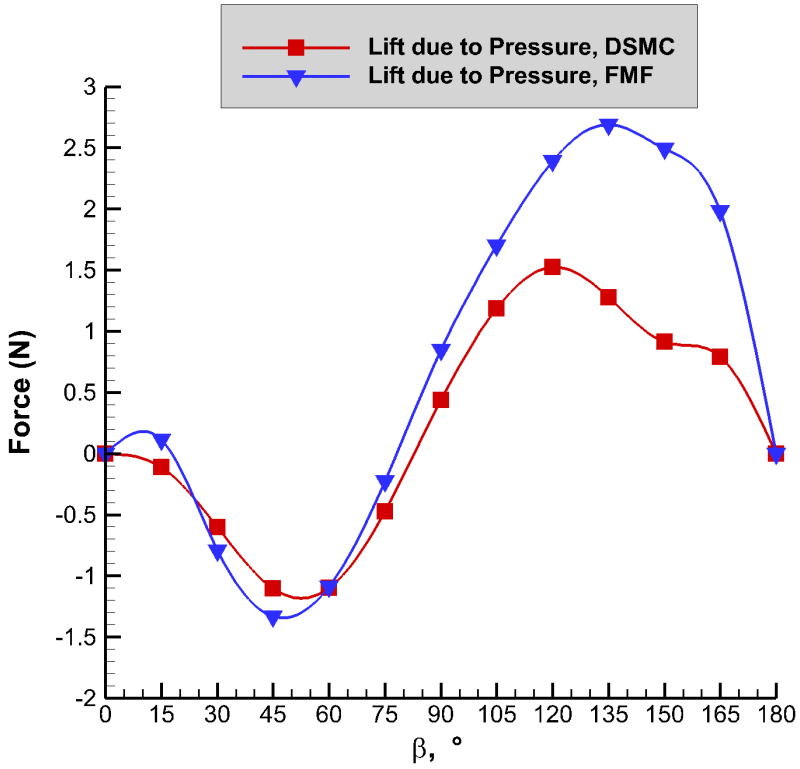

Figure 5.26: Lift due to pressure on the Starb48B, calculated using DSMC and free-molecular (FMF) analytical models for all orientations at a Knudsen number of 0.1.

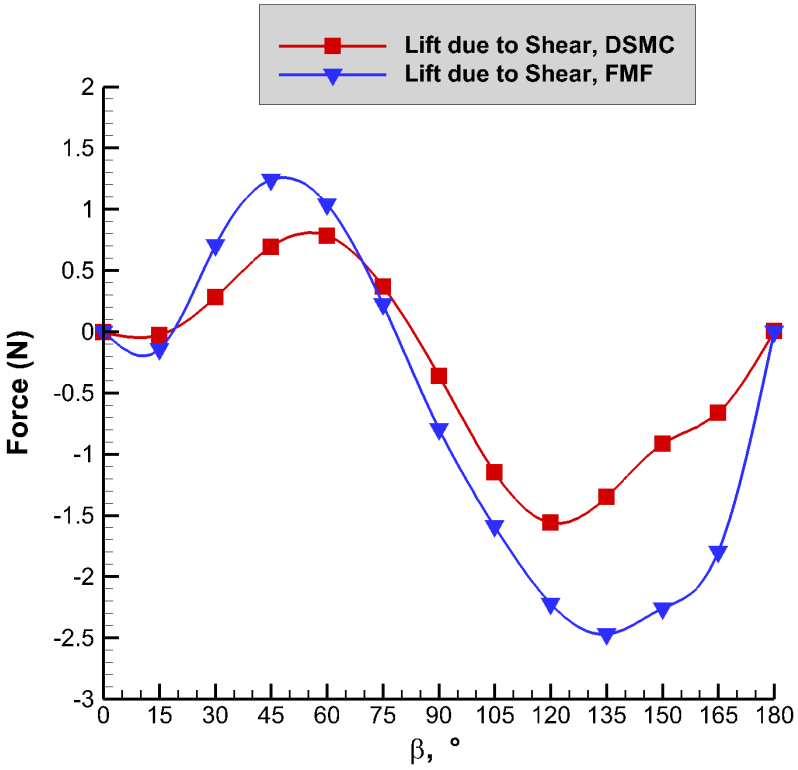

Figure 5.27: Lift due to shear stress on the Star48B, calculated using DSMC and free-molecular (FMF) analytical models for all orientations at a Knudsen number of 0.1.

Figures 5.26 and 5.27 display the expected growing disagreement between the modeling approaches for both the pressure and shear stress contributions. Quantitatively, the normalized root-mean-square deviance between all the lift due to pressure results across both models is 62.2%. The normalized root-mean-square deviance between all the lift due to shear stress results across both models is 59.7%. These errors are nearly twice as large as the errors experienced at a Knudsen number of 1. These error results are inflated due to the data points at $\beta = 0°$ and $\beta = 180°$ being close to zero, but relatively far apart, sometimes even with sign differences. These data points are enumerated in Table 5.9. Only a few surface elements need to be influenced by pressure in order to cause a result so close to zero to "flip" signs. The average values being close to zero also inflate the error differences between the lift force contribution.

Table 5.9: Lift due to pressure and shear stress on the Starb48B at specific β values for a Knudsen number of 0.1.

Lift due to Pressure (N)		
	FMF	**DSMC**
$\beta = 0°$	7.09×10^{-5}	2.62×10^{-4} $\pm 5.25 \times 10^{-8}$
$\beta = 180°$	4.80×10^{-4}	2.45×10^{-4} $\pm 4.89 \times 10^{-8}$
Lift due to Shear Stress (N)		
	FMF	**DSMC**
$\beta = 0°$	-7.28×10^{-5}	-4.89×10^{-3} $\pm -9.77 \times 10^{-7}$
$\beta = 180°$	-4.10×10^{-4}	2.80×10^{-3} $\pm 5.61 \times 10^{-7}$

To take the total lift across the body, the lift due to pressure and the lift due to shear stress are summed. This results in lift values relatively close to zero; yielding the curves in Figure 5.25. Because the lift is small, the differences between models are not expected to greatly change any orbital decay results, especially for a large piece of space debris as the 117 kg Star48B that is experiencing much larger drag at this Knudsen number. When compared to lift contribution results from $Kn = 1$, in Section 5.3, the differences between the modeling approaches have increased from around 25% to around 60%, showing the growing inadequacy of the free-molecular model to match DSMC results as Knudsen number lowers.

In order to calculate coefficients of drag and lift for use in the orbital decay model, a free-stream density is taken from [9]. At 101 km, where for Star48B $Kn = 0.1$, the free-stream density $\rho = 3.73 \times 10^{-7}$ kg m^{-3}. The orbital velocity is the circular orbital speed used throughout the $Kn = 0.1$ results: $V = 7840$ m s^{-1}. The aerodynamic coefficients are calculated for a full-body (not half, or meshed representation of) Star48B, and include the area as in Chapter 3, for use in the orbital decay modeling. The modeled force is multiplied by two to get the total force on the body.

The lift coefficient is calculated similarly.

Figure 5.28 shows C_DA and C_LA calculated for all models and orientations for $Kn = 0.1$ experienced by the Star48B body.

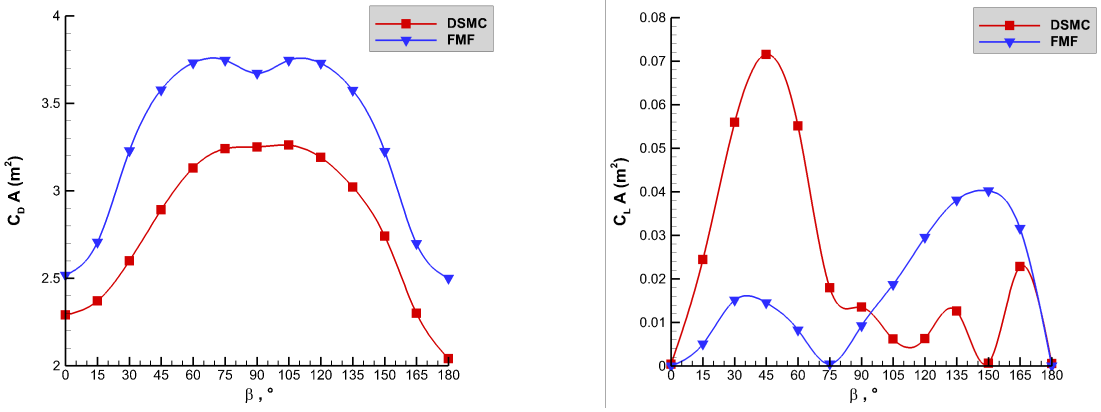

(a) (b)

Figure 5.28: Drag (a) and lift (b) coefficients calculated using DSMC and free-molecular (FMF) analytical models for all experiment orientations of the Star48B using both models for a Knudsen number of 0.1.

The average C_DA calculated using the DSMC results is $2.85 \pm 5.69 \times 10^{-4}$ m^2, while the average C_DA calculated using the free-molecular results is 3.34 m^2. The percent difference between the averages is 17.5%. The normalized root-mean-square deviation between all the C_DA results across both models is 15.3%. The average C_LA calculated using the DSMC results is $2.39 \times 10^{-2} \pm 4.79 \times 10^{-6}$ m^2, while the average C_LA calculated using the free-molecular analytical modeling results is 1.76×10^{-2} m^2. The percent difference between the averages is 26.6%. The normalized root-mean-square error between the coefficients of lift is exponentially elevated as the average is relatively near zero. The error percentage between the modeling approaches for the lift coefficient is therefore not a good metric to judge agreement between models.

5.4.2 $Kn = 0.1$: Moments and Angular Accelerations

Moments are treated in the same way as detailed in Section 5.2.2. Figure 5.29 displays the moment results about the three primary axes yielded by both models across all the Star48B orientations.

The aerodynamic moments about the X- and Y-axes are about an order of magnitude larger than those modeled about the Z-axis. This is because the flow-facing area changes are large as the relative velocity vector moves across the X-Y plane. Though the X- and Y- moments cancel out when projecting results to the entire body, Figure 5.29 shows the expected growing disagreement between the free-molecular and DSMC results at this Knudsen number.

Much of the same phenomena that create maximized and minimized moments for a Knudsen number of 1 happen at a Knudsen number of 0.1. In Figure 5.29 (a), the maximum aerodynamic moment about the X-axis is incurred when β is $90°$. Flow is distributed across the differing areas of the spherical forebody and nozzle cone aftbody and the differences in area cause a force distribution that pushes the Star48B about the X-axis. When $\beta = 0°$ or $180°$, the oncoming flow is applied symmetrically about the X-axis, causing the X-moment minima. In Figure 5.29 (b), the Y-moment has a maximum of about 4 N m for $\beta = 30°$. There is a minima of -5 N m, of nearly -10 N m for the DSMC results, at $\beta = 150°$. At $\beta = 30°$, the flow impacts a large part of the spherical aftbody in an angled way, and only some of the nozzle cone experiences non-negligible applied pressure, and vice-versa for $\beta = 150°$. The flow caught in the nozzle cone pushes more surface area, causing the absolute moment at $\beta = 150°$ to be larger than the absolute moment at $\beta = 30°$. The absolute minimum Y-moment occurs for $\beta = 0°$, where the flow is distributed evenly across the Y-axis.

For the Z-axis, in Figure 5.29 (c), the absolute moment is minimized when $\beta = 0°$ and $\beta =$

$180°$. The incoming flow at these angles again impacts a near-circular area which is even across the Z-axis, therefore a moment is not incurred. For the DSMC results, the absolute Z-moment is also minimized at $\beta = 90°$, where backflow evens out the pressure distribution to minimize the moment. The local maxima at $\beta = 15°$, $90°$, and $165°$ for the free-molecular results occur because the pressure force is not distributed evenly between the impacted spherical forebody and nozzle cone aftbody. The local minima at around $\beta = 45°$ and $\beta = 120°$ occur because the pressure distribution between the differing areas of the body is minimized at these angles. More of the nozzle cone is experiencing pressure, and less of the spherical forebody is experiencing pressure, which equalizes the moment about the Z-axis. The DSMC minima experienced at around $\beta = 120°$ happens because of extra surface impacts inside the nozzle cone, pushing a near-even pressure distribution slightly in the negative direction.

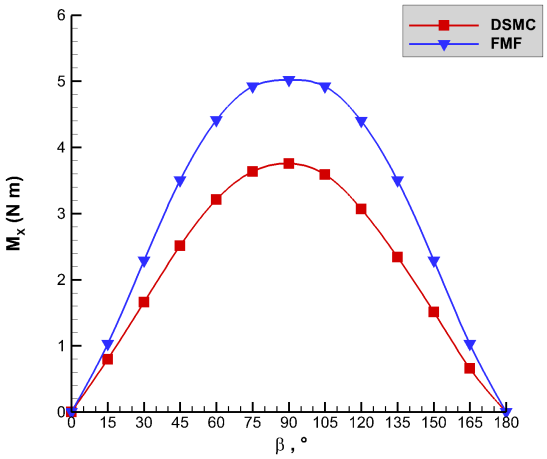

(a)

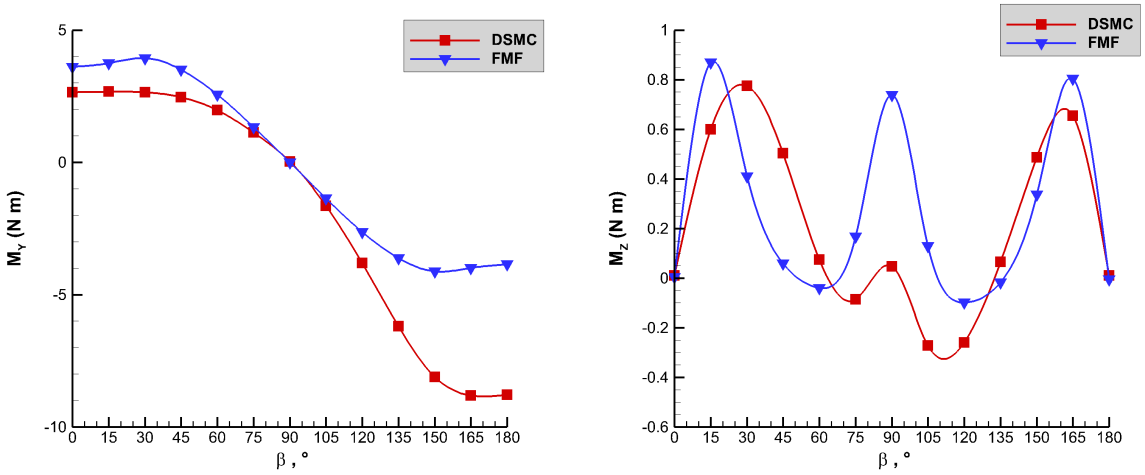

(b) (c)

Figure 5.29: Moments calculated using DSMC and free-molecular (FMF) analytical models for all experiment orientations of the Star48B about the: (a) X axis; (b) Y axis; (c) Z axis, for a Knudsen number of 0.1.

The moment averages are listed in Table 5.10. Table 5.10 portrays clearly that the free-molecular and DSMC modeling approaches yield differing results for this Knudsen number.

Qualitatively, Figure 5.29 displays growing disagreement between the DSMC and free-molecular results curves. In Table 5.10, the Y-moments are two orders of magnitude apart, indicating large

Table 5.10: Average moments calculated for a Knudsen number of 0.1 for the DSMC and free-molecular analytical modeling approaches across all β values.

Average	**FMF**	**DSMC**
$\mathbf{M}_X$ **(N m)**	3.11	2.23 $\pm 4.46 \times 10^{-4}$
$\mathbf{M}_Y$ **(N m)**	-6.32×10^{-2}	-1.73 $\pm -3.46 \times 10^{-4}$
$\mathbf{M}_Z$ **(N m)**	2.80×10^{-1}	2.17×10^{-1} $\pm 4.33 \times 10^{-5}$

differences in the modeling approaches. This is due to the average Y-moment being very close to zero and the DSMC Y-moments becoming more negative as β approaches $180°$. In Figure 5.29 (b), there is some agreement between the models with increasing deviance as β approaches $0°$ and $180°$. The deviance is caused by the blocking algorithm yielding zero pressure in the blocked zones for the free-molecular model, while the DSMC model follows particles and their interaction with the surfaces. The nozzle cone geometry exacerbates these differences, which causes the more extreme differences around $\beta = 180°$. The normalized root-mean-square deviance is also affected by the near-zero average.

The normalized root-mean-square deviance between all the X-axes moments is 33.1%. The normalized root-mean-square deviance between the Y-axes moments is 82.7%. The normalized root-mean-square deviance between the Z-axes moments is affected by the close-to-zero average, and is over 100%. Both the Y- and Z-moment normalized root-mean-square deviations are affected by the averages being near-zero; but do reflect the degrading accuracy of the free-molecular analytical model as Knudsen number decreases.

Because the Z-moments are the only ones that are non-zero across the whole Star48B body, the angular acceleration about the Z-axis is examined more thoroughly here. There is no data on the rotational behavior of the Star48B so there are no uncertainty error bars applied. The angular

acceleration is examined to visually inspect on what scale would aerodynamic moments induce rotational motion in the Star48B at this altitude.

Figure 5.30 shows the calculated angular acceleration about the Z-axis for the Star48B body using both models across all orientations. In Figure 5.30, the Z-moments across the orientations have been doubled, then divided by I_{ZZ}, to represent the moments incurred by the entire Star48B.

The interpolated average angular accelerations about the Z-axis incurred are $4.87 \times 10^{-1} \pm 9.73 \times 10^{-5}$ degrees s^{-2} using the DSMC method and 6.29×10^{-1} degrees s^{-2} using the free-molecular analytical method. The normalized root-mean-square deviance between the angular accelerations about the Z-axis is 29.3%. The error between the angular accelerations has increased by 10% as the Knudsen number lowered from 1 to 0.1.

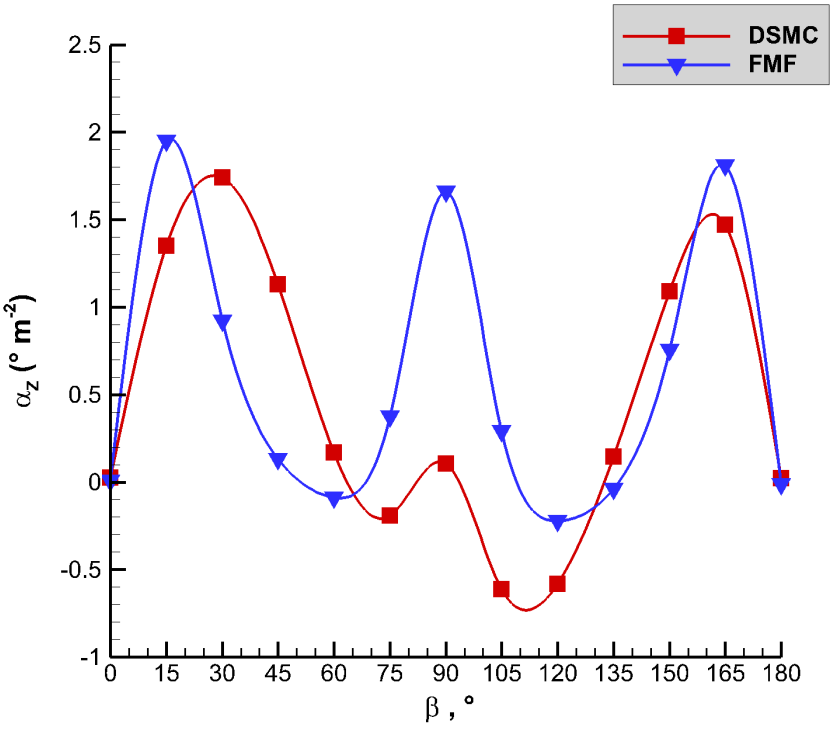

Figure 5.30: Angular acceleration about the Z-axis calculated using DSMC and free-molecular (FMF) analytical models for all experiment orientations of the Star48B, for a Knudsen number of 0.1.

The angular accelerations caused aerodynamically at this Knudsen number are still small. This makes sense: the Star48B is a relatively large, heavy piece of space debris, and a large force that is distributed unevenly is needed to cause a significant change in angular motion. Again at this altitude, the aerodynamic forces are still not large enough to make much of a difference. An average rotation rate of 4 rpm, or 24 degrees s^{-1}, would only be changed by about 2.6% if an angular acceleration of 6.3×10^{-1} degrees s^{-2} was applied for a second. While the aerodynamic moments are increasing, and their effect on rotational motion would be larger at this Knudsen number than for higher altitudes, the effect is still minimal.

5.5 Knudsen Number of 0.05

A Knudsen number of 0.05 is achieved for the Star48B body at 97 km of altitude. A Knudsen number of 0.05 is firmly in the transitional regime; continuum flow is defined as beginning at a Knudsen number of 0.01 [20]. At a Knudsen number of 0.05, the flowfields are becoming more dense and there is an expectation of large disagreement between the free-molecular and DSMC results. The circular orbital speed and atmospheric composition at this altitude are listed in Table 5.2.

The Star48B surface elements used at this altitude have a side length average of 6.88×10^{-3} m in order to be smaller than the free-stream mean free path compressed by a factor of 10 (8.29×10^{-3} m), and to capture the curvature of the Star48B shape. This refinement yields 1.25×10^{6} volume cells in the flowfield, and 1.98×10^{5} surface elements. As an example, the $\beta = 0^{\circ}$ orientation is presented. This orientation is presented for a direct visual comparison with the flowfields and surface undergoing flow at $Kn = 10$, in Section 5.2. All slices of the flowfield are taken at

$Z = 3.67 \times 10^{-2}$ m, which is close to the X-Y plane, the plane of symmetry. This slice is chosen in order to show both the fore spherical shape of the body as well as the aft nozzle cone of the body experiencing flow. The Star48B body is represented by the white "cut-out" of the slice of the body.

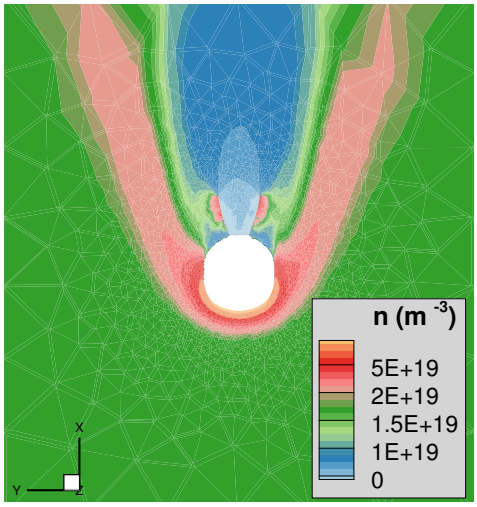

(a)

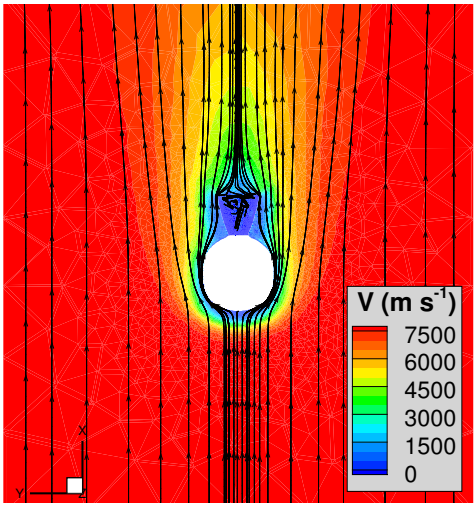

(b)

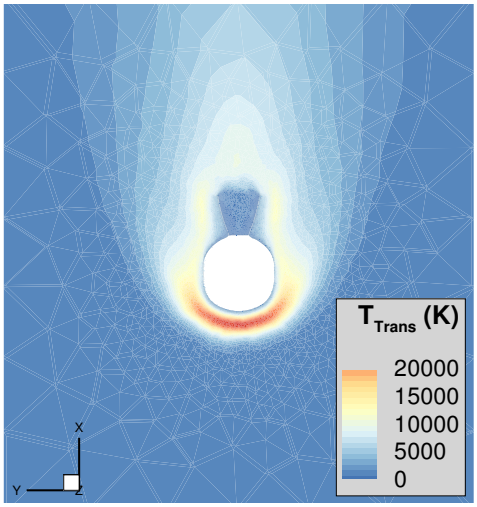

(c)

Figure 5.31: Flowfield contours at $Kn = 0.05$, $\beta = 0°$: (a) number density; (b) velocity; (c) translational temperature.

Figure 5.31 shows the flowfield contours computed using MONACO. The contours show that a shock is forming in front of the body at this Knudsen number. Comparing the contours at $Kn =$

0.05 with those at $Kn = 10$, the difference in the very-rarefied versus more dense flowfields can be seen clearly. Figure 5.31 (a) displays the number density contours, which demonstrate the shocked flow upstream of the spherical section of the Star48B. Downstream of the Star48B, there is shadowed, much less dense flow, and some of the nozzle cone experiences zero backflow penetration. There is backflow which comes into contact with the outside of the nozzle cone, however. In Figure 5.31 (b) the velocity streamlines are plotted. The β angle can be clearly seen in the direction of these streamlines. There is interesting disturbed flow behavior from the backflow that is able to penetrate the nozzle cone that is demonstrated by the streamlines. Inside the nozzle some flow is stagnant. Figure 5.31 (c) displays the translational temperature. The shock-like behavior of the flowfield can be seen upstream of the nozzle cone in the temperature contour.

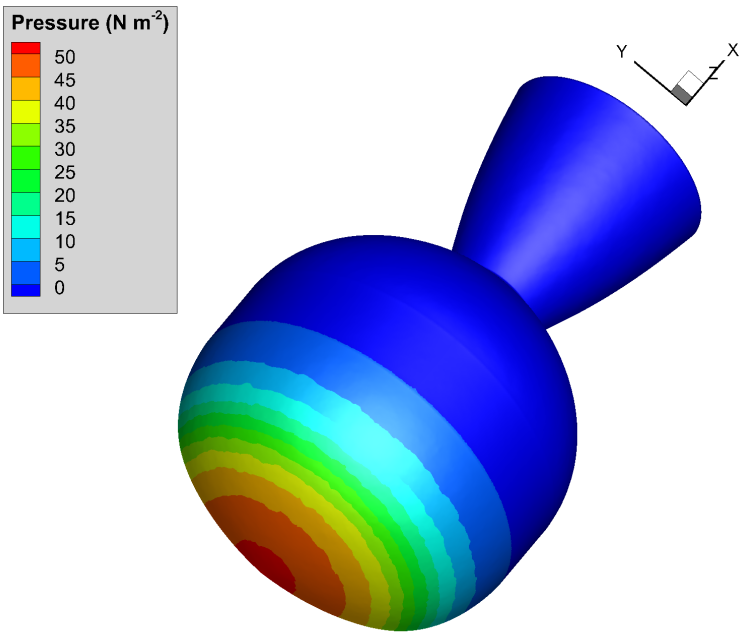

(a)

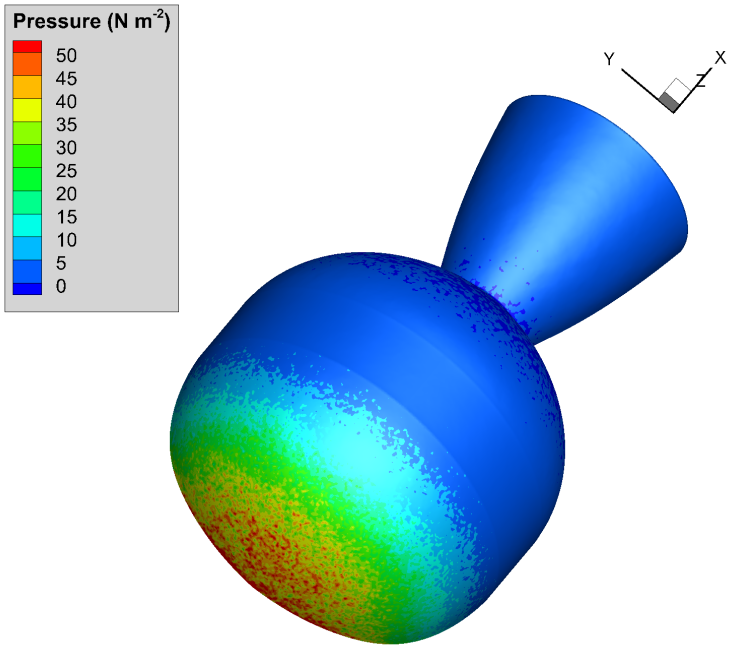

(b)

Figure 5.32: Pressure distribution at $Kn = 0.05$, $\beta = 0°$: calculated using: (a) free molecular theory; (b) DSMC.

Figures 5.32 displays an example of the surface pressure on the Star48B for the $\beta = 0^{\circ}$ case. There are several differences in the surface pressure distributions. The free-molecular surface pressure contours are visually similar to those for $Kn = 10$ in Section 5.2, as the β angle shown is the same, of course for this regime the pressure enacted on the surface is much higher. However, the DSMC contours are much more dispersed at this regime, reflecting the difference the collisional nature of this denser flow is having on the particle-dependent results. It is also evident when comparing Figures 5.32 (a) and (b) that the backflow experienced via simulation using DSMC is affecting the pressure distribution. The free-molecular analytical approach detects when cells directly experience flow; because it does not track particles, no pressure is seen on the backside of the Star48B in Figure 5.31 (a).

As expected, there is quantitative difference in the pressure distributions. The average pressure experienced by the surface is calculated as 3.53 N m^{-2} using the free-molecular method. This average is calculated by accounting for the pressure on each surface element over the entire body, weighting with respect to surface area, for this (the $\beta = 0^{\circ}$) orientation. The average pressure experienced over the body calculated by using MONACO results is $4.01 \pm 5.61 \times 10^{-3}$ N m^{-2}, and is calculated similarly. The statistical error for the DSMC pressure calculation is the Poisson statistical error of the DSMC results caused by the number of hits experienced by the body per surface element per time step and is enumerated in the next section. The difference in average pressure experienced by the body at this orientation is 11.9%. This error high, but is lower than the difference between the average pressures enumerated for $Kn = 0.1$, in Section 5.4. This is due to the geometry examined: for the $\beta = 180^{\circ}$ orientation, there is a 56.8% difference in average pressure across the body, on the order of the error displayed for a Knudsen number of 0.1. There is a lesser error in average pressure at $Kn = 0.05$ because the free-molecular pressure is elevated

for the surface elements normal to the oncoming flow, which raises the average pressure to become slightly more similar to the average DSMC pressure. Both metrics indicate that the free-molecular method is not appropriate for Knudsen numbers of 0.1 or lower.

5.5.1 $Kn = 0.05$: Drag and Lift

Now the drag and lift experienced over the body are compared between the two models. The drag and lift forces plotted and discussed in this section apply to only the half of the Star48B that is meshed and simulated. For use in other models (such as the orbital decay model), the forces are doubled to represent the entire body.

In order to compare models, the drag and lift forces gathered for each modeled orientation are interpolated over all values of β to yield an average value.

Figure 5.33 shows the calculated drag for all orientations using both approaches. The data points for individual simulation results are connected using splines to demonstrate the smooth transition of drag experienced as body rotation would occur.

The Poisson statistical error due to the number of hits experienced by the body per surface element per time step for MONACO DSMC simulations is calculated as in Equation 3.1. Using Equation 3.1, the average hits per sampling time step per surface element across the Star48B at this Knudsen number is 9.70×10^{-5}, the total number of surface elements is 1.98×10^{5}, and using 25,000 sampling steps: the Poisson statistical error of aerodynamic DSMC results is 0.14%. Error bars are not shown in the following figures because the statistical error is very small.

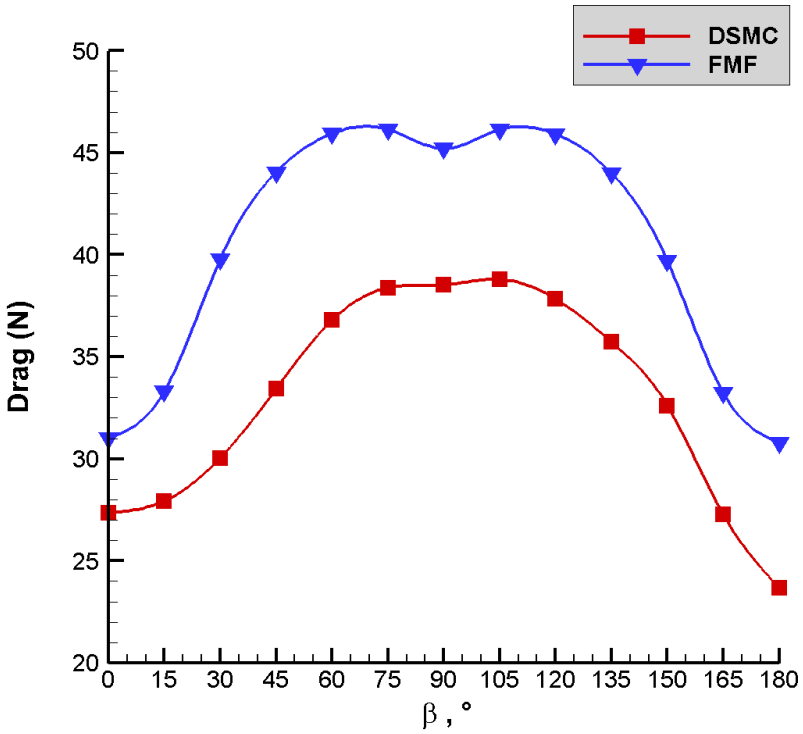

Figure 5.33: Drag calculated using DSMC and free-molecular (FMF) analytical models for all orientations analyzed of the Star48B at a Knudsen number of 0.05.

The same phenomena described in Section 5.4, for $Kn = 0.1$, happen here. Figure 5.33 shows that maximum drag values are achieved for $\beta = 75°$ and $\beta = 105°$. The same phenomena described in Section 5.2 and Section 5.3 happens for $Kn = 0.05$ in the free-molecular curve: for $\beta = 75°$ and $105°$, the maximum spherical body area and the maximum nozzle cone area are exposed to the oncoming flow. The small dip at $\beta = 90°$ is because less area of the nozzle cone is exposed to the flow. The nozzle has a smaller diameter near the spherical body and flares out, so when more of the flared area is exposed to the flow, the drag is increased.

The DSMC curve is more bell-shaped, and actually has one maximum at $\beta = 105°$; drag experienced at $\beta = 90°$ is larger than at $\beta = 75°$ by a few tenths of a Newton. The DSMC results differ from the free-molecular results in this way because there are more particles interacting with

each and with the surface. At $\beta = 105°$, the flow catches on some of the inside of the nozzle cone, increasing the drag to its maximum.

Minimum drag is achieved for $\beta = 0°$ and $\beta = 180°$. At these orientations, a minimal area is exposed to the flow: approximately at both angles, a semicircular area projection is exposed to direct pressure. For the DSMC curve, the extreme minimum is located at $\beta = 180°$; more flow is trapped inside the nozzle cone. The trapped flow collides with particles and the surface much more than at lower Knudsen numbers or other orientations. This trapped flow carries less momentum than free-stream flow, and therefore lowers the drag.

The average drag calculated using the MONACO results interpolated across all orientations is $33.6 \pm 4.70 \times 10^{-2}$ N. The average drag calculated using the free-molecular results is 41.2 N. The percent difference between the averages is 22.7%. The normalized root-mean-square deviance between all the drag results across both models is 19.7%. The error has increased by about 5% from the error experienced at a Knudsen number of 0.1. The free-molecular treatment continues to degrade as Knudsen number lowers and collisions between particles exponentially increase. Qualitatively, the drag curves are moving further and further apart as Knudsen number decreases, reflecting the disagreement between the models.

Figure 5.34 shows the calculated lift for all orientations using both methods. The lift displayed in Figure 5.34 is translated into an Earth-centric frame, which yields positive lift values. Lift is around two orders of magnitude smaller compared to drag due to the Star48B's symmetry and resemblance to a sphere; as spheres produce no lift, the geometry of the Star48B minimizes the lift. Resolved as described in Chapter 2, nearly all force applied to the Star48B body is attributed to drag. Unless a pressure gradient in a normal direction to the oncoming velocity is created by the body's geometry, drag will be the dominating force.

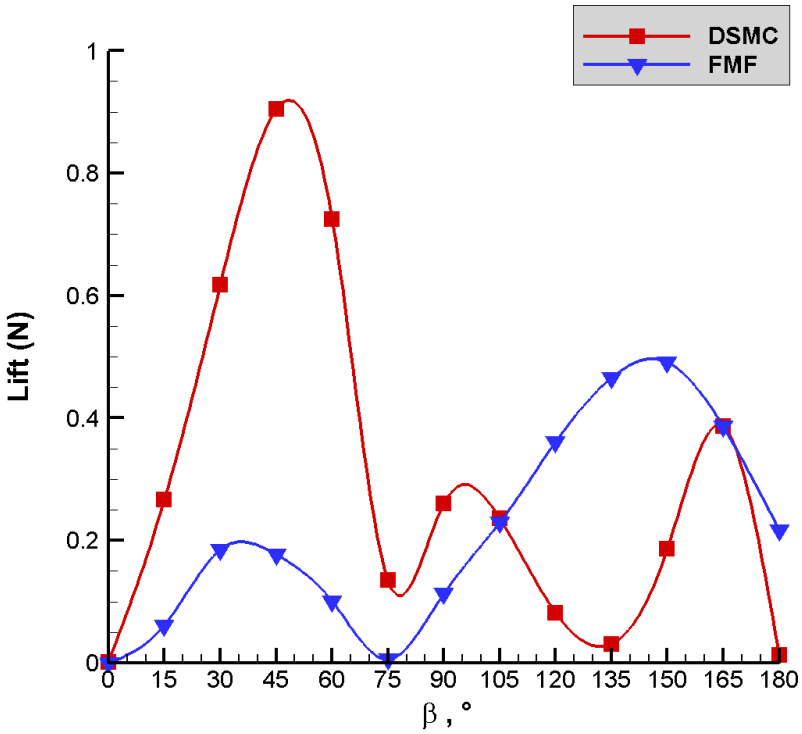

Figure 5.34: Lift calculated using DSMC and free-molecular (FMF) analytical models for all orientations of the Star48B at a Knudsen number of 0.05.

The average lift calculated using the MONACO results interpolated across all orientations is $3.20 \times 10^{-1} \pm 4.48 \times 10^{-4}$ N. The average lift calculated using the free-molecular results is 2.24×10^{-1} N. The percent difference between the averages is 30.0%. This error is around a 5% increase from the error between average lift forces at a Knudsen number of 0.1, which is the discrepancy increase expected. However, the error is again lower than the average lift error at a Knudsen number of 1. The error is minimized not because there is agreement between the models, but because there are coincidentally near-identical lift values at $\beta = 105°$ and $165°$. The lift curves are exhibiting opposite peaks, so the error cancels out. The normalized root-mean-square deviance is affected by the averages being relatively close to zero, and is not a good metric to judge the agreement between models.

Examining the lift force contributions is a better metric to judge the agreement or disagreement between the free-molecular and DSMC results. Qualitatively, it is evident that the lift curves in Figure 5.34 are further apart than in Figure 5.16; showing the expected differences between the models expected as the Knudsen number decreases. Therefore the lift is examined in more detail, as in previous sections.

In order to examine the modeling differences, both pressure and shear stress contributions to the lift force are inspected below. Figure 5.35 displays the pressure contribution to the lift force for both models, while Figure 5.36 displays the shear stress contribution to the lift force for both models.

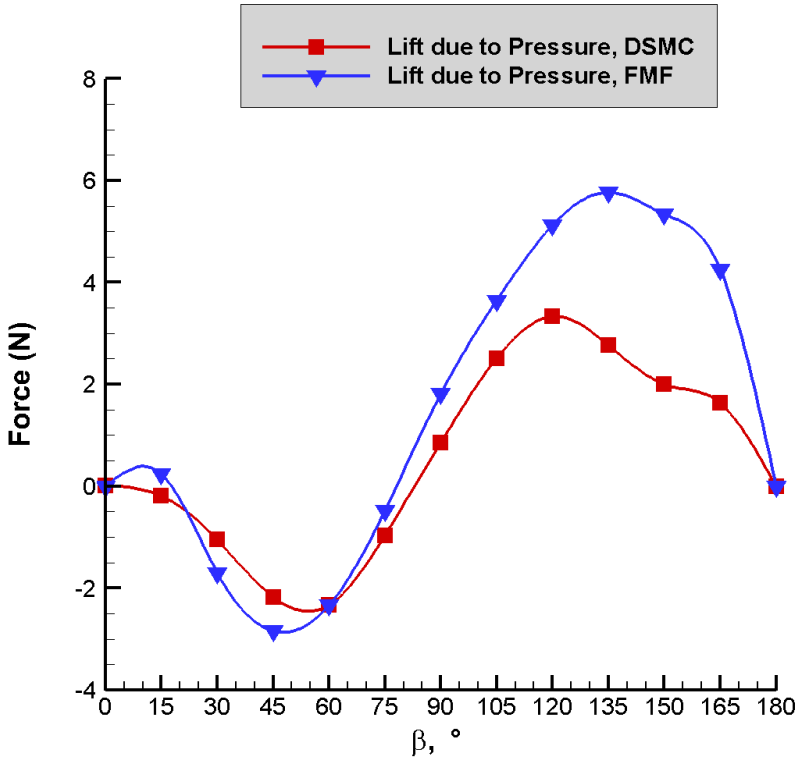

Figure 5.35: Lift due to pressure on the Starb48B, calculated using DSMC and free-molecular (FMF) analytical models for all orientations at a Knudsen number of 0.05.

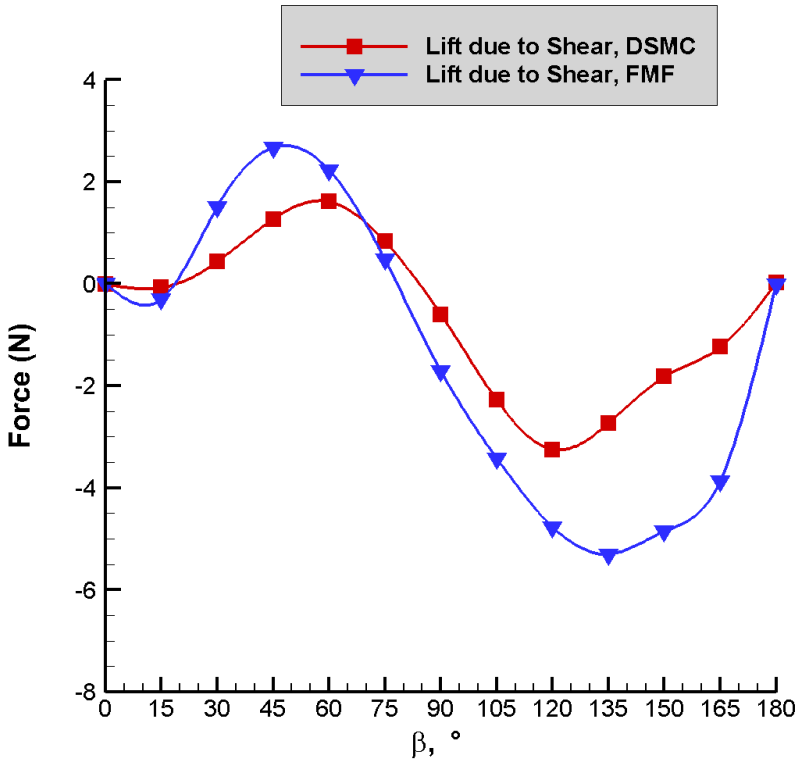

Figure 5.36: Lift due to shear stress on the Star48B, calculated using DSMC and free-molecular (FMF) analytical models for all orientations at a Knudsen number of 0.05.

Figures 5.35 and 5.36 display the expected disagreement between the modeling approaches for both the pressure and shear stress contributions. Quantitatively, the normalized root-mean-square deviance between all the lift due to pressure results across both models is 62.4%. The normalized root-mean-square deviance between all the lift due to shear stress results across both models is 64.7%. These errors are nearly twice as large as the errors experienced at a Knudsen number of 1; and of the same magnitude as the errors experienced at a Knudsen number of 0.1. These error results are slightly inflated due to the data points at $\beta = 0°$ and $\beta = 180°$ being relatively close to zero, but relatively far apart, sometimes even with sign differences. These data points are enumerated in Table 5.11. Only a few surface elements need to be influenced by pressure in order to cause a result so close to zero to "flip" signs. The average values being close to zero also inflate

the error differences between the lift force contribution.

Table 5.11: Lift due to pressure and shear stress on the Starb48B at specific β values for a Knudsen number of 0.05.

Lift due to Pressure (N)		
	FMF	**DSMC**
$\beta = 0°$	1.52×10^{-4}	1.28×10^{-2} $\pm 1.79 \times 10^{-5}$
$\beta = 180°$	1.03×10^{-3}	-2.90×10^{-3} $\pm -4.05 \times 10^{-6}$
Lift due to Shear Stress (N)		
	FMF	**DSMC**
$\beta = 0°$	-1.56×10^{-4}	-1.17×10^{-2} $\pm -9.77 \times 10^{-7}$
$\beta = 180°$	-8.80×10^{-4}	1.51×10^{-2} $\pm 2.11 \times 10^{-5}$

To take the total lift across the body, the lift due to pressure and the lift due to shear stress are summed. This results in lift values relatively close to zero when compared with the contributions; yielding the curves in Figure 5.34. Because the lift is relatively small, the differences between models are not expected to greatly change any orbital decay results, especially for a large piece of space debris as the 117 kg Star48B that is experiencing much larger drag at this Knudsen number. When compared to lift contribution results from $Kn = 1$, in Section 5.3, the differences between the modeling approaches have increased from around 25% to over 60%, and when compared to the lift contribution results from $Kn = 0.1$, in Section 5.4, the differences slightly increased, maintaining an error of over 60%. This reinforces the idea that for Knudsen numbers of 0.1 and below, the free-molecular model is not appropriate for this body.

In order to calculate coefficients of drag and lift for use in the orbital decay model, a free-stream density is taken from [9]. At 97 km, where for Star48B $Kn = 0.05$, the free-stream density $\rho = 8.00 \times 10^{-7}$ kg m^{-3}. The orbital velocity is the circular orbital speed used throughout the

$Kn = 0.05$ results: $V = 7850$ m s^{-1}. The aerodynamic coefficients are calculated for a full-body (not half, or meshed representation of) Star48B, and include the area as in Chapter 3, for use in the orbital decay modeling. The modeled force is multiplied by two to get the total force on the body. The lift coefficient is calculated similarly.

Figure 5.37 shows $C_D A$ and $C_L A$ calculated for all models and orientations for $Kn = 0.05$ experienced by the Star48B body.

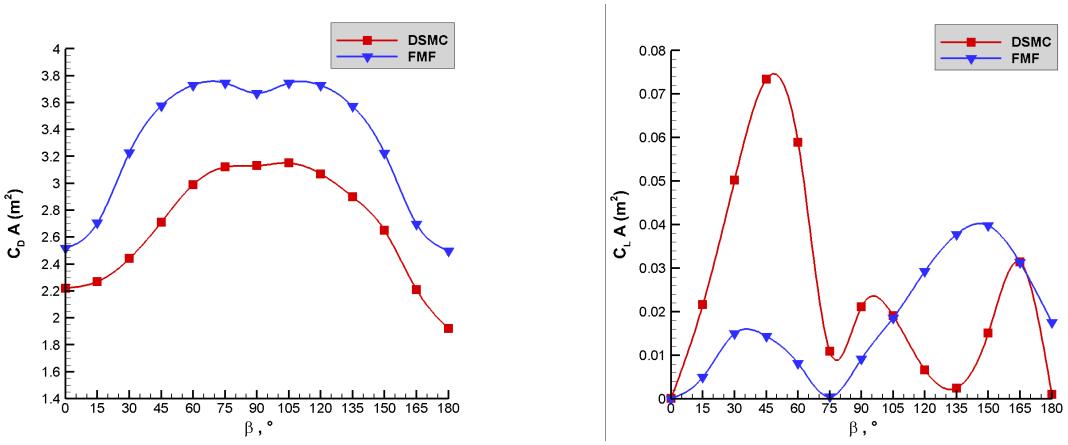

(a) (b)

Figure 5.37: Drag (a) and lift (b) coefficients calculated using DSMC and free-molecular (FMF) analytical models for all experiment orientations of the Star48B using both models for a Knudsen number of 0.05.

The average $C_D A$ calculated using the DSMC results is $2.73 \pm 3.82 \times 10^{-3}$ m^2, while the average $C_D A$ calculated using the free-molecular results is 3.34 m^2. The percent difference between the averages is 22.7%. The normalized root-mean-square deviation between all the $C_D A$ results across both models is 19.7%. The average $C_L A$ calculated using the DSMC results is $2.59 \times 10^{-2} \pm 3.63 \times 10^{-5}$ m^2, while the average $C_L A$ calculated using the free-molecular analytical modeling results is 1.82×10^{-2} m^2. The percent difference between the averages is 30.0%. The normalized root-mean-square error between the coefficients of lift is exponentially elevated as

the average is relatively near zero. The error percentage between the modeling approaches for the lift coefficient is therefore not a good metric to judge agreement between models.

5.5.2 $Kn = 0.05$: Moments and Angular Accelerations

Moments are treated in the same way as detailed in Section 5.2.2. Figure 5.38 displays the moment results about the three primary axes yielded by both models across all the Star48B orientations.

The aerodynamic moments about the X- and Y-axes are about an order of magnitude larger than those modeled about the Z-axis. This is because the flow-facing area changes are large as the relative velocity vector moves across the X-Y plane. Though the X- and Y- moments cancel out when projecting results to the entire body, Figure 5.38 shows the expected growing disagreement between the free-molecular and DSMC results at this Knudsen number.

Much of the same phenomena that create maximized and minimized moments for Knudsen numbers of 1 and 0.1 happen for a Knudsen number of 0.05. In Figure 5.38 (a), the maximum aerodynamic moment about the X-axis is incurred when β is $90°$. Flow is distributed across the differing areas of the spherical forebody and nozzle cone aftbody and the differences in area cause a force distribution that pushes the Star48B about the X-axis. When $\beta = 0°$ or $180°$, the oncoming flow is applied symmetrically about the X-axis, causing the X-moment minima. In Figure 5.38 (b), the Y-moment has a maximum for $\beta = 30°$. There is a minima at around $\beta = 165°$. At $\beta = 30°$, the flow impacts a large part of the spherical aftbody in an angled way, and only some of the nozzle cone experiences non-negligible applied pressure, and vice-versa for $\beta = 150°$. The flow caught in the nozzle cone, in the DSMC method, pushes more surface area, causing the absolute moment

at $\beta = 165°$ to be larger than the absolute moment at $\beta = 30°$. The absolute minimum Y-moment occurs for $\beta = 0°$, where the flow is distributed evenly across the Y-axis.

For the Z-axis, in Figure 5.38 (c), the absolute moment for the free-molecular model is minimized when $\beta = 0°$ and $\beta = 180°$. The incoming flow at these angles again impacts a near-circular area which is even across the Z-axis, therefore a moment is not incurred. For the DSMC results, the absolute Z-moment is minimized at $\beta = 90°$, where backflow that enters the nozzle cone causes the moment to be pushed slightly negative. The local maxima at $\beta = 15°$, $90°$, and $165°$ for the free-molecular results occur because the pressure force is not distributed evenly between the impacted spherical forebody and nozzle cone aftbody. The local minima at around $\beta = 45°$ and $\beta = 120°$ occur because the pressure distribution between the differing areas of the body is minimized at these angles. More of the nozzle cone is experiencing pressure, and less of the spherical forebody is experiencing pressure, which equalizes the moment about the Z-axis. The DSMC minima experienced at around $\beta = 120°$ happens because of extra surface impacts inside the nozzle cone, pushing a near-even pressure distribution in the negative direction.

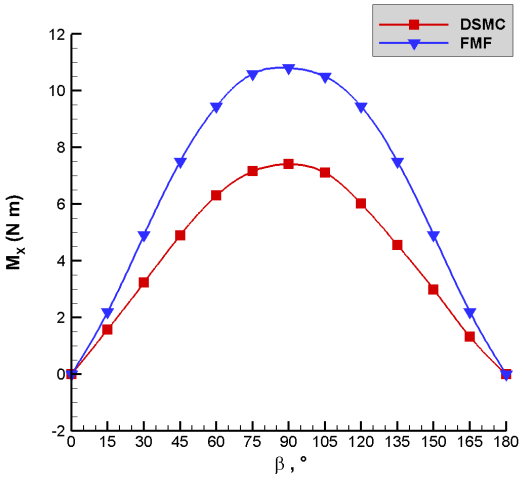

(a)

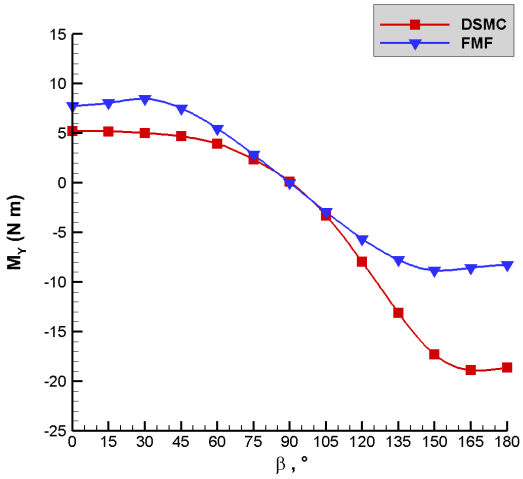

(b)

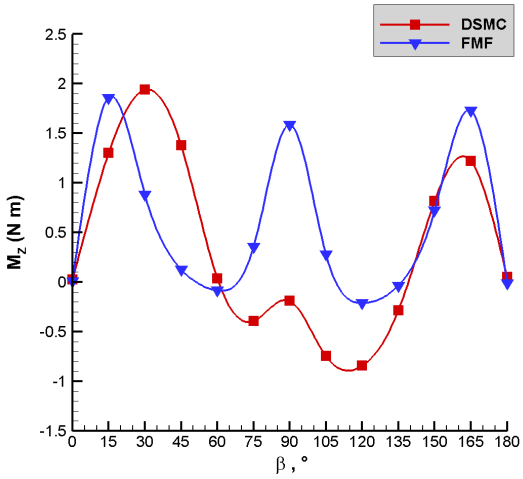

(c)

Figure 5.38: Moments calculated using DSMC and free-molecular (FMF) analytical models for all experiment orientations of the Star48B about the: (a) X axis; (b) Y axis; (c) Z axis, for a Knudsen number of 0.05.

The moment averages are listed in Table 5.12. Table 5.12 portrays clearly that the free-molecular and DSMC modeling approaches yield differing results for this Knudsen number.

Qualitatively, Figure 5.38 displays disagreement between the DSMC and free-molecular results curves. In Table 5.12, the Y-moments are over an order of magnitude apart, indicating large

Table 5.12: Average moments calculated for a Knudsen number of 0.05 for the DSMC and free-molecular analytical modeling approaches across all β values.

Average	FMF	DSMC
$\mathbf{M}_X$ **(N m)**	6.67	4.38 $\pm 6.13 \times 10^{-3}$
$\mathbf{M}_Y$ **(N m)**	-1.33×10^{-1}	-3.83 $\pm -5.36 \times 10^{-3}$
$\mathbf{M}_Z$ **(N m)**	6.02×10^{-1}	3.56×10^{-1} $\pm 4.98 \times 10^{-4}$

differences in the modeling approaches. This is due to the average Y-moment being very close to zero and the DSMC Y-moments becoming more negative as β approaches $180°$. In Figure 5.38 (b), there is some agreement between the models with increasing deviance as β approaches $0°$ and $180°$. The deviance is caused by the blocking algorithm yielding zero pressure in the blocked zones for the free-molecular model, while the DSMC model follows particles and their interaction with the surfaces. The nozzle cone geometry exacerbates the differences between the models as the Knudsen number lowers and there are more collisions with the DSMC particles and the inner nozzle cone walls. The normalized root-mean-square deviance is also affected by the relatively near-zero average.

The normalized root-mean-square deviance between all the X-axes moments is 40.2%. The normalized root-mean-square deviance between the Y-axes moments is 82.9%. The normalized root-mean-square deviance between the Z-axes moments is affected by the close-to-zero average, and is over 100%. Both the Y- and Z-moment normalized root-mean-square deviations are affected by the averages being near-zero; but do reflect the degrading accuracy of the free-molecular analytical model as Knudsen number decreases below 0.1.

Because the Z-moments are the only ones that are non-zero across the whole Star48B body, the angular acceleration about the Z-axis is examined more thoroughly here. There is no data on

the rotational behavior of the Star48B so there are no uncertainty error bars applied. The angular acceleration is examined to visually inspect on what scale would aerodynamic moments induce rotational motion in the Star48B at this altitude.

Figure 5.39 shows the calculated angular acceleration about the Z-axis for the Star48B body using both models across all orientations. In Figure 5.39, the Z-moments across the orientations have been doubled, then divided by I_{ZZ}, to represent the moments incurred by the entire Star48B.

The interpolated average angular accelerations about the Z-axis incurred are $8.01 \times 10^{-1} \pm 1.12 \times 10^{-3}$ degrees s^{-2} using the DSMC method and 1.35 degrees s^{-2} using the free-molecular analytical method. The normalized root-mean-square deviance between the angular accelerations about the Z-axis is over 100% as the angular accelerations are orders of magnitude apart.

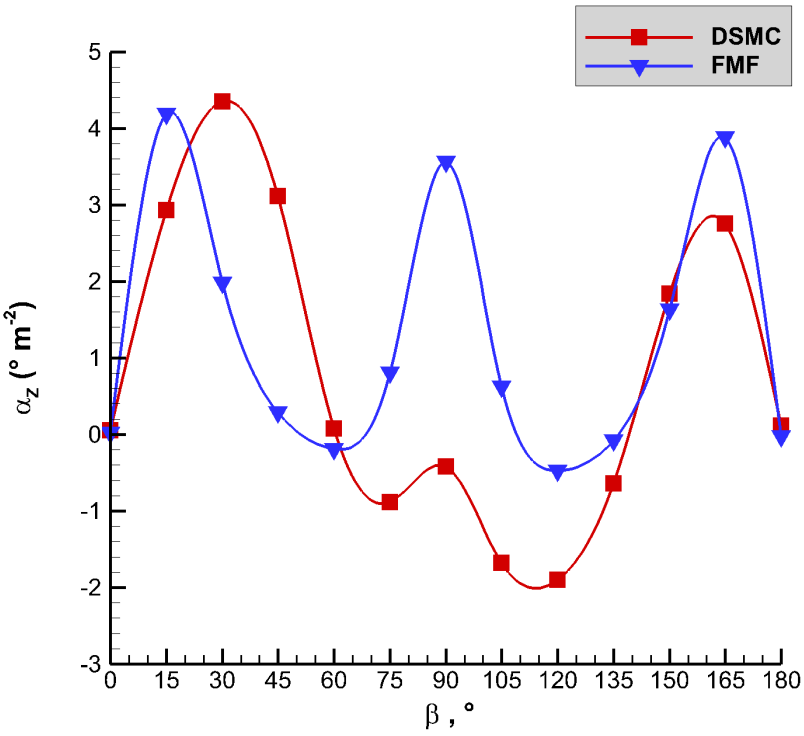

Figure 5.39: Angular acceleration about the Z-axis calculated using DSMC and free-molecular (FMF) analytical models for all experiment orientations of the Star48B, for a Knudsen number of 0.05.

The angular accelerations caused aerodynamically at this Knudsen number are still somewhat small; though larger than those experienced at high Knudsen numbers. The Star48B is a relatively large, heavy piece of space debris, and a large force that is distributed unevenly is needed to cause a significant change in angular motion. Even at this altitude, the aerodynamic forces are still not large enough to make a significant difference. An average rotation rate of 4 rpm, or 24 degrees s^{-1}, would be changed by about 4.17% if an angular acceleration of 1 degrees s^{-2} was applied for a second. While the aerodynamic moments are the largest examined for this body, and their effect on rotational motion is larger at this Knudsen number than for higher altitudes, the effect is small.

5.6 Orbital Decay Analyses

The orbital decay model developed in Section 2.3 is applied to the interpolated coefficients of drag and lift (C_DA and C_LA) to analyze the impact of the model used; as well as the impact of addressing tumbling motion on lifetime predictions. The aerodynamic coefficients, as before, are calculated across the entire projected Star48B body, a result of doubling the drag and lift forces calculated on the simulated half-Star48B.

In order to project realistic orbital decay, the tumbling of the Star48B is assumed, and the average C_DA and C_LA values discussed in Sections 5.2-5.5 are used. To measure how the tumbling assumption affects the orbital decay, two different sets of aerodynamic coefficients are used: the interpolated average coefficients, and the $\beta = 0^\circ$ coefficient results. The $\beta = 0^\circ$ results represent a typical approach to estimating aerodynamic coefficients, with only one flow-facing area used.

Though the Star48B began in a highly elliptical high-altitude orbit, the orbital decay measured in this work is projected to an orbital decay beginning from an altitude of 139 km, or a Knudsen

number of 10 for the Star48B. This is an appropriate assumption to make because as orbits degrade over time they become more and more circular, therefore experiencing such an orbit is highly probable for the Star48B on its descent. The initial orbit is a circular orbit with an altitude of 139 km and angular orbital elements (Ω, i, and ω_p) of 0°.

Table 5.13 contains the weighted average coefficients and the $\beta = 0°$ coefficients yielded from each modeling approach at each altitude used to model the Star48B's orbital decay. Statistical error is not included in Table 5.13 because it very small, and is not included in the orbital decay projections.

Table 5.13: Coefficients of lift and drag, resulting from the DSMC and FMF modeling approaches, used to project orbital decay of the Star48B.

Average Coefficients					
		DSMC		**FMF**	
Kn	**Alt (km)**	C_DA **(m^2)**	C_LA **(m^2)**	C_DA **(m^2)**	C_LA **(m^2)**
10	139	3.30	2.02×10^{-2}	3.35	2.05×10^{-2}
1	115	3.11	2.85×10^{-2}	3.34	1.84×10^{-2}
0.1	101	2.85	2.39×10^{-2}	3.34	1.76×10^{-2}
0.05	97	2.73	2.59×10^{-2}	3.34	1.82×10^{-2}
$\beta = 0°$ **Coefficients**					
		DSMC		**FMF**	
Kn	**Alt (km)**	C_DA **(m^2)**	C_LA **(m^2)**	C_DA **(m^2)**	C_LA **(m^2)**
10	139	2.54	1.03×10^{-4}	2.53	1.17×10^{-5}
1	115	2.41	3.03×10^{-4}	2.52	1.14×10^{-5}
0.1	101	2.29	3.94×10^{-4}	2.52	3.29×10^{-7}
0.05	97	2.22	9.32×10^{-5}	2.52	3.24×10^{-7}

The coefficients of drag and lift are interpolated to yield coefficients experienced throughout the Star48B's orbital decay. Linear interpolations are used for both models and both the weighted and $\beta = 0°$ only results; with an imposed exponentially reached asymptote as Knudsen increases to reflect the theoretical free-molecular limits, as in Section 4.6. Figure 5.40 plots the drag coefficients listed in Table 5.13, and the linear interpolations of these drag coefficients, across the altitudes

experienced in the modeled orbital decay.

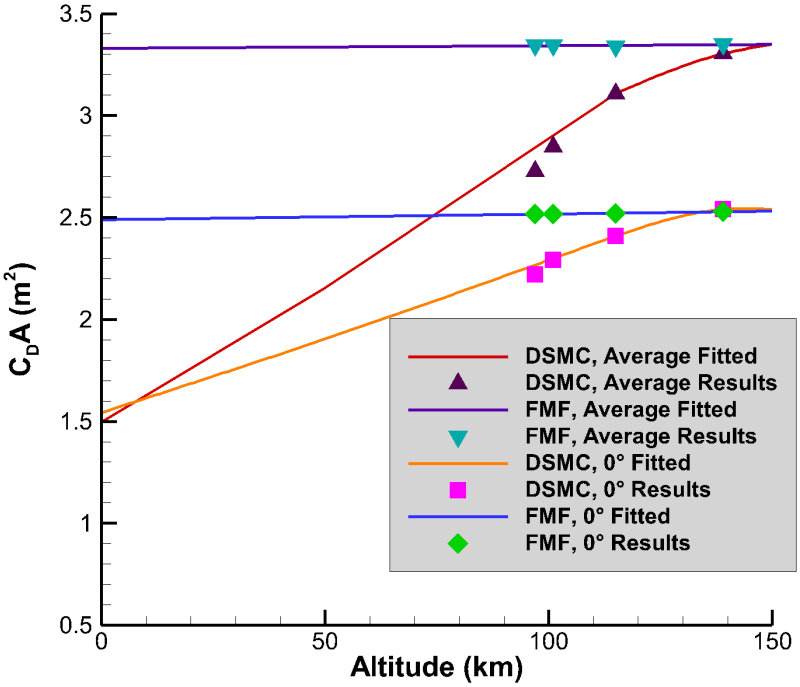

Figure 5.40: The average drag coefficient results and the $\beta = 0°$ drag coefficient results from both the free-molecular and DSMC approaches across the orbital decay altitudes modeled; and the interpolations of each set of coefficients.

Figure 5.40 clearly indicates the differences in modeling approaches and treatment of the tumbling versus static Star48B. There are marked differences between the $\beta = 0°$ only results and the average results for both models. When rotational motion of the Star48B is accounted for by including orientations other than $\beta = 0°$, the drag coefficient changes by about 25%. Additionally, Figure 5.40 displays the difference in the free-molecular and DSMC results as the altitude (and Knudsen number) decreases. At altitude of 139 km ($Kn = 10$), the coefficients are nearly identical. At 115 km ($Kn = 1$), the free-molecular and DSMC results are relatively close. But the DSMC results decrease linearly with altitude, and the free-molecular results remain consistent. The free-molecular results resemble hypersonic free-molecular limits for theoretical shapes. When

divided by the spherical projected area of 1.2 m^2, the $\beta = 0°$ free-molecular C_D is consistently around 2, the hypersonic limit of the coefficient of drag for a sphere in free-molecular flow, as discussed in Chapter 2.

Figure 5.41 plots the lift coefficients listed in Table 5.13, and the linear interpolations of the lift coefficients, across the altitudes experienced in the modeled orbital decay.

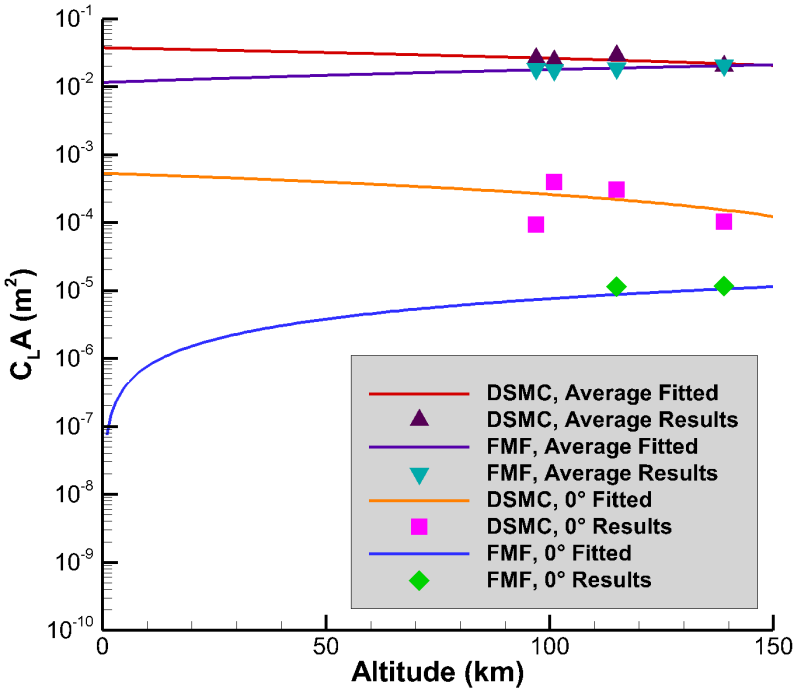

Figure 5.41: The average lift coefficient results and the $\beta = 0°$ lift coefficient results from both the free-molecular and DSMC approaches across the orbital decay altitudes modeled; and the linear interpolations of each set of coefficients.

Figure 5.41 is useful to contextualize how the models differ, and how the approach to rotational motion yields different lift values. The average lift coefficient data and linear fits are much larger and closer than the $\beta = 0°$ only data and fits. Again, at $\beta = 0°$, the Star48B resembles a sphere. Therefore, the lift is much closer to zero than even a small angle of attack creates. The DSMC approach creates higher lift at $\beta = 0°$ because the particles create backflow on the elongated

Star48B body and nozzle cone, whereas the free-molecular approach detects those cells as blocked by the spherical forebody.

Figure 5.42 displays the orbital decay from the starting altitude of 139 km ($Kn = 10$), projected using the linearly interpolated coefficients for each model according to the current altitude. The orbital decay models diverge as the altitude decreases, reflecting the changing coefficients of drag, which is the dominant factor affecting the speed of the orbital decay. There are visible differences between not only the free-molecular and DSMC models, but also the average and $\beta = 0°$ only approaches. Accounting for rotational motion has an effect on the projected orbital decay.

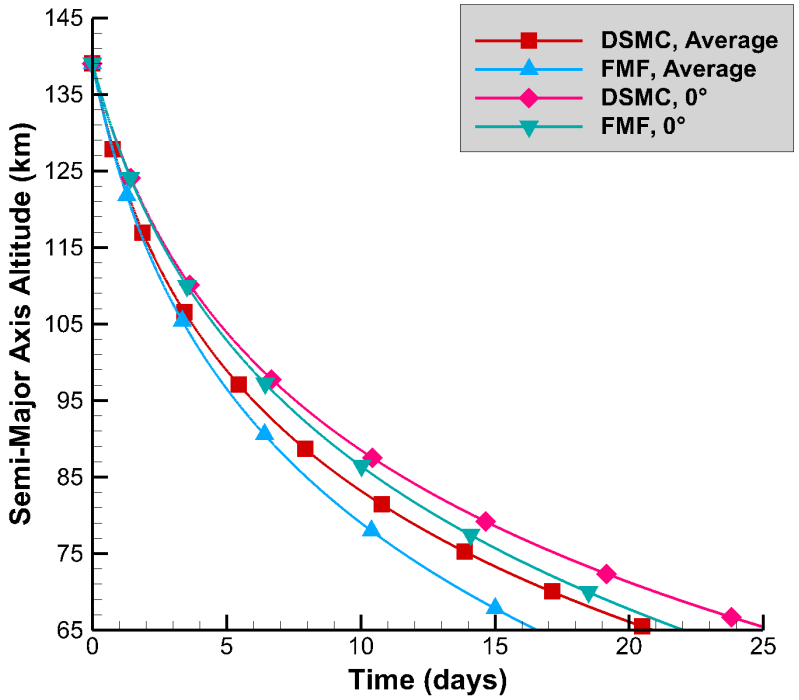

Figure 5.42: Orbital decay estimated from an altitude corresponding to $Kn = 10$ using average drag and lift coefficients, and $\beta = 0°$ drag and lift coefficients, from results obtained using both methods.

The orbital decay model is run until the Star48B achieves an altitude of 65 km for all modeling modes. Table 5.14 displays the time the Star48B took to achieve 65 km of altitude using each

modeling approach (DSMC and free-molecular) and each orientation scheme (averages for both coefficients, or $\beta = 0^\circ$ coefficients only). Table 5.15 contains the root-mean-square differences over the orbital decay and the percent deviation in time-to-reenter between all modeling modes.

Table 5.14: Time for the Star48B to achieve reentry altitude (or time-to-reenter) according to each modeling mode.

Modeling Mode	**Time-to-Reenter (days)**
DSMC, Averages	20.9
DSMC, $\beta = 0^\circ$	25.4
FMF, Averages	16.6
FMF, $\beta = 0^\circ$	22.0

Table 5.15: Root-mean-square differences over the Star48B orbital decay and time-to-reenter deviation between models and tumbling approaches.

Root-Mean-Square Differences Over Orbital Decay				
	DSMC, Averages	**DSMC,** $\beta = 0^\circ$	**FMF, Averages**	**FMF,** $\beta = 0^\circ$
DSMC, Averages	-	4.95 km	3.79 km	-
FMF, Averages	3.79 km	-	-	6.73 km
Time-to-Reenter Deviations				
	DSMC, Averages	**DSMC,** $\beta = 0^\circ$	**FMF, Averages**	**FMF,** $\beta = 0^\circ$
DSMC, Averages	-	21.6%	20.6%	-
FMF, Averages	20.6%	-	-	32.9%

The choice of using average coefficients about different body orientations effects the orbital decay predictions more than the choice of model, but both choices have non-negligible consequences when modeling orbital decay. There is a three or four day time-to-reenter difference between the free-molecular and DSMC approaches applied to the orbital decay. The free-molecular drag coefficients are elevated across lower altitudes and produce more rapid orbital decay. There is about a five day difference between the $\beta = 0^\circ$ stagnant approach versus the average, accounting for rotational motion, approach applied to either model's coefficients used in the orbital decay model. These are substantial differences when considering reentry timelines. The Star48B's drag is elevated when it rotates from the $\beta = 0^\circ$ position, and the orbital decay for a spinning Star48B is

quicker.

Again, as in Sections 3.6 and 4.6, an estimate is conducted to approximate how the changes in time-to-reenter translate to ground impact. Small changes in predicting reentry time changes projected debris impact by a large amount. A simple transformation of the information on time-to-reenter differences in Table 5.14 using the average rotation of the Earth (4.18×10^{-3} ° s^{-1}) yields an estimate in differences in ground footprint projection of impact.

For the Star48B, the impact location is changed by up to 200,000 km. Again, small changes in time-to-reenter cause spacecraft to complete many additional orbits around the Earth. Every contributing factor in the reentry process has a large affect on the impact location so accurate aerodynamic information is very important. Choice of model for the aerodynamic coefficients can have extremely large affects on the impact location prediction for a reentering spacecraft.

Table 5.14 points out that it is vital to account for satellite tumbling motion when the satellite has uneven projected areas. The drag varies over the body in a non-negligible way, and rocket bodies are known to have rotational motion in space [19]. Modeling constant flow-facing area drag affects time-to-reenter, and thereby affects ground impact predictions, by a significant amount. As stated before, for future work, more accurate orbital decay modeling will need to be used with the aerodynamic coefficients, but this gives a general idea of how differences in orbital lifetimes impact reentry crash landing predictions: for rocket bodies such as the Star48B, where fragmented impact has been documented [13] [40], modeling accurate ground impact locations is even more important. Therefore, it is advisable to account for rotational motion when calculating drag.

5.7 Star48B: Summary and Conclusions

In this chapter, the Star48B body was used to compare force and moment results across the free-molecular and the DSMC models for four Knudsen numbers: 10, 1, 0.1, and 0.05. These Knudsen numbers represent different flow regimes from firmly free-molecular ($Kn = 10$) to denser transitional flow ($Kn = 0.05$). Coefficients of drag and lift calculated using both modeling approaches were interpolated over and used to compare how the choice of model affects orbital lifetime predictions. The orbital decay predictions using free-molecular calculated aerodynamic coefficients differed from those using the DSMC-calculated aerodynamic coefficients by 20%.

Table 5.16 enumerates the normalized root-mean-square deviations between the models for the calculated drag, lift due to pressure, and y-moments. The lift due to pressure is presented as an example of differences in lift calculation for the models. The Z-moment errors are elevated due to the Z-moment averages being relatively close to zero, but are included as a comparison metric to track how differences in aerodynamic rotational motion increase as Knudsen number decreases. Table 5.16 shows that the free-molecular approach yields results similar to the DSMC approach for a Knudsen number of 10. The errors are bigger for $Kn = 1$, and become significantly larger once $Kn = 0.1$ is achieved.

Table 5.16: Normalized root-mean-square deviations between the free-molecular and DSMC results for the Star48B across all orientations for each Knudsen number for drag, lift due to pressure, and Y-moments.

	Force or Moment Compared		
Knudsen Number	**Drag**	**Lift due to Pressure**	**Z-Moment**
10	1.65%	10.2%	14.9%
1	7.05%	23.1%	30.1%
0.1	15.3%	62.2%	120%
0.05	19.7%	62.4%	130%

Table 5.17 lists the average core-hours required to run each model for one orientation at each Knudsen number, and the total core-hours to run all 13 simulations for every orientation of the Star48B at each Knudsen number. The free-molecular model's computational cost scales with the number of surface elements in the mesh used due to the blocking algorithm it employs. The DSMC core-hours are dependent on several factors, such as: the mesh size and the number of particles used as well as the time step, and number of time steps in the simulation.

Table 5.17: Average computational cost in core-hours for one simulation and total core-hours for simulating all 13 orientations of the Star48B using each model at each Knudsen number.

	C-Hs for One Simulation		**C-Hs for all orientations simulated**	
Knudsen Number	**FMF**	**DSMC**	**FMF**	**DSMC**
10	4.6×10^{-1}	51	6.0	660
1	4.3×10^{-1}	55	5.5	720
0.1	16	80	210	1000
0.05	16	63	210	810

Tables 5.16 and 5.17 together make interesting conclusions about where each model is appropriate. For a Knudsen number of 10, the free-molecular model saves hundreds of core-hours over simulating 13 orientations of the Star48B; and the drag calculated using the free-molecular model is accurate to the DSMC results within 2%. The lift and Z-moment free-molecular results are within 15% of the DSMC results at this Knudsen number as well, indicating decent agreement for relatively small values of lift and moments about the Z-axis. At this Knudsen number, over 100 free-molecular orientations can be run for the cost of one DSMC simulation. This indicates that at Knudsen numbers of 10 and higher, the free-molecular model is desirable to measure drag, and perhaps other forces and moments, in order to save computational cost; especially for bodies where rotational motion is of interest.

For a Knudsen number of 1, the errors are more elevated, with free-molecular drag within 10%

of DSMC drag. The free-molecular Z-moment is only accurate to the DSMC Z-moment to about 30%. This indicates that for very accurate lift or moment information, DSMC should be used at a Knudsen number of 1. However, because the free-molecular computational cost is so much lower than the DSMC computational cost at this Knudsen number, it may be desirable to run preliminary free-molecular analyses to get an idea of drag, lift, and moments, before conducting costly DSMC simulations.

When the Knudsen number drops to and below 0.1, the free-molecular model becomes much less appropriate. The free-molecular drag differs from the DSMC drag by about 15-20%, indicating that for accurate drag, DSMC must be used.

The orbital decay results reveal that the differences in projected orbital decay and impact are large when rotational motion is accounted for compared to a constant flow-facing area approach to the aerodynamic forces. Accounting for rotational motion led to differences in time-to-reenter of about 5 days for both the free-molecular and DSMC approaches. For rocket bodies that do impact the ground, therefore presenting real safety hazards, ground impact location prediction is very important. Additionally, rocket bodies are known to exhibit rotational motion in orbit. Therefore, these analyses recommend that drag accounts for several flow facing areas when modeling aerodynamic coefficients for orbital decay and reentry predictions.

CHAPTER 6

Conclusions

6.1 Summary

Space, especially LEO, is integral to the developed world's communications infrastructure. Spacecraft launches will continue to increase as time proceeds. As desirable orbits become progressively clogged with active and inactive spacecraft, the demand for more precise estimates of orbital lifetimes increases. There is a need for more-accurate estimates of forces on spacecraft and low-cost models of orbital forces in high altitudes. Additionally, one- and two-dimensional modeling of these forces are not sufficient when desiring high accuracy. The dynamics of tumbling spacecraft change the aerodynamic coefficients by as much as 40% for the TBEx CubeSat when compared to a static orientation at 0 angle of attack. Even though tumbling time-scales are small when compared with deorbiting time-scales, the exposure of differing flow-facing areas changes the overall force felt on spacecraft and impacts orbital decay predictions. Therefore three-dimensional simulations yielding force information will be exceedingly important in the near future.

This work introduced several novel concepts to the field of aerodynamics. First, a highly accurate method for modeling aerodynamic forces and moments in three-dimensions was developed

for the free-molecular regime for any arbitrary shape. Three-dimensional post-processing of the results from the DSMC code MONACO was expanded to yield forces and moments, including drag and lift dependent on oncoming flow orientation. Both of these methods were applied to three very different bodies: the TBEx CubeSat, the REBR reentry capsule, and the Star48B rocket motor. Four Knudsen number regimes were applied to all three bodies, testing these in free-molecular flow through dense transitional flow for the REBR ($Kn = 0 : 01$). The tumbling of the bodies was treated by viewing the flow from a body-fixed frame, and changing the incoming flow vector according to up to 16 different measured orientations. The flowfield was decoupled from the rotational motion of the body in order to model the dynamics effectively; this assumption is appropriate due to the time-scales of the expected rotational motion of each body. The results from the modeling approaches were compared across all orientations of drag, lift, and the incurred moments about the primary axes, as well as applied to a developed orbital decay model to estimate effects on lifetime predictions.

Modeling the TBEx revealed excellent agreement between the free-molecular and DSMC approaches above a Knudsen number of 10; good agreement at a Knudsen number of 10, and waning agreement once the Knudsen number descended to 1 and lower. Orbital decay projections on the TBEx results demonstrated the importance of considering tumbling when determining aerodynamic coefficients. The REBR was modeled at lower Knudsen numbers. Modeling the REBR indicated good agreement at a Knudsen number of 10, with agreement decreasing by 5-10% as Knudsen number decreased by a factor of 10. There were large disparities in modeling the forces and moments on the REBR at the continuum-limit of $Kn = 0.01$. Modeling the Star48B indicated that, especially for drag, the free-molecular model achieved good agreement for a Knudsen number of 10, with waning agreement once the Knudsen number dropped to 0.1. It is universally

preferable to use the free-molecular on bodies at or above a Knudsen number of 10. For Knudsen numbers of 1, the free-molecular model may be run prior to DSMC simulations to get a general idea of drag experienced. For Knudsen numbers of 0.1 and below, the free-molecular approach incurred significant errors.

The bodies represented differing shapes of common spacecraft: the TBEx is a representative CubeSat, the REBR is a representative reentry capsule, and the Star48B is a representative rocket motor. Working with comparatively different shapes indicated that the three-dimensional free-molecular model developed is appropriate for any shape well-represented by a surface mesh. The free-molecular model developed cuts costs by a factor of as much as 7500. For example, one TBEx simulation using MONACO at a Knudsen number of 10 took around 30 core-hours to complete. One free-molecular orientation model cost 0.15 core-hours to run to completion on the TBEx across all Knudsen numbers. For the REBR, the free-molecular model saves hundreds of core-hours in computational cost for every Knudsen number. For the Star48B, the free-molecular model could be run hundreds of times for each DSMC simulation, in terms of computational cost. The analytical approach is so comparatively cheap that it is always advantageous to run several orientations, even at lower Knudsen numbers, to obtain an estimate of forces and moments incurred.

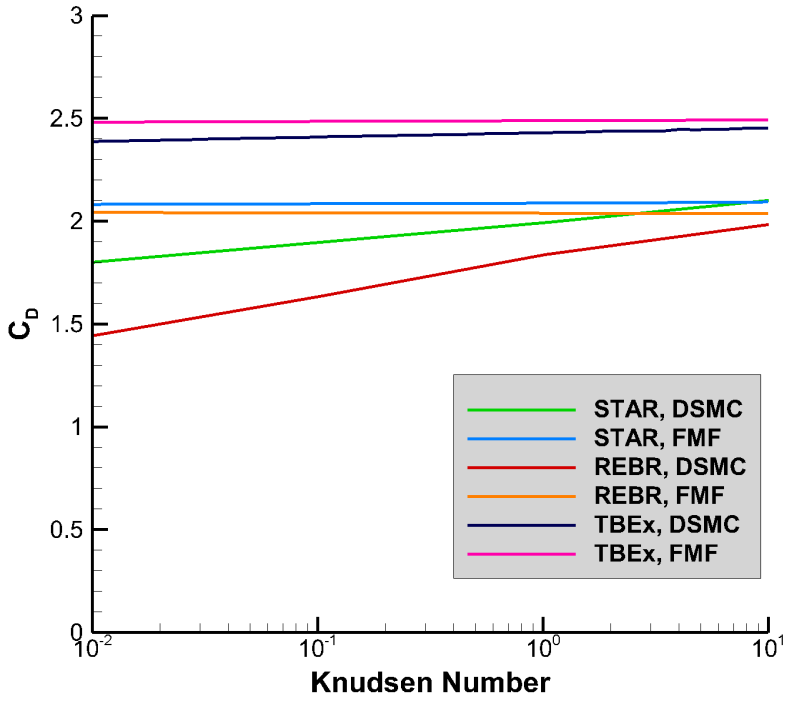

Figure 6.1: Constant drag coefficient (0° angle of attack) modeling results for each body (the TBEx, REBR, and Star48B) for the free-molecular and the DSMC approaches.

Figure 6.1 displays the constant flow-facing area (0° angle of attack) for each body, using each modeling approach. The coefficients of drag are displayed to compare the results without influence of the differing sizes of each body. Figure 6.1 shows that the REBR and Star48B drag coefficients approach the free-molecular hypersonic limit for a diffuse sphere 2 as the Knudsen number increases. This is expected, as from a 0° angle of attack, both the Star48B and REBR bodies are spheres. The TBEx is not spherical, and its drag coefficient is higher. The TBEx presents a "flat plate" like surface to the flow, but there is depth to the TBEx in the form of the CubeSat body as well as the depth of the solar panels and antennas. The coefficient of drag is therefore increased above the hypersonic limit for a diffuse flat plate normal to the flow 2. Figure 6.1 illustrates again that the free-molecular modeling approach is preferred at Knudsen numbers of 10

and above. The free-molecular method is a comparatively cheap way to approximate coefficients of drag for arbitrary bodies all the way up to Knudsen numbers of 1.

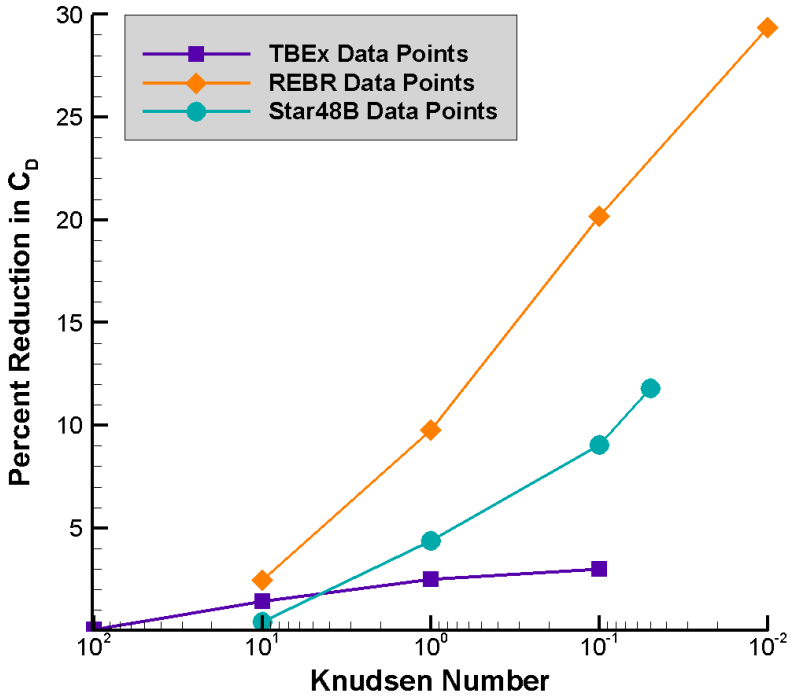

Figure 6.2: Percent reduction in constant drag coefficient (0° angle of attack) modeling results for each body (the TBEx, REBR, and Star48B) of the DSMC results versus the free-molecular results.

Figure 6.2 displays the percentage decrease of C_D DSMC results when compared to free-molecular results, for a constant flow facing area (0° angle of attack) of each body. Figure 6.2 makes the dependence of modeling accuracy on body shape evident: the effect of decreasing Knudsen number is much larger for the REBR than for the Star48B; and the effect of decreasing Knudsen number is much larger for the Star48B than the TBEx. This indicates that results are sensitive based on body shape. The Knudsen number at which the free-molecular modeling approach becomes inaccurate varies by body shape; therefore analyses on a specific body shape must be done to understand at exactly what Knudsen number the accuracy of the free-molecular

results when compared to the DSMC results becomes undesirable.

In Figure 6.1, it appears that the effect of the Knudsen number varies by shape. This affect is due to the Knudsen numbers analyzed being different for each shape, and is not dependent on the shape itself. The TBEx was modeled on Knudsen numbers of [100, 0.1], the Star48B on Knudsen numbers of [10, 0.05] and the REBR was modeled on Knudsen numbers of [10, 0.01]. Therefore, the fitted C_D DSMC results for the Star48B and REBR have an extra data point which lowers there slope when compared with the free-molecular results. More analysis should be conducted in the future on differing shapes to explore the dependence of Knudsen number where free-molecular approaches are no longer appropriate on three-dimensional shape.

The free-molecular approach becomes much less accurate when the Knudsen number drops below 1, as inter-molecular collisions become extremely important to the makeup of the flowfield. However, much of LEO exists in the free-molecular regime. The free-molecular modeling approach is therefore a powerful tool for gathering accurate estimations of experienced drag in LEO, prior to reentry, and is applicable to any body that can be represented by a surface mesh. The free-molecular model is very low-cost for any mesh that is appropriate for free-molecular flow (i.e., surface refined enough to represent curvature of the body).

Orbital decay analysis using the force analysis demonstrated the effect of different force models for each body. Differing orbital lifetime predictions using the simple orbital decay method applied inferred that tumbling does have a large effect on drag predictions, especially for non-aerodynamically stable bodies, such as the TBEx and Star48B. Aerodynamic coefficients only accounting for one angle of attack are missing information for passively orbiting bodies that almost certainly have rotational motion. Estimates of differences in ground impact distance were conducted for each body, which emphasized the need for accurate aerodynamic information. Ground

impact locations are highly sensitive due to reentry speed and motion of the Earth and slight differences in modeling of aerodynamic forces can change impact predicitons by thousands of kilometers.

6.2 Future Work

The findings in this thesis provoke several questions that could be investigated in future work. The analyses can be expanded to include differing accommodation coefficients, incorporating specular particle reflections off the surface, which may be appropriate for certain spacecraft outer materials. More-accurate atmospheric and gravity models could be used. CFD analysis could be included to identify the Knudsen number where CFD becomes preferable to DSMC, representing the desired modeling approaches for an entire reentry trajectory. The free-molecular modeling approach could be updated in a compiled language that could be parallelized on a cluster, therefore cutting wall time for extremely rarefied meshes. More bodies could be studied, such as many different CubeSat configurations. The REBR and Star48B, or bodies resembling them, could be meshed fully and tested at free-molecular Knudsen numbers to verify the information in this thesis as well as explore the effects the out-of-frame turning moment has. Higher-fidelity orbital decay and trajectory propagation models could be implemented. The models developed in the course of this work are modular, and can be "attached" or used in any other work that require forces and moments to be evaluated on bodies in rarefied flow. As more reentry data is gathered, these models can be compared to that data for validation purposes and modified as necessary. Lab experiments could also be conducted for validation data: representative spacecraft shapes placed in low-density wind tunnels could produce force measurements to be used for validation of model-

ing results. More sophisticated orbital decay trajectory methods could be implemented in order to project time-to-impact instead of time-to-reenter.

The orbital decay model developed in this work made several assumptions in order to reduce the number of inputs needed to estimate time-to-reenter for different bodies and situations. For future work, more sophisticated and accurate trajectory modeling should be implemented to grasp a better understanding in how different aerodynamic coefficient modeling affects impact location predictions. High-fidelity trajectory modeling including location relative to the Earth's surface could be implemented with high-fidelity wind and atmospheric data, date-tracking, and propagating the rotational motion of the Earth. Other variables could be included as well, such as the gravitational fluctuations in the Earth's field, the tilt of the Earth, and solar weather data that changes the Earth's atmosphere day to day. Such models would further reveal the effect of the aerodynamic coefficient results on impact time and location uncertainties.

More orbital and reentry data would improve all the modeling presented in this thesis. Imitating the mission design of the REBR, small spacecraft could be imbued with the ability to gather and transmit reentry data as their orbits degrade over time. Many small satellites already have some sensors and use space-based communication networks to transmit data to ground stations; extending the lifetime of these measurements into reentry would be immensely useful to further understanding reentry phenomena. Induced pressure information on spacecraft hardware surfaces would directly improve model predictions. Two-line-element (TLE) data could be used to improve the orbital modeling approach; interdisciplinary efforts to mine TLE data and empirically improve aerodynamic and orbital models would be a first step.

Lastly, all the modeling approaches discussed in this thesis could be applied to other planetary, or even solar, environments. Mars has a rarefied atmosphere; free-molecular simulations on Mars

entry vehicles could be performed, as an example.

APPENDIX A

TBEx: Force Results

This Appendix contains the figures representing the force results for the TBEx orientations at each Knudsen number in the cardinal (X, Y, and Z) directions. In the following appendix tables, "FMF" stands for free-molecular analytical results, and "NRMSD" stands for the root-mean-square deviation between the two methods across all orientations. The NRMSD listed here use the range of free-molecular results as the normalizing factor.

A.1 Knudsen Number of 100

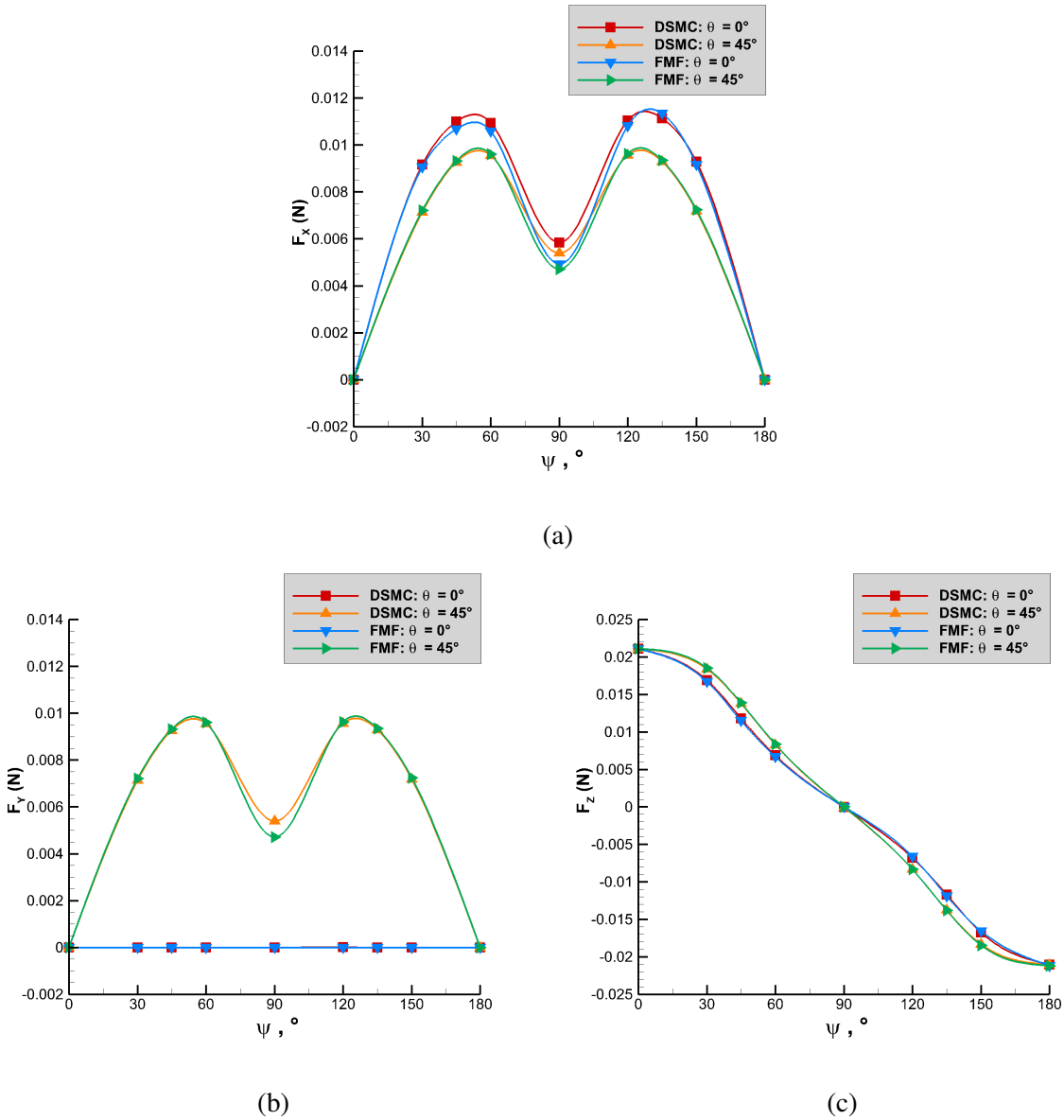

(a)

(b)

(c)

Figure A.1: Forces calculated using DSMC and free-molecular (FMF) analytical models for all experiment orientations of the TBEx in the: (a) X direction; (b) Y direction; (c) Z direction, for a Knudsen number of 100.

Table A.1: Average forces calculated for a Knudsen number of 100 for the DSMC and free-molecular analytical modeling approaches.

Average	**FMF**	**DSMC**	**NRMSD**
$\mathbf{F}_X$ **(N)**	7.08×10^{-3}	7.25×10^{-3} $\pm 5.80 \times 10^{-4}$	2.69%
$\mathbf{F}_Y$ **(N)**	3.28×10^{-3}	3.31×10^{-3} $\pm 2.65 \times 10^{-4}$	5.20%
$\mathbf{F}_Z$ **(N)**	-2.42×10^{-6}	1.55×10^{-5} $\pm 1.49 \times 10^{-4}$	0.35%

A.2 Knudsen Number of 10

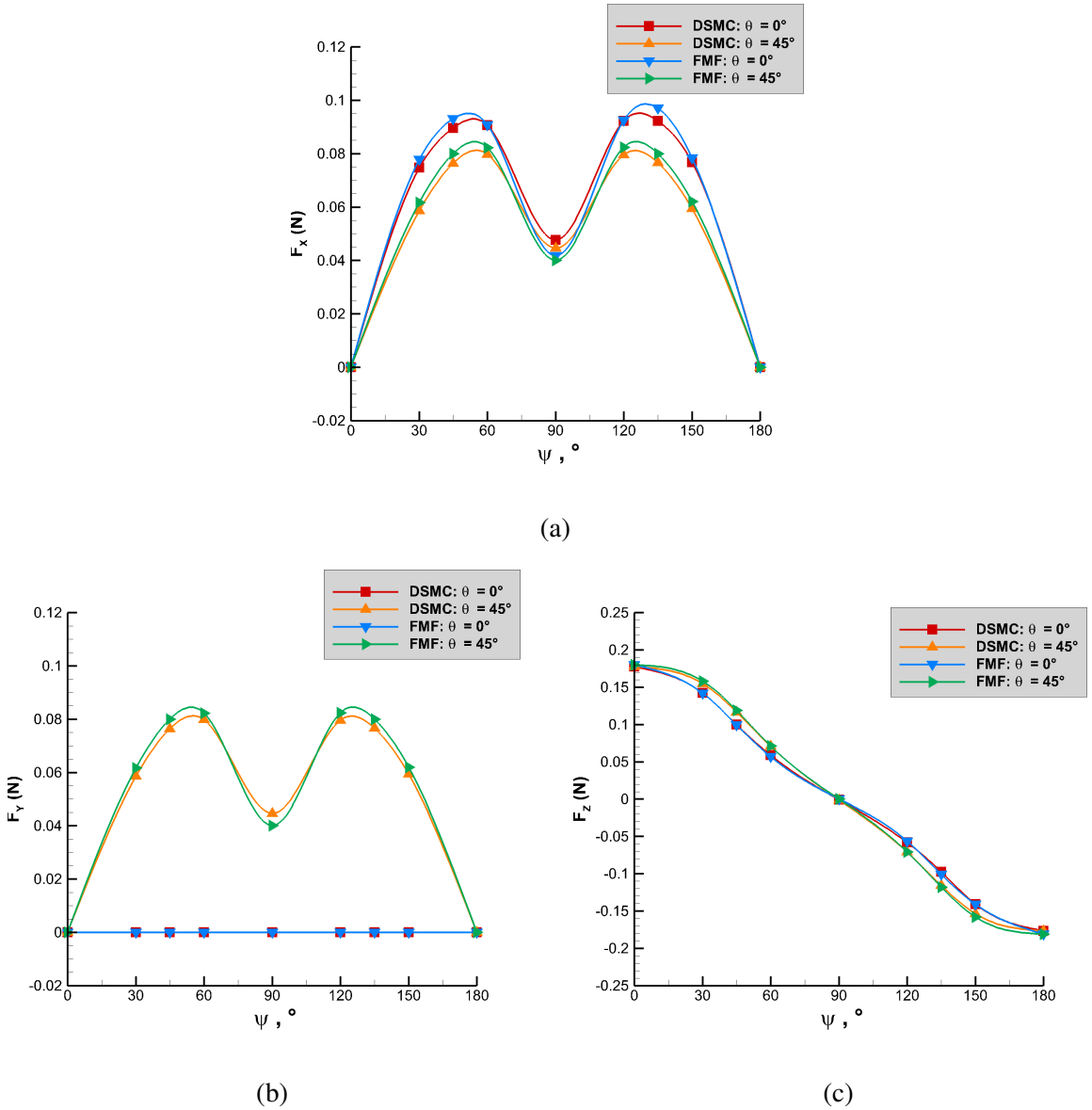

(a)

(b)

(c)

Figure A.2: Forces calculated using DSMC and free-molecular (FMF) analytical models for all experiment orientations of the TBEx in the: (a) X direction; (b) Y direction; (c) Z direction, for a Knudsen number of 10.

Table A.2: Average forces calculated for a Knudsen number of 10 for the DSMC and free-molecular analytical modeling approaches.

Average	**FMF**	**DSMC**	**NRMSD**
$\mathbf{F}_X$ **(N)**	5.99×10^{-2}	6.07×10^{-2} $\pm 4.86 \times 10^{-3}$	3.04%
$\mathbf{F}_Y$ **(N)**	2.80×10^{-2}	2.74×10^{-2} $\pm 2.19 \times 10^{-3}$	2.49%
$\mathbf{F}_Z$ **(N)**	1.25×10^{-5}	1.97×10^{-4} $\pm 1.58 \times 10^{-5}$	2.17%

A.3 Knudsen Number of 1

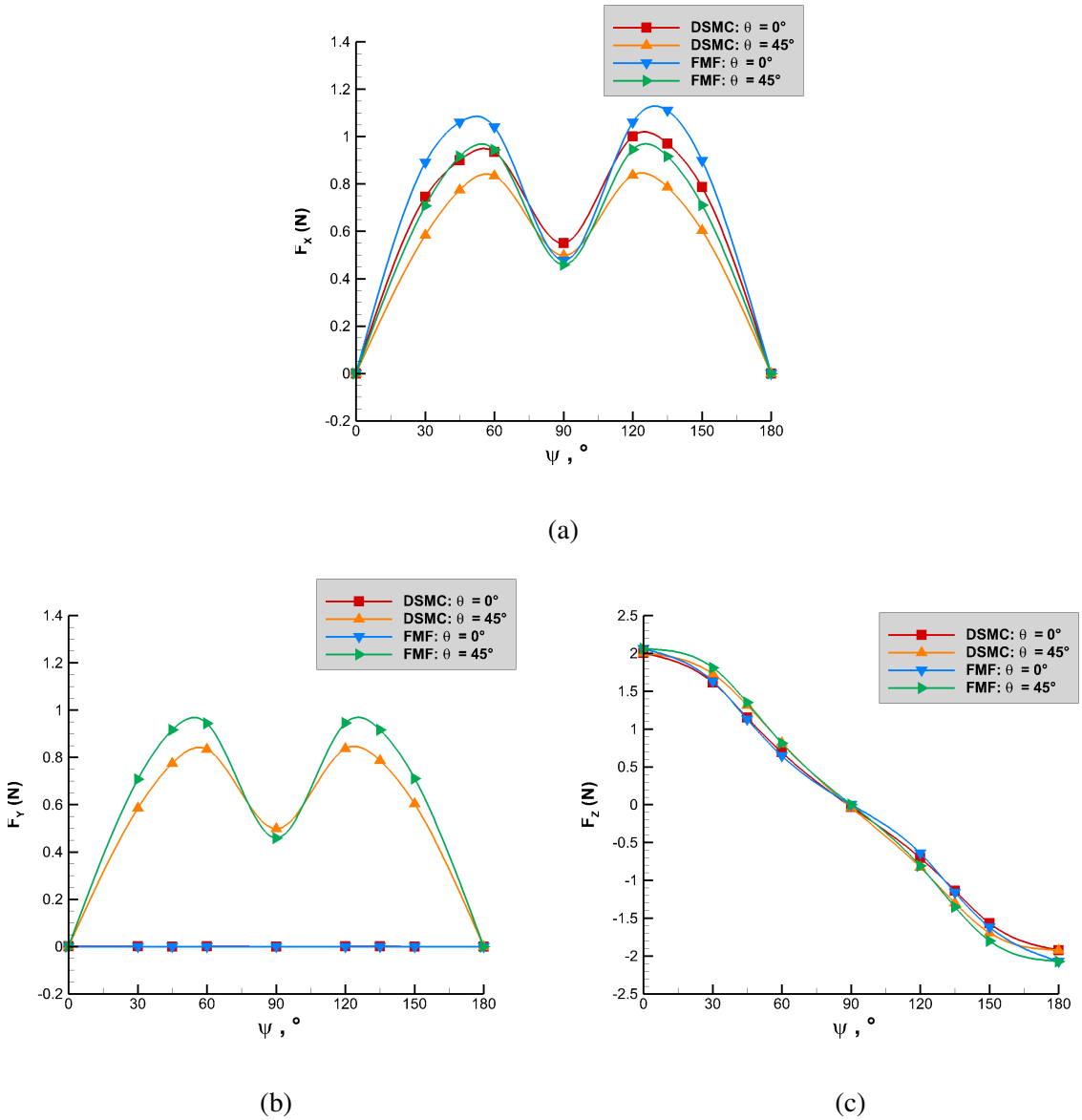

(a)

(b)

(c)

Figure A.3: Forces calculated using DSMC and free-molecular (FMF) analytical models for all experiment orientations of the TBEx in the: (a) X direction; (b) Y direction; (c) Z direction, for a Knudsen number of 1.

Table A.3: Average forces calculated for a Knudsen number of 1 for the DSMC and free-molecular analytical modeling approaches.

Average	**FMF**	**DSMC**	**NRMSD**
$\mathbf{F}_X$ **(N)**	6.95×10^{-1}	6.56×10^{-1} $\pm 5.25 \times 10^{-2}$	9.21%
$\mathbf{F}_Y$ **(N)**	3.21×10^{-1}	2.85×10^{-1} $\pm 2.28 \times 10^{-2}$	7.42%
$\mathbf{F}_Z$ **(N)**	-3.05×10^{-4}	6.18×10^{-3} $\pm 4.94 \times 10^{-4}$	1.64%

A.4 Knudsen Number of 0.1

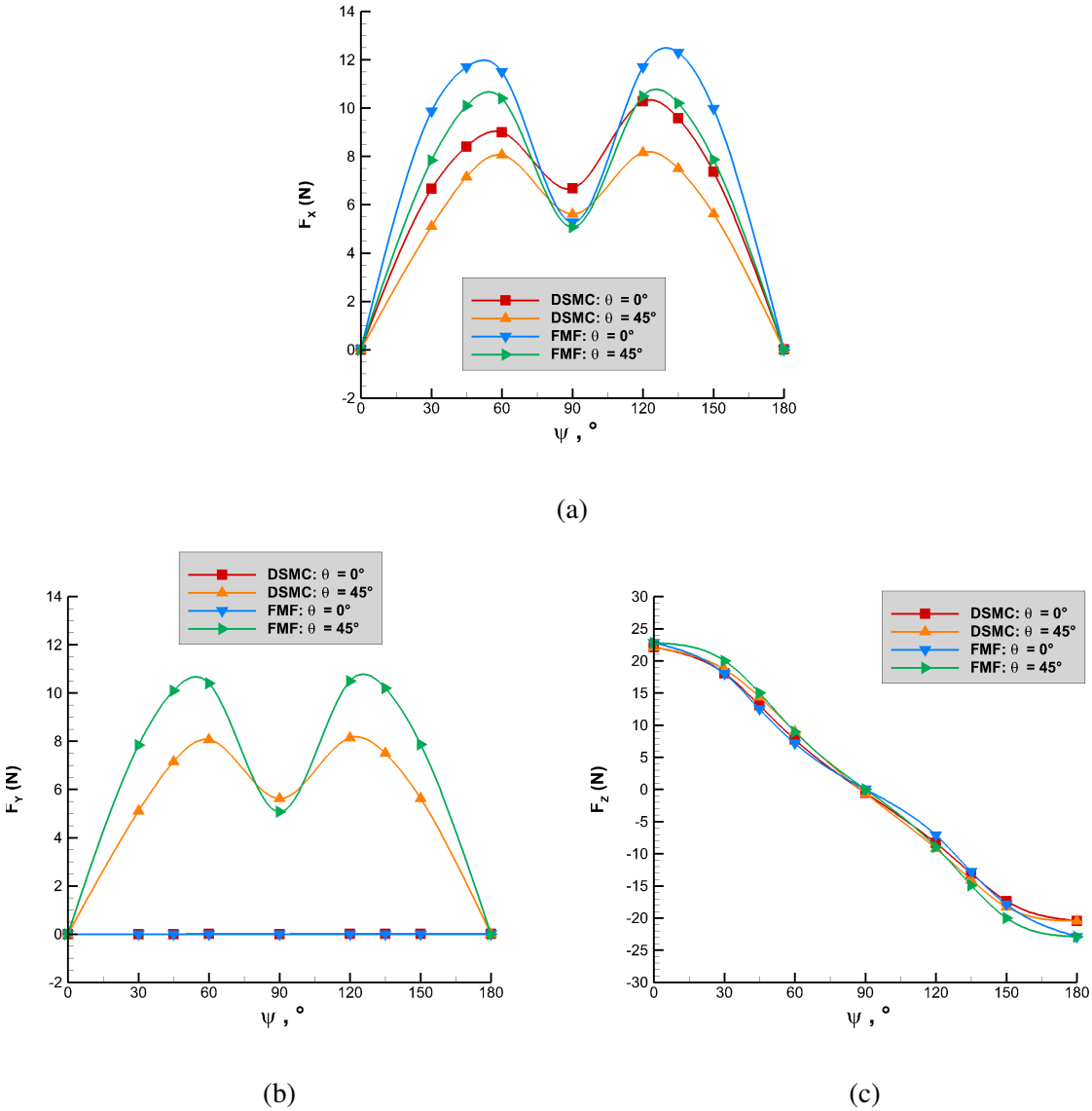

(a)

(b)

(c)

Figure A.4: Forces calculated using DSMC and free-molecular (FMF) analytical models for all experiment orientations of the TBEx in the: (a) X direction; (b) Y direction; (c) Z direction, for a Knudsen number of 0.1.

Table A.4: Average forces calculated for a Knudsen number of 0.1 for the DSMC and free-molecular analytical modeling approaches.

Average	**FMF**	**DSMC**	**NRMSD**
$\mathbf{F}_X$ **(N)**	7.69	6.15 $\pm 4.92 \times 10^{-1}$	21.2%
$\mathbf{F}_Y$ **(N)**	3.56	2.77 $\pm 2.85 \times 10^{-1}$	18.2%
$\mathbf{F}_Z$ **(N)**	-5.76×10^{-3}	7.66×10^{-2} $\pm 6.13 \times 10^{-3}$	2.58%

APPENDIX B

REBR: Additional Information and Results

Table B.1 enumerates the 12 orientations chosen to represent the REBR body. The left-hand column of Table B.1 is used for numbering the modeling orientations. The right-hand column contains a representative figure for each orientation. In each representative figure, the oncoming flow is pictured as one large streamline of the incoming flow at that orientation as modeled on the REBR body. The figures are pictured from the perspective of looking at the plane of symmetry that "slices" the REBR in half, and the REBR shape is concave due to that perspective. The red arrow in each representative figure in Table B.1 is the incoming flow velocity for that orientation; the box is the modeled farfield volume (for DSMC modeling).

Table B.1: Orientations used to model the REBR experiencing orbital velocities at the defined Knudsen numbers.

#	Ψ, °	Representative Figure
1	0	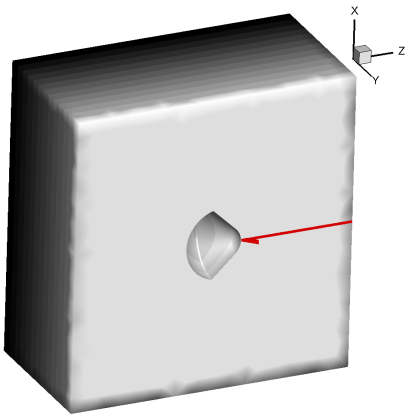
2	5	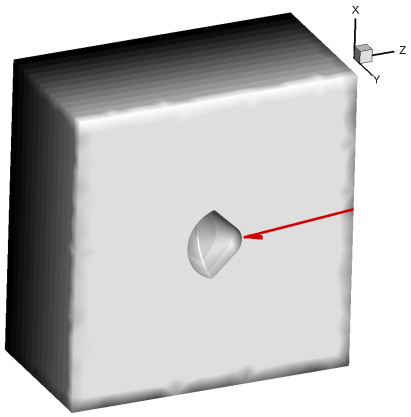
3	10	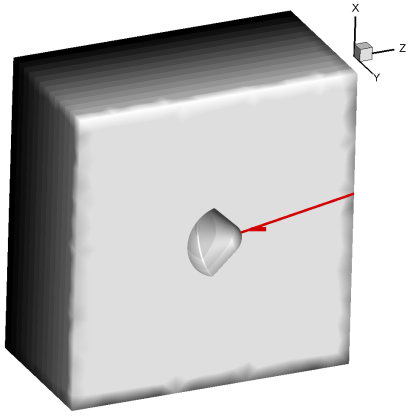

Continued on next page

Table B.1 – continued from previous page

#	ψ, $^\circ$	Representative Figure
4	20	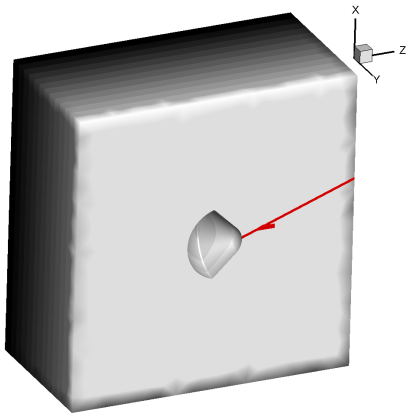
5	30	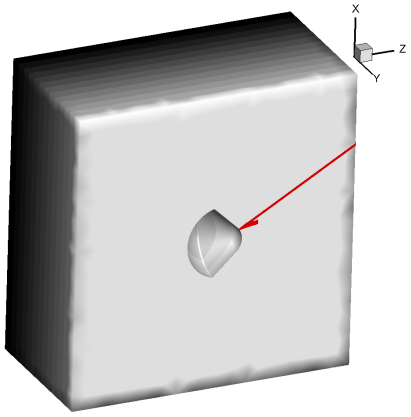
6	45	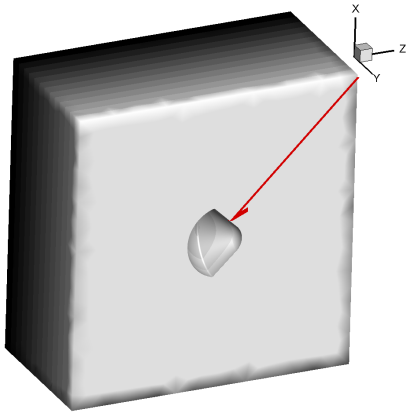

Continued on next page

Table B.1 – continued from previous page

#	ψ, °	Representative Figure
7	60	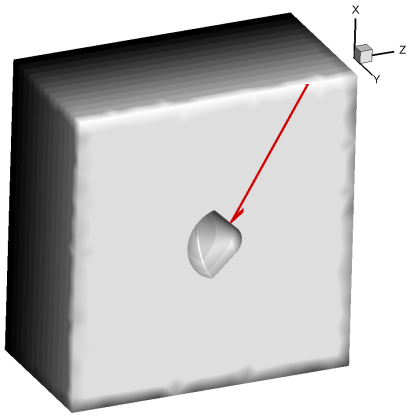
8	75	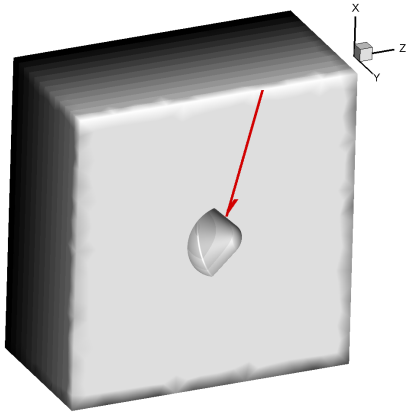
9	90	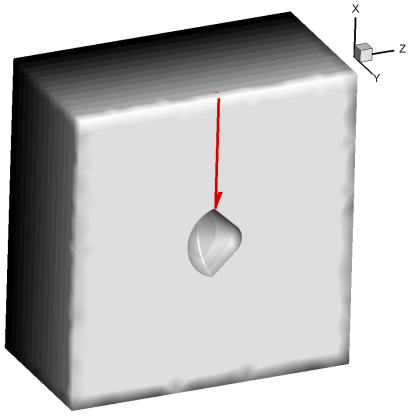

Continued on next page

Table B.1 – continued from previous page

#	ψ, °	Representative Figure
10	120	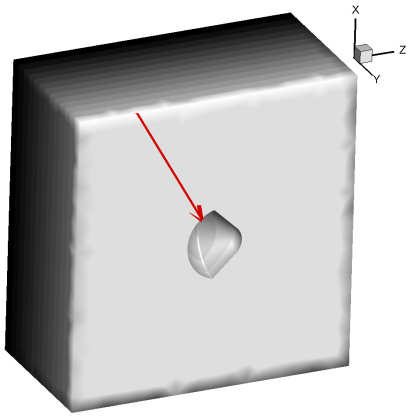
11	150	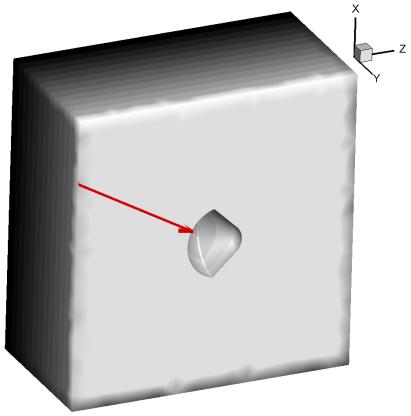
12	180	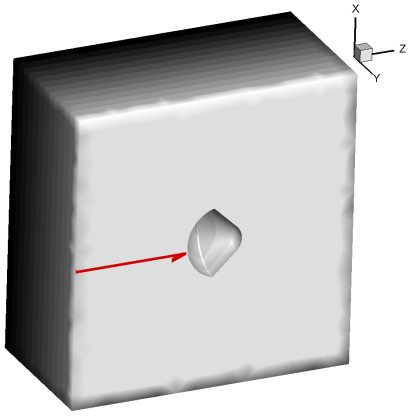

B.1 REBR: Force Results

This Appendix contains the figures representing the force results for the REBR orientations at each Knudsen number in the cardinal, non-symmetric (X and Z) directions. In the following appendix tables, “FMF” stands for free-molecular analytical results, and “NRMSD” stands for the root-mean-square deviation between the two methods across all orientations.

B.2 Knudsen Number of 10

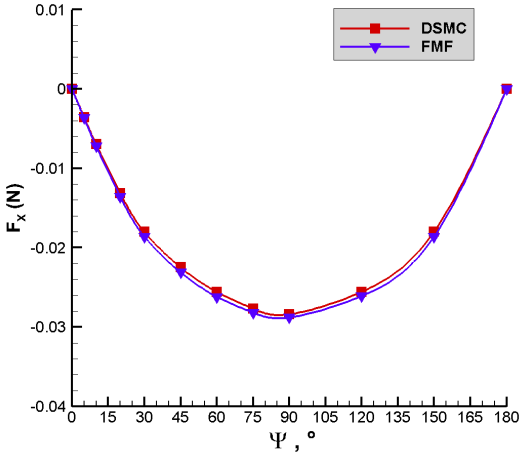

(a)

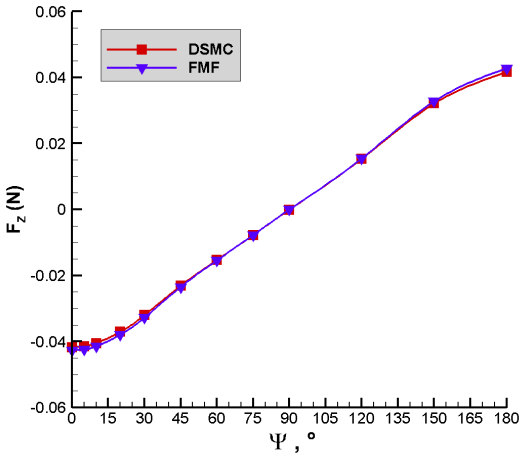

(b)

Figure B.1: Forces calculated using DSMC and free-molecular (FMF) analytical models for all experiment orientations of the REBR in the: (a) X direction and (b) Z direction for a Knudsen number of 10.

Table B.2: Average forces calculated for a Knudsen number of 10 for the DSMC and free-molecular analytical modeling approaches.

Average	**FMF**	**DSMC**	**NRMSD**
$\mathbf{F}_X$ **(N)**	-2.00×10^{-2}	-1.95×10^{-2} $\pm -1.17 \times 10^{-5}$	2.75%
$\mathbf{F}_Z$ **(N)**	-1.58×10^{-4}	-1.88×10^{-4} $\pm -1.13 \times 10^{-7}$	2.54%

B.3 Knudsen Number of 1

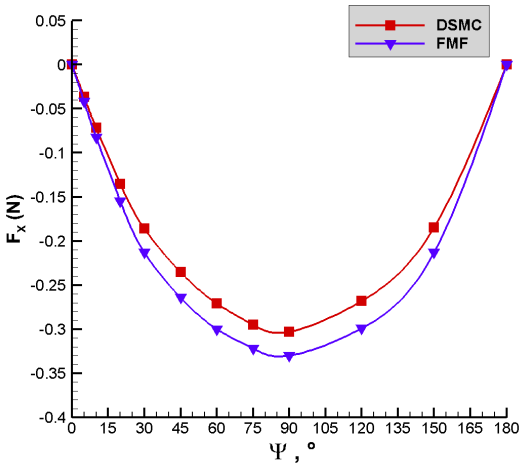

(a)

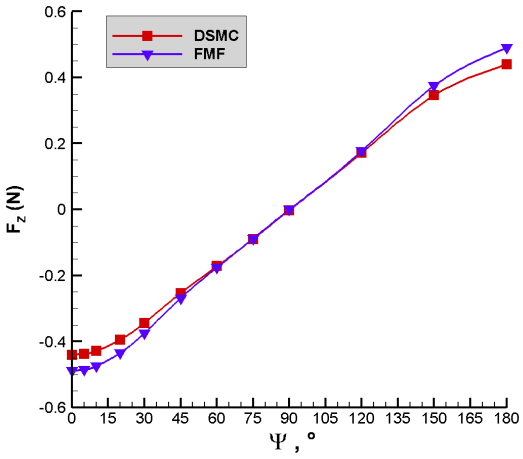

(b)

Figure B.2: Forces calculated using DSMC and free-molecular (FMF) analytical models for all experiment orientations of the REBR in the: (a) X direction and (c) Z direction, for a Knudsen number of 1.

Table B.3: Average forces calculated for a Knudsen number of 1 for the DSMC and free-molecular analytical modeling approaches.

Average	**FMF**	**DSMC**	**NRMSD**
$\mathbf{F}_X$ **(N)**	-2.28×10^{-1}	-2.05×10^{-1} $\pm -1.02 \times 10^{-4}$	12.3%
$\mathbf{F}_Z$ **(N)**	-1.91×10^{-3}	-2.31×10^{-3} $\pm -1.16 \times 10^{-6}$	10.3%

B.4 Knudsen Number of 0.1

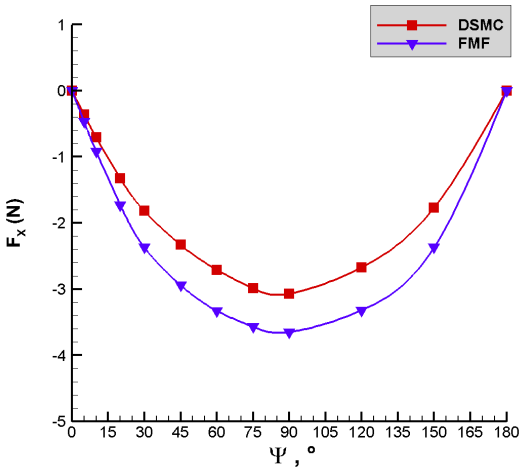

(a)

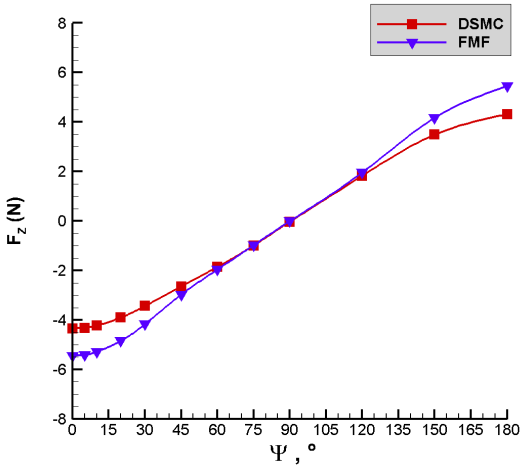

(b)

Figure B.3: Forces calculated using DSMC and free-molecular (FMF) analytical models for all experiment orientations of the REBR in the: (a) X direction and (c) Z direction, for a Knudsen number of 0.1.

Table B.4: Average forces calculated for a Knudsen number of 0.1 for the DSMC and free-molecular analytical modeling approaches.

Average	**FMF**	**DSMC**	**NRMSD**
$\mathbf{F}_X$ **(N)**	-2.54	-2.03 $\pm -1.02 \times 10^{-3}$	23.2%
$\mathbf{F}_Z$ **(N)**	-2.29×10^{-2}	-2.87×10^{-2} $\pm -1.43 \times 10^{-5}$	21.2%

B.5 Knudsen Number of 0.01

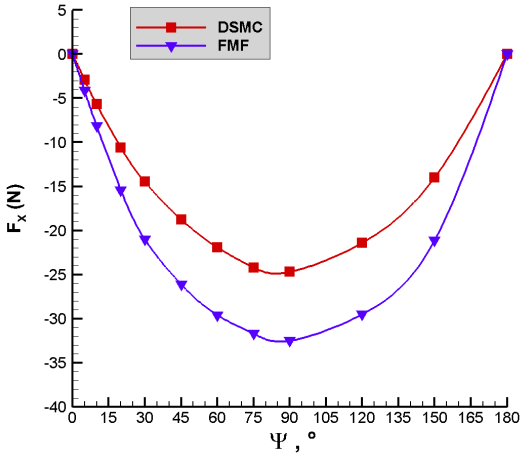

(a)

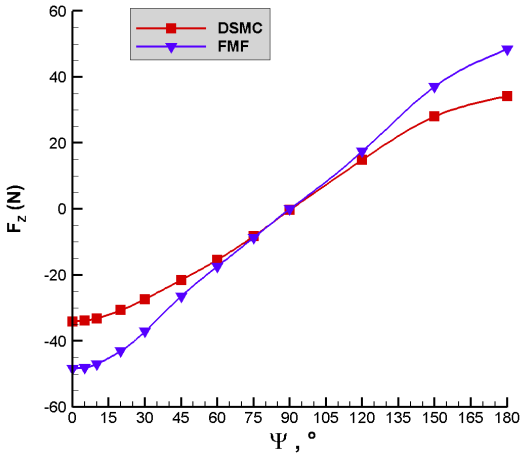

(b)

Figure B.4: Forces calculated using DSMC and free-molecular (FMF) analytical models for all experiment orientations of the REBR in the: (a) X direction and (c) Z direction, for a Knudsen number of 0.01.

Table B.5: Average forces calculated for a Knudsen number of 0.01 for the DSMC and free-molecular analytical modeling approaches.

Average	**FMF**	**DSMC**	**NRMSD**
$\mathbf{F}_X$ **(N)**	-22.5	-16.3 $\pm -\ 8.15 \times 10^{-3}$	32.4%
$\mathbf{F}_Z$ **(N)**	-2.05×10^{-1}	-2.07×10^{-1} $\pm -\ 1.04 \times 10^{-4}$	31.2%

APPENDIX C

Star48B: Force Results

This Appendix contains the figures representing the force results for the Star48B orientations at each Knudsen number in the cardinal, non-symmetric (X and Y) directions. In the following appendix tables, “FMF” stands for free-molecular analytical results, and “NRMSD” stands for the root-mean-square deviation between the two methods across all orientations.

C.1 Knudsen Number of 10

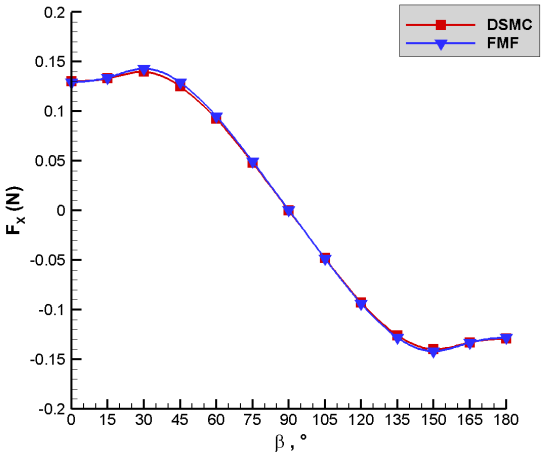

(a)

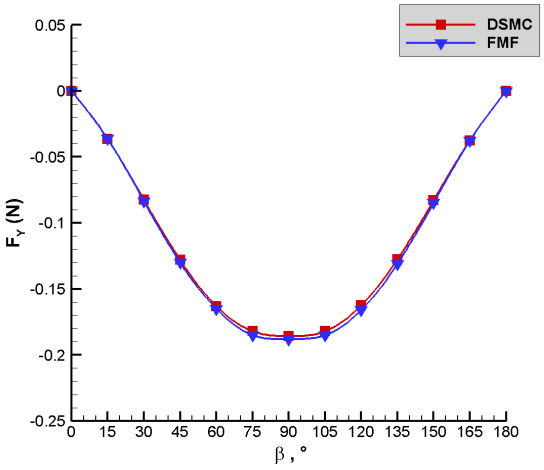

(b)

Figure C.1: Forces calculated using DSMC and free-molecular (FMF) analytical models for all experiment orientations of the Star48B in the: (a) X direction and (b) Y direction for a Knudsen number of 10.

Table C.1: Average forces calculated for a Knudsen number of 10 for the DSMC and free-molecular analytical modeling approaches.

Average	**FMF**	**DSMC**	**NRMSD**
$\mathbf{F}_X$ **(N)**	5.13×10^{-4}	-4.79×10^{-5} $\pm -2.40 \times 10^{-8}$	1.69%
$\mathbf{F}_Y$ **(N)**	-1.16×10^{-1}	-1.14×10^{-1} $\pm -5.71 \times 10^{-5}$	2.05%

C.2 Knudsen Number of 1

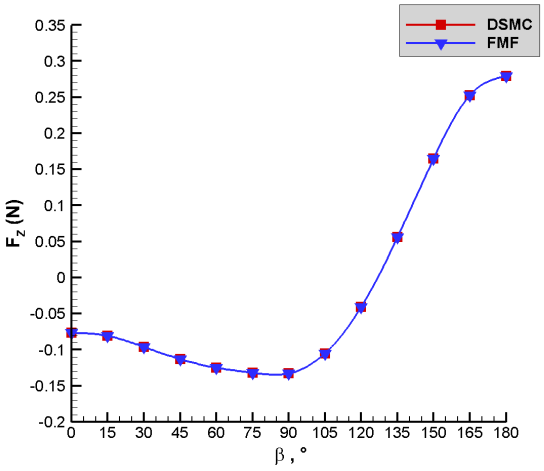

(a)

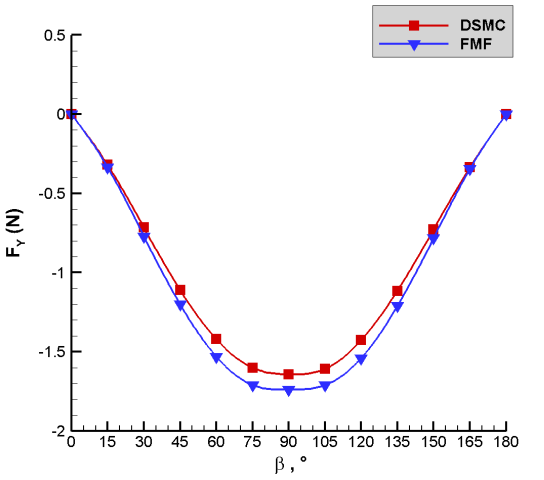

(b)

Figure C.2: Forces calculated using DSMC and free-molecular (FMF) analytical models for all experiment orientations of the Star48B in the: (a) X direction and (c) Y direction, for a Knudsen number of 1.

Table C.2: Average forces calculated for a Knudsen number of 1 for the DSMC and free-molecular analytical modeling approaches.

Average	**FMF**	**DSMC**	**NRMSD**
$\mathbf{F}_X$ **(N)**	4.02×10^{-3}	-5.57×10^{-3} $\pm -2.23 \times 10^{-6}$	7.95%
$\mathbf{F}_Y$ **(N)**	-1.07	-1.00 $\pm -4.01 \times 10^{-4}$	7.98%

C.3 Knudsen Number of 0.1

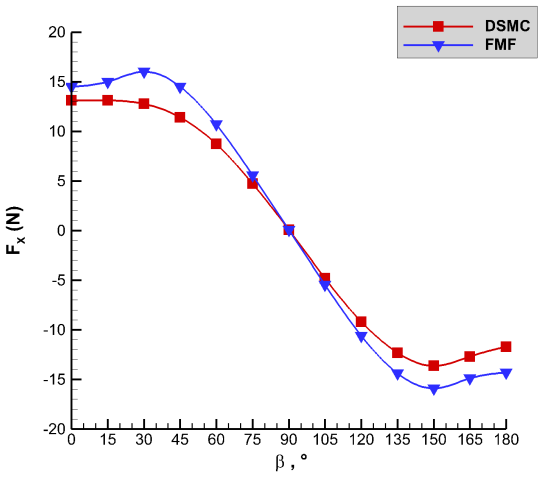

(a)

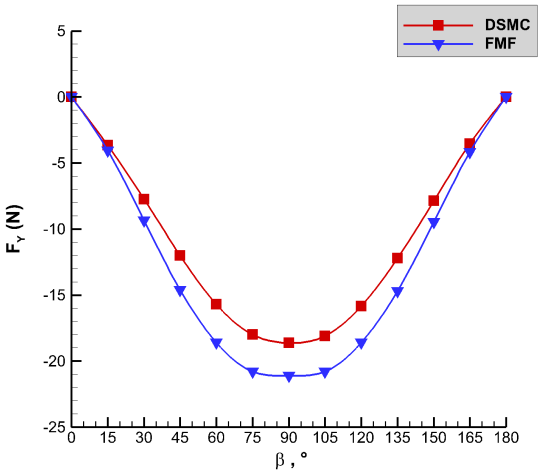

(b)

Figure C.3: Forces calculated using DSMC and free-molecular (FMF) analytical models for all experiment orientations of the Star48B in the: (a) X direction and (c) Y direction, for a Knudsen number of 0.1.

Table C.3: Average forces calculated for a Knudsen number of 0.1 for the DSMC and free-molecular analytical modeling approaches.

Average	**FMF**	**DSMC**	**NRMSD**
$\mathbf{F}_X$ **(N)**	5.44×10^{-2}	-9.78×10^{-2} $\pm -1.96 \times 10^{-5}$	17.3%
$\mathbf{F}_Y$ **(N)**	-13.0	-11.1 $\pm -2.22 \times 10^{-3}$	17.1%

C.4 Knudsen Number of 0.05

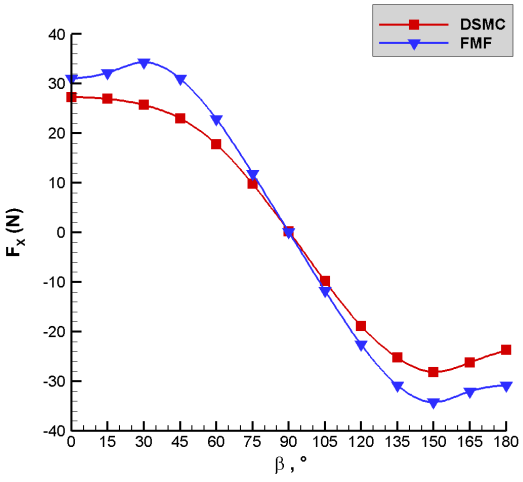

(a)

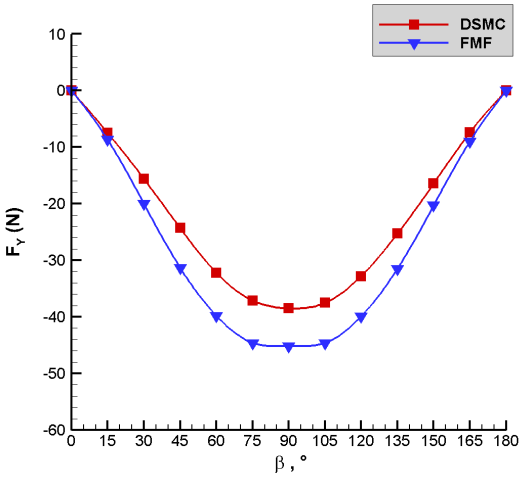

(b)

Figure C.4: Forces calculated using DSMC and free-molecular (FMF) analytical models for all experiment orientations of the Star48B in the: (a) X direction and (c) Y direction, for a Knudsen number of 0.05.

Table C.4: Average moments calculated for a Knudsen number of 0.05 for the DSMC and free-molecular analytical modeling approaches.

Average	**FMF**	**DSMC**	**NRMSD**
$\mathbf{F}_X$ **(N)**	1.01×10^{-1}	-2.48×10^{-1} $\pm -3.47 \times 10^{-4}$	21.6%
$\mathbf{F}_Y$ **(N)**	-27.9	-22.9 $\pm -3.21 \times 10^{-2}$	21.1%

BIBLIOGRAPHY

[1] "ESA's Annual Space Environment Report," Technical report, European Space Agency Space Debris Office, September 2020.

[2] Kulu, E., "Nanosatellite & CubeSat Database," 2021, https://www.nanosats.eu, Last accessed on 2021-01-21.

[3] Curzi, G., Modenini, D., and Tortora, P., "Large Constellations of Small Satellites: A Survey of Near Future Challenges and Missions," *Aerospace*, Vol. 7, No. 9, 2020, pp. 133:1–18.

[4] Turansky, C., *High-Fidelity Dynamic Modeling of Spacecraft in the Continuum-Rarefied Transition Regime*, Ph.D. thesis, University of Colorado, Boulder, 3775 Discovery Drive, Boulder, CO 80303, 2013.

[5] Curtis, H. D., *Orbital Mechanics for Engineering Students*, Elsevier, 2005.

[6] Kennewell, J., "Satellite Orbital Decay Calculations," Technical report, IPS Radio & Space Services, Sydney, Australia, 1999.

[7] Carter, D. and Radhakrishnan, R., "TBEX Orbital Lifetime Simulations," Technical report, University of Michigan Michigan Exploration Laboratory, 2015.

[8] "CubeSat Design Specification Rev.13," Technical report, The CubeSat Program, Cal Poly SLO, 2014.

[9] Picone, J. M., Hedin, A. E., Drob, D. P., and Aikin, A. C., "NRLMSISE-00 empirical model of the atmosphere: Statistical comparisons and scientific issues," *Journal of Geophysical Research: Space Physics*, Vol. 107, No. A12, 2002, pp. SIA 15–1–SIA 15–16.

[10] Weaver, M. A. and Ailor, W. H., "Reentry Breakup Recorder: Concept, Testing, Moving Forward," *AIAA SPACE Conference*, AIAA Paper 2012-5271, September 2012.

[11] "ATK Space Propulsion Products Catalog," catalog, TK Alliant Techsystems Thiokol Propulsion, May 2008.

[12] "U.S. Standard Atmosphere," Technical report, National Oceanic and Atmospheric Administration, National Aeronautics and Space Administration, 1976.

[13] Ailor, W., Hallman, W., Steckel, G., and Weaver, M., "Analysis of Reentered Debris and Implications for Survivability Modeling," *ESA SP-587*, In 4th European Conference on Space Debris (Vol. 587, p. 539), August 2005.

[14] Wang, T., "Analysis of Debris from the Collision of the Cosmos 2251 and the Iridium 33 Satellites," *Science & Global Security*, Vol. 18, 2010, pp. 87–118.

[15] Ailor, W., Dupzyk, I., Shepard, J., and Newfield, M., "REBR: An Innovative, Cost-Effective System for Return of Reentry Data," *AIAA SPACE Conference*, AIAA Paper 2012-5271, September 2007.

[16] Clark, S., "NASA: Tracking CubeSats is easy, but many stay in orbit too long," *Space Flight Now*, July 2015, https://spaceflightnow.com/2015/07/30/nasa-tracking-cubesats-is-easy-but-many-stay-in-orbit-too-long, Last accessed on 2021-01-21.

[17] Pilinski, M. D., Argrow, B. M., and Palo, S. E., "Semi-Empirical Satellite Accommodation Model for Spherical and Randomly Tumbling Objects," *Journal of Spacecraft and Rockets*, Vol. 50, No. 3, 2013, pp. 556–571.

[18] Hart, K. A., Simonis, K. R., Steinfeldt, B. A., and Braun, R. D., "Analytic Free-Molecular Aerodynamics for Rapid Propagation of Resident Space Objects," *Journal of Spacecraft and Rockets*, Vol. 55, No. 1, 2018, pp. 27–36.

[19] Pontieu, B. D., "Database of Photometric Periods of Artificial Satellites," *Advances in Space Research*, Vol. 19, No. 2, 1997, pp. 229–232.

[20] Boyd, I. D. and Schwartzentruber, T. E., *Nonequilibrium Gas Dynamics and Molecular Simulation*, Cambridge University Press, 2017.

[21] Messier, D., "NASA Prepares to Launch Twin Satellites to Study Signal Disruption from Space," Parabolic Arc, June 2019, http://www.parabolicarc.com/, Last accessed on 2021-01-21.

[22] Dietrich, S. and Boyd, I. D., "Scalar and Parallel Optimized Implementation of the Direct Simulation Monte Carlo Method," *Journal of Computational Physics*, Vol. 126, 1996, pp. 328–342.

[23] Kannenberg, K. C. and Boyd, I. D., "Three-Dimensional Monte Carlo Simulations of Plume Impingement," *Journal of Thermophysics and Heat Transfer*, Vol. 13, No. 2, 1999, pp. 226–235.

[24] Wiesel, W. E., *Spaceflight Dynamics*, McGraw-Hill, 1997.

[25] Gombosi, T. I., *Gaskinetic Theory*, Cambridge University Press, 1994.

[26] Roth, E. A., "The Gaussian Form of the Variation-of-Parameter Equations Formulated in Equinoctial Elements - Applications: Airdrag and Radiation Pressure," *Aeta Astronautica*, Vol. 12, No. 10, 1985, pp. 719–730.

[27] dePater, I. and Lissauer, J. J., *Planetary Sciences*, Cambridge University Press, 2010.

[28] Stephenson, A., "TBEx Launched, Deployed, and Operational," The Michigan eXploration Lab, August 2019, https://exploration.engin.umich.edu, Last accessed on 2021-01-21.

[29] Kaplan, C. I. and Boyd, I. D., "Drag Analysis of a Tumbling 3U CubeSat Experiencing Orbital Decay," *AIAA Aviation Forum*, AIAA Paper 2019-3264, June 2019.

[30] "U.S. Standard Atmosphere," Technical report, National Oceanic and Atmospheric Administration, National Aeronautics and Space Administration, 1962.

[31] Anderson, J. D., *Fundamentals of Aerodynamics*, McGraw Hill, 2001.

[32] Al-Obaidi, A. S. and Moo, J. X. Y., "Effect of atmospheric altitude on the drag of wing at subsonic and supersonic speeds," *Journal of Engineering Science and Technology*, Vol. 12, 05 2017, pp. 71–83.

[33] Rincon, P., "What is the SpaceX Crew Dragon?" BBC News, November 2019, https://www.bbc.com/news/science-environment-52840482, Last accessed on 2021-01-21.

[34] Corporation, T. A., "Satellite Reentry: Manipulating the Plunge," Aerospace News, May 5 2018, https://aerospace.org/article/satellite-reentry-manipulating-plunge, Last accessed on 2021-01-29.

[35] "N.A.S.A's Orion Spacecraft," Fact sheet, National Aeronautics and Space Administration, 2019, https://www.nasa.gov/exploration/systems/orion/media-resources, Last accessed on 2021-01-21.

[36] Kaplan, C. I. and Boyd, I. D., "Drag analysis of an orbiting tumbling body at the onset of reentry," *AIP Conference Proceedings*, In Proceedings of the 31st Rarefied Gas Dynamics Symposium, Glasgow, Scotland (Vol. 2132, p. 100006), 2019.

[37] Erwin, S., "Acquisition of Orbital ATK approved, company renamed Northrop Grumman Innovation Systems," Space News, June 2018, https://spacenews.com, Last accessed on 2021-01-21.

[38] Sanofsky, K. G. and McCluskey, P. M., "Critical Items List No. 10-02-01-05R/01," Fact sheet, ATK Alliant Techsystems Thiokol Propulsion, June 2002, CIL for Space Shuttle RSRM 10, Nozzle Subsystem 10-02, Nozzle and Aft Exit Cone 10-01-01.

[39] "Pam-D Debris Falls in Saudi Arabia," *The Orbital Debris Quarterly News*, The Orbital Debris Program Office at NASA Johnson Space Center, Houston TX, April 2001.

[40] Ailor, W., Hallman, W., Steckel, G., and Weaver, M., "Test Cases for Reentry Survivability Modeling," *ESA SP-699*, October 2011.